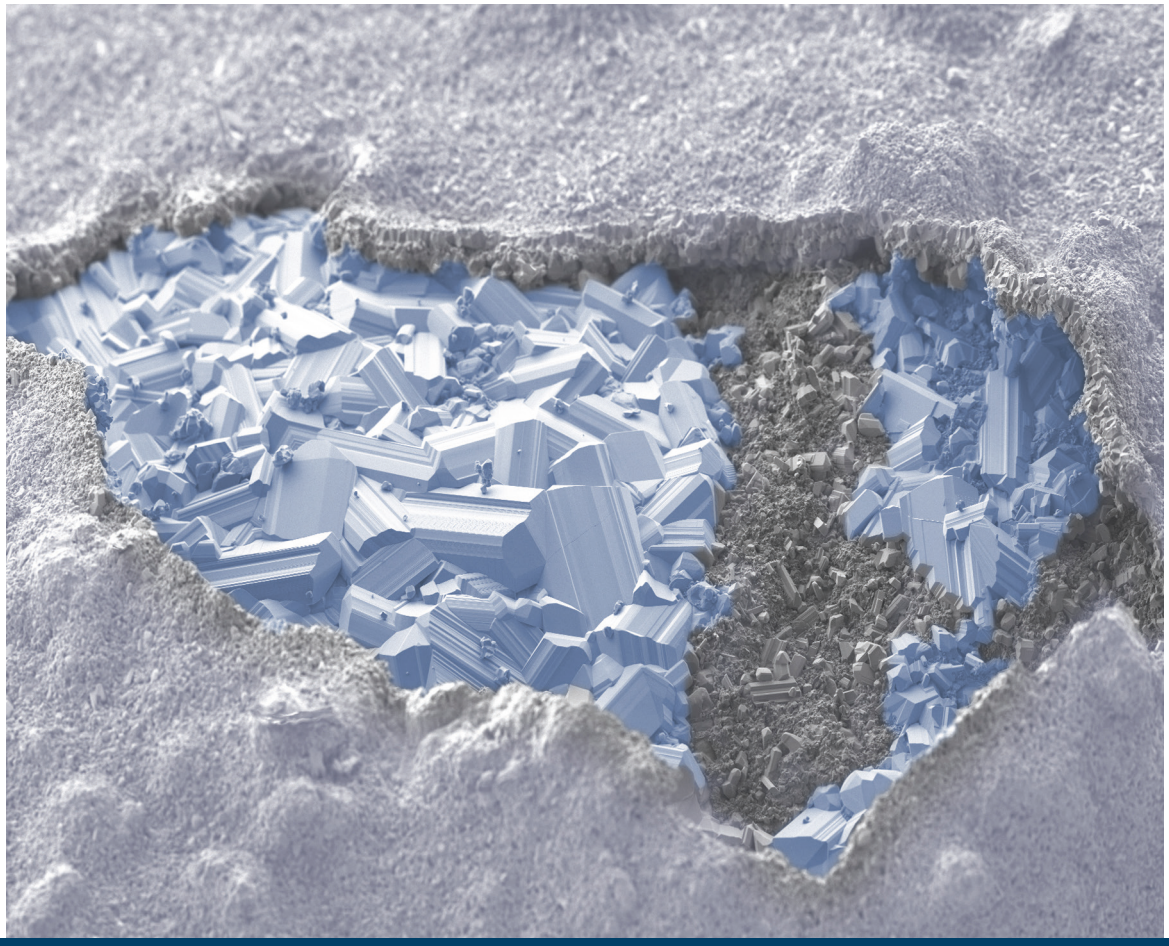

Development of components based on Ti_2AlC / fiber composites for aggressive environmental conditions

Sylvain Badie

Energie & Umwelt / Energy & Environment
Band / Volume 603
ISBN 978-3-95806-680-9

Mitglied der Helmholtz-Gemeinschaft

JÜLICH
Forschungszentrum

Schriften des Forschungszentrums Jülich
Reihe Energie & Umwelt / Energy & Environment Band / Volume 603

Forschungszentrum Jülich GmbH
Institut für Energie- und Klimaforschung
Werkstoffsynthese und Herstellungsverfahren (IEK-1)

Development of components based on Ti_2AlC/fiber composites for aggressive environmental conditions

Sylvain Badie

Schriften des Forschungszentrums Jülich
Reihe Energie & Umwelt / Energy & Environment Band / Volume 603

ISSN 1866-1793 ISBN 978-3-95806-680-9

Bibliografische Information der Deutschen Nationalbibliothek.
Die Deutsche Nationalbibliothek verzeichnet diese Publikation in der Deutschen Nationalbibliografie; detaillierte Bibliografische Daten sind im Internet über http://dnb.d-nb.de abrufbar.

Herausgeber und Vertrieb:	Forschungszentrum Jülich GmbH Zentralbibliothek, Verlag 52425 Jülich Tel.: +49 2461 61-5368 Fax: +49 2461 61-6103 zb-publikation@fz-juelich.de www.fz-juelich.de/zb
Umschlaggestaltung:	Grafische Medien, Forschungszentrum Jülich GmbH
Titelbild:	Die falsch eingefärbte rasterelektronenmikroskopische Aufnahme zeigt die Bruchfläche einer Al_2O_3-Blase, die sich während der Oxidation von Ti_2AlC bei 1200 °C nach 1250 Stunden gebildet hat. Eine Ursache für die Bildung solcher Blasen könnten die großen Wachstumsspannungen in der Aluminiumoxidschicht sein. Das Bild zeigt die Bildung großer Rutilkristalle, die wahrscheinlich auf lokale Veränderungen des Sauerstoffpartialdrucks zurückzuführen sind. Das Bild wurde von Frau Beatrix Göths am IEK-4 aufgenommen und von Frau Hiltrud Moitroux mittels Adobe Photoshop® koloriert.
Druck:	Grafische Medien, Forschungszentrum Jülich GmbH
Copyright:	Forschungszentrum Jülich 2022

Schriften des Forschungszentrums Jülich
Reihe Energie & Umwelt / Energy & Environment, Band / Volume 603

D 82 (Diss. RWTH Aachen University, 2022)

ISSN 1866-1793
ISBN 978-3-95806-680-9

Vollständig frei verfügbar über das Publikationsportal des Forschungszentrums Jülich (JuSER) unter www.fz-juelich.de/zb/openaccess.

This is an Open Access publication distributed under the terms of the Creative Commons Attribution License 4.0, which permits unrestricted use, distribution, and reproduction in any medium, provided the original work is properly cited.

Acknowledgements

Life is not always a long quiet river and I had to face several ups and downs during this PhD. The completion of this 3-year long project would not have been possible without the invaluable assistance and mental support from many contributors.
I would first like to express my deepest gratitude to my supervisor and scientific advisor, Prof. Dr.-Ing. Jesus Gonzalez-Julian. By offering me this PhD position you genuinely contributed to shape the foundations of my future professional career and strengthened my taste for research and science. Sharing your enlightening experience in the field of ceramic science and engineering was as priceless as your solid counsel and suggestions, your formidable positive attitude and the extraordinary motivation you conveyed to me. I hope our friendship will be durable.
I would also like to acknowledge the precious help of my trusted colleague Rimy Gabriel. Your hard-working, your perseverance, your warmheartedness and communicative optimism represented an inestimable support and inspiration to me.
My heartfelt obligation is also dedicated to my colleague and good friend Ralf Steinert. Our daily casual discussions helped me to divert negative thoughts and to take my mind off professional and personal issues and frustrations.
I thank profusely my PhD examination committee for their helpful input and comments to improve the quality of my thesis. My profound thankfulness is addressed to the committee members Univ.-Prof. Dr.-Ing. Daniela Zander and Prof. Dr.-Ing. habil. Hauke Springer. I am also greatly indebted to Prof. Dr.-Ing. Olivier Guillon for his valuable guidance in good scientific practice and for embodying a professional model.
My sincere appreciation also goes to all my colleagues in IEK-1 who supported me in many aspects. I address special thanks to Prof. Robert Vaßen for the instructive discussions and the conceptualization of the rumpling model, to Volker Bader for his assistance and expertise in heat treatments, to Dr. Doris Sebold for her conscientious and efficacious work on the SEM, to Hiltrud Moitroux for her patience and availability for the tremendous number of pictures I asked her to take, to Marie-Theres Gerhards for her compassion and her permanent high spirits. I would like to further address my sincere recognition to Yoo-Jung Sohn, Frank Kurze, Beatrix Göths, Sigrid Schwartz-Lückge, Jochen Fiebig, Andrea Hilgers, Martin Tandler, Ralf Kauert, to the workshop team, Erhan Sucuoglu, Annika Seifert, Ralf Laufs, the secretary team, Stefan Weitz, Sandra Schädel, Yvonne Lichtenfeld, Vicky Tirtey, and to Xiaoqiang Li, Teresa Go, Melina Poll, and many others. I also acknowledge colleagues from IEK-2, ZEA-1 and ZEA-3 for their helpful service and assistance.
Last but not least, I would like to thank from the absolute bottom of my heart my beloved parents, Ellen and Bruno Badie, and my dear sister Estelle Badie. They are my true pillars of life and their love, my unique sanctuary. I dedicate this work, with pride, to my grandparents Marguerite and Léon Badie, whose wisdom and magnanimity I keep in mind. Un très grand merci à vous tous !

Abstract

MAX phases are a promising family of materials with currently more than 150 different compositions, which are based on nanolayered carbides and nitrides. They exhibit unusual properties, bridging the gap between metals and ceramics, as they combine features from both categories. From their metallic aspect, they present good damage tolerance, thermal shock resistance, they are machinable and have high electrical conductivity; while their ceramic-like characteristics translate into high stiffness (high elastic modulus), high melting points (though incongruent), low density and good thermo-mechanical properties at high temperature, such as creep resistance. Additionally, they possess an intermediate coefficient of thermal expansion, a good radiation tolerance, and some of them exhibit excellent oxidation resistance and a self-healing ability under oxidizing environments.

This unique combination of properties is of capital interest for potential high-temperature applications, which involve severe corrosive conditions. MAX phases could serve as structural materials or protective coatings for gas turbines, heat exhausts, nozzles, heating elements, solar receivers in concentrated solar power facilities, but also as fuel cladding in nuclear power plants, catalysts and electrical contacts. However, their transfer to the market as end products has been hindered by different factors, and several aspects still remain unexplored. The present thesis aims to contribute to this latter point.

This work focuses on the fabrication of oxide ceramic fiber-reinforced (Al_2O_3 and $3Al_2O_3{\cdot}2SiO_2$) Ti_2AlC composites with more complex shapes than the traditionally produced samples found in literature, having basic geometries. Ti_2AlC powders were produced via the molten salt shielded synthesis, of which various parameters (synthesis temperature, holding time, molar ratio of elemental reactants, batch size) were optimized to satisfactorily come close to a high-purity product and relatively large contents. These powders were characterized and conditioned properly to serve as basis for a series of experiments.

To study the sinterability of monolithic Ti_2AlC and composites thereof, its densification via pressureless sintering and field assisted sintering technology/spark plasma sintering (FAST/SPS) was investigated. While the former required high temperatures (>1400 °C) and long holding times (>3 h) to achieve partial densification (up to max. 93% of the theoretical density), the latter turned out to effectively lead to near-complete consolidation (up to ~99%) at lower temperature (1200 °C) and within shorter times of at least 10 min.

As such, FAST/SPS was selected for the production of dense cylindrical substrates to fulfil the goals of investigating the oxidation performance and mechanical properties.

In parallel, as-synthesized highly pure Ti_2AlC powders were employed to produce feedstocks for powder injection molding. Whether bare, or in combination with oxide ceramic fibers, near net shape complex assemblies could rapidly be manufactured at affordable costs for industry. After extraction of the organic components, pressureless sintering was undertaken as a pre-sintering step. Further, the method of consolidation of complex shapes in a bed of graphite was employed using the FAST/SPS technology and demonstrated interesting preliminary results.

In addition, the oxidation performance of Ti_2AlC-based substrates and composites, whether bare or coated with yttria-stabilized-zirconia was scrutinized. Two main trends were observed: the first concerned the formation of dense Al_2O_3 scales and their protective nature, allowing the considered specimens to demonstrate outstanding performance, as much under isothermal static as cyclic conditions. These survived up to 1500 hours when subjected to harsh conditions and proved the high compatibility of Ti_2AlC with conventional thermal barrier coating materials. The second trend, which is less reported in literature, involved the breakaway oxidation of components. Depending on the machining conditions and surface preparation, the anomalous growth of rutile-TiO_2 outpaced the slowly growing Al_2O_3 and eventually led to catastrophic consumption of the base material.

So as to present these outcomes in a logical order, the structure of this work is as follows: **Chapter I** introduces the main concepts about MAX phases and establishes a state of the art from various perspectives (synthesis, oxidation, mechanical properties). **Chapter II** exposes the various experimental procedures employed. **Chapter III** deals with the synthesis of Ti_2AlC, its optimization and the characterization of the obtained pulverulent products. **Chapter IV** presents the fabrication of complex shapes via injection molding. **Chapter V** displays outcomes of the densification studies. **Chapter VI** provides an extensive description of oxidation results. **Chapter VII** exposes some mechanical properties. **Chapter VIII** gives conclusions and an outlook to the present work.

Kurzfassung

MAX Phasen sind eine vielversprechende Werkstofffamilie mit derzeit mehr als 150 verschiedenen Zusammensetzungen, die auf nano-geschichteten Karbiden und Nitriden beruhen. Sie schließen die Lücke zwischen Metallen und Keramiken, da sie Eigenschaften aus beiden Kategorien vereinen. Aus metallischer Sicht weisen sie eine gute Schadenstoleranz und Temperaturwechselbeständigkeit auf, lassen sich maschinell bearbeiten und haben eine hohe elektrische Leitfähigkeit. Ihre keramikähnlichen Eigenschaften äußern sich in einer hohen Steifigkeit (hoher Elastizitätsmodul), einem hohen Schmelzpunkt (wenn auch inkongruent), einer geringen Dichte und guten thermomechanischen Eigenschaften bei hohen Temperaturen, wie zum Beispiel die Kriechfestigkeit. Außerdem besitzen sie einen mittleren Wärmeausdehnungskoeffizienten, eine gute Strahlungstoleranz und einige von ihnen weisen eine ausgezeichnete Oxidationsbeständigkeit und Selbstheilungsfähigkeit auf.
Diese einzigartige Kombination von Eigenschaften ist von großem Interesse für potenzielle Hochtemperaturanwendungen, bei denen starke Korrosionsbedingungen herrschen. MAX-Phasen könnten als Strukturwerkstoffe oder Schutzbeschichtungen für Gasturbinen, Abgasanlagen, Hochtemperaturdüsen, Heizelemente, Solarreceiver in Solarkraftwerken, aber auch als Brennstoffhüllen in Kernkraftwerken, Katalysatoren und elektrische Kontakte dienen. Ihre Markteinführung als Endprodukte wurde jedoch durch verschiedene Faktoren behindert, und mehrere Aspekte bleiben noch unerforscht. Die vorliegende Doktorarbeit soll einen Beitrag zu diesem letzten Punkt leisten.
Diese Arbeit konzentriert sich auf die Herstellung von oxidkeramischen, faserverstärkten (Al_2O_3 und $3Al_2O_3$-$2SiO_2$) Ti_2AlC-Verbundwerkstoffen mit komplexeren Formen als die traditionell hergestellten Proben, die in der Literatur zu finden sind und Grundgeometrien aufweisen. Ti_2AlC Pulver wurden mittels der „molten salt shielded synthesis“ Methode hergestellt, bei der verschiedene Parameter (Synthesetemperatur, Haltezeit, Molverhältnis der elementaren Reaktanten, Chargengröße) optimiert wurden, um einem hochreinen Produkt zufriedenstellend nahe zu kommen. Diese Pulver wurden charakterisiert und entsprechend konditioniert, um als Grundlage für eine Reihe von Experimenten zu dienen.
Um die Sinterbarkeit von monolithischem Ti_2AlC und dessen Kompositen zu untersuchen, wurde deren Verdichtung durch druckloses Sintern und feldunterstütztes Sintern/Spark-Plasma-Sintern (FAST/SPS) untersucht. Während Ersteres hohe Temperaturen (>1400 °C) und lange Haltezeiten (>3 Std.) erforderte, um eine partielle Verdichtung (bis max. 93 % der theoretischen Dichte) zu erreichen, stellte sich heraus, dass Letzteres bei niedrigerer Temperatur (1200 °C) und innerhalb kürzerer Zeiten von mindestens 10 min effektiv zu einer nahezu vollständigen Verdichtung (bis ~99 %) führte.
Daher wurde FAST/SPS für die Herstellung von dichten zylindrischen Substraten ausgewählt, um die Ziele der Untersuchung des Oxidationsverhaltens und der mechanischen Eigenschaften zu erfüllen.
Parallel dazu wurden synthetisierte hochreine Ti_2AlC Pulver zur Herstellung von Feedstocks für den Pulverspritzguss verwendet. Ob blank oder in Kombination mit oxidkeramischen Fasern, konnten schnell endkonturnahe komplexe Formen hergestellt werden. Nach der Extraktion der organischen Komponenten wurde ein druckloses Sintern als Vorsinterschritt durchgeführt. Weiterhin wurde die Methode der Konsolidierung komplexer Formen in einem Graphitbett mit der FAST/SPS-Technologie eingesetzt und zeigte interessante vorläufige Ergebnisse.
Darüber hinaus wurde das Oxidationsverhalten von Ti_2AlC-basierten Substraten und Kompositen, ob blank oder mit Yttrium-stabilisiertem Zirkoniumdioxid beschichtet, unter die Lupe genommen. Es wurden zwei Haupttrends beobachtet: Der erste betraf die Bildung von dichten Al_2O_3 Schichten und deren schützende Natur, die es den betrachteten Proben

ermöglichte, sowohl unter isothermen statischen als auch unter zyklischen Bedingungen hervorragende Leistungen zu zeigen. Diese überlebten bis zu 1500 Stunden unter aggressiven Bedingungen und bewiesen die hohe Kompatibilität von Ti_2AlC mit herkömmlichen Wärmedämmschichtmaterialien. Der zweite Trend, über den in der Literatur weniger berichtet wird, betrifft die sogenannte „breakaway oxidation“ von Bauteilen. Abhängig von den Bearbeitungsbedingungen und der Oberflächenvorbereitung überholte das abnormale Wachstum von Rutil-TiO_2 das langsam wachsende Al_2O_3 und führte schließlich zu einem katastrophalen Verbrauch des Grundmaterials.
Um diese Ergebnisse in einer logischen Reihenfolge zu präsentieren, ist diese Arbeit wie folgt aufgebaut: **Kapitel I** führt in die wichtigsten Konzepte über MAX-Phasen ein und stellt den Stand der Technik aus verschiedenen Perspektiven (Synthese, Oxidation, mechanische Eigenschaften) dar. **Kapitel II** stellt die verschiedenen experimentellen Verfahren dar. **Kapitel III** beschäftigt sich mit der Synthese von Ti_2AlC, deren Optimierung und der Charakterisierung der erhaltenen pulverförmigen Produkte. **Kapitel IV** stellt die Herstellung komplexer Formen durch Spritzgießen vor. **Kapitel V** zeigt die Ergebnisse der Verdichtungsstudien. **Kapitel VI** liefert eine ausführliche Beschreibung der Oxidationsergebnisse. **Kapitel VII** stellt einige mechanische Eigenschaften dar. **Kapitel VIII** gibt Schlussfolgerungen und einen Ausblick auf die vorliegende Arbeit.

Abbreviations

APS	Atmospheric Plasma Spraying
BDTT	Brittle-to-Ductile Transition Temperature
BPTT	Brittle-to-Plastic Transition Temperature
BSE	Back-Scattered Electrons
CG	Coarse-Grained
CIM	Ceramic Injection Molding
CMAS	Calcium-Magnesium-Alumina-Silicate
CMCs	Ceramic Matrix Composites
CTE	Coefficient of Thermal Expansion
DP	Dislocation Pileup
DTA	Differential Thermal Analysis
EB-PVD	Electron Beam-Physical Vapor Deposition
EBSD	Electron Back-Scatter Diffraction
EDX/EDS	Energy Dispersive X-ray Spectroscopy
FAST/SPS	Field Assisted Sintering Technology/Spark Plasma Sintering
FEPA	Federation of European Producers of Abrasives
FG	Fine-Grained
FIB	Focused Ion Beam
FOD	Fiber Orientation Distribution
HP	Hot Pressing
HIP	Hot Isostatic Pressing
HT	High-Temperature
HVAF	High-Velocity Air-Fuel
HVOF	High-Velocity Oxy-Fuel
IKB	Incipient Kink Band
IM	Injection Molding
KNE	Kinking Non-linear Elastic
LSI	Liquid Silicon Infiltration
MDW	Mobile Dislocation Wall
MIM	Metal Injection Molding
MS^3	Molten Salt Shielded Synthesis
N/A	Not Applicable
NASA	National Aeronautics and Space Administration
OM	Optical Microscopy
OPS	Oxide Polishing Suspension
PBS	Powder Bed Sintering
PIM	Powder Injection Molding
PS	Pressureless Sintering
PSD	Particle Size Distribution
PS-PVD	Plasma Spray-Physical Vapor Deposition
RD	Relative Density
RMI	Reactive Melt Infiltration
RPM	Revolutions Per Minute
RT	Room Temperature
SB	Sand-Blasted
SE	Secondary Electrons
SEM	Scanning Electron Microscopy
SENB	Single-Edge Notched Beam

SHS	Self-propagating High-temperature Synthesis
SLM	Selective Laser Melting
SPS	Spark Plasma Sintering
TBCs	Thermal Barrier Coatings
TD	Theoretical Density
TEM	Transmission Electron Microscopy
TGA	Thermo-Gravimetric Analysis
TGO	Thermally Grown Oxide
XRD	X-Ray Diffraction
YSZ	Yttria-Stabilized-Zirconia

List of symbols

A	Area of fiber cross-section
a	Half-diagonal length of indent, or cone slant length, or internal sphere radius (rumpling model)
b	External sphere radius (rumpling model)
C	Circularity
C_1, C_2	Elastic constants
d	Average diagonal length of indent, or spacing between atomic planes (XRD), or TGO thickness
d_1	First diagonal length of indent
d_2	Second diagonal length of indent
D_{10}	10% of particles with diameter less than this value
D_{50}	50% of particles with diameter less than this value
D_{90}	90% of particles with diameter less than this value
E	Young's modulus
F	Force
f	Volume fraction of reinforcement phase
H	Height of the spherical cap (rumpling model)
HV, Hv	Hardness
K_{1C}	Critical stress intensity factor
k_{ox}	Oxidation constant
l	Palmqvist crack length
L/D	Length-to-diameter ratio
L/2	Base radius of spherical cap (rumpling model)
m/z	Mass to charge ratio
P	Perimeter of fiber cross-section, or internal pressure in hollow sphere (rumpling model)
R	Universal gas constant
r	March-Dollase parameter
R_a	Arithmetical mean roughness
R_{max}	Maximal roughness depth
R_q	Root mean squared roughness
R_z	Mean roughness depth
S	Shrinkage
S_w	Distribution slope parameter
t	Time
t_n, t_{n+1}	Time at increments n, $n+1$ (rumpling model)
t_{tot}	Total time

t_0	Start time of isothermal plateau (rumpling model)
t_{50}	End time of isothermal plateau (rumpling model)
U	Activation energy
V	Volume of spherical dome (rumpling model)
$\dot{V}$	Time derivative of V
X	Degree of rumpling
$\Delta m/A$	Mass gain per unit area
$\dot{\varepsilon}$	Creep rate
$\dot{\varepsilon}_0$	Creep constant
η	Degree of preferred orientation
ν	Poisson's ratio
Φ	Constraint factor
σ_i	Hydrostatic stress in reinforcement phase
σ_m	Backstress in matrix
σ_r, σ_θ, σ_φ	Stress solutions in spherical coordinates r, θ, φ

Table of content

Chapter I: Introduction

I-1 State of the art

Global climate change is our current major concern, as its alarming repercussions threaten our life condition on Earth. Humankind has realized the absolute need to reduce the emission of greenhouse gases (GHGs) and to eventually target carbon neutrality. Three major events are the evidence of an international political response to climate change: the Rio Earth Summit in 1992 with the adoption of the "Rio Convention" aiming the stabilization of anthropogenic concentrations of GHGs in the atmosphere [1]; the Kyoto Protocol adopted during the 3rd Conference of Parties (COP3) in 1997 defining measures and targets to mitigate GHG emissions [1,2]; and the 21st Conference of Parties (COP21) in December 2015, during which the Paris Agreement was established with the goal to maintaining global warming below 2 °C by the end of the century [1].

As a consequence, current technologies need to be redesigned and new solutions to be developed. The essential key element is the advancement in materials science and engineering. In fact, in order to promote a sustainable and environmentally-friendly policy, strategic fields such as transport and energy development require new advanced material systems to be devised. Every new technology aims higher yield and efficiency resulting in materials to be exposed to more aggressive environments, higher temperatures and significant stresses. In particular, energy production is a determinant topic for mankind and necessitates research to be actively conducted in this area.

Since the first Industrial Revolution, one of the most remarkable inventions remains the steam engine, which transformed our society in many aspects. From transportation to agriculture to industrial processes, steam engines became the main source of power. They were the forerunners of today's gas turbines and combustion engines and were gradually replaced by them in the 20th century. Power-generation turbines have been used in many severe environments such as in jet engines (Figure 1. 1) or in nuclear, chemical, fossil fuel and concentrated solar power plants.

Technological advancement goes hand in hand with materials science and engineering, as performance and efficiency depend on the material selection. For example, in a gas turbine the thermal efficiency η depends on the temperature difference between inlet (hot gases) and outlet (colder gases) and is given by the Carnot cycle via the following formula [3]:

$$\eta = 1 - \frac{T(cold)}{T(hot)} \qquad \text{(Equation 1)}$$

The higher the difference in temperature, the more heat can be converted to power and so, the more work can be extracted from the system, thus improving the performance. This has been mainly achieved so far by increasing the turbine entry temperature (TET), and thus, by carefully selecting appropriate materials. However, their melting points are the major limits and have restricted the operating conditions. Well-established for decades, nickel-based superalloys are still in use as structural materials in turbine engines (blades, disks, shafts, impellers) as they show suitable high temperature mechanical properties – such as high strength, fracture toughness, ductility, long fatigue life and creep resistance – as well as good corrosion and oxidation resistance [3,4].

However, Ni-superalloys with low aluminum (Al) content were found to form a brittle NiO layer prone to premature spallation. These can operate at temperatures beyond 800 °C and can

occasionally tolerate temperatures of up to 1200 °C when air-cooled and protected by ceramic thermal barrier coatings (TBC). The latter, coupled with metallic overlay coatings commonly of MCrAlX type, where M=Ni and/or Co and X=Y, La, Zr, Hf, allow the TET to be increased. On the one hand, overlay coatings provide excellent protection against hot corrosion and high temperature oxidation when compact and adherent external alumina (Al_2O_3) scales are exclusively formed. On the other hand, TBC – commonly Yttria Stabilized Zirconia (Y_2O_3-ZrO_2, designated as YSZ) due to the lowest thermal conductivity amongst polycrystalline oxide ceramics and minute variation of thermal conductivity over a broad range of temperature – thermally insulate the underlying material by decreasing the steady-state heat flux and the metal temperature [3].

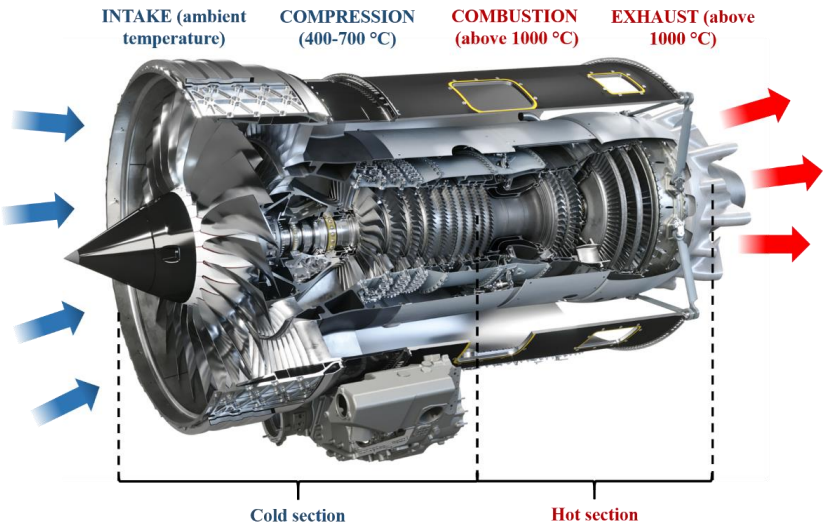

Figure 1. 1: Cutaway view of the Rolls-Royce Pearl 15 turbine engine (Photo Credit: Rolls Royce Corporation.)

Extensive research is carried out nowadays to achieve higher efficiency and superalloys are restricted by the targeted increasing operating temperatures. Materials with better characteristics than Ni-based superalloys and fulfilling criteria such as low density for weight reduction, excellent oxidation resistance and mechanical properties are under development. Especially materials with low thermal expansion are desired, as they reduce the thermal stresses which are introduced during operation [5]. Impressively, engine dimensions can significantly change during use (several centimeters). Therefore, low CTE is also essential for dimensional control and minimizing the gaps between components. In fact, these would create detrimental variations in primary and secondary air flows that would, in turn, cause losses in pressure, efficiency and overall performance of the turbine engine, while specific fuel consumption would increase. Intermetallic compounds, such as the aluminides Ti_3Al, TiAl, NiAl or FeAl have lower density as compared to superalloys and proved well for temperatures not exceeding 700-750 °C [5]. However, their limited toughness and poor oxidation resistance at higher temperature does not make them a material of choice for turbine sections but rather for initial stages of the compressor.

Alongside alloys and metallic-based materials, ceramics turned out to be a promising alternative for gas turbine hardware, as their higher melting points and lower densities usually allow for higher specific thermo-mechanical properties. The introduction of ceramics as high temperature materials for turbine components is recent compared to superalloys, but exceptionally

promising [6]. However, in their monolithic form, they suffer from brittleness, low fracture toughness and thus, high flaw sensitivity, only allowing for a narrow range of mechanical tolerance. To bypass this issue, ceramic matrix composites (CMCs) have been developed since the early 1960s [7], consisting of a ceramic matrix and a ceramic reinforcement (fibers, particles, whiskers, etc.). Carbon/carbon systems were the first thermo-structural composites developed as alternative materials for rocket propulsion and re-entry thermal protection, conceived to tolerate extremely high temperatures for short times, accompanied by a partial material consumption [8]. Although they have demonstrated superior properties as compared to conventional materials for example for high performance brakes, they exhibit high sensitivity to oxidation, which makes them poor candidates for oxidizing environments. Instead, aeronautical and space applications rapidly found interest in silicon carbide/silicon carbide (SiC/SiC) CMCs [6], developed in the early 1990s by Snecma Propulsion Solide [7]. That is due to their capability of withstanding high thermal fluxes and mechanical loads in air, accompanied by the reduction of up to 2% of fuel burn and a decrease of the total turbine weight by over 50% [9]. Only recently these have been introduced on the market by GE aviation after more than 30 years of maturation activities and extensive testing [9]. Despite their excellent response up to 1500 °C in protective atmospheres, one of their major weak points in oxidizing environments resides in the interphase located between fibers and matrix and most of the time made of a multi-layered carbonaceous material (e.g. pyrolytic carbon) [8]. In addition, the manufacturing routes employed to produce SiC/SiC CMCs are slow, expensive and require high temperatures and vacuum to facilitate the infiltration of liquid precursors in preforms [10]. The risk of damaging fibers as well as the problematical residual porosity limiting their thermal conductivity are other concerns. Last but not least, SiC/SiC CMCs have limited environmental durability when exposed to water vapor or certain oxidizing/reducing gas mixtures. The glassy protective silica that forms upon oxidation reacts with water vapor to form volatile hydroxides and oxyhydroxides leading to a considerable recession of the SiC surface [11]. For this reason, the so called environmental barrier coatings (EBCs) are needed to prevent this reaction [12], involving additional coating procedures and costs. Therefore, the complexity of processing techniques, the architecture of complex layered structures and the high involved costs restrict the industrialization and use of SiC/SiC CMCs.

In parallel, ultra-high temperature ceramics (UHTCs) – binary early transition borides, carbides and nitrides – have also emerged as potential candidates for high-temperature applications, especially for hypersonic flight and re-entry in atmosphere. They would be suitable for harsh oxidizing and corrosive environments, mostly due to their extremely high melting points (> 3000 °C), good resistance to radiation and high heat fluxes and chemical stability [13]. However, even after 30 years of research, they are still limited by various aspects. Most of them are heavy materials. The hafnium and tantalum-based compounds, for instance, have higher densities (11-14 $g \cdot cm^{-3}$) than superalloys, while these of other UHTCs range between 5 and 7 $g \cdot cm^{-3}$ [14]. UHTCs also suffer from poor flaw tolerance and low thermal shock resistance, which classically leads to catastrophic failure if no reinforcements are used [15]. In addition, the most widely studied UHTCs, ZrB_2 and HfB_2, are boria (B_2O_3) formers. B_2O_3 is stable up to 1200 °C but starts evaporating above this temperature. As such, the protective barrier no longer exists and porous scales are formed. Efforts have been invested to stabilize it, but improvements are still required [16]. Finally, similarly to SiC-based CMCs, issues are faced for UHTC-CMCs in terms of processing routes and densification [13,14]. In the latter case, hot pressing and spark plasma sintering conditions were investigated, but involved very high temperatures (1800-2300 °C) or pressures to barely achieve near-full densification [17]. As such, UHTCs and CMCs thereof still cannot be considered as cost-effective substitution materials for superalloys.

Nearby UHTCs or SiC/SiC CMCs, additional potential candidates are MAX phases. These present some advantages as compared to UHTCs and SiC such as low density, good damage tolerance, high fracture toughness, easy processing and intermediate sintering temperatures. In

this regard, Al-containing MAX phases are of particular interest, among which, Ti_2AlC proved to be the most promising composition due to its excellent oxidation and corrosion resistance. The present work is produced within the framework of the BMBF-program "Nachwuchsgruppen" under the topic "MAX phase composites: new materials for elevated temperature service (MAXCOM, grant number: 03SF0534)". The MAXCOM project aims to manufacture novel Ti_3SiC_2, Cr_2AlC and Ti_2AlC-based CMCs, employed for higher operating temperatures and efficiency, and characterize their mechanical properties and oxidation resistance. The focus of the present thesis is set on Ti_2AlC-based systems, with a particular interest for their response in oxidizing environments and an emphasis on the influence of post manufacturing surface conditioning. The fundamental aim of this work is to develop and optimize a complete manufacturing route to fabricate complex shapes of fiber-reinforced Ti_2AlC composites. It encompasses the fine-tuning of parameters of a molten salt based synthesis method, the near net shaping via injection molding, the densification with and without external pressure and electric field, and the oxidation response of the produced parts.
In the first place, a description of general features about MAX phases is given in the following section.

I-2 MAX phases, a general overview

$M_{n+1}AX_n$ phases – also designated as MAX phases – are nanolayered, early transition-metal carbides, nitrides and carbonitrides [18,19]. The name "MAX" comes from their chemical formula (Figure 1. 2): "M" is an early transition metal, "A" an element from the A-group (predominantly metalloids and post-transition metals from groups 13 and 14), and "X" is carbon (C) and/or nitrogen (N). The integer *n* varies between 1 and 3.

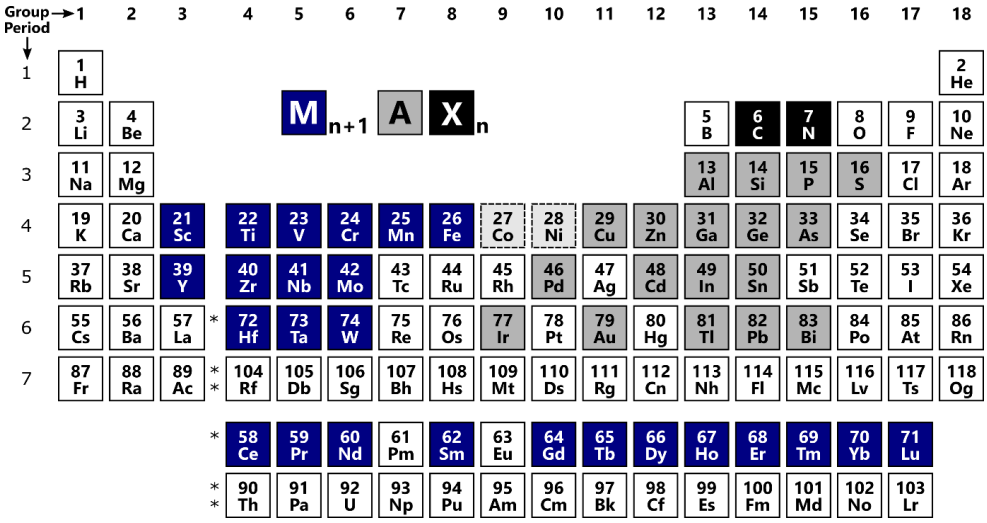

Figure 1. 2: Elements from the periodic table being encompassed in the MAX phase chemical compositions, based on the most recent report [23].

These phases were first discovered in the 1960's by German and Austrian scientists Wolfgang Jeitschko, Hans Nowotny and Fritz Benesovsky. The very first published studies in 1963-1967 [20–22] – not all have been cited here – labelled them as H-phases and listed around 30 compounds, pointing out their hexagonal close-packed crystallographic structure. These works were the first to mention that H-phases were arranged as sheets of T_6C-octahedra (at that time

the formula M_2AX was designated as T_2MC) forming 2D structures linked by T-M metallic bonds.

Until the mid-1990's, MAX phases almost sank into oblivion, with only few reports of their synthesis, crystal structure and properties. However, in 1996, Barsoum and co-workers started re-exploring ternary carbides and nitrides by investigating the properties of Ti_3SiC_2 [24] and initiated a resurgence of interest for MAX phases. Their chemical diversity could be clearly evidenced in the recent review paper of Sokol et al. [23] where it has been claimed that no less than 155 MAX phase compositions currently exist.

The hexagonal crystal structure of MAX phases is depicted on Figure 1. 3. They crystallize in the space group $D_{6h}^4 - P6_3/mmc$. The "M" elements are arranged in octahedra, of which the sites are occupied by "X" atoms. These M_6X arrangements are strictly identical to the binary carbides and nitrides of rock salt like lattice structure. They are linked together by edges M-M bonds, while the M-A bonding is of metallic nature, as the distances were found to be smaller than the sum of the respective metallic radii [21].

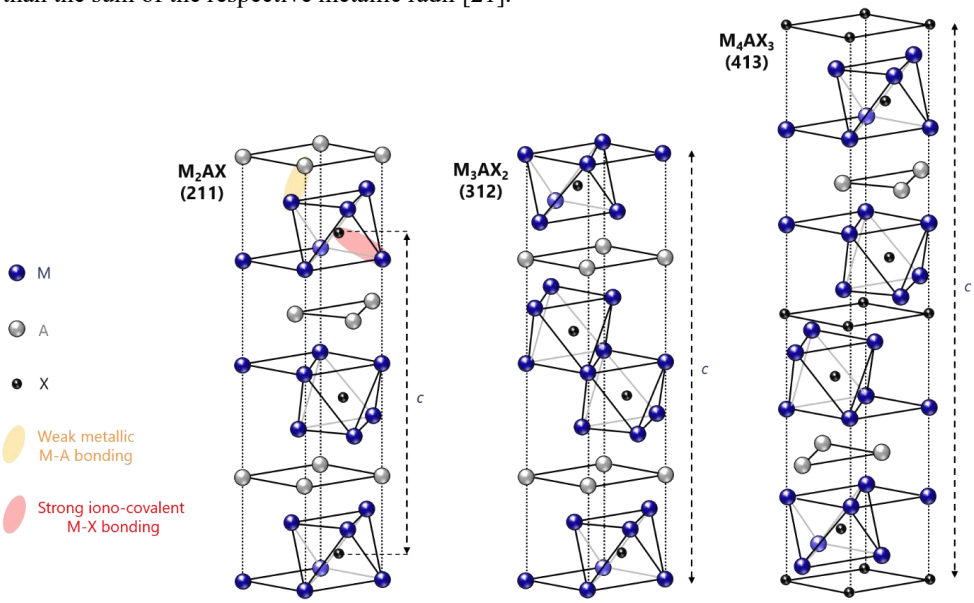

Figure 1. 3: MAX phase unit cells with different *n*-integer. Lattice parameter *c* is given for each configuration. Adapted from [18].

As such, the overall structure is a near-close-packed arrangement of M_6X layers interleaved with layers of A-group elements. The difference in crystal structure arises from the integer *n*, which gives the number of "M" layers stacked between "A" layers. In this way, as depicted on Figure 1. 3, for *n*=1 (M_2AX or 211 phases), there are two, for *n*=2 (M_3AX_2 or 312 phases), there are three and for *n*=3 (M_4AX_3 or 413 phases), there are four. Nevertheless, most of the compositions are 211 phases (Figure 1. 4). Depending on the elements coming into play, some values of *n* are not thermodynamically favorable. For example, in the Cr-Al-C system, solely *n*=1 results in stable phases, while for the Ti-Al-C system, *n*=1 and *n*=2 are possible values. Larger *n* values were also reported for the latter system, but these were based on density functional theory (DFT) calculations and were not yet the target of a synthesis [25]. Nowadays, MAX phases are known to occur in their ternary forms (Figure 1. 4), but also as quaternary phases. The formers encompass conventional structures but also hybrid phases [23,26], which have been found to result from a sequence of half unit cells of the most regular MAX phases.

The latter embrace solid-solutions, out-of-plane (*o*-MAX) [27] and in-plane (*i*-MAX) [28] ordered phases. In the case of solid solutions, M, A or X sites can undergo atomic substitution.

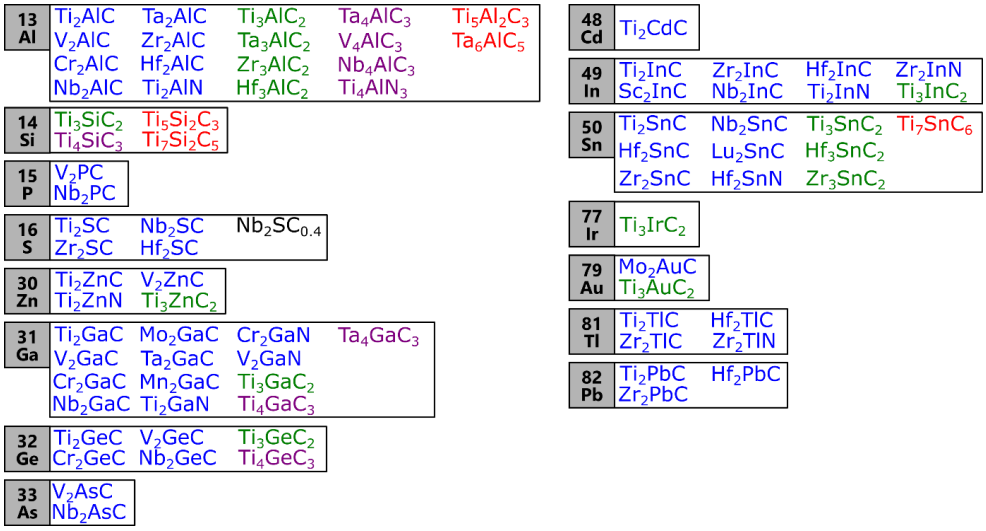

Figure 1. 4: List of ternary MAX phases: 211, 312, 413 and hybrid phases are highlighted in blue, green, purple, and red, respectively. Adapted from [23].

Additions of elements such as Fe [29], Mn [29], Au [30], Ir [30], Bi [31] or Cu [32] have been investigated and have led to interesting new properties, such as magnetization, enhanced electrical properties or catalysis [33]. In 2014, *o*-MAX phases with general formula (M', M'')$_{n+1}$AlC$_n$ have been discovered [27] but their synthesis is currently restricted to Al-containing carbides of 312 and 413 compositions. In that case, M layers of one early transition metal (M') separates one or two layers of the second M element (M''). Like ternary carbides, *o*-MAX phases have the $P6_3/mmc$ symmetry [23,27]. That is not the case of *i*-MAX phases for which the crystal structure is monoclinic or orthorhombic [23,28], although these have a similar chemical formula. As quaternary MAX phases are out of the scope of the dissertation's topic, these are not further dealt with and not incorporated in Figure 1. 4.

MAX phases have been found to exhibit uncommon properties [18], so much so that these "thermodynamically stable nanolaminates [19]" are often said to bridge the gap between metals and ceramics. Their most characteristic attribute is undoubtedly their machinability. Unlike conventional structural ceramics with high specific stiffness, MAX phases are readily machinable with traditional cutting, milling, or turning tools, resulting from flaking rather than plastic deformation. Additionally, and that is typically against the basic concept of ceramics, MAX phases are found to be able to plastically deform above their brittle-to-plastic transition temperature (BPTT), which was found to be between 1000 and 1100 °C for Al-containing MAX phases [18]. Alongside their relatively low Vickers hardness (*Hv*), they demonstrate much higher damage tolerance and fracture toughness than conventional structural ceramics, by virtue of their layered structure [18].

In addition to their noteworthy mechanical features, MAX phases exhibit good electrical and thermal conductivities on account of a high density of states at the Fermi energy, essentially dominated by overlapping orbitals of M atoms [18]. From the viewpoint of electrical properties, they behave like metallic conductors with a resistivity in the 0.02-2.00 μΩ·m range, which is several orders of magnitude lower than most advanced ceramics [34]. Apart from presenting an interest in electronic applications, MAX phases can therefore easily be machined by electric

discharge machining (EDM) to produce components with precise dimensions. In agreement with their high electrical conductivity, MAX phases are also good thermal conductors [18,34]. Their thermal conductivities vary between 12 and 60 $W \cdot m^{-1} \cdot K^{-1}$ at room temperature. These values are usually higher or fairly close to those of the corresponding transition metals such as titanium (Ti) with 21 $W \cdot m^{-1} \cdot K^{-1}$ [35], zirconium (Zr) with 22 $W \cdot m^{-1} \cdot K^{-1}$ [35], vanadium (V) with 31 $W \cdot m^{-1} \cdot K^{-1}$ [35] or chromium (Cr) with 92 $W \cdot m^{-1} \cdot K^{-1}$ [35], and common binary transition metal carbides such as boron carbide (B_4C) with ~14 $W \cdot m^{-1} \cdot K^{-1}$ [36] or titanium carbide (TiC) with 27 $W \cdot m^{-1} \cdot K^{-1}$ [37], though still lower than pure single-crystalline SiC (490 $W \cdot m^{-1} \cdot K^{-1}$ [38]) or polycrystalline SiC sintered e.g. with BeO (270 $W \cdot m^{-1} \cdot K^{-1}$ [39]), La_2O_3 and Y_2O_3 (167 $W \cdot m^{-1} \cdot K^{-1}$) or vanadium and boron sintering additives (55-70 $W \cdot m^{-1} \cdot K^{-1}$ [40]).
Furthermore, some MAX phase compositions are of particular interest for high-temperature applications as they possess intermediate coefficients of thermal expansion (CTE) ranging from 8 x 10^{-6} K^{-1} to 10 x 10^{-6} K^{-1}, with only few exceptions such as Nb_4AlC_3 or Cr_2AlC having lower and larger values [34]. In addition, they exhibit good oxidation resistance. Thereby, some of the Al-containing MAX phases have been listed among the most interesting candidates. Especially Cr_2AlC, Ti_3AlC_2 and Ti_2AlC have been the subject of numerous studies [41]. As a dense Al_2O_3 layer forms *in situ*, the underlying MAX phase is protected.
The growth of the Al_2O_3 scale was found to obey a parabolic law for Ti_3AlC_2 [42,43], while Ti_2AlC rather demonstrated parabolic to near-cubic kinetics. From these three compositions, latter shows the highest potential for different reasons:

(i) The CTE of Ti_2AlC (8.2 x $10^{-6} \cdot K^{-1}$ for T = 25-1300 °C [44]) and Al_2O_3 (8.0 x $10^{-6} \cdot K^{-1}$ and 9.0 x $10^{-6} \cdot K^{-1}$ for T = 25-1000 °C and 25-1500 °C respectively [45]) result in a good match, hence a reduction of residual thermal stresses and the probability of scale spallation.

(ii) It has a higher concentration of Al as its 312 counterpart, and thus, a higher probability of forming Al_2O_3 on account of the higher activity of Al; (iii) its density is the lowest, which is a critical parameter to consider for weight reduction.

(iii) Contrary to Cr_2AlC, Ti_2AlC does not form a porous layer underneath the oxide scale, which is considered problematic in long-term exposures (Figure 1. 5) [34], as it can promote rapid oxygen ingress or weaken the oxide scale adhesion.

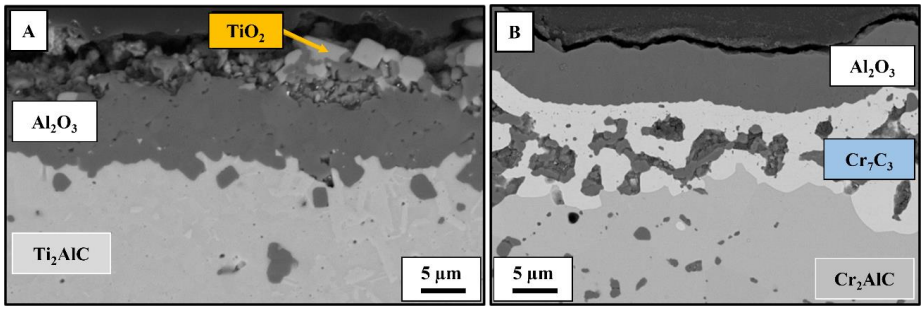

Figure 1. 5: Oxide scale morphology for (A) Ti_2AlC and (B) Cr_2AlC after oxidation at 1200 °C. Adapted from [34].

However, unlike Cr_2AlC for which solely Al oxidizes and forms a continuous Al_2O_3 layer, $Ti_{n+1}AlX_n$ MAX phases experience the oxidation of Ti as well. This competition between Al_2O_3 and TiO_2 is usually not harmful for the system's integrity, though, in some specific cases, the uncontrolled overgrowth of TiO_2 can be a serious issue.
In spite of the numerous studies stemming from the increasing interest for MAX phases since the late 1990s, their implementation to the market is still lacking. Apart from patents mentioning

about Al-MAX phases (Ti_2AlC, Ti_3AlC_2 and Cr_2AlC) [46,47] and Ti_3SiC_2-based [48] bronze and copper composites as alternatives to carbon sliding plates used for high-speed train pantographs in China, there exists no mention of commercial applications [34]. The company Kanthal® used to produce Ti_2AlC and Ti_3SiC_2 powders under the registered trademark MAXTHAL®, but the production is currently dormant. The lack of MAX phase-based end products is primarily due to the difficulty in synthesizing large quantities of powders with high purities. Added to that comes the duration of licensing procedures in strategic areas requiring strict standards [34].
In reason of its high potential for applications in severe high-temperature oxidizing environments such as heating elements, gas burner nozzles, turbine engines, ignition devices and many more [18], focus has been set on Ti_2AlC in the framework of the present thesis.
As such, this work targets to reduce the gap between research and commercialization by exploring different tracks: the optimization and upscaling of a synthesis procedure to achieve the production of large quantities of high purity Ti_2AlC powders; the manufacturing of realistic complex geometries by a near net shaping technique and the fabrication of $Ti_2AlC/Al_2O_{3(f)}$ composites; the investigation and selection of optimal post-processing densification methods; the study and understanding of the impact of surface metrology on oxidation mechanisms. A more detailed review of mechanical properties and oxidation resistance of Ti_2AlC is exposed further in this work, after describing the various synthesis and processing routes explored so far.

I-3 Synthesis of Ti_2AlC

The availability of MAX phase powders, and specifically of Ti_2AlC in the framework of this thesis, is and has been extremely restricted since their discovery. As mentioned earlier, Kanthal® – a company part of Sandvik Group – used to commercialize mostly Ti_2AlC and Ti_3SiC_2 powders. However, they interrupted the production as not fulfilling the purity standards required for the transfer of MAX phases to industry [34].
Purity is a major concern when it comes to the synthesis of MAX phases. In fact, secondary phases and impurities can drastically alter properties and sometimes curtail the targeted performance. In the Ti-Al-C system, the competition between Ti_2AlC and the more stable Ti_3AlC_2 complicates the control of purity as these share the same precursors [49]. Particularly the synthesis of Ti_2AlC has been found to present challenges as compared to other ternary species in the Ti-Al-C system [50]. An overview of some of the numerous synthesis outcomes mentioning about end-product purity can be found in Table 1. 1.
In the pioneering studies of Jeitschko et al. [20,21] in the 1960s, homogeneous compounds were generally produced by a double hot-pressing (HP) technique at 1200-1300 °C and/or annealing in sealed silica tubes around 800 °C for long times (up to 800 h) depending on the composition. Quantitative mention of purity was inexistent in these studies.
Later, in 1975-76, Ivchenko et al. [51,52] produced Ti_2AlC via a direct synthesis involving, first, TiC, Al and Ti powders and, second, elemental reactants. These were cold-compacted and heated for 1 h at temperatures ranging from 600 to 1600 °C depending on the initial reactants. The synthesis was performed under argon atmosphere to avoid evaporation of high vapor pressure Al. For the first set of starting materials, Ti_2AlC appeared at 1000 °C through the reaction of TiC and previously forming titanium aluminide (TiAl). For the second set, the temperature was significantly lower (600 °C) on account of a higher reactivity of elemental reactants as compared to TiC. At that time, the authors claimed having obtained single-phase compositions, which in actual fact, might not have been the case. With perspective and considering that quantitative elemental/phase analysis methods such as inductively coupled plasma (ICP) techniques [53] or Rietveld refinement [54] were at their early stages of

Table 1. 1: Various reported synthesis routes and corresponding phase composition. Volume fraction and molar fraction are given by ^{a} and ^{b}, respectively.

Year	Reference	Synthesis route	Raw materials and synthesis parameters	Quantitative phase analysis	Observed phases (wt.%)
2000	[44]	Reactive hot isostatic pressing	Ti, Al_4C_3, graphite powders, argon, 30 h at 1300 °C, 40 MPa	SEM + image analysis	Ti_2AlC (96%), Ti_3P + Al_2O_3 (4%) [a]
2007	[49]	Solid-liquid reaction synthesis	Ti, Al, graphite powders	XRD + Rietveld refinement	Ti_2AlC (>99%)
2016	[56]	Pressureless sintering	Ti, Al, TiC powders with (Ti:Al:TiC=1.00:1.05:0.95), argon, 1400 °C	XRD + SEM + EBSD + image analysis	Ti_2AlC (95.14%), Al_2O_3 (3.3%), TiAl (1.4%), TiC (0.16%) [a]
2010	[57]	Pressureless sintering	Maxthal 211, argon, 1 h at 1500 °C	XRD	Ti_2AlC (92%), TiC (5%), Al_2O_3 (3%) [a]
2010	[58]	Spark plasma sintering	CVD in-situ grown CNTs on TiAl particles using $Co(NO_3)\cdot 6H_2O$ as catalyst, vacuum, 1200 °C, 50 kN	XRD	Ti_2AlC (92%), TiC (5%), Ti_2Al_5 (3%)
2015	[59]	(A) Arc melting + (B) annealing + (C) quenching	(A) Ti, Al, graphite powders, argon, 5 min + (B) 6 h at 1350 °C + 12 h at 1250 °C + 750 h at 650 °C + (C) 200 °C/s in water	XRD + Rietveld refinement	Ti_2AlC (47%), Ti_3AlC_2 (30%), $TiAl_3$ (23%)
2009	[60]	Self-propagating high-temperature synthesis (SHS)	Ti, Al, carbon black powders + additions of TiC or Al_4C_3 with (Ti:Al:C=2:1:1), argon	XRD + Peak intensity integration formula	Ti_2AlC (80-90%), TiC (20-10%)
2010	[61]	Mechanically activated SHS	Ti, Al, graphite powders, ~2000 K, argon	XRD + Pattern deconvolution	Ti_2AlC (95%), TiC (5%) or (Ti_2AlC + Ti_3AlC_2) (99.7%) when increasing Al content
2019	[62]	SHS	Ti, Al, graphite powders, argon	XRD + Rietveld refinement	Ti_2AlC (95.4%), $TiAl_2$ (4.6%) Ti_2AlC (87.5%), Ti_3AlC_2 (10.8%), TiC (1.6%)
2011	[63]	Proprietary method developed by 3-ONE-2	N/A	XRD + Rietveld refinement	Ti_2AlC (67%), TiC (19%), Ti_3AlC_2 (14%) [b]
2011	[64]	Proprietary method developed by Kanthal AB (Sandvik)	Maxthal 211	XRD + Rietveld refinement	Ti_2AlC (84.3%), Ti_3AlC_2 (6.5%), TiC (5.1%), TiAl (4.1%)
2017	[65]	Proprietary method developed by Kanthal AB (Sandvik), combustion synthesis	Maxthal 211	XRD + Rietveld refinement	Ti_2AlC (68.33%), Ti_3AlC_2 (14.02%), TiC (7.86%), $Ti_{1.2}Al_{0.8}$ (9.79%)
2018	[66]	Molten salt synthesis	Ti, Al, graphite powders, in 50:50 NaCl:KCl mixture, argon, 2 h at 1000 °C	XRD + Rietveld refinement	Ti_2AlC (88%), $Ti_{0.9}Al_{1.1}$ (12%)

development, that seems rational. Even after milling the compacts back to powdered material and HP in vacuum at 1500 °C, the compositions were claimed to be unaltered.
During the following three decades of their discovery, only few isolated manuscripts were published, mostly about Ti_3SiC_2, resulting from little interest given to MAX phases [18].
It is only in 1994 that Pietzka and Schuster [55], from the group of professor Nowotny in Vienna, synthesized Ti_2AlC by reactive sintering under hydrogen gas, starting with cold-compacted powders of Ti, TiAl, Al, TiC, aluminum carbide (Al_4C_3) and graphite (C). Dwell time was set to 20 h, significantly longer than the 1 h holding time reported in the work of Ivchenko and Kosolapova [51,52]. Additional information on MAX phases from the Ti-Al-C system have been provided, such as incongruent melting points of Ti_2AlC (1625 ± 10 °C) and Ti_3AlC (1580 ± 10 °C), as well as the fact that Ti_3AlC_2 does not decompose in the liquid state. The 312 phase was observed between 1000 °C and 1300 °C, and decomposed at 1360 °C. This study was the first to compile existing thermochemical data in the Ti-Al-C system to provide a detailed overview of reaction schemes and phase equilibria.
However, the first veritable breakthrough in the study of MAX phases arrived in 1996 [24], when Barsoum and El-Raghy published their first paper on Ti_3SiC_2. It marked the beginning of a surge of publications on the topic. One year later, in 1997, Barsoum et al. [67] reported the synthesis of phase pure polycrystalline Ti_2AlC by HP a cold-compacted mixture of Ti, Al_4C_3 and graphite at 1600 °C and 40 MPa for 4 h.
Then, three years later, Barsoum and co-workers [44] reiterated the synthesis of Ti_2AlC, starting with the same reactants as in their previous study [67], but via reactive hot isostatic pressing (HIP) at 1300 °C and 40 MPa for 30 h. They reported an average grain size of approximately 25 μm. A dwell time of 30 h in their conditions was required to promote further reaction and disappearance of substoichiometric TiC and Ti_3AlC_2 phases.
In 2001, the first synthesis study of Ti-Al-C MAX phases using self-propagating high-temperature synthesis (SHS) was reported by Łopaciński et al. [50]. This method was invented in the early 1970s by Merzhanov and Borovinskaya [68]. It consists in the combustion and the propagation of the resulting heat wave throughout a green sample or powder mixture, involving a series of high-temperature reactions. In Łopaciński's study, the procedure led to high impurity concentration (TiC, Al_4C_3) when elemental reactants were used. By replacing Ti and Al by TiAl, they achieved higher purities, though observing multiple reflections in their X-ray diffraction (XRD) patterns corresponding to ancillary phases such as Ti_3AlC_2, TiC, $TiAl_2O_5$, $Ti_{1-x}Al_{1-x}$ and Ti_5Al_{11}.
In 2002, Khoptiar and Gotman [69] employed the SHS technique on a stoichiometric powder blend of elemental reactants to synthesize Ti_2AlC. As to bypass the issue of high porosity in combustion products, they proceeded to a pressure-assisted SHS method and applied 30 MPa right after the onset of combustion. They employed pre-compacted (80 to 90% dense) cylinders. SHS of 80% dense compacts without external pressure led to the coexistence of Ti_2AlC and $TiAl_3$. With external pressure (30 MPa), Ti_2AlC (more than 90 vol. %), substoichiometric TiC_{1-x} and a phase assumed to be a mixture of Ti_2AlC and $TiAl_3$ were highlighted. However, SHS of 90% dense compacts did not lead to the formation of Ti_2AlC, but rather aluminides and plenty of unreacted Ti and Al. Ti_2AlC was believed to be formed by a peritectic reaction between TiC_{1-x} and molten Ti-aluminides. The pressure-assisted SHS technique led to highly dense compacts (> 98%), though the amount of TiC_{1-x} drastically increased as compared to the pressureless synthesized porous samples.
Numerous studies on SHS seemed promising for the fabrication of high-purity Ti_2AlC powders and compacts. However, there was a need for fine-tuning synthesis parameters. Yeh and Shen [60] conducted a study in which they started with a stoichiometric ratio of elemental reactants and additions of either TiC or Al_4C_3. While SHS of reactants without additions yielded an 85 wt. % pure product, adding TiC helped increasing the purity to 90 wt. % Ti_2AlC. Al_4C_3 was not effective to increasing the purity, as it promoted less exothermic reactions. They reported grains

10-20 µm in size on average. SHS proved to be an ultrafast synthesis technique as Ti_2AlC could be produced in a couple of seconds (Figure 1. 6).
Further, Liang et al. [70] managed to obtain 95 wt. % pure Ti_2AlC by proceeding to laser-induced SHS of elemental reactants with additions of 0.3 mol of tin (Sn). To the contrary of Yeh and Shen's study [60], TiC additions did not lead to enhancing the overall purity. Neither did excess amounts of Al. In all cases, TiC was found as ancillary phase coexisting with Ti_2AlC, but was present in significantly lower amounts for Sn-containing mixtures. Similarly to previous studies [60,71], average grain length and width yielded 10-20 µm and 2 µm respectively.
An additional study by Hendaoui et al. [61] reported a maximum yield of 99.7% of Ti_2AlC and Ti_3AlC_2 obtained by SHS after a mechanical activation of elemental powders and additions of excess Al.

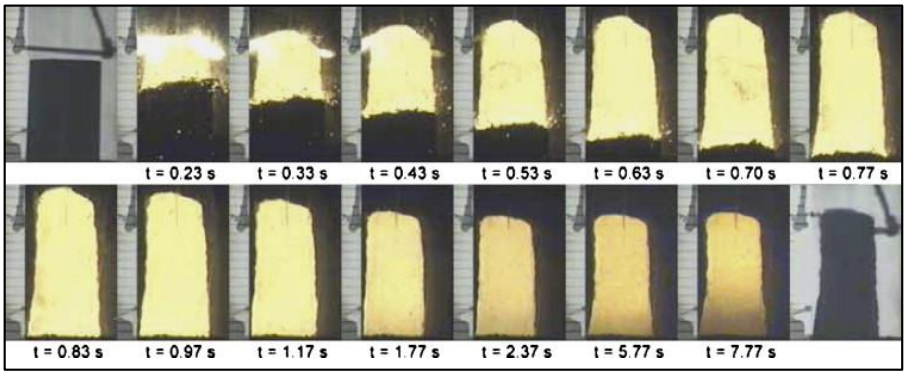

Figure 1. 6: SHS sequence showing the self-sustained propagation of the planar reaction front after ignition of a Ti-Al-C powder compact with 70% relative density and sample shrinkage [60].

Another SHS route was described by Vershinnikov and Kovalev [72]. They proceeded to a magnesiothermic reduction of anatase TiO_2, reaching a purity of up to 96 wt. % Ti_2AlC, along with 4 wt. % TiC.
As an alternative to SHS, for which the exothermicity of reactions has usually represented a challenge to the good control of purity and microstructure, a solid-liquid reaction synthesis method was reported by Wang and Zhou [73]. Starting materials were Ti, Al and graphite powders, which were hot-pressed at 30 MPa at temperatures varying between 1100 °C and 1400 °. Their study was the first to focus on probable reaction mechanisms. In the initial stage of the synthesis procedure, Al is melting and a reaction between Ti and liquid Al takes place. At 850 °C, aluminides (TiAl, Ti_3Al) are formed and coexist with unreacted Ti and C. At 1000 °C, the reaction with graphite leads to the formation of Ti_2AlC and Ti_3AlC via different mechanisms. Increasing the reaction temperature by 100 °C resulted in significant increase in Ti_2AlC reflections in XRD patterns. Aluminides and TiC were still present, but their respective reflections vanished at 1300 °C and 1400 °C. Qualitatively, Wang and Zhou obtained predominantly phase pure bulk Ti_2AlC samples. Microstructural analyses highlighted elongated grains with average length of several tens of micrometers.
In 2008, Hashimoto et al. [74] obtained phase-pure Ti_2AlC by conventional solid-state reaction. They fired a mixture of Al, Ti and TiC with a molar ratio of respective reactants of 1:1:0.75 at 1300 °C for 4 h. Further, they studied the influence of additions of different oxides (Al_2O_3, Y_2O_3, MgO, CaO and TiO_2) on the final density of compacts sintered without external pressure. While the sintering additive-free Ti_2AlC yielded 94.2%, the highest relative density (96.0%) was reached with 5 wt. % Al_2O_3 additions.

As a matter of cost reduction, Hendaoui et al. [75] investigated the synthesis of Ti_2AlC via the aluminothermic reduction of a TiO_2/Al/C mixture. While their products mainly contained Ti_2AlC, secondary phases of Ti_3AlC_2, TiC and Al_2O_3 were detected. A decrease in the TiC content could be observed when a 2 mol excess of Al was used.
An identical starting composition to that of Barsoum et al. [44,67] was used by Gauthier-Brunet et al. [76]. They proceeded by reactive sintering between 570 °C and 1400 °C for 1 h of a high-pressure cold-compacted mixture, eventually having TiC impurities in the as-synthesized product at the highest sintering temperature. The mechanism of Ti_2AlC formation they assumed was rather a reaction between the metastable Ti_3AlC and graphite.
Solid-state reaction was also employed by Benitez et al. [56] to produce 95 vol.% pure Ti_2AlC, with ancillary phases being Al_2O_3, TiAl and TiC.
Inspired from the early studies of Barsoum and co-workers [44,67], HP was revisited later for the synthesis of Ti_2AlC [77]. It was conducted using Ti, TiC, Al and active carbon as starting powders. Due to the higher reactivity of Al as compared to Al_4C_3 employed in Barsoum's work [44,67], HP at 1400 °C within short times (1-3 h) led to phase pure and 98% dense Ti_2AlC. This temperature was found to be optimal, as titanium aluminides and TiC were additionally observed at 1300 °C and Ti_3AlC_2 at 1500 °C.
With the advent of recent field assisted sintering technologies and their commercialization in the 1990s [78], synthesis of Ti_2AlC achieved by spark plasma sintering (SPS) of elemental reactants was reported [71]. The synthesis temperature (1100 °C) and dwell time (1 h) required to obtain high-purity products was significantly lower than previous HP [67,73] or HIP [44] based works. A slight Al hyper-stoichiometry of 1.2 mol was used to compensate evaporation losses and increase the purity of the final product. Microstructural analyses highlighted average grain length and thickness of 20 and 5 µm respectively. For the sake of comparison, the same powder blends served for HP runs, using, as for SPS, the same Al hyper-stoichiometries ranging from 1.0 to 1.3 mol. In that case, lower purities were achieved in all cases and the end products contained secondary phases of TiC, TiAl and Ti_5Al_{11}.
The issue of phase transformation in the Ti-Al-C system was first addressed by Kisi et al. [49] in 2007. The synthesis of Ti_2AlC was carried out according to Wang and Zhou's [73] work and led to a > 99% pure product. By mixing the previously milled Ti_2AlC powder with TiC, pressing compacts and sintering them at 1350-1450 °C for up to 5 h, they could observe a phenomenon of inter-conversion from lower (Ti_2AlC) to higher (Ti_3AlC_2) order Ti-Al-C MAX phases. The assumed mechanism at the Ti_2AlC/TiC interface was the diffusion of weaklier bonded Al out of Ti_2AlC and in the TiC crystal structure, creating multiple stacking faults on {111} planes. It is presumably followed by Ti out-diffusion and the collapse of the Ti_2AlC structure, where TiC_6 octahedra come closer to each other, and the enlargement of the TiC lattice, eventually leading to the formation of Ti_3AlC_2.
A study published by Spencer et al. [63] in 2011 reported the use of Ti_2AlC powder synthesized and delivered by the company 3-ONE-2. The powder contained significant amounts of Ti_3AlC_2 and TiC. While HIP at 1400 °C for 3 h did not show any phase degradation, HP at 1500 °C for 4 h, led to a full conversion of 211 into 312, for reasons mentioned above [49].
The same year, a study of thermal stability of Ti_2AlC in high-vacuum was published by Pang et al. [64]. The employed powder was provided by the company Kanthal AB, and contained impurities of TiC, TiAl and Ti_3AlC_2. They demonstrated that high vapor pressure Al is highly prone to sublimation above 1400 °C, resulting in the formation of a thick TiC_x layer.
As a matter of cost reduction, Li et al. [79] reported the synthesis of pure Ti_2AlC powders using cheaper raw materials. Commercial TiH_2 was employed instead of Ti, as its price is 10% less. In addition, dehydrogenation was not required and products could be synthesized via conventional reactive sintering.
Up to now, solid-state reaction synthesis has remained a classical method to produce almost pure and small batches of Ti_2AlC powder. Solid-liquid or solid-solid reaction, reactive

sintering, pressureless sintering are other terms found in literature, the two last designations indicating that the obtained product is in compact form, not as powder. In parallel, HP and HIP have usually led to highly dense compacts and have required high temperatures. The scaling up is limited by the dimensions of the die. All these synthesis techniques have led to porous or dense samples, necessitating additional milling (ball milling, drilling) steps to end up with a powdered product. Through these extra steps, there might be a risk of impurity incorporation and additional costs necessarily come into play.

More recently, in 2018, the first ionic-liquid medium assisted route was reported by Galvin et al. [66], in which Ti_2AlC was synthesized using a molten salt method. They separately used NaCl, KCl and a NaCl/KCl mixture as synthesis medium. They reached a maximal purity of 88 wt. % Ti_2AlC, when performing the experiment at 1000 °C in argon for 5 h and using the NaCl/KCl mixture. The as-synthesized Ti_2AlC was recovered by grinding with mortar and pestle and washing out the salt with water. It showed that, for the first time, high purity Ti_2AlC could be produced at lower temperatures than usual and that, through this method, the recovery of powdered MAX phase was extremely simple.

Inspired by this study, a similar technique termed molten salt shielded synthesis (MS^3) was employed by Dash et al. [80,81] one year later to produce high-purity MAX phases. However, the novelty lied in the use of a new salt, potassium bromide (KBr), enabling the process to be carried out in air instead of protective atmosphere and, like the previous study [66], at lower temperatures. The interest lied in the fact that KBr can reach a pressed density > 95% when applying a punch pressure above 80 MPa [82]. In fact, the gas-tight salt encapsulation shields the raw materials from oxygen, hence avoiding their oxidation. Therefore, processing costs associated with the use of protective gas as well as thermal energy can be reduced. It is believed that the inter-diffusion of elements in the menstruum of molten salt is enhanced and that certain reactions take place earlier as they would in the solid state. The finely granulated powder recovered by a simple washing step can be further processed into desired components via conventional ceramic processing.

Depending on the application, Ti_2AlC can be produced from any synthesis routes presented so far. For laboratory purposes, small batches are desired as their purity remains high. The SHS and HP methods are still widespread. In fact, in 2019, Rutkowski et al. [62] managed to obtain a 95.4 wt.% pure sample by SHS, while the purity of hot pressed Ti_2AlC reached up to 98.7 wt.%. Nevertheless, secondary phases including intermetallic compounds (titanium aluminides), TiC and Ti_3AlC_2 are unavoidable. The challenge remains to limit and control their concentration in the final product and during the subsequent processing steps.

Alongside powders and bulk samples, the synthesis of MAX phase thin films has been extensively studied from the early 2000s. In spite of their potential and high achievable purity, these systems are not comparable to bulk samples. The conventional synthesis routes employed for thin films – such as e.g., magnetron sputtering or pulsed laser deposition – are not suitable for the production of powders [34].

In 2004, Wilhelmsson et al. [83] deposited for the first time epitaxial thin films in the Ti-Al-C system by magnetron sputtering from elemental targets. They showed that the formation of Ti_2AlC and Ti_3AlC_2 required a substrate temperature of at least 900 °C, otherwise resulting in cubic (Ti,Al)C or perovskite-type Ti_3AlC phases at 700 °C and 800 °C respectively. The thin films were highly crystalline and yielded resistivities slightly higher than those reported for bulk samples.

An in depth investigation of the deposition of these ternary compounds was provided in 2006 by Wilhelmsson et al. [84]. The difficulty in forming MAX phases below 800 °C was found due to the low diffusion rate of A-element (Al), which had to reach the surface of the growing film and be present in sufficient concentration to trigger the nucleation of Ti_2AlC or Ti_3AlC_2 phases.

The efficiency of another physical vapor deposition technique to produce epitaxial Ti_2AlC thin films was demonstrated by Rosén et al. [85]. The appropriate MAX phase stoichiometry was achieved by employing pulsed discharge arcs on elemental cathode targets and adjusting the ion flux to obtain the optimal deposition rates. Similarly, to the previous studies using magnetron sputtering, a temperature of 900 °C was required to obtain nearly phase pure Ti_2AlC with minor TiC impurities and cubic precipitates.
Nonetheless, even though their mention is noteworthy, thin films are not the focus of the present thesis, as they do not allow for the production of Ti_2AlC MAX phase powders.
In summary, synthesis routes are numerous to produce MAX phases and more specifically here, Ti_2AlC. However, not all of them lead to highly pure products and need to be carefully selected depending on further employed processing methods. An increasing interest for complex shapes has put more severe requirements on the science of ceramic processing, including MAX phases. In order to bring them closer to industry, realistic studies have to be performed while limiting the alteration of the synthesized products.

I-4 Processing of Ti_2AlC

Ti_2AlC powders constitute the raw materials for different kinds of processing techniques, whether they are used as feedstock for spraying technologies or employed as suspension for other various coating routes. Even though most of the synthesis routes (HP, HIP, SPS) result in a fairly compacted product, latter is generally of very simple shape. Often, comminution means are required to reobtain a powdered material that can further be processed in different ways. Nowadays, components with complex geometries are highly required in heavy-duty advanced applications, to such an extent that research in the field of ceramic processing becomes a necessity.

I-4.1 Porous templates, foams and coatings

Besides the need to manufacture bulk samples, porous templates and coatings are of interest for lightweight structural components, mechanical damping, thermal insulation, catalysis, or hot gas filter technology.
Porous Ti_2AlC can be produced through incomplete densification during pressureless sintering [86]. However, it does not allow for a control of pore size and morphology and is more of an undesired outcome in an attempt to densify a Ti_2AlC compact. The typical method to produce porous Ti_2AlC bodies has consisted in using a sacrificial pore former or space holder that can be easily eliminated before sintering. So far, sodium chloride (NaCl) [87], ammonium bicarbonate (NH_4HCO_3) [88] or white crystalline sugar [89] have been used. The volume fraction of porosity and pore size have been adjusted by varying the particle size distribution. The replica method employing sacrificial polymeric templates [90] and gel casting [91] were also reported for Ti_3AlC_2 and Ti_2AlC, respectively. Depending on the processing method, the size, morphology and nature of pores changes. Gel casting, for instance, leads to a high degree of interconnectivity between cells, as shown in Figure 1. 7B, with tailorable window size, whereas pores produced by the space holder method do not exhibit this feature Figure 1. 7A.
In parallel, various other studies focused on the production of Ti_2AlC coatings using spraying technologies. High velocity oxy-fuel spraying (HVOF) [92] of MAXTHAL 211 powder was reported for the first time in 2008. Depending on the gas flow rate, the density and thickness of the coatings as well as the number of cracks and delamination could be controlled. Low purities resulting from decomposition were reported in other studies [93,94], where coatings were composed of only 53 wt.% Ti_2AlC. A large fraction of pores (~13%) and a significant decrease in purity (26 wt.%) was also noticed in Ti_2AlC coatings produced by a plasma spray method

[95]. Usually, all techniques utilizing hot flames or plasma subject the MAX phase powder particles to tremendous temperatures, largely exceeding the melting point of the material. In turn, phase decomposition occurs and alters the coating's properties.

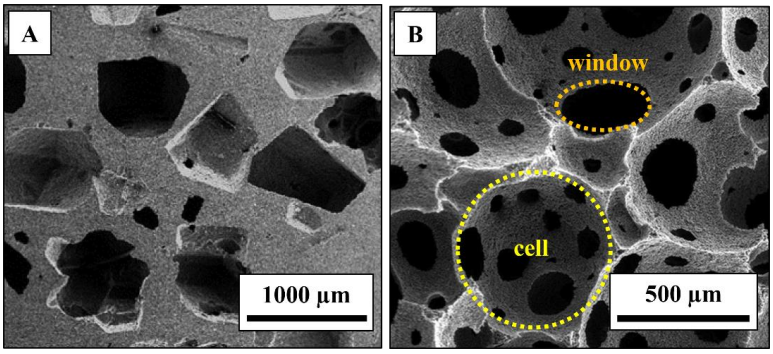

Figure 1. 7: Ti_2AlC foams produced by (A) the space holder technique and by (B) gel casting. Adapted from [89] and [91].

In fact, the decrease in Ti_2AlC content as well as cracked and porous coatings can be detrimental to the good oxidation performance of the considered MAX phase. Cold spraying of Ti_2AlC was first demonstrated in by Gutzmann et al. [96] as an alternative to high-temperature coating technologies, as the process temperature was below the melting point of Ti_2AlC. Coatings with less defects and phase dissociation – on account of lower heat transfer – were reported with high velocity air fuel (HVAF) spraying [97].
Despite the interest for porous architectures, stochastic foams and coatings, complex shapes and lattice structures with controlled design represent the highest potential due to a better control of properties. This goes hand in hand with the advent of additive manufacturing (AM).

I-4.2 Complex shapes

The main interest for potential industrial applications remains the possibility to produce MAX phase components with more elaborate shapes. Although it can be achieved by machining HP or HIP compacts, this method still has limits in terms of shape and size of parts to be manufactured. In addition, fast shaping techniques are required in industry for mass-production and cost reduction.
Rapid production of near net shape MAX phase parts is possible via emerging AM routes [98–100] (for cellular and lattice materials) or existing and well-established methods such as injection molding (IM) [101,102] (for bulk components). However, these are barely reported for Ti_2AlC. As such, this section also incorporates outcomes from other MAX phases, of which the production route can be applied to Ti_2AlC.
AM appeared in the 1980s, with the invention of stereolithography by Charles W. Hull [103]. It initially consisted in fabricating "solid objects by successively printing thin layers of a curable material" [103] as Hull described in his patent. So, at its early stages, it was essentially employed to manufacture polymeric systems using resins that were curable by ultraviolet (UV) light, electron beams, radiation, etc. A so called STL (Standard Tessellation Language) file was created as standard computer file for all AM techniques. It establishes the link between the model created by computer-aided design (CAD) and the manufactured 3D prototype [104].
Various other AM techniques have emerged and nowadays, apply to other categories of materials too. Powder bed fusion methods such as selective laser sintering (SLS), selective laser melting (SLM) and 3D-printing (3DP), or inkjet printing (IP), contour crafting (CC), laminated

object manufacturing (LOM) are examples of main methods of AM applicable to metals and ceramics [105]. The expiry of the first patents has given rise to a surge in research and development of AM techniques. It is promised a great future, but currently, it is still limited in many aspects, particularly when it comes to fabricate compositional complex materials or composites.

AM of MAX phases has been performed just a decade ago. Classically, 3D-printing was found an efficacious method to produce cellular and bulk MAX phase assemblies. The first paper reporting on the additive manufacturing of Ti_3SiC_2 was published in 2011 [99]. A combined method of 3D-printing TiC green bodies and liquid silicon infiltration (LSI) was employed to achieve the formation of a Ti_3SiC_2-based ceramic. However, the content of impurities such as TiC, SiC, $TiSi_2$ represented more than half the composite's volume fraction. In 2015, Ma et al. [100] followed a similar route to produce Ti_3SiC_2 ceramics, but replacing the LSI step by reactive melt infiltration (RMI). In these cases, the challenges resided in the control of purity, microstructure and end dimensions. In comparison, robocasting (RC) of Cr_2AlC – a variant of direct ink writing – turned out to be more reliable and cheaper through the use of aqueous-based dispersions [98].

The very first Ti_2AlC lattice structures (Figure 1. 8, A-C) were manufactured using direct ink writing [106] and contained a porosity fraction ranging from 44 to 63 vol.%. Contrary to porous structures such as foams, lattice materials are more symmetrical and the cell design more controlled. The highly viscous suspensions were extruded into filaments and stacked into a 3D architecture exhibiting a larger compressive strength (up to 89 MPa) than foams (up to 2.79 MPa) [91]. This is the only publication on AM of Ti_2AlC so far, demonstrating the novelty of the process but also the lack of knowledge and data in this field. In parallel, the possibility of fabricating MAX phases by SLM – in particular Ti_3SiC_2 and Cr_2AlC – was mentioned in a patent [107]. It claimed the feasibility of two different routes (SLM of elemental reactants or of stoichiometric MAX phase compositions) as an alternative to existing techniques employing a binder. However, no results were presented and the obvious problematic of incongruent melting of MAX phases was not alluded to. In addition, major drawbacks of AM are the time-consuming nature of the processes as a result of a layer-by-layer prototyping, high costs and limited adhesion between layers. Furthermore, the high power input required to melt ceramics with high melting point is not ideal. When employed in SLS or SLM, high power lasers can also induce thermal shock conditions for metals. Therefore, an alternative and more cost-effective solution is injection molding.

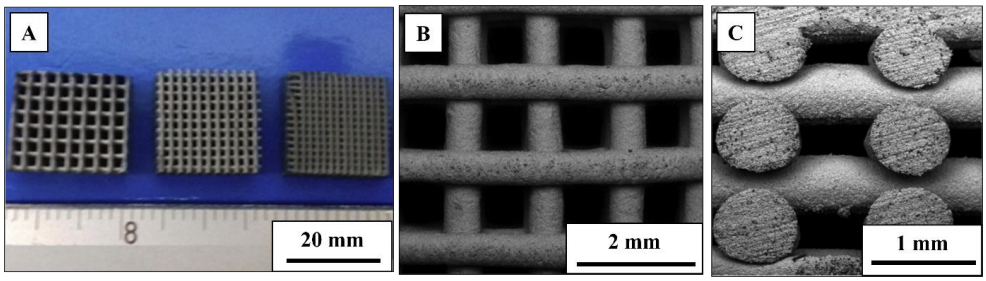

Figure 1. 8: Ti_2AlC scaffolds produced by direct ink writing: (A) overview of structures with different spacing between printed filaments, (B) and (C) magnification thereof. Adapted from [106].

IM is much older than AM and originated from a patent published in 1872 by the Hyatt brothers in the United States of America (USA) [108,109]. They mentioned that their invention – at that time known as "packing machine" – was "subjecting the compound to heavy pressure in a heated mold" [108]. The term "injection molding" appeared later in 1925 and this technique

has been quickly developing since the late 1920's [110]. The essential contributions to that technology came from the USA and Germany, resulting from the gradual interest for plastics. These, indeed, are attractive due to their lower melting/softening temperatures than metals and ceramics, enabling easier shaping and molding. Nowadays, with extrusion, IM is dominant in the industry of plastics [109] to manufacture various kinds of articles, from everyday life consumer products to thermoplastic parts in engineering systems. However, as a proof of its versatility, the process was rapidly adapted to metals and ceramics – just like AM techniques – allowing the production of advanced components with complex geometries.
IM technique rapidly turned out to be a suitable method for mass-production, allying fast processing with variability in mold design and material combination. Especially powder injection molding (PIM) has remained a powerful manufacturing technique to rapidly produce near-net shape metallic or ceramic high-performance precision parts [111]. PIM designates the general process of mixing a polymeric binder with a metallic or ceramic powder. In the former case, the term metallic injection molding (MIM) is employed, while in the latter case, ceramic injection molding (CIM) is used. Both PIM and CIM apply to MAX phases, for which few publications exist. Not only the IM of millimeter-sized monolithic Ti_2AlC building blocks [102] was investigated, but also Ti_3SiC_2, Ti_2AlC and $Ti_2AlC/SiC_{(f)}$ components (Figure 1. 9, A-C) with high surface quality were successfully produced [101]. In fact, in the latter study, the average mean roughness of Ti_2AlC injection-molded gear wheels yielded 1.38 µm and edges/curvatures were sharp and well-defined. A recent study [112] also reported about the production of porous Ti_3SiC_2 samples without using a spacer holder or sacrificial pore formers. However, in latter case, the residual porosity was rather a result of the inherent low sinterability of MAX phases under pressureless sintering conditions. The interest of this rapid manufacturing technique lies in the possibility to produce fiber-reinforced parts with excellent fiber dispersion, aiming higher temperature strength retention and mechanical properties than their monolithic counterparts.

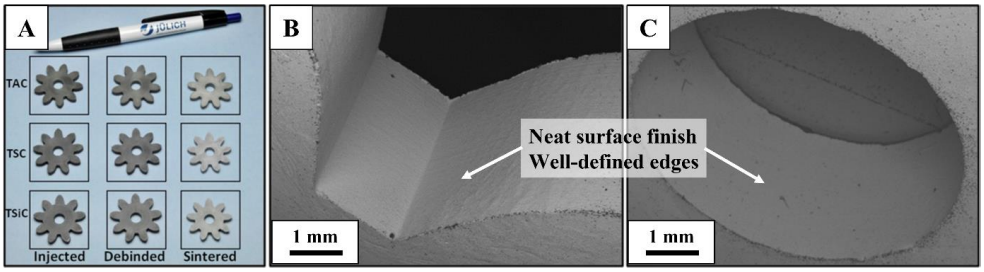

Figure 1. 9: MAX phase gears produced by powder injection molding: (A) Ti_2AlC, Ti_3SiC_2 and $Ti_2AlC/SiC_{(f)}$ components, (B) and (C) magnification thereof showing high-quality surface finish. Adapted from [101].

Despite the fact that IM is a well-established technology, its application to newly discovered and emerging materials such as MAX phases is limited. The lack of knowledge on PIM of Ti_2AlC is noticeable by the confined number of publications on that topic. Extensive research is required to be undertaken to understand the fundamental mechanisms coming into play during PIM and the subsequent processing steps (debinding, sintering), and that is precisely one of the goals of the present thesis.

I-5 Oxidation performance of Ti_2AlC

In order to fulfil the requirements of strict standards imposed by aviation, aerospace and other advanced fields, the manufactured components must exhibit excellent oxidation

performance in environments involving high-temperatures and oxidizing/corroding conditions. Even though studies about processing of Ti_2AlC are still missing, it can be said otherwise of work focusing on the oxidation of this MAX phase composition. In this specific case and contrary to Cr_2AlC, two elements can potentially be oxidized, namely, Ti and Al. Depending on the preferential selective oxidation of one element, the type of oxidation can change from passivating to catastrophic and unprotecting. The present section describes both types in details, as oxidation represents the core of this thesis.

I-5.1 Fundamental mechanisms

As mentioned previously in the section *I-2 MAX phases, a general overview*, the interest for Ti_2AlC lies in the fact that it naturally forms a protective aluminum oxide layer. One reason of preferential formation of Al_2O_3 can be found through ab initio modelling and vacancy-mediated diffusion. Liao et al. [113] found that the migration of Al monovacancies (V_{Al}) in Ti_2AlC was energetically the most favorable, with an activation energy almost 3 and 4 times lower than for Ti (V_{Ti}) and C (V_C) vacancies respectively. Therefore, the diffusion of Al in Ti_2AlC is predominant. Further, it was found that Al-defective Ti_2Al_xC is stable for significant sub-stoichiometries [114] in the range of $1 \leq x \leq 0.5$. Beyond x=0.5, the phase tends to decompose into $TiC_{0.5}$ and Al. An additional interesting feature is the Al_2O_3 scale's strong adhesive strength on Ti_2AlC, which exceeds 85 MPa and is higher than values reported for Al_2O_3/stainless steel and Al_2O_3/NiAl alloy couples [115].
Furthermore, first-principles calculations performed by Dahlqvist et al. [116] interestingly demonstrated that Ti_2AlC is stable upon incorporation of large oxygen concentrations. The formation of a $Ti_2Al(C_{1-x},O_x)$ oxycarbide phase through the substitution of C atoms by oxygen was found to occur for x as high as 0.75, without phase alteration/decomposition.
However, before exploring the different outcomes gathered during the last two decades about the oxidation of Ti_2AlC, one has to recall fundamental principles.
An important contribution to the understanding of the oxidation of metals and alloys was brought by Carl Wagner in the 20th century [117]. As part of the pioneers, he found the diffusion of species through the oxide scale to be the time-determining event. More precisely, it has been noticed that metal ions and electrons diffuse across the oxide scales that form on the metal's surface. While cations and electrons move in the metal → gas phase direction, anions diffuse in the opposite gas phase → metal direction as depicted bellow (Figure 1. 10).

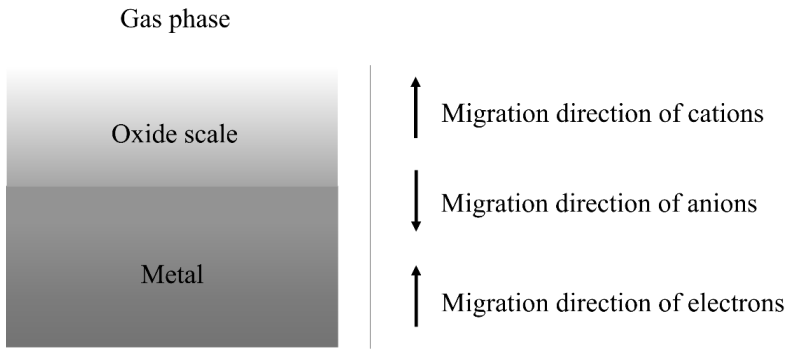

Figure 1. 10: Cross-section of an oxide scale that forms on a metallic material.

Wagner established the formula for the measure of the overall electromotive force in the growing oxide scale, assuming the presence of unassailable electrodes on both sides. In brief,

it consists in the summation of potential differences between electrodes and oxide as well as the potential drop across the scale (diffusion potential). In the same work [117], he linked the temporal increase in scale thickness $\Delta\xi$ to the initial thickness of the already existing oxide layer by means of a proportionality factor (time constant k') as follows:

$$\frac{d(\Delta\xi)}{dt} = \frac{k\prime}{\Delta\xi} \qquad \text{(Equation 2)}$$

Further, he mentioned that the mass gain (Δm) of a piece of metal heated in an atmosphere containing a component X (X= oxygen or a halogen gas) is proportional to the existing amount of X in the oxide scale. Thus, he established the following equation, relating the mass gain to the considered area q, the time t and a proportionality factor k'':

$$\frac{1}{t}\left(\frac{\Delta m}{q}\right)^2 = k'' \qquad \text{(Equation 3)}$$

In an analogous way, the description of the oxidation of MAX phases is based on the fundamental understanding of scale growth on metals described by Carl Wagner. As mentioned earlier, Ti_2AlC is the most attractive Al_2O_3-forming MAX phase composition. Two oxides, Al_2O_3 (Equation 4) and TiO_2 (Equation 5), are in competition and the selective oxidation of each can be expressed as follows [118]:

$$4Ti_2AlC + 3y.O_2 \rightarrow 4Ti_2Al_{1-x}C + 2y.Al_2O_3 \qquad \text{(Equation 4)}$$

$$Ti_2AlC + 2y.O_2 \rightarrow 2Ti_{2-2x}AlC + 2y.TiO_2 \qquad \text{(Equation 5)}$$

At longer oxidation times, carbon additionally diffuses through the oxide scale and oxidizes into CO_2- as follows:

$$Ti_2AlC + O_2 \rightarrow Al_2O_3 + TiO_2 + CO_2 \qquad \text{(Equation 6)}$$

The formation of continuous Al_2O_3 (Equation 4) is the desired outcome. As mentioned before, alumina scales – when present as α-alumina (corundum) – are dense and protective and proved their effectiveness in the case of oxidized bond-coats on superalloys [3]. Due to its large band gap, the conduction of electrons is slowed down. In addition, α-Al_2O_3 is most of the time stoichiometric, i.e., with a low concentration of oxygen vacancies. These two aspects are responsible for the slow growth rate of α-Al_2O_3 [119]. To the contrary, TiO_2 (Equation 5) is non-protective and has already demonstrated issues, e.g. in the case of intermetallic compounds (TiAl, Ti_3Al) [120]. Therefore, even if its formation cannot be fully curtailed, at least it has to be restricted.

This competition between Al_2O_3 and TiO_2 depends upon various factors, such as temperature, dwell time, oxygen partial pressure, and microstructure, purity, porosity, surface roughness of the Ti_2AlC base material.

Another important property of Ti_2AlC when it comes to oxidation performance is highlighted in Figure 1. 11. In fact, the coefficient of thermal expansion (CTE) of Ti_2AlC with one of its formed oxide α-Al_2O_3 represents an excellent match [34], and therefore allows for a significant reduction of thermal stresses. As such, premature spallation of the grown alumina scale can be prevented, generally occurring when the mismatch between substrate and oxide scale is large.

The first study of the oxidation of Ti_2AlC dates back to 2001 [121,122], in which parabolic oxidation kinetics (Equation 7) were reported for short times (~20 h) at temperatures in the range of 1000-1100 °C. At longer times, demixing occurred with formation of a rutile (TiO_2)

rich solid solution, which changed oxidation kinetics to a linear behavior. In this way, the first study of oxidation of Ti_2AlC was reporting a phenomenon known as breakaway oxidation and did not praise the excellent oxidation resistance of Ti_2AlC.

$$\left(\frac{\Delta m}{A}\right)^2 = k_p t \qquad \text{(Equation 7)}$$

with $\left(\frac{\Delta m}{A}\right)$ the mass gain per unit surface area, k_p the parabolic rate constant and t the exposure time.

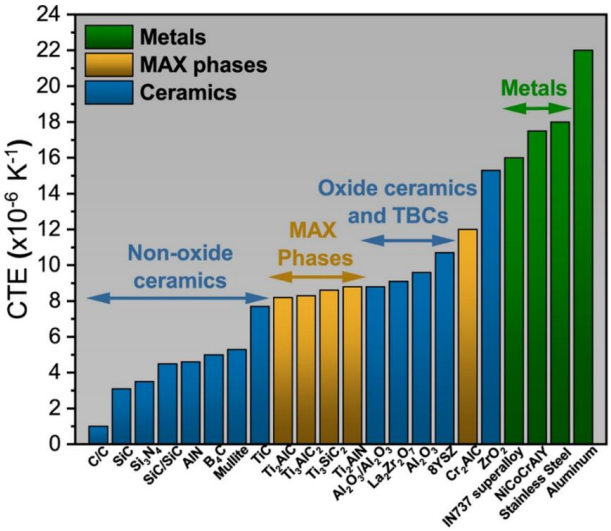

Figure 1. 11: Classification of conventional ceramics, metals and MAX phases in ascending order of their coefficient of thermal expansion [34].

As to differentiate between the usual "normal" protective oxidation and the uncommon "abnormal" breakaway oxidation of Ti_2AlC, the present section is divided into two parts, each of both being equally important to address and providing an overview of oxidation outcomes gathered for Ti_2AlC so far.
Oxidation of bulk Ti_2AlC, coatings and powders are listed the same way, though their expected performance differs from each other. The section dealing with breakaway oxidation additionally contains work conducted on Ti_3AlC_2 – as breakaway oxidation of Ti_2AlC is too infrequently reported – but the features of which would resemble what was observed for its 211 phase counterpart.

I-5.2 Oxidation of Ti_2AlC

Shortly after the very first report of oxidation of Ti_2AlC from Barsoum and coworkers [121,122], Wang and Zhou [123] demonstrated for the first time that the oxidation of Ti_2AlC rather obeyed cubic kinetics (Equation 8), when bulk samples were exposed in air for 20 h at temperatures in the range 1000-1300 °C.

$$\left(\frac{\Delta m}{A}\right)^3 = k_c t \qquad \text{(Equation 8)}$$

with $\left(\frac{\Delta m}{A}\right)$ the mass gain per unit surface area, k_c the cubic reaction rate constant and t the exposure time.

They reported a k_c of 1.12 x 10^{-10} $kg^3 \cdot m^{-6} \cdot s^{-1}$ for an oxidation temperature of 1200 °C (this temperature is of significance in the present thesis, as most experiments were carried out at 1200 °C). In the investigated range of temperature, they could observe the presence of α-Al_2O_3 as main oxide and rutile TiO_2 and mentioned that aluminum titanate (Al_2TiO_5) was absent even at 1300 °C, to the contrary of what could be noticed for Ti_3AlC_2. In addition, they evidenced the higher growth rate of TiO_2 as compared to Al_2O_3 and explained the presence of larger TiO_2 grains atop the protective scale as a result of Al_2O_3 grain boundary diffusion of Ti. The thickness of Al_2O_3 obviously increased with increasing temperature. They additionally based themselves on thermodynamical considerations and justified the presence of Al_2O_3 as inner scale due to its higher stability than TiO_2 at lower oxygen partial pressure (as it decreases with oxidation time due to the formation of the substrate/oxide interface).

Surprisingly, various other studies contradicted the initial outcomes published earlier. For example, the oxidation of Ti_2AlC was also found to follow a parabolic trend for up to 8 h at temperatures varying between 1100 °C and 1300 °C, despite a coarse microstructure (average grain size was around 100 µm) [124]. This trend was additionally recognised in the very first long term isothermal oxidation study performed at 1200 °C in air for 1000 h, which resulted in adherent Al_2O_3 scales, just like for shorter times [124]. Furthermore, continuous and adherent Al_2O_3 scales were also found on samples oxidized at higher temperatures of 1400 °C (500 h) and 1500 °C. As such, the work of Sundberg et al. [124] initiated the commercialization of Ti_2AlC under the registered trademark of Maxthal®, for the fabrication of heating elements and other high temperature applications.

Just as for the study of Wang and Zhou [123], other authors [125,126] found that a cubic growth rate (Equation 8) of the oxide scale was the most representative of oxidation kinetics of Ti_2AlC. In the first study [125], the temperature range was set between 1000 °C and 1400 °C and the dwell time to 25 h. It was emphasized that cubic kinetics can just be considered as first approximation, as the grown scale was composed of a complex arrangement of three different oxides and not pure alumina. Rutile TiO_2 and α-Al_2O_3 were detected – the signal of latter increased with oxidation time – when Ti_2AlC was oxidized at 1000 °C and 1200 °C, while Al_2TiO_5 was evidenced at 1400 °C, resulting from a solid-state reaction of the two coexisting oxides mentioned before. A thin Ti_3AlC_2 layer formed right underneath the oxide scale as the surface-near area was depleted with Al. The thickness of the protective alumina scale reached 15 µm after 1000 1-hour cycles at 1200 °C. Just like previous oxidation studies, the adherence of the oxide scale was found to be excellent. As a complement, photoluminescence experiments were carried out to estimate residual stresses in the scale. These were compressive in nature and yielded a maximum of 0.65 GPa, a value stated to be much lower than other alumina forming materials. Moreover, these stresses were found to tend towards a constant value with increasing oxidation time. In the second study [126], longer oxidation times (up to 120 h) of polished Ti_2AlC were investigated in air and in a water vapor saturated environment. The oxidation constants were one order of magnitude lower than those reported earlier [123] and yielded 1.0 x 10^{-11} and 1.2 x 10^{-11} $kg^3 \cdot m^{-6} \cdot s^{-1}$ in dry and humid conditions, respectively. Thus, humidity was suggested to have a non-detrimental effect on the overall oxidation resistance of Ti_2AlC above 1100 °C. The thickness of the oxide scale at 1200 °C reached 10 µm after 120 h for both samples oxidized in air and steam. While two usual oxides (Al_2O_3, TiO_2) were observed in air, the recession of TiO_2 above 1200 °C in steam could be documented as resulting from the formation of $TiO(OH)_2$ gaseous species. A simplified schematic of the oxide morphology generally found on Ti_2AlC and a typical cross-section are depicted in Figure 1. 12, including the typical thickness values reported so far.

Additional studies compared the oxidation performance of Ti_2AlC bulk samples with that of coatings [127] and thin films [128]. Bulk samples oxidized at 700 °C for almost 1000 h exhibited an oxide scale less than 2 µm in thickness and composed of a bottom thin α-Al_2O_3 layer and a top thick TiO_2 layer with alumina inclusions. After 168 h at 1200 °C, bulk samples presented 10 µm thick Al_2O_3 scales, atop of which large TiO_2 nodules were visible. These outcomes were consistent with previously reported observations [125,126]. Nonetheless, Ti_2AlC coatings manifested bad oxidation resistance at 700 and 900 °C as they contained detrimental TiC and titanium aluminide impurities. Contrary to bulk samples, Ti_2AlC coatings were oxidized across their entire thickness, not fulfilling protective characteristics. On the other hand, it could be concluded that coatings deposited with higher gas flow exhibited slightly superior oxidation resistance, probably on account of higher coating densities.
Similar results were obtained for Ti-Al-C films essentially composed of Ti_2AlC [128]. Even though low oxidation rates were reported at 600 and 700 °C, rapid consumption of the coating occurred at 800 and 900 °C. Part of their outcomes is therefore described in the second section on breakaway oxidation.

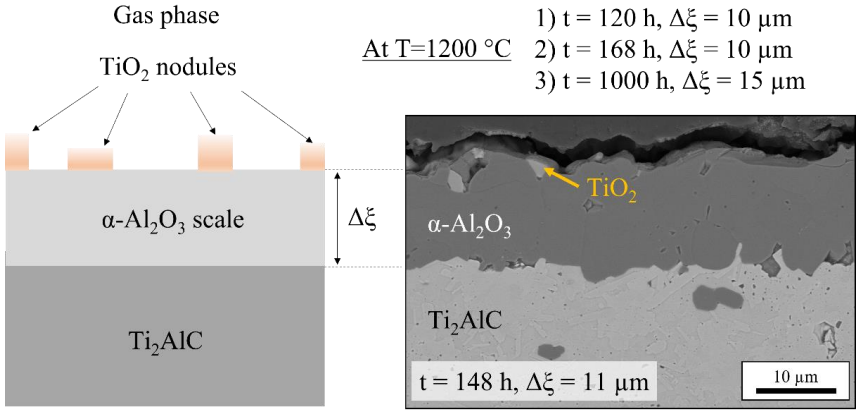

Figure 1. 12: Simplified depiction of the oxidation of Ti_2AlC in air and reported scale thickness values for T = 1200 °C taken from 1) [126], 2) [127] and 3) [125]. SEM image is from the present work.

Oxidation of Ti_2AlC thin films was performed at even lower temperature [129]. At 500 °C and within less than 15 min, the coexistence of amorphous Al_2O_3 clusters – preferentially forming in valleys and on plateaus formed by protruding Ti_2AlC grains – along with carbon-rich titania (TiO_xC_y) were reported. It complemented low to intermediate-temperature oxidation studies and confirmed that the oxidation resistance of Ti_2AlC below 700 °C is low.
In 2011, the first ultra-high temperature (3000 °C) study was carried out by Song et al. [130] by subjecting a Ti_2AlC specimen to on oxyacetylene flame. The sample exhibited a coarse microstructure of lamellar grains and its surface was polished down to 1 µm. α-Al_2O_3, rutile TiO_2 and Al_2TiO_5 were the three oxide phases coexisting on the oxidized surfaces after 30 s at up to 3000 °C. A two-layer arrangement of oxides formed – the outer scale being porous and composed of the three aforementioned oxide species – while the inner layer was porous too and consisted of Al-depleted Ti_2AlC and TiC_xO_y. Such harsh conditions obviously resulted in the sublimation of high vapor pressure Al. Even though the outcomes of ultra-high temperature oxidation testing are worth to be documented, they are of little significance for MAX phases, which are not destined to be used the same way as UHTCs. Another high-temperature study [131] reported the oxidation resistance of Ti_2AlC at temperatures above 1600 °C. The samples demonstrated good oxidation resistance at 1600 °C after 10 min, as well as at 1650 °C after 5

min. Even though these oxidation times are extremely short and prolonged exposure would necessarily lead to compositional changes within the material, this work showed that Ti_2AlC is capable of withstanding high peak temperatures. At 1700 °C and 1800 °C, Ti_2AlC thermally decomposed, as the selected temperatures were above its incongruent melting point [55]. Combined with cracking of the oxide scale, the samples began to bulge, indicating the limit in operating temperature for this material.

A more fundamental study [132] consisted in investigating the initial stage of oxidation of polished (1 µm) Ti_2AlC at 1200 °C via transmission electron microscopy (TEM). Within 3 min, two distinct layers of Al_2O_3 and TiO_2 grew and were separated from the Ti_2AlC material by a thin discontinuous cubic titanium carbide (TiC) layer. The oxidation of Ti_2AlC starts with the outward diffusion of Al, leading to the formation of a thin TiC layer, followed by the outward diffusion of Ti through Al_2O_3 grain boundaries. The crystallographic orientations found in the Al_2O_3 structure are dictated by the orientation of basal or prism atomic planes in Ti_2AlC.

Later, an atomistic model was proposed to explain the formation mechanisms of oxides on Ti_2AlC at different temperatures [133], partly based on results from previous studies. At 900 °C, a scale of rutile TiO_2 exclusively forms, resulting from the inward and outward diffusion of O^{2-} and Ti^{4+} ions, respectively. At 1000 °C, few α-Al_2O_3 grains start to nucleate and grow, but the TiO_2 scale remains predominant. It is in the temperature range of 1100-1300 °C that alumina is found to form the inner protective scale, atop which TiO_2 composes a discontinuous layer. At 1400 °C, the reaction between TiO_2 and Al_2O_3 results in the formation of Al_2TiO_5. Three oxides with different CTE coexist. The volume expansion resulting from this reaction as well was the mismatch in CTE leads to the formation of cracks in the oxide scale, causing significant oxygen ingress. The fissuring propagates towards the oxide/MAX phase interface, acting as short-circuit channels for oxygen and promoting severe oxidation of the base Ti_2AlC material.

Apart from studies analysing the effect of temperature (1000-1400 °C) and the effort invested in comprehending the fundamental mechanisms of oxide formation, the influence of surface defects or surface finish was still missing. That is why a model was proposed to describe the microstructure of the grown oxide scale above cavities, when Ti_2AlC was oxidized at 1200 °C [134]. For cavities smaller than 2 µm, rutile TiO_2 was not found above the dense Al_2O_3 layer. Above a cavity size of 2 µm, the thickness of both Al_2O_3 and TiO_2 gradually increased. Larger islands of TiO_2 clusters were observed above larger cavities, while the microstructure of Al_2O_3 itself was found to be different from the one usually observed on flat surfaces. It was concluded that the Al_2O_3 grains growing within cavities do not form a scale as compact as on flat surfaces, therefore facilitating the outward diffusion of Ti atoms. It proved that a careful tailoring of the near-surface area is necessary to control the build-up of oxides.

The interesting self-healing ability of Ti_2AlC was first explicitly unveiled and described in 2012 by two Dutch groups [135,136]. In the first work [135], indentation-induced cracks could be healed several times at 1200 °C essentially via sealing with grown Al_2O_3 and minor amounts of TiO_2 grains. The indents themselves, though, showed a higher propensity of large rutile patch formation above a thin Al_2O_3 scale. The fissure-healed samples exhibited even higher flexural strength than the initial undamaged specimen. In the second study, Yang et al. [136] discovered that the largest healable cavity on the Ti_2AlC surface at 1200 °C and within 20 h is 10 µm in width. They reported that besides cavity size, its shape also plays a significant role. Cavities with thinner openings showed exclusive Al_2O_3 formation due to gradual neck sealing and reduction of the cavity's inner oxygen concentration. Additionally, they observed a multi-layered arrangement of oxides in the early stages of oxidation, different in both the cases of oxidized cleavage and non-cleavages planes. When cleavage planes (basal planes) are exposed, the outward diffusion of Al is slower. The formation of stacked scales of Al_2O_3 and TiO_2 was deduced. This stacking was not assumed on exposed non-cleavage planes (prismatic surfaces) as the outward diffusion of Al was found to be faster along basal planes. Though, at longer oxidation times, this multi-layered arrangement vanished. A first inner layer of compact

columnar Al_2O_3 grains grew on Ti_2AlC samples, followed by a second outer layer of equiaxed Al_2O_3 grains, and this, independently of the crystal orientation of the base material.
The oxidation kinetics of Ti_2AlC and its "sister" phase Ti_3AlC_2 have been the subject of a long debate over the past two decades. Neither parabolic nor cubic oxidation kinetics were reported in the study of Song et al. [137], where polished Ti_2AlC was oxidized under dry air at 1200 °C for up to 80 h. Instead, they mentioned that the exponent *n* from the power law relationship (Equation 9) varied from 7 to 4 between early and later stages of oxidation. In the former case, the higher value was suggested being linked to rutile formation and fast Al_2O_3 grain nucleation. In the latter case, the decrease of *n* was related to Al_2O_3 grain growth and hence, the increase in diffusion length.

$$\left(\frac{\Delta m}{A}\right)^n = k_m t \qquad \text{(Equation 9)}$$

with $\left(\frac{\Delta m}{A}\right)$ the mass gain per unit surface area, k_m the oxidation rate constant, t the exposure time and *n* the power law exponent. Therefore, the determination of oxidation kinetics for Ti_2AlC should rather be considered on a case-by-case basis, as various parameters determine the build-up of oxide scales.
In the decade following the first oxidation study of Barsoum et al. [121,122], research essentially focused on high-temperature oxidation with temperatures exceeding 1000 °C. The considered range of 1000-1400 °C was carefully targeted after considering the stability of the high-temperature form of alumina, α-Al_2O_3. Key was to avoid the formation of less protective transition phases, such as γ-Al_2O_3, θ-Al_2O_3 or the metastable orthorhombic polymorph of α-Al_2O_3 [119].
Most of these oxidation outcomes were compiled in the review paper of Tallman et al. [41] in 2013, where the inconsistency in observation of oxidation kinetics has been discussed. Additionally, they carried out the very first long-term oxidation experiment with Ti_2AlC at 1200 °C in air for about 3000 h, eventually concluding that oxidation kinetics can be approximated to a cubic trend. Nevertheless, they mentioned that a realistic way to anticipate Al_2O_3 scale growth on Ti_2AlC was to use power law fitting – as Song et al. [137] did – instead of applying a parabolic or cubic fit to the results. The measurement of Al_2O_3 grain size during long-term isothermal oxidation showed that grain coarsening kinetics follow a power law. It was evidenced and confirmed that the diffusion of ionic species (Al^{3+}, Ti^{4+}, O^{2-}) along alumina grain boundaries was the rate-limiting step.
Later, in 2015, a study published by J.L. Smialek reported near-cubic kinetics of commercial MAXthal Ti_2AlC. The polished samples were oxidized for 100 h between 1100 °C and 1300 °C in a thermogravimetric analysis (TGA) furnace. An initial significant mass gain increase was related to rapid build-up of TiO_2, known to take place at low temperature. Smialek mentioned that, when this mass gain offset was subtracted from the total weight change, the isothermal oxidation behavior of Ti_2AlC coincided to that of FeCrAl alloys, which are also alumina forming materials. In addition, he found the scale growth to be cubic, on account of cubic grain growth.
At that time, a series of oxidation studies had been performed, all identical in one specific aspect: they were all conducted isothermally, i.e., with a heating ramp, an isothermal plateau and a cooling sequence. However, in real conditions, operating temperatures fluctuate and involve thermal stresses of different nature. As such, cyclic oxidation testing was performed with Ti_2AlC in the 600-1000 °C range in air [138]. Oxidation kinetics were found to follow a parabolic trend above 700 °C, and scales were dense and spallation-resistant. It proved that under cyclic temperature variation, the response of Ti_2AlC is still excellent and comparable to that of isothermal experiments.
In order to simulate the exposure of materials to realistic operating conditions, burner rigs have been conventionally used. For that, the samples come into contact with the flame exiting a

burner nozzle. The first burner rig oxidation testing of Ti_2AlC was carried out at 1100-1300 °C, in a 10 % water vapor environment, with a combustion gas velocity of 25 m/s [139]. It showed that cubic kinetics were more appropriate to describe the oxidation of Ti_2AlC in these specific conditions. Clusters of TiO_2 crystals usually observed atop the Al_2O_3 scale disappeared after exposure in the high-pressure burner rig environment. Without observing significant weight loss, it has been concluded that vanishing of TiO_2 colonies resulted from their reaction with water vapor and the evaporation of $TiO(OH)_2$ species.

Until two studies published in 2017 [65,140], oxidation testing had primarily been carried out on bulk samples, without having considered the oxidation of powdered Ti_2AlC, which is for example used in high-temperature coating facilities. Obviously, the oxidation of powder as compared to bulk Ti_2AlC is faster given its higher specific surface area. Thus, at temperatures above 1000 °C, Ti_2AlC powder particles were entirely transformed into TiO_2 and Al_2O_3 [65]. A relationship between powder particle size and oxidation behavior was established [140]. Coarser Ti_2AlC powders started to oxidize at higher temperature (400 °C) than fine particles (300 °C), as latter, obviously, showed higher specific surface area. These outcomes were retrieved from TGA runs. As such, oxidation times were limited to 1-2 h. Logically, Ti_2AlC powders are not intended for long-term oxidation experiments, but their oxidation resistance rather represents an interest for coating technologies, where particles may be subjected to high temperatures for short times.

As oxidation is only a form of corrosion, it is reasonable to mention about corrosion studies performed so far on Ti_2AlC and to include them in this part. Two concrete studies on the use of Ti_2AlC as protective coating for thermal barrier coatings (TBCs) against calcium-magnesium-alumina-silicate (CMAS) attack were published in 2019-2020 by Guo et al. [141] and Yan et al. [142] respectively. In turbine engines, CMAS hazard is a detrimental issue to the integrity of components as the mixed salt, when molten, irremediably corrodes structural parts. Their studies showed the first promising outcomes. The reaction of CMAS with Ti_2AlC led to the formation of large crystalline areas of anorthite ($CaAl_2Si_2O_8$) and melilite ($Ca_2(Mg_{0.25}Al_{0.75})(Si_{1.25}Al_{0.75})O_7$) above a protective layer of Al_2O_3. The crystallization caused by diffusion of Al and Ti from the coating inhibited further penetration of molten CMAS in Ti_2AlC. A pre-oxidation step at 1200 °C for 10 h resulted in superior corrosion resistance due to the formation of a thin Al_2O_3 scale prior to CMAS attack. In general, experiments conducted at 1250 °C for up to 16 h resulted in the crystallization of anorthite right above the Al_2O_3 scale, without formation of melilite. The affected area was smaller. The pre-oxidation step helped in reducing the rate at which Al was depleted from the underlying Ti_2AlC coating.

The influence of microstructure and texture was particularly emphasized in the last two years [143,144]. In 2020, a study published by Yu et al. [143] demonstrated that the microstructure of the bulk Ti_2AlC material played an important role in its oxidation. Fine-grained samples (1-5 µm) exhibited cubic oxidation kinetics with a rate yielding 3.3×10^{-12} $kg^3 \cdot m^{-6} \cdot s^{-1}$ at 1100 °C, which was of the same order of magnitude as values reported for similar microstructures at the same temperature [41,123,126]. To the contrary, coarse-grained Ti_2AlC (15-150 µm) was found to follow parabolic oxidation kinetics as already mentioned in a previous study [121,122], with formation of a mixed Al- and Ti-oxide layer. Alongside the exhaustion of Al, Ti_2AlC grains locally decomposed into TiC, this transformation not having been observed for fine-grained microstructures. This study is worth being considered, especially as the Ti_2AlC microstructures dealt with in the present thesis are fine-grained. Further, Li et al. [144] studied the influence of grain orientation in Ti_2AlC and Ti_3AlC_2 on their respective oxidation resistance. From the textured surfaces, these being transversal to basal planes demonstrated superior oxidation resistance at 1300 °C, with formation of a continuous protective Al_2O_3 layer. This was due to facilitated diffusion of Al along basal planes towards the surface. Further results of this study are mentioned in the next section, *I-5.3 Breakaway oxidation of Ti_2AlC and Ti_3AlC_2*.

In summary, the complex outcomes of oxidation of the Ti_2AlC phase and its 312 homolog have been compiled during the last two decades. It showed that Ti_2AlC has to be employed at temperatures exceeding 700 °C and preferentially in the 1000-1300 °C range in order to promote the growth of a stable, protective and free-of-cracks α-Al_2O_3 scale. There is still uncertainty when it comes to oxidation kinetics, as some studies defend a parabolic law while others describe cubic behavior. Yet, grain size and orientation seem to be the major feature to examine. Considering that numerous parameters influence the build-up of oxide scales atop Ti_2AlC, a power law behavior would be a better fit, and has to be adapted on a case-by-case basis. Additionally, bulk samples exhibit better performance than coatings or thin films, in reason of larger reservoirs of Al. When these are depleted below a certain concentration limit, or when parameters are not carefully controlled, non-passivating oxidation can take place.

I-5.3 Breakaway oxidation of Ti_2AlC and Ti_3AlC_2

Although many studies reported the excellent parabolic to cubic oxidation behavior of Ti_2AlC, some mentioned unusual features, addressed as being in the category of breakaway oxidation. This phenomenon corresponds to excessive oxidation rates and significant mass gain over short periods of time. Breakaway oxidation can be defined as chemical failure, whether intrinsic or mechanically induced, depending on the considered temperature, time of exposure and sample section thickness [145] leading to non-protective scaling. It is not a new concept, and has been extensively described for alloys [145–148]. The mass flux of cations from the base material towards the oxide/base material interface balances the mass transport of cations through the growing oxide scale and induces a solute depletion in the near-surface area. Breakaway oxidation occurs when the mass-balance condition is not fulfilled anymore, i.e., when the concentration (or activity) of the preferentially oxidized element at the interface decreases below that in equilibrium with the oxide. Thus, the subsequent increase of the oxygen activity allows reactions with other elements to be thermodynamically favorable. Breakaway oxidation is of major importance if MAX phases were to be transferred to the market for high-temperature applications. As the oxidation of Ti_3AlC_2 follows an identical reasoning as Ti_2AlC – not considering the fact that its oxidation resistance is lower than that of the 211 phase – and as most of the MAX phase breakaway studies have mentioned the 312 phase, work carried out on this phase was incorporated in the present section too.

As highlighted in the section *I-5.1 Fundamental mechanisms*, the very first two-part oxidation study of Ti_2AlC in 2001 [121,122] documented the formation of thick multi-striated oxide scales forming at temperatures above 1000 °C. These were composed of inconsistent stratified layers of a $(Ti_{1-y}Al_y)O_{2-y/2}$ solid solution – arising from kinetic demixing due to the dissolution and diffusion of Al^{3+} ions from low to high oxygen partial pressure areas, an Al_2O_3-rich region, and planes of porosity. These abnormal scales were hundreds of micrometers thick and not only observed for Ti_2AlC, but also for $Ti_2AlC_{0.5}N_{0.5}$, $Ti_4AlN_{2.9}$ and Ti_3AlC_2. All samples, predominantly pure, exhibited an average grain size ranging from 20 to 30 µm, which, with the employed surface finish (600 grit = P1200), might constitute the causes of breakaway oxidation. However, this term was not employed by Barsoum and his co-workers, as little was known about the oxidation of these compounds.

To the contrary of bulk MAX phases, coatings experience anomalous or rapid oxidation way faster and at lower temperatures due to high specific impurity content, presence of coating defects and pores or less volume providing insufficient amounts of Al in a long-term scenario. The latter is the main reason of breakaway oxidation in most of the scenarios and affects coatings more than bulk materials.

In fact, some studies [127,128] showed that coatings were fully consumed at temperatures above 800-900 °C. The oxidized films were composed of mixed oxide layers of TiO_2 and Al_2O_3. Emphasis was set on the need to design thicker coatings with larger grains to avoid catastrophic

oxidation. Ti_2AlC coatings were also applied on 316 L austenitic stainless-steel substrates and oxidized in air and water vapor at 750 °C for 200 h [149]. In dry air, the scale was overall protective, even though iron (Fe) and chromium (Cr) diffused from the substrate outwards and were found enriching the upper Al_2O_3 and TiO_2 layers. In water vapor, though, the coatings experienced breakaway oxidation as a result of cracks propagating from substrate to surface and acting as short-circuit channels. Similarly, 4-12 µm thick Ti_2AlC coatings applied on zirconium alloy substrates were oxidized in steam in the 1000-1200 °C temperature range [150]. Although it has been claimed that the oxidation resistance of the Zirlo substrate could be enhanced and even though coatings are not expected to yield similar performance as bulk materials, the morphology of the oxide scale is in all point similar to what can be observed in breakaway oxidation studies of bulk materials. First, a layering (as thick or several times as thick as the Ti_2AlC coating) of mixed alumina and titania containing a large fraction of porosity was documented. Second, the work was restricted to very short oxidation times (30 min at most).

As mentioned in the previous section, oxidation temperatures have to be selected according to the stability domain of α-Al_2O_3. Issues arise when Ti_2AlC [151] or Ti_3AlC_2 [152] are exposed to temperatures lower than 700 °C. Actually, in the 600-700 °C range, the transformation of metastable anatase-TiO_2 to thermodynamically stable rutile-TiO_2 takes place in absence of dopants or large concentrations of impurities [153]. This phase transition or the volume expansion caused by the formation of metastable anatase-TiO_2 generate cracks along weaker crystallographic planes. This was found as a probable reason for the low protectivity of Ti-Al-C MAX phases and higher oxidation kinetics below 700 °C. In addition, this phenomenon is accentuated in presence of water vapor [154] and can unequivocally lead to breakaway oxidation within extremely short times (2-5 h). De facto, the eased penetration of hydrogen and its dissolution in the oxide lattice promotes the formation of oxygen vacancies, in turn responsible for faster mass transport. Further studies confirmed these low-temperature oxidation outcomes [138].

For the same reason, Ti_2AlC oxidized in steam above 1400 °C underwent chemical failure [155]. That phenomenon was related to the faster diffusion of smaller hydrogen-containing species (resulting from the dissociation of water molecules) in Al_2O_3 and generation of voids at the oxide/substrate interface, plus at Al_2O_3 grain boundaries and within Al_2O_3 grains. The accumulation of stresses in the oxide scale led to micro-cracking, delamination, and fracture followed by linear oxidation kinetics and bulk material consumption.

The first explicit mention of breakaway oxidation of MAX phases came from Li et al. [156]. It occurred for Ti_3AlC_2 samples oxidized for a long time in air at 1100 °C (Figure 1. 13).

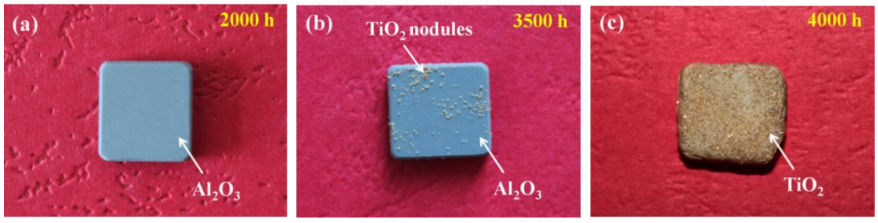

Figure 1. 13: Long term oxidation outcomes at 1100 °C for Ti_3AlC_2 showing TiO_2-rich nodules and subsequent breakaway oxidation, adapted from [156].

Up to 2000 h of isothermal oxidation, the oxide scale was mainly composed of dense and protective Al_2O_3. After 3500 h, orange to brownish TiO_2 macro-nodules were visible and scattered across the whole sample. At this stage, the localized exhaustion of Al led to a diminishing outward flux of A-element atoms, hence oxidation of near-surface Ti started.

Astonishingly, within the following 500 h of the isothermal oxidation run, the sample's surface was covered in its entirety with TiO_2. This outcome highlighted rapid runaway oxidation kinetics, following a linear trend, as soon as the Al_2O_3 scale lost its protectiveness. Cross-sectional analyses showed a similar stratification of mixed oxide layers and pores as reported in previous studies [121,122].
Part of all these results were compiled in a NASA report by J.L. Smialek [157]. Additionally, it expounded for the first time on damage-induced breakaway oxidation of Ti_2AlC (Figure 1. 14). Rapid overgrowth of large TiO_2 nodules and patches at spot-welded, metal punched, diamond stylus scratched, and oxy-acetylene torch melted areas was observed within extremely short oxidation times (1-5 h) at 1200 °C.

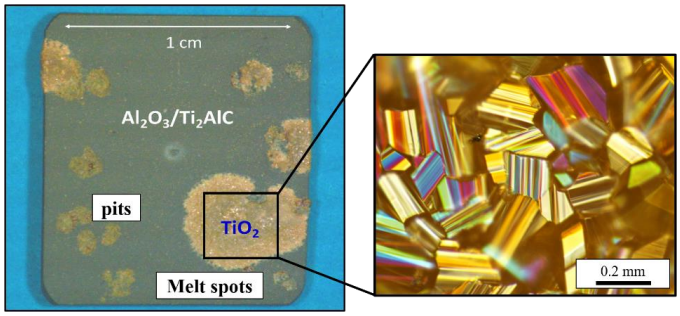

Figure 1. 14: Breakaway oxidation observed at damaged surface spots, with overgrowth of strongly twinned TiO_2 crystals, adapted from [157].

The influence of surface roughness was also briefly pointed out (Figure 1. 15), but this has been the only study reporting about this effect: excessive TiO_2 overgrowth on 180 grit ground surfaces was observed, while less rutile formation could be noted for 2400 grit polished surfaces.

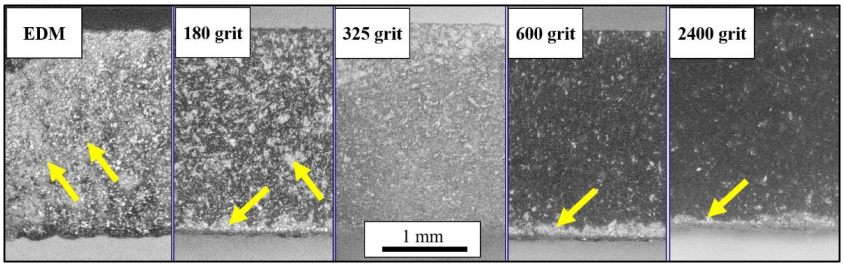

Figure 1. 15: Effect of surface roughness on the oxide morphology forming on Ti_2AlC after oxidation at 1200 °C, adapted from [157]. Yellow arrows point at rutile-TiO_2 patches.

The good control of surface finish is not the only mandatory criterion to avoid chemical failure of Ti-Al-C MAX phases. Likewise, the orientation of grains within the bulk material was found to play an essential role in the build-up of oxides on its surface. In the previous section, the work of Li et al. [144] has been mentioned. Part of their outcomes can be listed here. While Ti_2AlC and Ti_3AlC_2 textured surfaces perpendicular to basal planes exhibited high oxidation resistance on account of easier outward diffusion of Al, surfaces with exposed basal planes presented features typical of breakaway oxidation. These surfaces were subjects of abnormal oxidation as Al diffusion perpendicular to basal planes is known to be significantly slower.

Therefore, yellowish/orangish thick and highly porous striated scales of mixed oxides (Al_2O_3, TiO_2, Al_2TiO_5) were formed.
In parallel with studies unveiling and praising the excellent oxidation performance of Ti_2AlC, other manuscripts have consistently focussed on the deliberate triggering of breakaway oxidation. As one comes closer and closer to a potential transfer of MAX phases to the market, it seems that the understanding of this problematical issue is more important than ever.
Machine-learning was used recently to assess the oxidation stability of Ti_2AlC [118]. In the 300-2000 K range, Al_2O_3 was found to be present at all oxygen fractions due to its high chemical activity and exothermic nature, while TiO_2 only at high oxygen contents. In order to intentionally provoke breakaway oxidation, an experiment on a thin wedge-shaped sample at 1200 °C was conducted (Figure 1. 16).

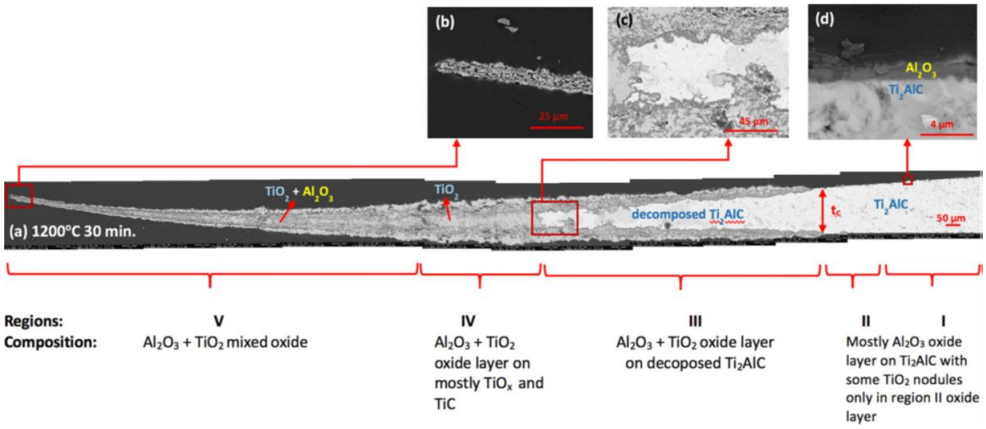

Figure 1. 16: Breakaway oxidation after 30 min at 1200 °C of a wedge-shaped sample [118].

Within 30 min, the tip of the sample, i.e., the thinnest area, experienced the same typical stratification of oxides observed in breakaway conditions. They pointed out that Al-deficient $Ti_2Al_{1-x}C$ decomposed into Ti_3AlC_2 and TiC, which are the species responsible for the mixed oxide scale build-up. They estimated breakaway oxidation to start for an Al-deficiency of ~5 at.%.
With the same reasoning involving extremely thin sections, breakaway oxidation was reported for Ti_3AlC_2 foils at 1100 °C in air [158]. They showed that the thickness of their foils and wedge-shaped samples was a determining parameter for the transition from selective Al oxidation to breakaway oxidation. Similar to previous studies on breakaway oxidation, they observed the formation of large nodules of mixed oxide scales, having a micro-banding morphology of alternating layers of TiO_2-rich and Al_2O_3-rich regions. Thin foils with a thickness of 85 µm were promptly subjected to breakaway oxidation, while 95 µm thick samples started to anomalously oxidize after 12.5 h at maximum temperature. For samples with a thickness larger than 110 µm, the time after which this mechanism started was further delayed, confirming the time-dependent depletion phenomenon.
Strategies have been developed to circumvent breakaway oxidation, even though, so far, there is no magic remedy to this issue.

I-5.4 Improvement of the oxidation of Ti-Al-C MAX phases

Several strategies to improve the oxidation of Ti_2AlC and Ti_3AlC_2 have been reported. For example, Donchev et al. [159] reported slightly superior oxidation resistance of a (Ti,

Nb)$_2$AlC solid solution as compared to pure non-alloyed Ti_2AlC. A fluorine treatment prior to oxidation also helped in slightly reducing the total mass gain.
Not only "M"-element substitutions were reported to enhance the oxidation resistance of Ti_2AlC. Wang et al. [160] managed to reduce the self-healing temperature of 211 via an "A"-element substitution. In fact, indentation-induced cracks in $Ti_2(Al_{0.6}Sn_{0.4})C$ coatings were found to self-heal at a temperature as low as 700 °C, and even exhibited superior oxidation resistance at 800 °C than the unhealed coatings.
Further, the anomalous low-temperature (600 °C) oxidation of Ti_3AlC_2 could be suppressed through additions of TiB_2 particles [161]. These promoted the formation of glassy B_2O_3 providing a low- and intermediate-temperature oxidation barrier, reducing the overall oxidation rate in the 500-900 °C range. At higher temperatures (T=1000-1400 °C), B_2O_3 became gaseous and led to the generation of voids within the Al_2O_3 scale and at the substrate/oxide interface [162]. These pores decreased the total area over which Ti^{4+} could diffuse outwards and modified the oxidation kinetics to logarithmic.
High-temperatures pre-oxidation steps were also reported to improve the intermediate-temperature oxidation and corrosion resistance of Ti-Al-C MAX phases. On the one hand, for Ti_3AlC_2, the formation of anatase TiO_2 at intermediate temperatures (500 and 600 °C) – usually responsible for microcrack formation in the oxide scale – could be inhibited via a pre-oxidation treatment at 1000-1300 °C for 2 h, as a result of build-up of protective scales [163]. On the other hand, a similar treatment resulted in a higher corrosion resistance of Ti_2AlC against molten Na_2SO_4 [164]. In fact, the protective Al_2O_3 scale constituted an almost impervious layer to the molten salt and significantly reduced the time at which a reaction between salt and substrate would occur.
These solutions have mainly focused on bypassing the negative effect of breakaway oxidation arising at lower temperatures. However, these do not apply to high-temperature treatments.
Furthermore, the maximum operating temperature of MAX phases is limited, so that ceramic top-coats are absolutely required for long-term operation above 1300 °C. Such as for superalloys, thermal barrier coatings are needed for MAX phases.

I-5.5 MAX phases and thermal barrier coatings

Thermal barrier coatings (TBCs) are employed in turbine engines in order to protect components subjected to high temperatures. They can typically reduce the surface temperature of internally cooled parts by 100 °C to 300 °C [165,166], depending on the coating thickness (usually varying between 100 and 500 µm). Conventionally, along newly developed compositions, 7 wt.% YSZ (compositions may also vary between 6 and 8 wt.%) [167] is still widely used as it proved to be a reliable material over more than three decades and possesses interesting mechanical properties.
Although not being numerous, studies about YSZ-coated MAX phases have been conducted essentially by two groups in NASA Glenn Research Center and Forschungszentrum Jülich GmbH. These are restricted to Cr_2AlC and Ti_2AlC and encompass furnace thermal cycling and burner rig testing. As presented in Figure 1. 11, MAX phases have a promising compatibility with the conventionally used YSZ TBC. Especially Ti_2AlC (8.2×10^{-6} K^{-1} between 25 °C and 1300 °C) [44], alongside its excellent oxidation resistance, shows a good match in CTE with YSZ ($10\text{-}11 \times 10^{-6}$ K^{-1}) [34]. In addition, unlike superalloys, Al-containing MAX phases do not require bond-coats, which fulfil the function of oxidation-resistant layer. As such, additional coating procedures can be spared and hence extra costs too. Furthermore, the probability of incorporating stresses due to numerous interfaces is reduced.
The first study of TBC-coated MAX phase substrates is only 5 years old [168]. In the 1100-1300 °C range, the furnace cycling durability of 8YSZ/Ti_2AlC systems was investigated, of which TBC were deposited both by atmospheric plasma spraying (APS) and plasma spray-

physical vapor deposition (PS-PVD) on commercial MAXthal 211 (Figure 1. 17). The coatings were approximately 80-100 µm thick. This work demonstrated the superior durability of PS-PVD YSZ-coated Ti_2AlC – which survived more than 2500 accumulated hours – over similar APS-coated systems (failure at 1300 °C after 500 h). The thickness of the thermally grown Al_2O_3 exceeded 30 µm, which is 5 times more what can be found in the case of bond coats on superalloys. The failure of the APS-coated systems resulted from the development of pores and cracks as well as YSZ phase transformation at 1300 °C. An interfacial reaction between Al_2O_3, TiO_2 and YSZ was also reported, resulting in the formation of an YZrTiAl-O phase.

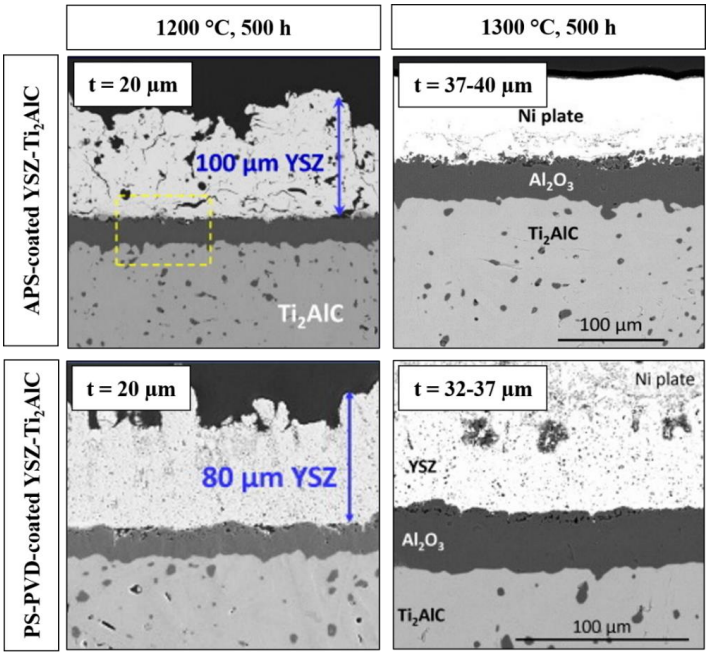

Figure 1. 17: Thermal cycling outcomes for APS and PS-PVD-coated YSZ-Ti_2AlC systems, after 500 h at 1200 °C and 1300 °C, adapted from [168]. The thickness (t) of the thermally grown Al_2O_3 is indicated in each case.

Similarly, furnace thermal cycling of YSZ/Cr_2AlC coated both by APS and PS-PVD was also studied [157]. The outcomes were the same as for Ti_2AlC: the APS-coated samples showed coating failure after 400 h at 1150-1200 °C, while for the PS-PVD-coated Cr_2AlC specimen, the YSZ coating remained intact in the same cycling conditions. However, a phenomenon termed as moisture-induced spallation was noticed, leading to the interfacial decohesion of the Al_2O_3 scale. APS-coated Cr_2AlC systems were reported to survive up to 500 h at 1100 °C and 1200 °C under furnace cyclic condition [169] without any sign of alteration. It proved the high compatibility of YSZ with Al-MAX phases. However, an important finding for YSZ/Cr_2AlC cycled at 1300 °C was the formation of highly porous Cr_7C_3 carbide layers underneath the Al_2O_3 scale, resulting from the depletion of Al. Thus, the time to coating failure was reduced to 268 h. YSZ/Cr_2AlC coatings applied on Inconel 738 substrates tested under burner rig conditions failed after 62 h [170] at an extreme surface temperature of 1400 °C (substrate temperature of 1050 °C) for the same reason. As pointed out in the section *I-5.3 Breakaway oxidation of Ti_2AlC and Ti_3AlC_2*, coatings experience a different mechanism of oxidation. The formation of dense Al_2O_3 scales on bulk MAX phase samples is not entirely transferable to coatings. That is why oxidation of the Cr_2AlC bond coat throughout its entire thickness as a consequence of the open

porosity was observed. Inter-diffusion of substrate elements in the bond coat was also identified as a possible cause of premature system failure.
Interestingly, Gonzalez et al. [169] mentioned for the first time (for MAX phases) the phenomenon of scale rumpling, i.e., the Al_2O_3 scale was highly wavy at 1200 °C and 1300 °C. A more plane oxide layer could be observed for cycling experiments performed at 1100 °C. The thickness of Al_2O_3 varied between ~9 µm (at 1100 °C) and ~40 µm (at 1300 °C), a comparable outcome to Ti_2AlC.
The impressive durability of PS-PVD 7YSZ-coated Ti_2AlC under harsh high-velocity (100 m/s) burner rig conditions was documented recently (Figure 1. 18) [171]. No visible deterioration of the coating could be observed after cycling the system at 1300 °C for an impressive 500 h. These results demonstrated promising compatibility between YSZ TBC and Ti_2AlC substrates, especially as 10 % water vapor was added to the combustion gas, simulating more realistic aggressive gas turbine environments. Surprisingly, while one can think that conditions are harsher and would involve thicker scales to be formed, the thickness was found to be half that of furnace cycled samples under similar conditions (Figure 1. 17).

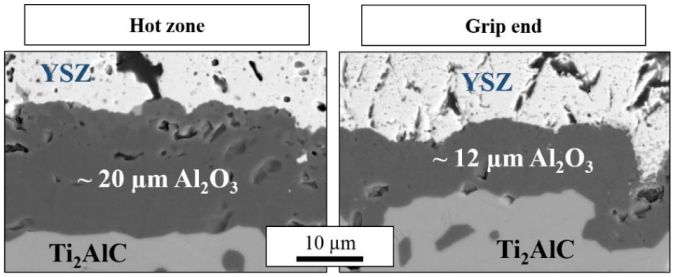

Figure 1. 18: Burner rig thermal cycling outcomes for PS-PVD-coated YSZ-Ti_2AlC systems, after 500 h at 1300 °C, adapted from [171].

This section reviewed the important aspects of the oxidation of Al-based MAX phases with a particular focus on Ti_2AlC, the phase of interest in the present thesis. However, oxidation resistance is one important feature, amongst others. If one considers a potential transfer of Al-MAX phases to aerospace applications, the subjection of structural components to centrifugal creep stresses has to be considered. Therefore, the following section presents fundamental mechanisms responsible for the good mechanical performance of MAX phases. Then, a short review of the basic mechanical properties of Ti_2AlC such as hardness, toughness, compressive strength and creep resistance is exposed.

I-6 Mechanical properties of Ti_2AlC

In addition to its excellent oxidation resistance, Ti_2AlC possess interesting mechanical properties. In fact, MAX phases in general are known to be damage tolerant and display unusual mechanical features due to the hybrid type of bonding (metallic, iono-covalent) and their nanolayered structure. Before mentioning about hardness, toughness and compression strength of Ti_2AlC, it is important to recall fundamental mechanisms taking place at the atomic scale.
Contrary to metals possessing more than 5 slip systems – making them ductile – or structural ceramics (such as binary carbides or nitrides) having none, MAX phases are found to be plastically anisotropic and have 2 independent slip systems.
Above their brittle-to-plastic transition temperature (BPTT), the critical stress intensity factor (K_{IC}) was found to decrease and indicates that no additional slip systems are activated [172]. This endows them not with a ductile but a pseudo-plastic fashion.

In MAX phases, there is a confinement of dislocations in two dimensions, leading to so called plastic anisotropy. These preferentially glide along basal planes in grains of favorable orientation and either form dislocation pileups (DPs) and loops on the same slip plane or so called incipient kink bands (IKBs) on a multitude of parallel planes [18,86] as shown in Figure 1. 19.

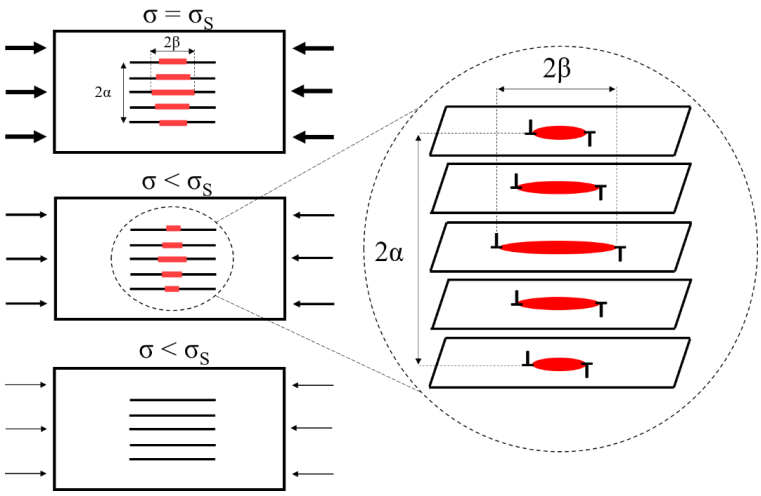

Figure 1. 19: Incipient kink band (IKB) with length 2α and width 2β forming when the stress σ exceeds a threshold σ_S. When the load diminishes or is removed, it shrinks and vanishes. It shows the fully and spontaneously reversible feature of IKBs. Adapted from [18,57].

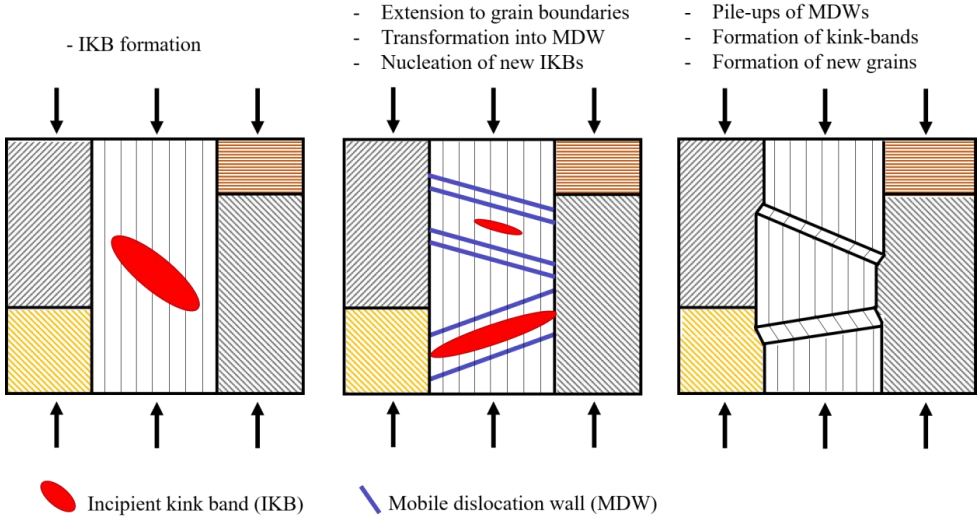

Figure 1. 20: Schematic of nucleation and growth of incipient kink bands in a hard grain and subsequent evolution towards mobile dislocation walls, which accumulate and transform into kink bands. Adapted from [175].

When the applied stress reduces or is removed, they tend to shrink in a fully reversible manner. The notion of kink band formation was first introduced by Orowan in 1942 [173]. In his work, he demonstrated that cadmium single crystals, when axially loaded, can collapse and their glide planes can form specific kink structures, which are then allowed to broaden. Later, Frank and Stroh [174] complemented this explanation and proved that a kink band – " a thin plate of sheared material, transverse to a slip direction" – result from dislocation pairs or loops being generated in many parallel slip planes. IKBs naturally grow as dislocation loops, gradually appear in neighbouring parallel atomic planes and extend to grain boundaries where they are arrested. When stresses exceed a certain value and/or at higher temperatures, they degenerate into mobile dislocation walls (MDWs) [18,175], which are normal to slip planes (basal planes), as depicted in Figure 1. 20. These can in turn lead to the formation of kink bands and kink boundaries, as shown for different classical MAX phase composition in Figure 1. 21 [34].
Both DPs and IKBs allow MAX phases to elastically as well as reversibly deform and store the strain energy in a nonlinear way. That is to say, their stress-strain curves result in a hysteretic loop of which the area represents the total dissipated energy. That is why MAX phases are classified as kinking nonlinear elastic (KNE) solids [57].

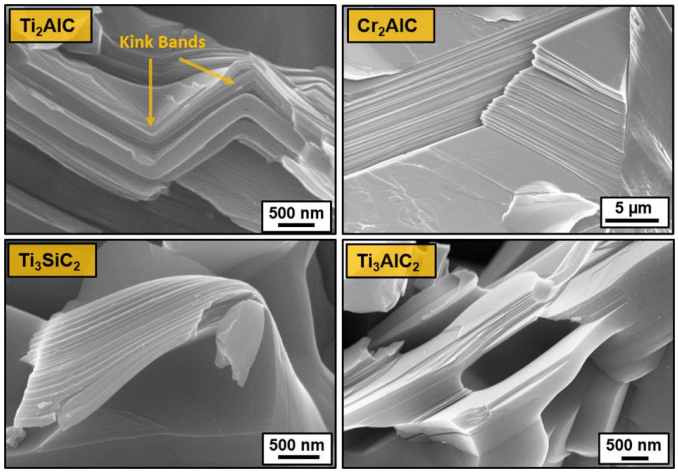

Figure 1. 21: Micrographs of the typical layered structure of four common MAX phases and observed kinking [34].

Due to these mechanisms on a microscale, one of the major hallmark of MAX phases has persisted over the years as being their machinability, which is literally improbable or extremely difficult for other structural ceramics. However, also hardness, fracture toughness, compressive strength and creep resistance depend upon them.

Hardness of Ti_2AlC

Despite being quite stiff (with a Young's modulus of around 300 GPa), Ti_2AlC, just like all MAX phases, is a relatively soft material as its hardness (*Hv*) ranges between 3 and 7 GPa [18,34,44,67,73]. Typically, these values are close to one order of magnitude lower than the equivalent binary carbides or nitrides, with a hardness in the range 20-30 GPa [34]. No cracks are usually observed around the indent, as depicted on Figure 1. 22, demonstrating the formidable ability of the MAX phase ceramics to absorb fracture energy. The variance in hardness values of Ti_2AlC measured over the years arises from different parameters, such as

sample's density [74], grain size [74] and orientation, purity and extrinsic additions [74], applied load [71,77,176,177].

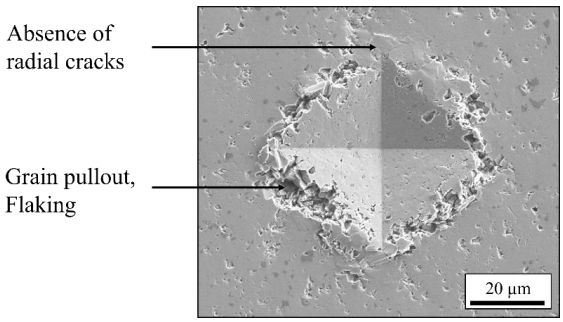

Figure 1. 22: Hardness indentation on Ti_2AlC with an applied load of 9.8 N showing absence of cracks propagating from indentation corners.

The hardness of films and coatings determined by nanoindentation generally did not fall within the range of values for bulk MAX phases, classically determined in micro and macroindentation conditions. As such, Wilhelmsson et al. [83] measured *Hv* = 13-20 GPa for thin epitaxial Ti_3AlC_2 films, the variation depending strongly on the indentation depth.

Fracture toughness and flexural strength of Ti_2AlC

The report of fracture toughness – given by the critical stress intensity factor K_{IC} – of Ti_2AlC is infrequent. However, the average value determined by the single-edge-notched-beam (SENB) test yielded 6.5 $MPa \cdot m^{1/2}$ for a coarse-grained (CG) microstructure [73]. It falls within the classical range for MAX phases, between 5 and 8 $MPa \cdot m^{1/2}$, when non-textured [18,34]. However, the texturing of MAX phases can lead to anisotropic toughening and a significant increase in fracture toughness in the direction parallel to the *c*-axis. In this way, K_{IC} values of up to 17.9 $MPa \cdot m^{1/2}$ could be achieved for Nb_4AlC_3 [178], a factor 2.5 larger than the untextured samples. In fact, the orientation of grains provides cooperation mechanisms that can prevent the formation and development of microcracks. Just like for other structural ceramics, fracture toughness of MAX phases increases with grain size [18]. That is not the case of flexural strength, for which a Hall-Petch relationship applies. For CG Ti_2AlC a flexural strength of 275 MPa was reported [73]. However, it significantly increased for fine-grained (FG) Ti_2AlC, up to 606 ± 20 MPa [177]. The latter value is amongst the largest reported for MAX phases so far by three-point and four-point bending test methods [18,177]. Again, texturing can lead to a significant enhancement of flexural strength, as already mentioned for the fracture toughness of Nb_4AlC_3, and could be increased by a factor 3.5 for the same MAX phase. Texturing of Ti_2AlC was reported once, but the flexural strength of such samples has not been measured yet [144].

Room temperature compressive strength of Ti_2AlC

In parallel, studies about the performance of Ti_2AlC and mechanisms coming into play under compressive loading conditions were conducted at room temperature [56,57,176,177,179–181]. Zhou and Barsoum [57] were the first to classify and encompass Ti_2AlC, Ti_3AlC_2 and their corresponding carbonitride solid solutions in the family of KNE solids, described earlier in this section. This was due to the fact that stress-strain curves of these MAX phases, stressed under cyclic compressive loads, resulted in fully reversible hysteresis

loops. In fact, the nonlinear strain energy could be dissipated through the formation of IKBs and DPs. The extent to which energy dissipation took place could directly be linked to grain size via a direct Hall-Petch relationship. In other words, the larger the grain size, the larger the dissipated energy. Similarly, dense and porous Ti_2AlC present a repeatable hysteretic behavior when subjected to quasi-static and cyclic compression [180]. The main energy-dissipating mechanism was assumed to be the friction during sliding of crack faces, described by the Coulomb's friction law. The ratio E_{eff}/E_0 on Figure 1. 23 is typically used to estimate the crack density.

The highest room temperature compressive strength of Ti_2AlC is above 1000 MPa and for FG samples, which is among the largest values reported for MAX phases [177]. In fact, various authors disclosed a compressive strength of 1057 ± 84 MPa [177] or 1037 ± 21 MPa parallel and 952 ± 6 MPa perpendicular to the pressing direction [176]. With intermediate (20-25 µm) and coarse grain sizes (100-200 µm), the compressive strength of Ti_2AlC literally dropped down to 540 MPa and 393 MPa, respectively [44]. The significant influence of grain size [181] is depicted in Figure 1. 24.

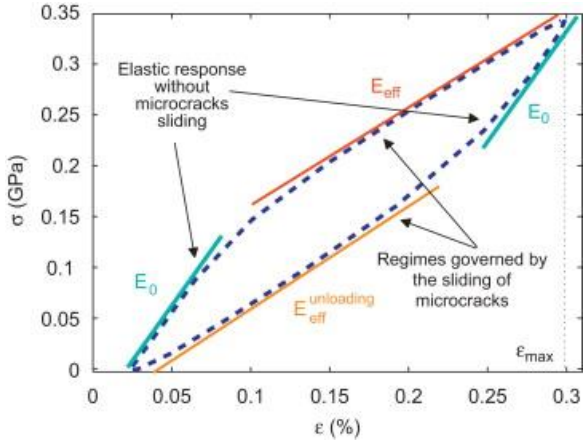

Figure 1. 23: Different regimes found along the hysteretic loops during cyclic compressive testing of Ti_2AlC samples [180].

Additionally, cyclic compressive testing of FG and CG Ti_2AlC highlighted the presence of four distinct regions in the stress-strain curves, each of all governed by specific deformation mechanisms [56,179]. The first region corresponds to a pure linear elastic behavior. The second region is characterized by the hysteretic behavior and the dissipation of energy due to incompatibility stresses and gliding of dislocations concentrated on basal planes of soft grains. The third region coincides with the accumulation of dislocation walls, a larger dissipation of strain energy and the formation of low-angle kink bands, while the fourth region extends until failure and is characterized by microcrack evolution and crack face friction. Grain length was found to directly influence the compressive strength following a Hall-Petch relationship, whereas grain thickness as well as the amount of titanium aluminide impurities up to a volume fraction of 17% had an insignificant role.

Interestingly, a correlation between the stacking sequence of MX layers and non-classical crystallographic slip in Ti-Al-C systems could be established [182]. Micro-compression tests performed on single crystal micropillars demonstrated that the inherent critical resolved shear stress in Ti_2AlC, i.e., the stress required to activate slip in a specific crystallographic direction in a single crystal, was lower than in Ti_3AlC_2, which has a larger atomic stacking given by the *n* index in $Ti_{n+1}AX_n$. This stacking of MX layers was also found to influence kinking, and

therefore, the dissipated energy [57]. Ti_2AlC having less $Ti_{n+1}X_n$ layers interleaved between Al layers, it is therefore softer than Ti_3AlC_2 and shows larger hysteresis loops.

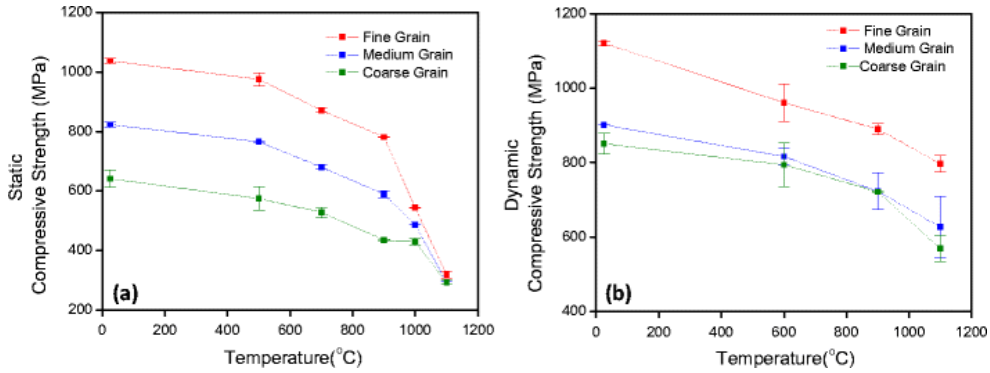

Figure 1. 24: Compressive strength evolution versus temperature for three different microstructures, (a) in static and (b) dynamic loading conditions [181].

High-temperature compressive strength and creep performance

In addition to a good room temperature mechanical performance, high-temperature mechanical properties of MAX phases are of major interest for applications where the temperature exceeds 1000 °C. Polycrystalline Ti_2AlC, like other MAX phases, was found at an early stage to behave differently below and above the BPTT. In fact, under compression and at room temperature, Ti_2AlC mainly deforms through a combination of delamination, kink-bands, dislocation slip, grain rotation, cavitation and intergranular fracture [183]. It was found that coarse-grained samples experienced significant grain refinement due to the accumulation of kink bands, contrary to fine-grained microstructures, for which kinking of small aspect ratio grains was more difficult [184]. To the contrary, above the BPTT the deformation mainly ensues through plastic flow [183]. In that case, the phenomenon of grain refinement was more pronounced for coarse-grained Ti_2AlC, albeit texturing resulting from the compressive deformation was less significant than for fine-grained specimens [184]. This sort of "ductility" that MAX phases present at higher temperatures was the reason why the transition temperature was first denominated as brittle-to-ductile (BDTT). In addition, while samples were observed to shear into two pieces under compression at room temperature, these yielded at high temperature at significantly lower stresses. Furthermore, below the BPTT, the strength in compression increases with decreasing grain size, while this effect becomes inversed above the BPTT (inverse Hall-Petch relationship) and more pronounced the higher the temperature [184]. In the latter case, for coarse-grained samples, this is due to easier kink band formation and basal slip activation at higher temperature. For fine-grained Ti_2AlC – initially presenting high compressive strength below the BPTT due to less kinking – higher test temperatures induce grain boundary sliding, rapidly counteracting and exceeding the Hall-Petch strengthening mechanism and leading to a decrease of the compressive strength.
The effect of strain rate on the thermo-mechanical response of fine-grained (~4.2 µm) Ti_2AlC was investigated by Parrikar et al. [185]. To do so, they measured the compressive strength in both dynamic and quasi-static loading conditions in the 25-1200 °C range. The study demonstrated that under dynamic loads, brittle fracture was observed over the whole range of temperature, contrary to the samples loaded under static conditions. The fracture toughness and compressive strength at room temperature (1600 MPa) in dynamic conditions were almost 35% higher than the values measured under quasi-static loading. At 1200 °C, under dynamic

conditions, the strength in compression was nearly halved (850 MPa). They concluded that low strain rates are required to plastically deform Ti_2AlC by more than 25% and that dynamic conditions shift the BPTT to higher temperatures (1000-1100 °C) as compared to static conditions (800-900 °C).
More importantly, the creep resistance of MAX phases has been reported in a few studies, among which Ti_3SiC_2 was the most investigated phase in both tensile and compressive regime [186–189]. In the Ti-Al-C system, a few studies about bending creep of Ti_3AlC_2 [190], tensile creep of Ti_2AlC [191] and tensile creep of Ti_3AlC_2 exist [192]. In the case of bending creep of Ti_3AlC_2, it was found that cavities typically develop nearby the tensile surface – initiating crack formation – and that its failure was mainly due to subcritical crack growth [190]. For the tensile creep of Ti_2AlC [191], a stress exponent (n=2.5) close to that of coarse-grained (n=2.0) [187] and fine-grained (n=1.5) Ti_3SiC_2 [186] was reported. A lower activation energy and higher strain at failure as for Ti_3SiC_2 was determined. The material was found to deform through dislocation motion (dislocation creep) and possibly grain boundary sliding, as evidenced by extensive formation of kink-bands on the fractured surfaces. Under tensile conditions, a detailed transmission electron microscope (TEM) study was destined to analyze the creep deformation mechanisms of Ti_3AlC_2 at 900 and 1000 °C [192] and showed that dislocations and dislocation arrays were essentially localized in (0001) basal planes. The low concentration of stacking faults and intragranular defects – believed to be a conglomerate of dislocations – were assumed to contribute to a lesser extent to the overall plasticity of Ti_3AlC_2.

Thermal shock behavior

Apart from studying the effect of "slow" dynamic loadings at high temperature, Ti_2AlC has also been subjected to more drastic and rapid stresses. In fact, Bai et al. [193] studied its thermal shock behavior with quenching temperatures in the range of 200-1400 °C. While unquenched bending bars showed a flexural strength of 600 MPa, a rapid decrease of the retained strength upon quenching in cold water was observed around a quenching temperature of 500 °C, where it decreased to ~200 MPa. The retained strength then stabilized in a plateau until a quenching temperature of 1400 °C. Repeated quenching for 5 cycles showed a slightly lower retained strength. However, as compared to brittle ceramics, Ti_2AlC presented a better ability to withstand drastic changes of temperature and accommodated thermomechanical stresses through the formation of mobile basal dislocations.
In summary, Ti_2AlC counts amongst the most interesting ternary compositions, exhibiting good thermomechanical properties in addition to its excellent oxidation resistance. Nevertheless, limitations have been observed in all these aspects and reinforcing Ti_2AlC with another material to form a composite would help enhancing its performance. In this way, the manufacturing of MAX phase ceramic matrix composites constitutes a fascinating track to pursue.

I-7 Ceramic Matrix Composites

I-7.1 Introduction to ceramic matrix composites

The major limitation of monolithic ceramics is their brittleness. In order to achieve a quasi-ductile mechanical behavior even at high temperature, the development of a new class of materials – Ceramic Matrix Composites (CMCs) – was initiated about half a century ago [194]. CMCs are manufactured by embedding inorganic fibers in ceramic matrices. The use of particles or nano-reinforcements (e.g., carbon nanotubes) is also conceivable, though CMCs essentially refer to the fiber-reinforced materials. Polymeric and glass fibers are not included

as their respective degradation and softening temperatures are low. Carbon fibers are the only organic fibers which are used in CMCs [194].
Ceramic fibers can be polycrystalline or amorphous and are divided in two main categories depending on their nature: non-oxide and oxide ceramic fibers. The former primarily encompass covalent Si-based fibers such as silicon carbide (SiC), silicon nitride (Si_3N_4), Si-C-O, Si-C-N-O, Si-B-C-N. These are usually fabricated by a combined spinning process of polycarbosilane or polycarbosilazane precursors and subsequent curing and pyrolysis treatments [194,195]. While non-oxide fibers, such as carbon or silicon carbide, possess outstanding high temperature mechanical properties (high tensile modulus, high tensile strength), these are prone to oxidation and thus, require the use of environmental barrier coatings (EBCs). Even though carbon fibers are extremely cheap, the prices of silicon carbide fibers are fairly high. The second category concerns oxide fibers such as alumina (Al_2O_3), mullite ($3Al_2O_3 \cdot 2SiO_2$), zirconia (ZrO_2), etc. Oxide fibers have lower tensile strength and are less creep resistant than their covalent homologs, but in exchange, are insensitive to oxidation [194]. Their prices are more affordable than silicon carbide fibers.
Unlike polymer or metal matrix composites, CMCs are known to be inverse composites [194], i.e., at low strain (0.1%), the failure strain at yield of the matrix is lower than the failure strain of the fibers. Therefore, microcracks are preferentially generated in the ceramic matrix and propagate towards fibers. Depending on the fiber/matrix interface bonding, two scenarios are conceivable (Figure 1. 25): if the interface is strong, through-fiber crack propagation is expected, and the dissipation of fracture energy is minimal; if the interface is weak, cracks are deflected along fibers and the composite possess a better fracture toughness. In the latter case, the separation between fibers and matrix is known as debonding. When a large surface area of the fiber is detached from the matrix, it becomes load-bearing, it means that most of the applied stress is transferred to the reinforcement component. Thus, it is important to select fibers with high strength, such as high tensile modulus. Once the yield stress is reached, fiber breakage is likely to occur. Fiber gliding is then an additional energy-dissipating phenomenon as interfacial friction is involved.

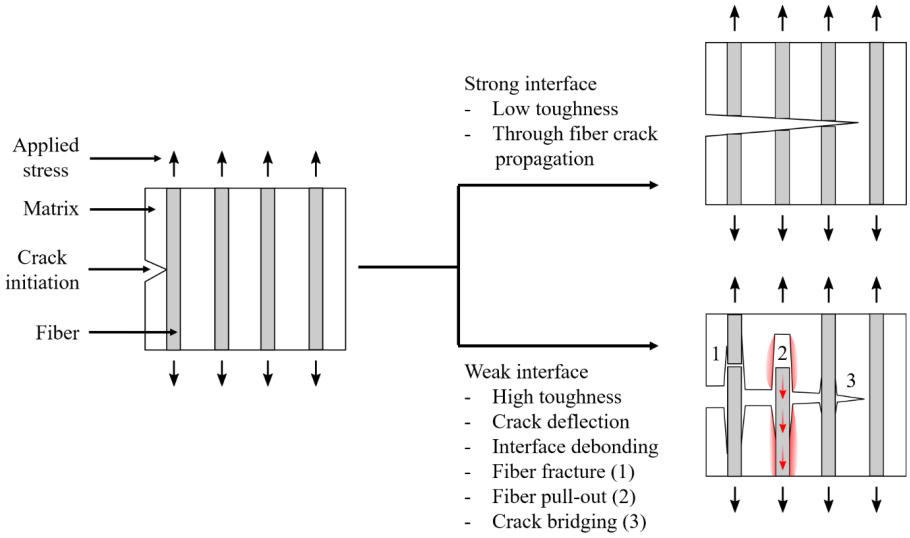

Figure 1. 25: Fracture mechanisms in CMCs, with strong interface (typically without coatings) and weak interface. In the latter case, fiber sliding (2) generates frictional energy dissipation.

Coatings for alumina fibers have been developed and investigated, but they are limited to few specific materials. Usually, β-aluminas, CaF_2 or monazite ($LaPO_4$) have been used [196,197]. Even though debonding was found to occur with these systems, fiber degradation and grain coarsening localized at the interface and occurring during fabrication or annealing procedures were observed issues. Most of the time, a decrease in fiber strength was noticed.
In addition, the tailoring of properties strongly depends upon the processing of fibers, whether these are short or continuous, non-woven or woven. Continuous fibers have higher mechanical properties and can be shaped into 2D or 3D oriented textile structures. These have the highest stiffness and therefore, the highest reinforcement effect.
The major drawback, though, resides in the difficulty of using continuous fibers or textiles in manufacturing methods for complex shapes. These cannot be used in the injection molding process or in other well-established methods for processing of ceramics (slip casting, tape casting, deposition, etc.). That is different for short fibers which can be employed in feedstocks and are thus suitable for the fabrication of components with complex geometries. Even though short fibers have a lower reinforcement effect as continuous ones, that is of less significance for Ti_2AlC-based CMCs considering that MAX phases already exhibit a good mechanical response.

I-7.2 MAX phase composites

Even though the inherent properties of MAX phases are unusual, composites thereof have proven superior characteristics, as much from a mechanical viewpoint as thermomechanical or in terms of oxidation resistance. Studies have demonstrated that careful selection of the second-phase material is of great significance. Fiber-reinforced MAX phase composites are essentially mentioned hereinbelow [189,198,199], but particles have also been used, whether produced *in situ* [200,201] or through extrinsic additions [202].

Particulate reinforcements

Despite the use of MAX phase particles as reinforcement in polymeric and metal matrices, the focus in this section is primarily set on CMCs and the use of MAX phases as matrix. Most studies about particle-reinforced MAX phases deal with in-situ formed CMCs [203–206], rather than with extrinsic additions. In fact, Ti_3SiC_2 reinforced with different particles (TiC [203,204], SiC [204], TiB_2+TiC [206]) were directly produced by reactive hot isostatic pressing, hot pressing (HP) or spark plasma sintering. In all cases, primarily the hardness could be greatly improved, with peak values reaching up to 16 GPa with SiC [204] and 20 GPa with TiC [203]. Additionally, the Ti_3SiC_2/(TiB_2+TiC) composites with the largest volume fraction of TiB_2 demonstrated enhanced oxidation as a result of boron silicate scales and low parabolic rate constants. Similarly, Cr_2AlC/Al_2O_3 composites could be produced by in-situ HP, and only the improvement of hardness was qualitatively assessed. However, these in-situ CMC production routes present some disadvantages, such as e.g., the poor control over particle morphology. Ti_3SiC_2 extrinsically reinforced with cubic boron nitride (cBN) particles was also successfully produced by a high pressure (4.5 GPa) and high temperature procedure [202]. However, the stability of Ti_3SiC_2 could only be maintained due to high pressure, otherwise resulting in a full reaction with cBN.

Fiber reinforcements

Fibers have also been used in combination with MAX phase matrices in several systems. For example, Cr_2AlC composites containing 5 and 10 wt.% SiC fibers were manufactured by FAST/SPS [198]. The dispersion in the MAX phase matrix was excellent on account of the

short size and weak interactions between SiC fibers. These had a length and mean diameter of 70 µm and 7 µm, respectively. On account of the short dwell time (10 min) in the SPS furnace, no reaction layer between fiber and matrix could be observed. As compared to monolithic Cr_2AlC, the addition of 10 wt.% short SiC fibers led to an improvement of the wear resistance by up to 80%, while the friction coefficient experienced a drop of up to 20%.
However, significant build-up of reaction layers between non-oxide covalent fibers and Cr_2AlC have also been reported [199]. Carbon fibers were found to strongly react with the matrix, leading to carbide (Cr_3C_2, Cr_7C_3) and aluminide (Cr_2Al) phases, while interdiffusion was observed and Cr from the matrix found within C-fibers themselves. With SiC fibers, similar outcomes were reported after sintering and reaction layers were composed of Cr_5Si_3C, Al_4C_3 and Cr_3C_2 phases. In both cases, an alteration of fibers and a worsening of shape evenness has been noted. These phenomena were drastically accentuated after burner rig testing, as the harsh oxidizing conditions promoted the formation of the abovementioned species. However, even at high volume fraction, the C and SiC fibers were perfectly dispersed in the Cr_2AlC matrix. Latter outcome was not observed for Al_2O_3 fibers, which were found to form stripes of agglomerates even at low concentration (Figure 1. 26). Nevertheless, the positive aspect of oxide fibers was the absence of reaction with Cr_2AlC, even after oxidation under extreme burner rig conditions.

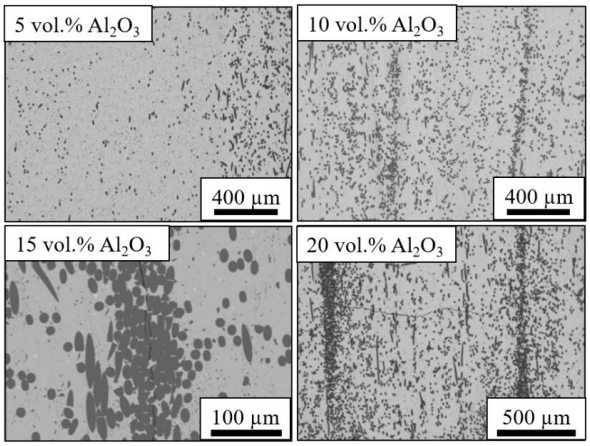

Figure 1. 26: Fiber agglomeration in Cr_2AlC/Al_2O_3 composites produced by FAST/SPS with 1 mm long fibers. Adapted from [199].

Reaction zones at the interface between fibers and matrix have also been reported for Ti_3SiC_2/C_f composites [207], while an optimal compatibility of this MAX phase was found with SiC fibers [208].
Further, high-temperature mechanical properties of SiC whisker [188] and short SiC fiber-reinforced Ti_3SiC_2 [189] composites have been investigated. Compressive creep of Ti_3SiC_2 reinforced with 10 and 20 vol.% SiC whiskers was first determined between 1100 °C and 1300 °C for a range of stress between 20 and 120 MPa. The addition of whiskers greatly decreased the creep rate. A dominant dislocation-based deformation was assumed for monolithic Ti_3SiC_2, while, with increasing whisker content, the mechanism gradually changed to viscoplastic and viscoelastic creep. In terms of dispersion of the reinforcement phase, high whisker volume fraction was found to lead to their agglomeration. To the contrary, short SiC fibers were less prone to this phenomenon, as already reported for Cr_2AlC [198,199]. However, upon deformation, near-fiber cavity formation was a preponderant observation. Unlike whiskers, short SiC fibers did not systematically improve the creep response. The activation energy for

creep increased for coarse-grained Ti_3SiC_2, while it remained unchanged for fine-grained microstructures.
To summarize, SiC fibers are preferentially targeted for Si-based MAX phases such as Ti_3SiC_2. However, due to their reaction with Al-containing MAX phases, their use with the latter is not possible without appropriate coatings. That is why, in the latter case, oxide fibers such as Al_2O_3 are preferred. In addition, the success of coatings has not been proven yet for a prolonged use.

I-7.3 Composites in the Ti-Al-C system

Composites of Ti_2AlC and Ti_3AlC_2 have also been manufactured, though their studies are relatively new and mainly set the focus on reactivity between reinforcement and matrix.
Ti_2AlC could be used as a component for multi-layered coatings of carbon fibers [209]. 400 nm thin coatings composed of an inner TiC and an outer Ti_2AlC layers have allowed for a weakening of the interfacial bonding, but the tensile strength of fibers has been drastically diminished. However, the main interest lies in the use of Ti_2AlC as matrix material, combined with high-performance fibers, for an operation in high-temperature oxidizing environments.
Just like Cr_2AlC [199], Ti_2AlC reacts with SiC up to temperatures of 1550 °C [208]. Reaction layers are known to form at the Ti_2AlC/SiC interface and are mainly composed of $Ti_3(Al_{1-x}Si_x)C_2$, TiC and $Al_{1+x}Ti_{1-x}$ (with x ranging from 0 to 1). Such interphases have also been observed for $Ti_3AlC_2/SiC_{(f)}$ composites – when SiC fibers coated with a carbon-rich non-stoichiometric SiC coating (SCS) were used – processed by hot-pressing [210]. At 1250 °C, the reaction between SCS and Ti_3AlC_2 was mild. The thin reaction layer (~ 1µm) was mainly composed of binary carbides (Al_4C_3, substoichiometric TiC_x), resulting from diffusion of Ti and Al from the matrix into the SCS coating, and Si from the SiC fiber core diffused into the SCS coating. These assemblies exhibited non-catastrophic failure typical of carbon or boron nitride (BN) coated SiC fiber-reinforced SiC composites. However, a drastic alteration of fibers was observed at 1300 °C, with reaction layers of several tens of micrometers (Figure 1. 27).

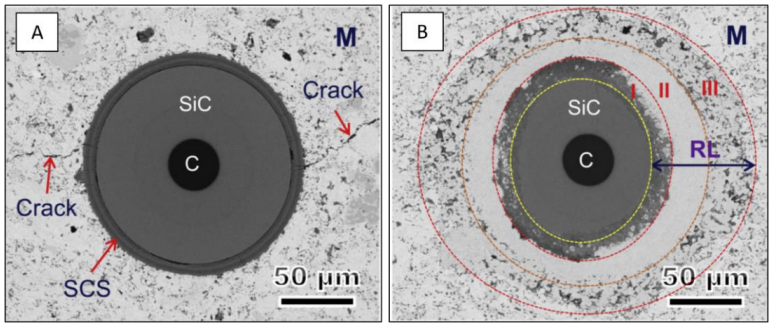

Figure 1. 27: SiC (SCS) fiber-reinforced Ti_3AlC_2 composite: (A) Minimal fiber/matrix reaction at 1250 °C and (B) substantial multi-layered region around fibers resulting from interdiffusion of elements and loss of fiber integrity [210].

The SCS coating was entirely consumed and three different distinct regions of Al_4C_3, TiC and a third layer of complex composition were observed. Diffusional transport of Si into the Ti_3AlC_2 matrix was reported, resulting in a $Ti_3(Al,Si)C_2$ solid solution. These composites demonstrated a brittle fracture behavior, on account of significant loss of fiber integrity. With an additional Ti coating on the SCS-based fibers, the Ti_3AlC_2/Ti-coated $SiC_{(f)}$ samples demonstrated enhanced flexural strength as compared to non-coated SiC fiber composites, as fibers were kept unharmed due to the presence of the Ti barrier [211]. Interface reaction layers between Ti_2AlC and SiC have also been reported in injection-molded composites [101] after pressureless

sintering at 1350 °C. As mentioned earlier, combining SiC fibers with Ti_2AlC is therefore not suitable for high-temperature applications.
To the contrary, as expected for Al-containing MAX phases, studies showed that Ti_2AlC did not react with Al_2O_3 fibers [63], making oxide reinforcements a material of choice for Ti_2AlC-based composites.
Nevertheless, the presence of Al_2O_3 fibers delayed the densification of the samples upon hot-pressing, respectively, hot-isostatic-pressing. Strong fiber agglomeration and fiber sintering at high temperature could be observed (Figure 1. 28).

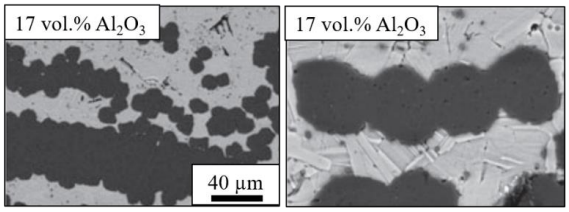

Figure 1. 28: Fiber agglomeration in Ti_2AlC/Al_2O_3 composites manufactured via hot pressing with ~5 cm long fibers. Adapted from [63]. For the right micrograph, the scale bar is missing in the reference, but the fiber diameter was reported to be 10 µm.

Such composites, as compared to the monolithic Ti_2AlC ceramic, exhibited an improvement of the compressive fracture strength by 39.7 and 32.6%, when 20 vol.% of Nextel™ 720 aluminosilicate and 20 vol.% Nextel™ 610 alumina fibers were respectively added [212].
Ti_2AlC has recently been combined with two dimensional alumina braids [213] and manufactured as stacked laminates. As compared to monolithic fine-grained Ti_2AlC, the characteristic strength and the Weibull modulus of the composites were lower, suggesting a different failure mechanism. This recent study paved the way to the processing of Ti_2AlC composites with highly ordered ceramic textiles, presenting interesting anisotropic properties (such as tailorable direction-dependent electrical properties).
With the overview about synthesis, processing and oxidation resistance of Ti_2AlC, as well as the targeted ceramic fiber-reinforcement, the reader can therefore comprehend the purpose of the present thesis. The key aspects in the fabrication of Ti_2AlC/Al_2O_3(f) composites with complex geometries will be the control of purity of the matrix material and the assessment of optimal injection molding and sintering parameters. Some mechanical properties and the oxidation resistance of composites will be assessed to have a first glimpse of the performance of these novel composites.

Chapter II: Experimental procedures

II-1 Preparation of raw materials

II-1.1 Synthesis of Ti_2AlC powders

The Ti_2AlC MAX phase powders were synthesized employing the Molten Salt Shielded Synthesis (MS^3) method developed at the Institute of Energy and Climate Research (IEK-1) by Dash et al. [80] (**Error! Reference source not found.**).

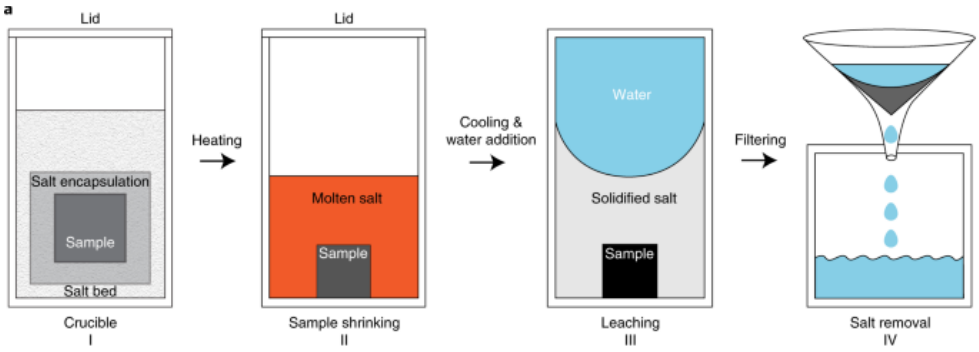

Figure 2. 1: Molten Salt Shielded Synthesis (MS^3) process [80].

The sequence of steps was as follows: First, elemental powders of titanium (Ti, -325 mesh, 99.5%, Alfa Aesar), aluminum (Al, -325 mesh, 99.5%, Alfa Aesar) and graphite (APS 7-11 µm, 99%, Alfa Aesar) were mixed in a different Ti:Al:C ratio, as shown in Table 2. 1. Batches TAC-1 to TAC-6 contained stoichiometric proportions of elemental reactants, while TAC-7 to TAC-9 were carbon-deficient. Slight Al excesses were used for TAC-10 and TAC-11. Potassium bromide salt (KBr, 99%, Alfa Aesar) was mixed with the starting precursors in a 1:1 weight ratio.

Second, the raw materials were mixed in ethanol using zirconia balls (Ø 5 mm) and a 3D shaker mixer (Turbula, Willy A. Bachofen AG, Switzerland) for 24 h. Afterwards, the mixture was dried in a rotary evaporator (Rotavapor R-215, BÜCHI Labortechnik AG, Switzerland) at 70 °C, followed by sieving through a 300 µm sieve. The dried mixture was then compacted into 20 mm-diameter pellets at 200 MPa with a uniaxial hand press (PW 10, P/O/Weber GmbH, Germany).

Afterwards, the pellets were placed in a cylindrical alumina crucible, which was subsequently filled to the brim with KBr and compacted. The alumina crucibles were heated in a high-temperature furnace (HT 32/17, Nabertherm GmbH, Germany) in air at a rate of 5 °C/min with different holding times at peak temperatures from 950 °C to 1050 °C, as indicated in Table 2. 1. After cooling, the crucible was washed with hot water to remove the recrystallized salt. The relatively soft pellet was crushed in a mortar. Vacuum filtration of the obtained Ti_2AlC powder was carried out with boiling deionized water and ethanol to further reduce the salt content. Regularly, samples from the recovered water were taken, to which a drop of a silver nitrate ($AgNO_3$) solution was added. The formation of a cloudy milk-white precipitate indicated the presence of residual KBr. These washing steps were repeated until no precipitate was visually

evidenced. Finally, the powder was dried at 70 °C in an oven for one day and passed through a 25 µm sieve.
The influence of three temperatures (950 °C, 1000 °C and 1050 °C), four holding times (1 h, 5 h, 10 h and 15 h) and different Ti:Al:C stoichiometries (2:1:1, 2:1.1:1, 2:1.05:1, 2:1:0.8, 2:1:0.9 and 2:1:0.95) on phase composition were investigated (Table 2. 1).

Table 2. 1: Variation of parameters (temperature, holding time, molar ratio) for the synthesis of Ti_2AlC by MS[3].

Sample nomenclature	Temperature (°C)	Holding time (h)	Stoichiometry Ti:Al:C
TAC-1	950	5	2:1:1
TAC-2	1000	5	2:1:1
TAC-3	1050	5	2:1:1
TAC-4	1000	1	2:1:1
TAC-2	1000	5	2:1:1
TAC-5	1000	10	2:1:1
TAC-6	1000	15	2:1:1
TAC-7	1000	5	2:1:0.8
TAC-8	1000	5	2:1:0.9
TAC-9	1000	5	2:1:0.95
TAC-2	1000	5	2:1:1
TAC-10	1000	5	2:1.05:1
TAC-11	1000	5	2:1.1:1

The optimized parameters being selected, a large-scale batch production was undertaken. Batches of up to 1 kg were produced at once. The mixing of elemental reactants in appropriate quantities was similar to the previous optimization study described above. The final step required the powder/ethanol mixture to be dried in large laboratory glass bowls placed in an oven for two days, after which pellets of 100 mm in diameter were compacted in an uniaxial electrohydraulic 2-column press (PW 100 E-PRESSYS, P/O/Weber GmbH, Germany) with maximal compressive force of 1000 kN. The pellets were then inserted in large cylindrical alumina crucibles until half their height, the residual volume being completed with KBr and compacted. The heating (resp. cooling) rates were reduced to 1 °C/min to avoid thermal shock and enable temperature homogenization in the larger volume. The Ti_2AlC powder recovered at the end of the procedure was used for all the subsequent processing routes described below.

II-1.2 Alumina fibers

Two types of commercial alumina fibers from the company 3M (3M Advanced Materials Division, 3M Center, USA) were used: Nextel™ 610 and Nextel™ 720. Details of their composition and various properties are listed in Table 2. 2, retrieved from the *3M™ Nextel™ Ceramic Fibers and Textiles: Technical Reference Guide*. These fibers possess an organic coating termed “sizing” to protect them from degradation and breakage during transport. As such, solvent desizing was performed in different media (water, ethanol and acetone) by magnetic stirring of fibers in the corresponding solvents and compared to oxidative

desizing. Latter was carried out at a rate of 5 °C/min to 700 °C for 30 min in air in a high-temperature furnace (HT 32/17, Nabertherm GmbH, Germany).

Table 2. 2: Properties of alumina and aluminosilicate fibers.

Properties/features	Nextel™ 610	Nextel™ 720
Chemical composition (wt.%)	>99 Al_2O_3	85 Al_2O_3, 15 SiO_2
Crystal phase	α-Al_2O_3	α-Al_2O_3 + mullite
Crystal size (nm)	<500	<500
Melting point (°C)	2000	1800
Continuous use temperature (°C)	1000	1150
Filament diameter (μm)	11-13	12-14
Density ($g.cm^{-3}$)	3.9	3.4
Filament tensile modulus (GPa)	370	250
Thermal expansion (100-1100 °C) ($10^{-6}\cdot K^{-1}$)	8.0	6.0

II-2 Manufacturing of complex shapes

II-2.1 Feedstock preparation

The Ti_2AlC powder synthesized by MS^3 was used for the production of feedstocks for powder injection molding (PIM). It was mixed with a binder system optimized in a previous study [214], to produce feedstocks with 50 vol.% solid content.
The binder was composed of 60 vol.% paraffin wax (Paraffin 65, Sigma-Aldrich CHEMIE GmbH, Germany), 35 vol.% of a polyethylene copolymer (Hostalen GA 7260 G, Lyondellbasell, Netherlands), and 5 vol% stearic acid (Merck KGaA, Germany). Paraffin was used as filler to ensure optimal flowing of the feedstock during the injection molding procedure, Hostalen served as backbone for injected parts and helped maintaining their mechanical stability until the onset of sintering, while stearic acid was employed to decrease the feedstock's viscosity and allow a bridging between binder and powder [111]. The components were mixed at 170 °C for 2 h in a laboratory kneader (HKD-T 06 D, IKA-Werke GmbH & Co. KG, Staufen, Germany) equipped with duplex blades (Figure 2. 2, A and B). Afterwards, the feedstock was cooled down to room temperature and granulated (Figure 2. 2, C and D) in a cutting mill (B 06.08, Wanner Technik GmbH, Germany). Feedstocks containing short desized Al_2O_3 fibers were also produced. The fiber sizing was removed by a short oxidative treatment mentioned earlier. The same mixing procedure as described above was followed, with the addition of either 1 mm hand-chopped alumina fibers (Nextel™ 610, 3M, USA) or 3.2 mm chopped alumina-mullite fibers (Nextel™ 720, 3M, USA). These two types of fibers are referred to as N610 and N720 in this work.

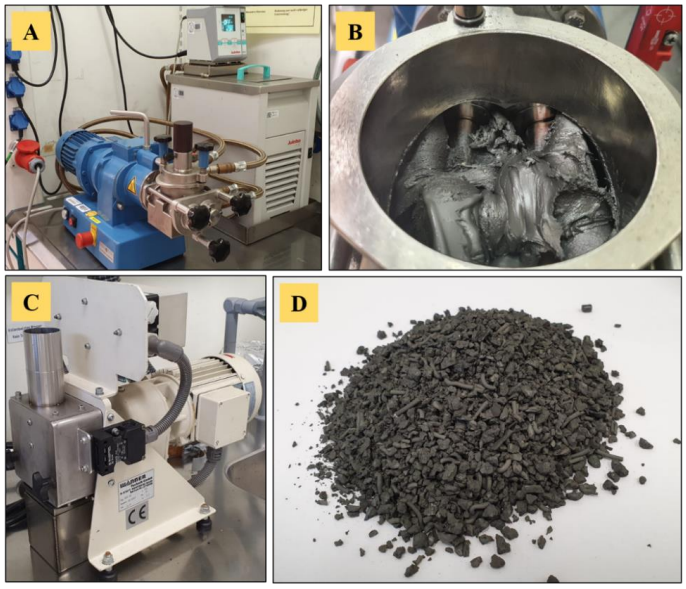

Figure 2. 2: Feedstock preparation procedure: (A) duplex kneader in foreground, external temperature regulating unit and silicone oil bath in background, (B) feedstock's optimal toothpaste-like consistency after kneading, (C) shredder, (D) granulated feedstock ready for injection molding.

II-2.2 Powder Injection Molding

In this work, different components were molded in an injection molding machine (BOY XS, Dr. BOY GmbH, Neustadt, Germany) depicted on Figure 2. 3. All components were injection molded at a pressure of 800 bar with a mold temperature of 90 °C and a screw temperature profile varying between 175 °C nearby the feed hopper and 185 °C at the nozzle. The mold was maintained at constant temperature via an external temperature regulating system (STW 1-1,5-15-M1, Single Temperiertechnik GmbH, Hochdorf, Germany). The barrel temperature was selected based on a previous work [101], as the viscosity of Ti_2AlC-based feedstocks was found to be the lowest in this temperature range. After the injection step, the components were kept for 25 s in the mold to solidify before being ejected. In addition, a mold manufactured for Rolls Royce by Schunk Sintermetalltechnik GmbH (Thale, Germany) was used for the injection molding of so-called retaining plates.

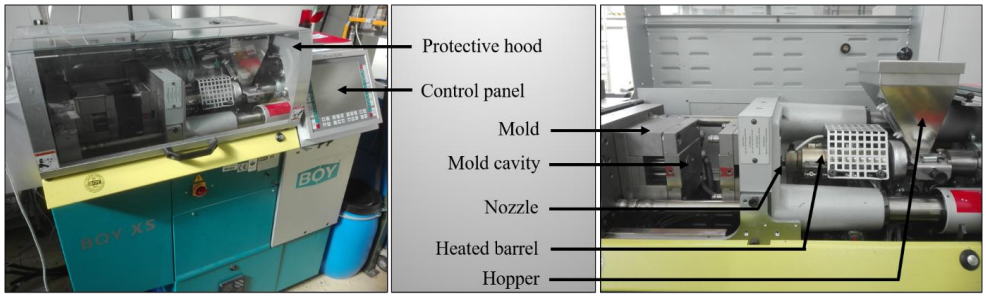

Figure 2. 3: Micro-injection molding machine BOY XS.

These components are employed by Rolls Royce in turbine engines to clamp and secure turbine blades in the corresponding discs (Figure 2. 4), so as to avoid their displacement relative to the rotor base body. The schematic of their location in turbine engines is not disclosed here, as it is a company secret. These components were molded in a semi-industrial injection molding machine depicted on Figure 2. 5 (Allrounder 370 U, ARBURG GmbH & Co. KG, Loßburg, Germany) at a pressure of 600 bar with a barrel temperature of 190 °C.

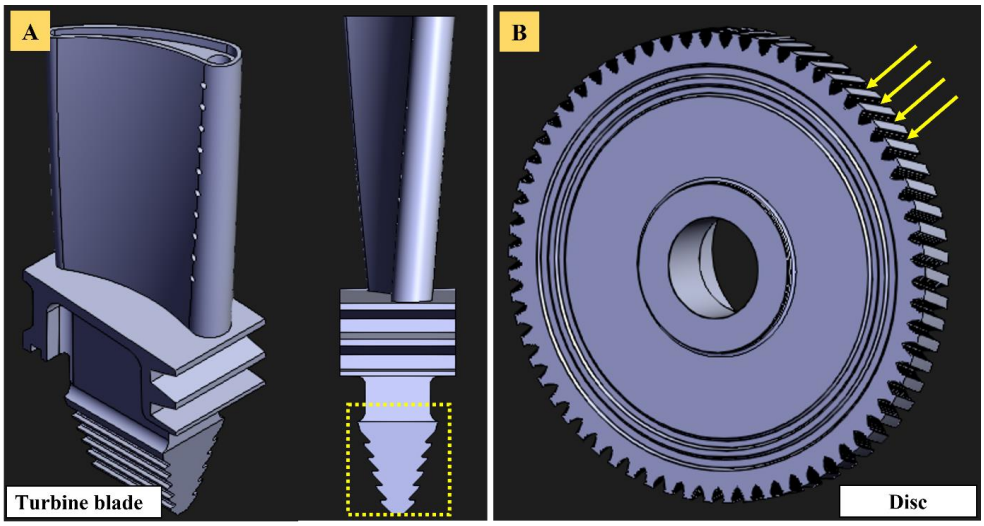

Figure 2. 4: Models of a turbine blade (A) and a turbine disc (B), retrieved and adapted from https://grabcad.com/. The yellow dashed square in (A) indicates the area which fits into the disc grooves pointed at by arrows in (B).

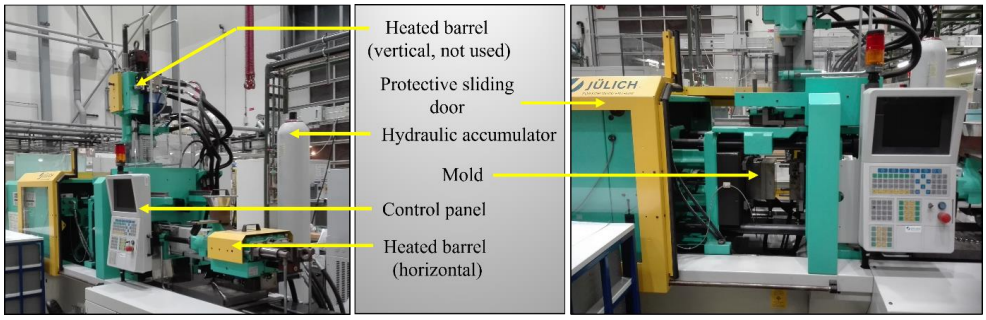

Figure 2. 5: Semi-industrial injection molding machine Allrounder 370U.

Due to the extremely narrow diameter of the mold connections, the external temperature control unit (Presto® A40, JULABO GmbH, Seelbach, Germany) could not be used, as not fulfilling the pressure requirement to convey the heat transfer fluid into the mold channels. Instead, as a rudimentary alternative, a heating plate (RCT basic, IKA®-Werke GmbH & Co. KG, Staufen, Germany) was set at a temperature of 250 °C and held against one side of the mold for 2 min, after which the injection molding cycle was started immediately. The parts were injected with a metering volume of 12 cm^3 and a flow of 30 cm^3/s. The decompression was adjusted to 2 cm^3 and the cooling time in the mold was 10 s before ejection.

II-2.3 Chemical and thermal debinding

Partial binder removal (essentially paraffin wax and stearic acid were reported to dissolve [214]) ensued through solvent extraction in n-hexane at 60 °C for 48 h. The injection molded parts were placed on metallic grids, stacked in up to four levels, and immersed in a glass container filled with n-hexane. The solvent was heated to 60 °C on a hot plate (RCT basic, IKA®-Werke GmbH & Co. KG, Staufen, Germany) and the temperature regulated via a plugged thermometer. Magnetic stirring was performed at 500-600 rounds per minute (RPM) to homogenize and promote solvent extraction through convective flow. A glass lid was firmly clamped to the container with a sealing O-ring. A cooling tower was additionally connected to the lid and the whole set-up was installed in a fume hood. These measures were undertaken to avoid leaking of potentially hazardous n-hexane vapor and for its recondensation.

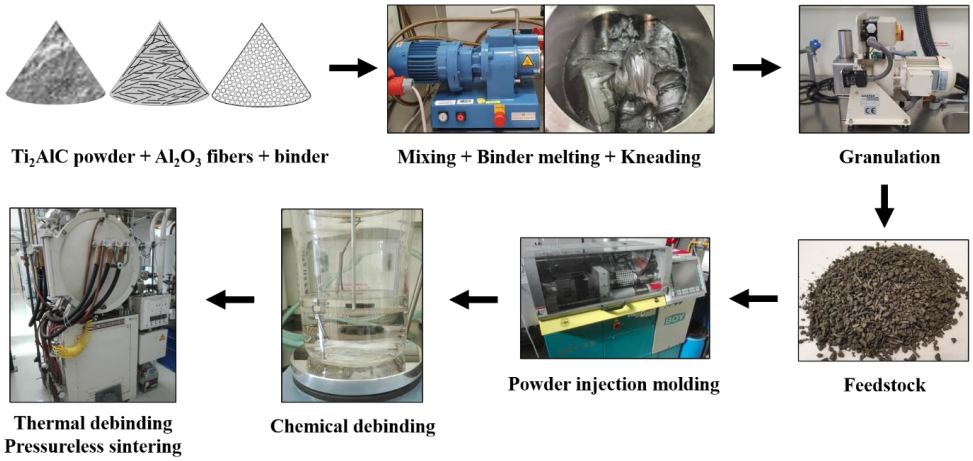

Figure 2. 6: Overview flowchart of the procedure employed to produce complex shapes.

Afterwards, thermogravimetric analysis (TGA) was performed in a high-temperature furnace (STA 449 F1 Jupiter, Netzsch, Germany) used for differential thermal analysis (DTA), coupled to a mass spectrometer (QMS 403 Aeolos) to determine the temperature required for thermal debinding. Granulated feedstock material was heated in flowing argon up to 600 °C at a rate of 5 °C/min, using flows of 50 mL/min and 20 mL/min to flush the furnace and protect the scale, respectively. Binder burnout was carried out at 2 °C/min up to 500 °C for 2 h in argon in a high-temperature furnace (type 121212 WM, Thermal Technology GmbH, Germany). The parts were placed on zirconia milling balls in alumina crucibles, to avoid the direct contact between crucible and components and potential bonding issues. The crucibles were covered in a casing made of molybdenum plates. The heating rate was maintained as low as possible to avoid rapid build-up of gaseous species within the injection-molded parts. In the same furnace cycle, a sintering step was performed, which is described in the section below.
Figure 2. 6 is a summarizing overview of the procedure followed to produce Ti_2AlC-based complex shapes.

II-3 Densification procedures

II-3.1 Pressureless sintering of Ti_2AlC

Ti_2AlC pellets with a diameter of 13 mm and a height of 9 mm were prepared by uniaxial pressing at 200 MPa in a steel die (PW 10, P/O/Weber GmbH, Germany). Pressureless sintering was carried out in a vacuum chamber furnace (HTK 25 Mo/16-1G Ar, Gero Hochtemperaturöfen GmbH, Germany), under vacuum and argon atmosphere. The samples were heated up to maximal temperatures of 1300 °C and 1400 °C at a rate of 5 °C/min with an isothermal holding time of 3 h.

II-3.2 FAST/SPS

FAST/SPS was employed to sinter Ti_2AlC pellets. Ti_2AlC powder was pre-compacted at 50 MPa in a graphite die (inner diameter of 20 or 30 mm). Graphite foil was used between powder and graphite die/punches to enable mechanical, electrical and thermal contact during sintering as well as to prevent reactions between the die and Ti_2AlC. The die was additionally lined with a carbon felt for better thermal insulation. The Ti_2AlC powder was densified in a FAST/SPS furnace (FCT-HPD5, FCT Systeme GmbH, Germany) shown in Figure 2. 7 at a heating rate of 100 °C/min up to 1200 °C and 50 MPa uniaxial pressure in vacuum (~4 mbar). The pressure was applied at the beginning of the sintering cycle before heating.

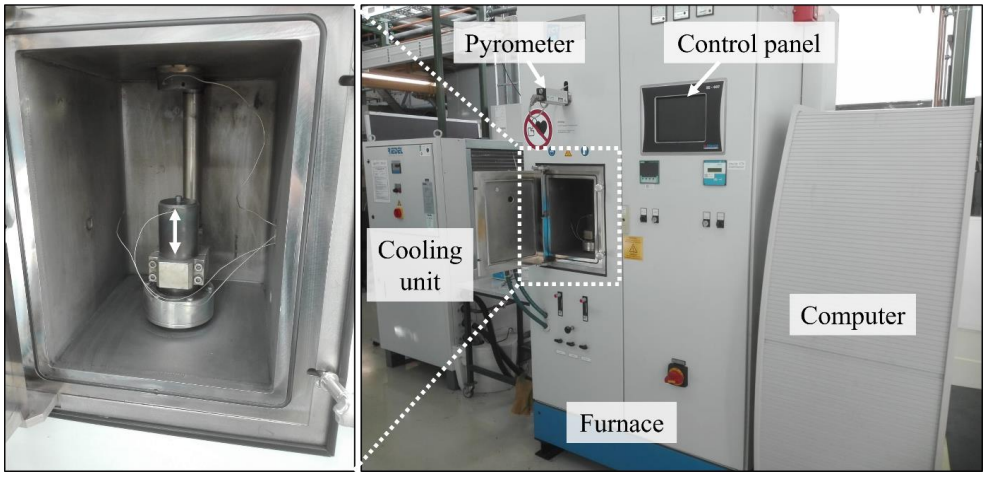

Figure 2. 7: FAST/SPS furnace HPD5 at IEK-1 and magnification on the chamber, where the graphite die is inserted.

The temperature was monitored using an axial pyrometer, which was focused on the surface of the upper drilled punch, close to the specimen. To study the influence of dwell time on microstructure evolution, the samples were hold at the maximal temperature and pressure for 10 min, 30 min and 60 min.
The optimal dwell times of 10 min and 15 min were selected for the manufacturing of Ø 20 mm and Ø 30 mm Ti_2AlC substrates, respectively.
After FAST/SPS, the remainder of graphite foil was first roughly removed with a scalpel before employing the appropriate surface finishing technique, depending on the intended experiment.

II-3.3 Pressureless sintering of complex shapes

After the thermal debinding step described above (see *section II-2.3*), near net shape injection molded monolithic and composite parts were sintered by PS at 5 °C/min up to 1250 °C for 5 h under argon in the same high-temperature furnace (type 121212 WM, Thermal Technology GmbH, Germany). In addition, some parts were further densified in the same furnace by PS in a second cycle at 5 °C/min up to 1400 °C for 3 h, so as to avoid deformation of the thin molybdenum plates used during the first thermal debinding/pre-sintering stage.

II-3.4 Powder bed sintering of complex shapes

Injection molded complex shapes were further densified by following the approach of electroconsolidation [215–217] in a graphite powder bed (Figure 2. 8) in a FAST/SPS furnace (FCT-HPD5, FCT Systeme GmbH, Germany).

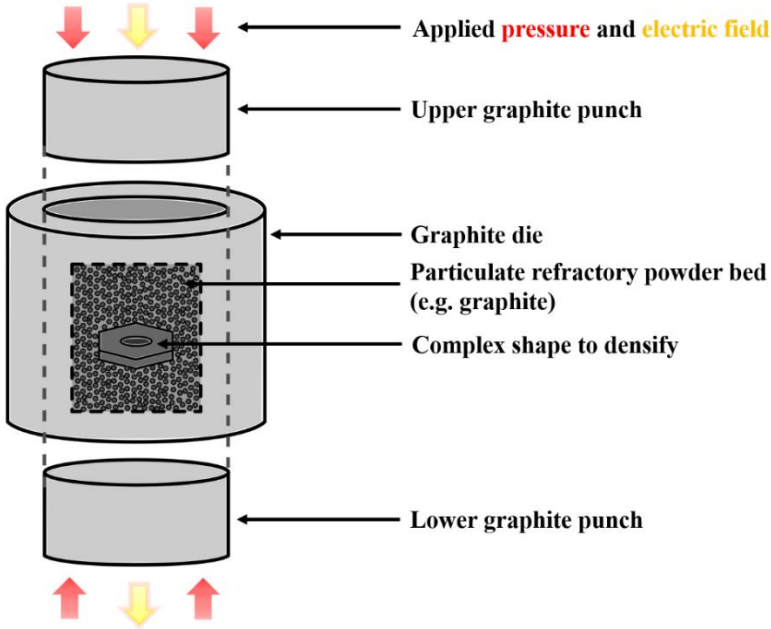

Figure 2. 8: Principle of powder bed sintering of a complex shape.

The parts pre-densified by PS at 1250 °C were placed in a graphite die and immersed in coarse graphite powder (-20+80 mesh, 99.9%, Alfa Aesar). Graphite foil was used between die and powder as well as between powder and Ti_2AlC pre-sintered parts. In this way, it ensured mechanical load transfer and electrical and thermal contact, minimizing reactions and coarse particle imprints at the Ti_2AlC/graphite powder interface. Powder bed sintering (PBS) was carried out at 100 °C/min up to 1200 °C and 50 MPa uniaxial pressure in vacuum (~4 mbar), with a dwell time of 10-15 min depending on the size of the die (Ø 20-30 mm).
Similar attempts for larger components were carried out with larger tools (Ø 45-100 mm) in a FAST/SPS furnace (FCT-HPD25, FCT Systeme GmbH, Germany), employing higher loads (up to 250 kN).

II-4 Oxidation performance

II-4.1 Oxidation of Ti_2AlC

Ti_2AlC substrates produced by FAST/SPS were used for oxidation experiments. In order to investigate the influence of surface roughness on the morphology of grown oxides, a Ø 20 mm pellet sintered by FAST/SPS was cut into three portions using a diamond-studded wire saw (HSD 25, Haas Drahtsägen, Mannheim, Germany). All parts were embedded in a fast cold-curing resin. The first portion was ground with P80 silicon carbide (SiC) abrasive paper, meanwhile the second sample was sandblasted (MHG Strahlanlagen GmbH, Germany) at a pressure of 4 bar with coarse F36 (420-595 µm) Al_2O_3 particles. The third part was ground with P4000 SiC paper, followed by polishing with 3 µm and 1 µm monocrystalline diamond suspensions (Cloeren Technology GmbH, Wegberg, Germany) and eventually polished with 0.05 µm alkaline colloidal silica (Cloeren Technology GmbH, Wegberg, Germany). In the present work, "P-grade" abrasive paper refers to the scale of the Federation of European Producers of Abrasives (FEPA). Removal of the parts ensued mechanically and chemically, by dissolving the residues of resin in acetone. All three parts were oxidized in static air in a high-temperature furnace (HTC 03/15, Nabertherm GmbH, Germany) at a rate of 10 °C/min until 1200 °C, and kept at this temperature for 50 h.
The sample nomenclature is as follows: sandblasted, ground and polished samples are designated as TAC-SB, TAC-P80, TAC-OPS, respectively. OPS stands for oxide polishing suspension.

II-4.2 Breakaway oxidation of Ti_2AlC

Breakaway oxidation was noticed several times at sharp edges. Additionally, some samples exhibited blisters on their surface. In order to investigate the triggering mechanisms, different parallel procedures were undertaken on the samples mentioned above, i.e., with different surface finish. These were oxidized in a high-temperature furnace (HT 32/17, Nabertherm GmbH, Germany) under static air at 1200 °C for different times, ranging from 24 to 1300 h, to understand the mechanism of blister formation. Further, some blisters that were formed during the isothermal oxidation were removed with a scalpel, and the samples re-oxidized at 1200 °C for 5 min in the same furnace. In this specific study, samples cut with a diamond-studded wire saw were oxidized at 1200 °C in air for 15 min in the same furnace.
In parallel, thermogravimetric analysis (TGA) was performed in a high-temperature DTA furnace (STA 449 F1 Jupiter, Netzsch, Germany). A polished Ti_2AlC sample was heated in air up to 1200 °C at a rate of 10 °C/min with an isothermal holding time of 50 h, using air flows of 50 mL/min and 20 mL/min to flush the furnace and protect the scale, respectively. A sandblasted Ti_2AlC sample was oxidized using the same cycle pattern as for the polished sample. After 50 h, a blister formed and was removed with a scalpel. The specimen was then re-oxidized in the DTA furnace under the same conditions for an additional 50 h. These two samples were then kept in a high-temperature furnace (HT 32/17, Nabertherm GmbH, Germany) under static air at 1200 °C for up to 1300 h, and their mass gain monitored in regular intervals of minimum 24 h, after cooling them down to room temperature for 1 h.

II-4.3 YSZ-coated Ti_2AlC

II-4.3.1 Coating procedure

Ti_2AlC substrates with a diameter of 20 mm (for furnace thermal cycling runs) or 30 mm (for burner rig testing, Figure 2. 9, A) produced by FAST/SPS (see *section II-3.2*) were grit blasted at 2-3 bar with F36 (420-595 µm) Al_2O_3 particles and subsequently degreased in acetone for 3 minutes, before coating with thermal barrier coatings (TBCs)
Commercial 7-8 wt.% Yttria Stabilized Zirconia (YSZ) powder (204NS, 92% ZrO_2 + 8% Y_2O_3, Oerlikon Metco, USA) was deposited by Atmospheric Plasma Spraying (APS, Figure 2. 9, B) using a conventional DC plasma torch TriplexPro 210 (Oerlikon Metco, Switzerland). First, the Ti_2AlC substrates were preheated to ~120 °C with two torch passes. Afterwards, YSZ was coated under following conditions: 12 coating passes at a current of 420 A, a standoff distance of 200 mm, and with argon as carrier gas.
The mass and thickness of the samples were measured before and after the coating procedure. Coated samples are depicted further in Figure 2. 13.

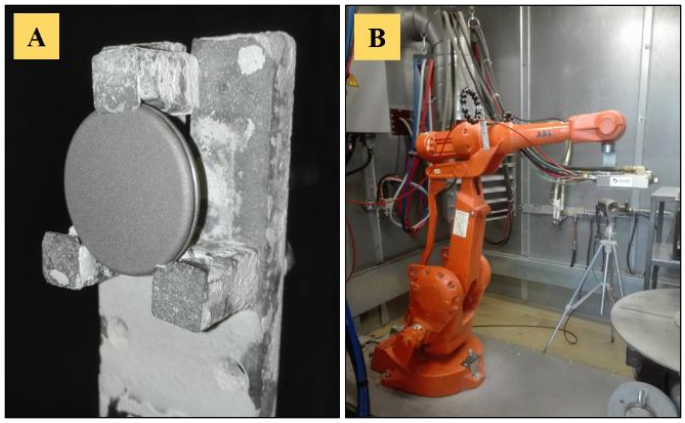

Figure 2. 9: Thermal barrier coating procedure of a (A) Ø 30 mm Ti_2AlC substrate for burner rig testing using (B) the APS plasma torch mounted on a robotic arm.

II-4.3.2 Furnace thermal cycling

The YSZ-coated Ti_2AlC substrates were tested under cyclic oxidation conditions at three different temperatures. The oxidation at 1100 °C was performed in a custom-made automatic high-temperature vertical furnace (based on a standard tube furnace, Carbolite GmbH, Germany) with 1-hour cycles at maximal temperature, followed by 15-minutes cooling sequences in ambient air. A high-temperature chamber furnace (HT 32/17, Nabertherm GmbH, Germany) was used for "manual" oxidation experiments (Figure 2. 10, A) performed in the 1200-1300 °C range in static air under thermal cycling conditions similar to those used by Gonzalez et al. [169]. These were 23 h at maximal temperature followed by a 1 h cooling down to room temperature outside the furnace, repeated five times. Then, a longer cycle of 71 h at maximal temperature followed by a 1 h cooling was performed. These 6 cycles were repeated until the YSZ coating failed. The samples' mass was recorded in regular intervals. An experiment was conducted to measure the cooling rate of the sample from 1200 °C to room temperature as soon as it was taken out of the furnace. To do so, a high temperature pyrometer (KT 150, Heitronics Infrarot Messtechnik GmbH, Germany, Figure 2. 10, B) was used in the

1200-200 °C range, followed by the use of a digital infrared thermometer (BP25, Trotec GmbH & Co. KG, Heinsberg, Germany, Figure 2. 10, C) from ~200 °C to room temperature.

Figure 2. 10: Furnace thermal cycling setup: (A) porous Al_2O_3 plate with sample taken out of the furnace, (B) high-temperature pyrometer, (C) low-temperature laser pyrometer.

II-4.4 Burner rig testing

In parallel, samples were prepared for burner rig testing. Ti_2AlC substrates with a diameter of 30 mm produced by FAST/SPS (see *section II-3.2*) were turned at the Central Institute for Engineering, Electronics and Analytics (ZEA-1) at Forschungszentrum Jülich GmbH. This procedure was extremely challenging and represented a major issue in the present work. First, turning the as-sintered pellets with a lathe has constantly led to fragmented edges (Figure 2. 11, A and D, black and white arrows) and fractured samples (Figure 2. 11, B).

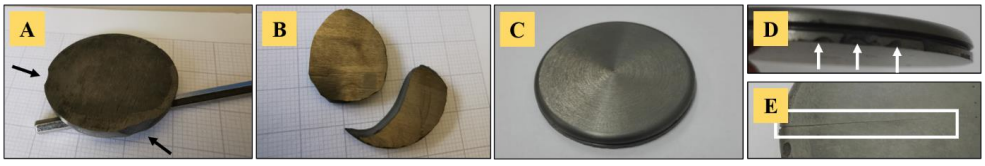

Figure 2. 11: Burner rig Ti_2AlC substrates (Ø 30 mm) turned at ZEA-1 showing manufacturing issues: (A) large, fragmented areas at edges, (B) burst and fractured sample, (C) intact sample, (D) fragmented edge below the groove, (C) crack arising after sink erosion.

The hole required to insert the thermocouple to measure the substrate temperature during burner rig testing was produced by sink erosion. This procedure led to long cracks arising along one half of the samples (Figure 2. 11, E), eventually triggering its rupture. All these samples were unusable and the number of unbroken specimens (Figure 2. 11, C) was extremely limited.
An alternative way was followed to bypass the issue encountered during sink erosion, which consisted in using a coating of known emissivity. Magnetite (Fe_3O_4) is classically used and produced via the Bitter method (Figure 2. 12). The substrates were coated on their back side with Fe_3O_4 in order to monitor the temperature during the experiment by means of a pyrometer. The colloidal Fe_3O_4-suspension was synthesized by coprecipitation in alkaline medium by mixing two solutions (*A* and *B*). Solution *A* was composed of ferrous chloride ($FeCl_2$, 99.5%, Alfa Aesar), ferric chloride ($FeCl_3$, 98%, Alfa Aesar) and deionized water (Figure 2. 12, A), while *B* was a solution of sodium hydroxide. Once poured in solution A (Figure 2. 12, B), the precipitation of Fe_3O_4 particles darkened the suspension. After filtration, rinsing and drying, the product was recovered in form of fine powder (Figure 2. 12, C). Afterwards, Fe_3O_4 particles were mixed with a soap solution, which was in turn applied on the back side of the burner rig

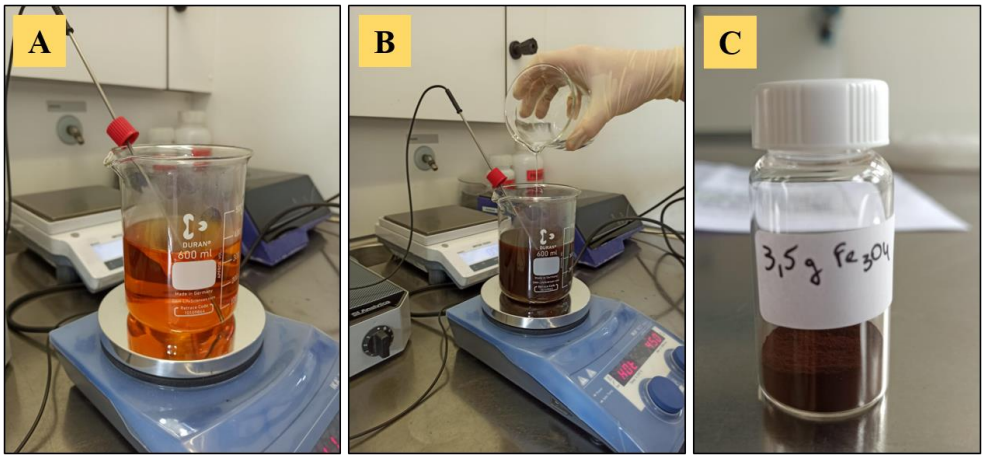

Figure 2. 12: Synthesis of magnetite following the Bitter method: (A) aqueous solution *A* containing ferrous and ferric chloride, (B) addition of aqueous solution *B* of sodium hydroxide and (C) recovery of fine Fe_3O_4 powder after filtration and drying.

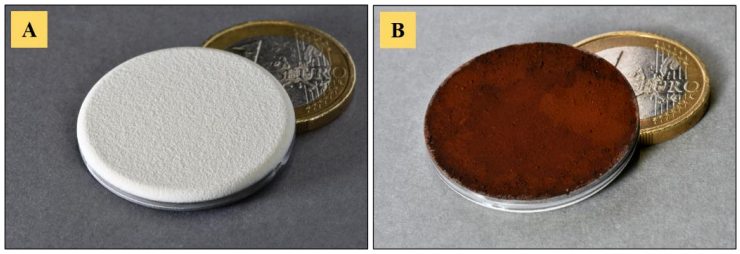

Figure 2. 13: Coated burner rig Ti_2AlC substrates (Ø 30 mm): (A) front side coated with YSZ, (B) back side covered with Fe_3O_4 particles.

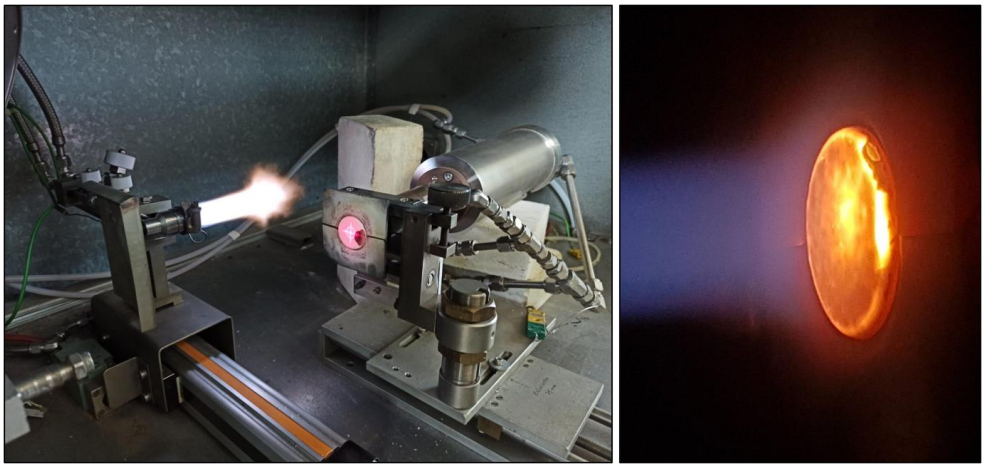

Figure 2. 14: Burner rig apparatus at Forschungszentrum Jülich GmbH, Institute of Energy and Climate Research (IEK-1).

substrate (Figure 2. 13, B). The front side was coated by APS with a YSZ TBC in the same way as for substrates for thermal cycling experiments (Figure 2. 13, A).
These substrates were tested under gradient conditions in a burner rig facility (Figure 2. 14), following a procedure similar to that of Gonzalez et al. [218]. In summary, a mixture of natural gas (CH_4) and oxygen in a 1:2.2 ratio, with a water content of approximately 60%, was combusted in a gas burner. Both front and back side surface temperatures were measured with long-wave pyrometers. The whole setup was controlled by programmable logic controllers and the gas fluxes were adjusted by mass flow controllers. Gases had a velocity of ~8 m/s (~Mach 0.03), calculated from flow rates and nozzle dimensions. The sample was thermally cycled 503 times at a surface temperature of 1400 °C. According to the sample's dimensions (3000 µm thickness), its thermal conductivity (taken as 34 W/mK), the YSZ coating thickness (~400 µm) and the thermal conductivity of the latter (1 W/mK), the interface temperature was calculated to be equal to ~1100 °C.
One thermal cycle consisted of a 5 min heating sequence when the flame plume impacted the sample, which was followed by a 2 min cooling step (cold compressed air on the sample's back side) once the burner moved away from the sample on the lateral rail. The sample was tested for a total of 3500 min (58 hours and 20 minutes). As steady-state conditions were reached after ~90 seconds of heating, the sample remained approximately 1750 minutes (29 hours and 10 minutes) at surface temperatures of 1400 °C ± 50 °C.

II-5 Mechanical properties

II-5.1 Vickers hardness and apparent toughness

Vickers hardness (*HV*) measurements were carried out on PBS parts using a hardness tester (Duramin A-300, Struers, Denmark). Loads of 1, 5, 10, 20 and 30 kilogram-force (kgf) were used. The loads were maintained for 15 sec at 1 kgf, and for 5 sec at 5, 10, 20 and 30 kgf. *HV* was determined both by the software program (ecos, Emco-test, Austria) and by measuring the diagonals d_1 and d_2 of indents on SEM images. In latter case, *HV* was determined via the following formula:

$$HV \approx 0.1891 \frac{F}{d^2} \qquad \text{(Equation 10)}$$

where *F* is the force in N and $d = \frac{d_1+d_2}{2}$. *HV* had the unit of GPa.
Further, the apparent fracture toughness K_{1C} was calculated by measuring the length of radial cracks propagating from corners of the indentations and using the following formula [219]:

$$\frac{K_{1C}\Phi}{H a^{\frac{1}{2}}} \left(\frac{H}{E\Phi}\right)^{\frac{2}{5}} = 0.048 \left(\frac{l}{a}\right)^{-\frac{1}{2}} \qquad \text{(Equation 11)}$$

with Φ a constraint factor (~3), *H* the hardness, *E* (=277 GPa [220]) the Young's modulus of Ti_2AlC, *a* the half-diagonal of the indent and *l* the Palmqvist crack length.

II-5.2 High-temperature compression tests

Ti_2AlC samples (monolithic and N610 fiber-reinforced) for compression tests were manufactured from FAST/SPS pellets. For the monolithic samples, conventional FAST/SPS of Ti_2AlC powder was employed, while for the composite samples, Ti_2AlC/N610/ethanol suspensions with the appropriate volume fractions (5 and 10 vol.%) were poured into a

FAST/SPS graphite die placed on a vacuum filtration setup. Paraffin foil was tightened above the glass funnel and pierced once vacuum had drawn it around the die.

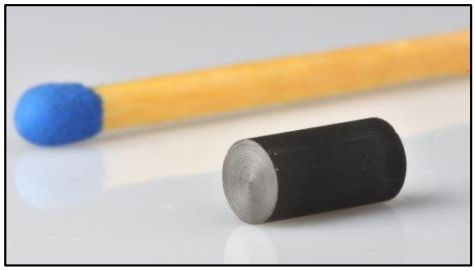

Figure 2. 15: Cylinder machined via EDM for compression tests.

As such, the suspension was forced into the graphite die and sedimentation of both powder particles and fibers occurred simultaneously. This procedure was followed to avoid deposit and agglomeration of fibers above denser Ti_2AlC particles, hence a more homogeneous dispersion was expected. The services of the Central Institute for Engineering, Electronics and Analytics (ZEA-1) were required to electric discharge machine (EDM) cylinders of 4 mm in diameter and 8 mm height (Figure 2. 15). Room temperature and high-temperature (1000-1100 °C) compression tests were performed by the group of Dr. Wakako Araki from Saitama University, Department of Mechanical Engineering in Japan.

II-6 Characterization methods

II-6.1 Particle size distribution

Particle size distribution (PSD) of the as-synthesized Ti_2AlC powders was measured by laser diffraction (Horiba LA950-V2, Retsch GmbH, Germany).

II-6.2 Qualitative/quantitative phase analysis

Phase composition of the synthesized powders and consolidated samples were determined by X-ray diffraction (XRD) using a Bragg-Brentano diffractometer in θ-2θ geometry (D4 Endeavor, Bruker AXS GmbH, Germany). X-ray diffraction is a method used to determine crystallographic features of materials. X-ray beams of wavelength λ incoming on the sample with an incident angle θ are diffracted in specific directions when reaching atomic planes, separated from each other by a distance d. Depending on the scattered waves, destructive or constructive interference occurs. In the latter case, an intensity signal is retrieved, and diffraction patterns (or reflexions) are observed. Bragg's law relates these parameters for coherent scattering as follows:

$$2dsin\theta = n\lambda \qquad \text{(Equation 12)}$$

where n is the diffraction order. In this work, the scans were conducted with a step size of 0.02° 2θ and a step time of 0.75 s in the 2θ = 5°-80° range. Diffractograms were plotted in the 2θ = 7°-80° range. Qualitative phase analysis was performed with the HighScore Plus 3.0.5 software (PANalytical B.V., Netherlands). Rietveld refinement was done with TOPAS V4 (Bruker AXS GmbH, Germany) to quantitatively determine the weight fraction of phases. The degree of preferred orientation (η) of raw powders and sintered samples was calculated after determining

the March-Dollase parameter (r) with the TOPAS software. The following formula was used [221]:

$$\eta = 100\%[\frac{(1-r)^3}{1-r^3}]^{1/2} \quad \text{(Equation 13)}$$

Titanium (Ti), aluminum (Al) and potassium (K) contents were analyzed at the Central Institute for Engineering, Electronics and Analytics (ZEA-3), using inductively coupled plasma optical emission spectrometry (ICP-OES, iCAP 7600, Thermo Fisher Scientific, USA), meanwhile carbon (C) and oxygen (O) contents were measured using carbon/sulfur and nitrogen/oxygen/hydrogen-determinators (CS600 and TCH600, Leco Instrumente GmbH, Germany), respectively.

II-6.3 Microstructural characterization

Parts intended for microstructural analysis were embedded in a low-viscosity slow-curing epoxy (EpoFix, Struers ApS, Denmark). Embedded samples (apart from those destined to fracture analysis and powdered materials) were ground by hand on silicon carbide grinding paper fixed on an automatic grinding & polishing machine (Saphir 550, ATM, Germany). The abrasive grit size was gradually decreased from coarse (P80) to fine (P4000). The polishing procedure was undertaken with automatic polishing machines (MiniMet™ 1000, Buehler, Germany) on perforated cloths soaked with diamond particle suspensions of 3 µm and 1 µm. The final step consisted in using colloidal silica of 0.05 µm.

Morphology of as-synthesized powder particles, microstructure of bulk samples, cross-sections, fracture surfaces and oxide morphology were characterized using scanning electron microscopy (SEM, Zeiss Ultra55, Zeiss Gemini 450, Zeiss Crossbeam 540, Carl Zeiss AG, Germany as well as a tabletop microscope TM3000, Hitachi High-Technologies Corporation, Japan). In addition, elemental composition was characterized by energy-dispersive X-ray spectroscopy (EDS, X-Max 80 mm^2 and Ultim Max 170 mm^2, Oxford Instruments, United Kingdom) coupled to the SEM setups. Crystal orientation and grain size were characterized using electron backscatter diffraction (EBSD-Camera, Nordlys II, EBSD-Software, Aztec, Oxford Instruments, United Kingdom) coupled to SEM (Zeiss Merlin, Carl Zeiss AG, Germany). Crystal structures were retrieved from the Inorganic Crystal Structure Database (ICSD).

Low magnification microstructural characterization was done by optical microscopy (OM, Axio Vert. A1, Carl Zeiss Microscopy GmbH, Germany) coupled with a camera (AxioCam MRc, Carl Zeiss Microscopy GmbH, Germany) and a software (AxioVision SE64 Rel. 4.9.1 SP1, Carl Zeiss Microscopy GmbH, Germany). Using the MosaiX function in the AxioVision software, overview images through tiles overlapping were captured.

Image analysis was performed on SEM and OM images of low to intermediate magnification with the image processing package Fiji of ImageJ (NIH, Bestheda, Maryland, USA) to investigate porosity. The values reported in this work were averaged over up to 20 images to come closer to a realistic estimation of pore concentration. Fiber orientation in injection molded Ti_2AlC composites was determined via the software package OrientationJ (written by Daniel Sage, Biomedical Image Group, EPFL, Switzerland). OM images were binarized before running the analysis. In addition, vector field and fiber orientation distribution (FOD) were determined for particular areas in injection molded components. Further, circularity of single fiber cross-sections was determined to deduce the orientation. SEM images were converted to 8-bit, binarized, and major artefacts such as alumina grains or cavities filtered out. Single fibers were selected, of which shape descriptors (roundness, circularity) were determined using the standard features of ImageJ.

Bulk and absolute densities of green compacts and sintered samples were determined using mass-volume measurements and volume displacement by Archimedes' principle, respectively. Based on these results, on Rietveld refinement and on values of theoretical density (TD), relative density (RD) of multiphase specimen was estimated using the rule of mixture.

Surface roughness of parts intended for oxidation experiments was characterized using a non-contact profilometer (cyberSCAN CT 350T, cyberTECHNOLOGIES GmbH, Germany) equipped with a chromatic sensor head (CHRocodile E1000, Precitec Optronic GmbH, Germany). Surfaces (~4 mm x 4.5 mm) were analyzed with a scan step size of 50 µm in x-direction and increments of 1 µm in y-direction. Arithmetical mean roughness (R_a), root mean squared roughness (R_q), mean roughness depth (R_z) and maximum roughness depth (R_{max}) were determined using the SCAN CT 8.10 surface metrology software.

Chapter III: Synthesis of Ti_2AlC powders

Ti_2AlC powders were produced via Molten Salt Shielded Synthesis (MS^3) [80]. Through the immersion in a bed of potassium bromide salt, this method enables to synthesize non-oxide powders in air without risking the oxidation of elemental reactants or final products at higher temperatures. It has been used previously to produce Ti_3SiC_2 [80,81] and other compositions [80] with high purity but in small quantities. One of the numerous goals of the present thesis is to optimize the synthesis parameters of Ti_2AlC powders, such as temperature, dwell time, stoichiometry, and to adapt them to a scaling up decision. In fact, the production of feedstocks for injection molding demands large quantities of powders. The advantage of the MS^3 process in limiting the oxidation of reactants and products can be seen on Figure 3. 1. Solely the upper pellet presented a thin blue oxide layer. These impurities could be easily removed by gently grinding all sides of the pellet stack. Additionally, Figure 3. 1 clearly provides a visual clue of the high yield of the MS^3 process. Batches of up to 1 kg could be synthesized in a single furnace cycle.

Figure 3. 1: Stack of 10 Ti_2AlC pellets (Ø 100 mm) retrieved after MS^3. Each pellet is ~15 mm thick.

Three synthesis parameters were varied independently, temperature, composition and holding time (Table 2. 1). At first, the maximal temperature was optimized with values between 950 °C and 1050 °C, keeping the stoichiometry and holding time constant. The sample predominantly contained Ti_2AlC for all the temperatures (Figure 3. 2), although the diffractograms revealed the presence of secondary phases such as Ti_3AlC_2, TiC, unreacted Ti and residual graphite. KBr was also detected in low amounts in all samples (most visible at $2\theta = 27°$ and $2\theta = 47.7°$), being entrapped within uncrushed hard agglomerates. The main peak of graphite (002) overlaps with KBr (200). The remainder of Ti reacted at higher temperature ($T \geq 1000$ °C), and its reflection (101) at $2\theta = 40.1°$ disappeared on the corresponding diffractograms. The fraction of Ti_3AlC_2 gradually increased with temperature due to the reactions between Ti_2AlC and TiC. As stated by Wang et al. [222], three non-overlapping peaks ($2\theta = 9.5°$ for Ti_3AlC_2 (002), $2\theta = 13°$ for Ti_2AlC (002) and $2\theta = 35.9°$ for TiC (111)) can be considered in order to have a first estimation of phase composition. Rietveld refinement corroborated the presence of 83 wt. % Ti_2AlC, 13 wt. % Ti_3AlC_2, 3 wt. % TiC and traces of Ti at 950 °C (Table 3. 1).

The expected formation mechanisms of Ti_2AlC resemble reactions proposed in literature for solid-state reaction routes [76,223]. A solid-state reaction between Ti and C is expected before reaching the melting point of Al (Equation 14). Fan et al. [224] reported the formation of a thin sub-stoichiometric TiC shell on Ti particles by solid-state diffusion of C. At ~660 °C, Al reached its melting point (Equation 15), surrounding discrete particles of graphite and Ti. Diffusion of elements in the melt is enhanced and compounds are essentially formed via solid-liquid reaction. Type-I aluminides [225] – TiAl and Ti_3Al – nucleated on Ti particles (Equations 16 and 17).

Table 3. 1: Composition depending on the variation of parameters from Table 2. 1. *Indicates the presence of non-negligible traces. Minute amounts (<1 wt.%) of KBr, Al_2O_3 and free carbon were detected in all samples.

Sample nomenclature	**Detected phases (mass fraction)**
TAC-1	Ti_2AlC (83%), Ti_3AlC_2 (13%), TiC (3%), Ti*
TAC-2	Ti_2AlC (83%), Ti_3AlC_2 (17%)
TAC-3	Ti_2AlC (73%), Ti_3AlC_2 (27%)
TAC-4	Ti_2AlC (41%), TiAl (24%), TiC (23%), Ti_3Al (8%), C (4%)
TAC-5	Ti_2AlC (75%), Ti_3AlC_2 (25%)
TAC-6	Ti_2AlC (75%), Ti_3AlC_2 (25%)
TAC-7	Ti_2AlC (90%), Ti_3Al (3%), TiAl (3%), TiC (2%), Ti (2%)
TAC-8	Ti_2AlC (91%), Ti_3AlC_2 (6%), Ti (2%), TiC*
TAC-9	Ti_2AlC (82%), Ti_3AlC_2 (13%), Ti (3%), TiC (2%)
TAC-10	Ti_2AlC (82%), Ti_3AlC_2 (16%), $TiAl_3$ (2%)
TAC-11	Ti_2AlC (67%), Ti_3AlC_2 (23%), $TiAl_3$ (5%), Ti_2Al_5 (4%), Ti*

Gauthier-Brunet et al.[76] reported the formation of Ti_3Al layers around Ti particles in the case of reactive sintering. In our case at this range of temperature, KBr is still in a solid state.

$Ti_{(s)} + xC_{(s)} \rightarrow TiC_{x(s)}$ (Equation 14)
$Al_{(s)} \rightarrow Al_{(l)}$ (Equation 15)
$Ti_{(s)} + Al_{(l)} \rightarrow TiAl_{(s)}$ (Equation 16)
$3Ti_{(s)} + Al_{(l)} \rightarrow Ti_3Al_{(s)}$ (Equation 17)

At 735 °C, KBr reached its melting point, enveloping the remainder of molten Al, graphite, unreacted Ti, TiC- and Ti_xAl-templated Ti particles. As expected in a molten salt process, atomic diffusion is enhanced by the presence of a liquid media. Quenching performed with a Ti-Si-C system [81] and molten salt diffusion experiments with pure Ti [80] showed that large diffusion spheres were present around elements from the starting materials and that elements diffused deeply into the molten salt. It suggests a high solubility of Ti in molten KBr. The dissolution of graphite in titanium aluminides was reported in the 800-900 °C range for reactive sintering [76]. In a molten salt medium though, it is unlikely that graphite dissolves and the process is believed to be based on a “template growth” scheme as reported by Liu et al. for TiC coatings on graphite flakes [226]. The formation of the intermediate Ti_3AlC phase (Equation

18) can be expected in the present work, but through a different mechanism. However, its presence was not evidenced.

$Ti_3Al_{(s)} + C_{(s)} \rightarrow Ti_3AlC_{(s)}$ (Equation 18)

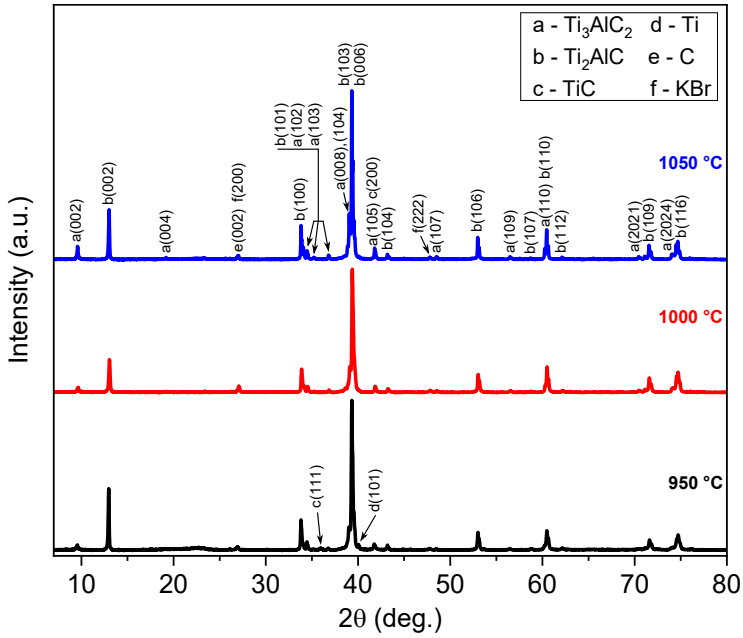

Figure 3. 2: XRD diffractograms obtained for different MS[3] synthesis temperatures at constant molar ratio Ti:Al:C = 2:1:1 and holding time t = 5 h.

This phase was found to be stable up to 1200 °C during reactive sintering [76]. However, in the present work, Ti_3AlC may have reacted in its entirety with C and Ti-Al intermetallic compounds before 950 °C (Equation 19), since no peaks attributed to this phase were observed on the corresponding diffractogram (Figure 3. 2). The reduction of reaction temperatures is enabled by the presence of the KBr melt and the improved solid-liquid diffusion in this medium, hence reaction kinetics are different from solid-state synthesis. In fact, the formation of Ti_2AlC at 900 °C was already reported by Galvin et al. [66] for a molten salt synthesis process in argon.

$Ti_3AlC_{(s)} + C_{(s)} \rightarrow Ti_2AlC_{(s)} + TiC$ (Equation 19)

At 1000 °C, the composition was essentially biphasic (83 wt. % Ti_2AlC, 17 wt. % Ti_3AlC_2). Ti_2AlC further reacted with TiC to form Ti_3AlC_2 according to Equation 20. This reaction occurred at lower temperature than reported [76]. The possibility of a peritectic reaction between TiC_x and liquid Ti-aluminides as reported by Khoptiar et al. [69] for SHS is dismissed. The reaction temperature reached in the present work is far below the melting point of these intermetallics. At 1050 °C, the content of Ti_3AlC_2 increased at the expense of Ti_2AlC. In fact, an increase of 50 °C in the process temperature caused a decrease of 10 % in the Ti_2AlC content.

$Ti_2AlC_{(s)} + TiC_{(s)} \rightarrow Ti_3AlC_{2(s)}$ (Equation 20)

Thus, below 1000 °C, reactions were not completed and residual TiC, Ti and C were detected. At 1000 °C, the composition was essentially biphasic and samples predominantly contained Ti_2AlC and Ti_3AlC_2. Above 1000 °C, phase transformation started to occur, hence a reduction in Ti_2AlC purity was noticed. Therefore, the intermediate temperature of 1000 °C was considered as a good compromise to maintain a high Ti_2AlC phase purity, without having detrimental impurities for oxidation experiments.

Furthermore, the holding time was optimized, fixing the other parameters at 1000 °C for the maximal temperature and 2:1:1 for the molar ratio. Figure 3. 3 displays XRD patterns of samples held for 1 h, 5 h, 10 h and 15 h. For the shortest holding time, intermetallics (TiAl, Ti_3Al) and TiC were present in considerable amounts due to incomplete reactions between raw materials, representing over half the weight fraction of the sample (Table 3. 1). Presence of TiC and aluminides were also reported for short dwell times (2 h), and an increase to 5 h promoted formation of more Ti_2AlC [66]. The absence of Ti_3AlC suggests that formation kinetics of Ti_3AlC and Ti_2AlC are probably much different. Gauthier-Brunet et al. [76] described a slow and fast formation of former (Equation 18) and latter (Equation 19) phases respectively. Additionally, no peak for Ti_3AlC_2 was evidenced for a 1 h dwell time, pointing out slow formation kinetics for this phase too (Equation 20). Increasing the holding time to 5 h promoted the reaction of Ti-aluminides, TiC and remaining graphite to form additional Ti_2AlC and Ti_3AlC_2 phases. The characteristic strong reflections of both phases appeared and overlapped over the 2θ = 38-40° range. Longer holding times generated an increasing percentage of Ti_3AlC_2, visible through a slight dissociation of Ti_3AlC_2 (008) and Ti_2AlC (006) in the above mentioned 2θ range and a decrease in the Ti_2AlC (002) to Ti_3AlC_2 (002) peak intensity ratio.

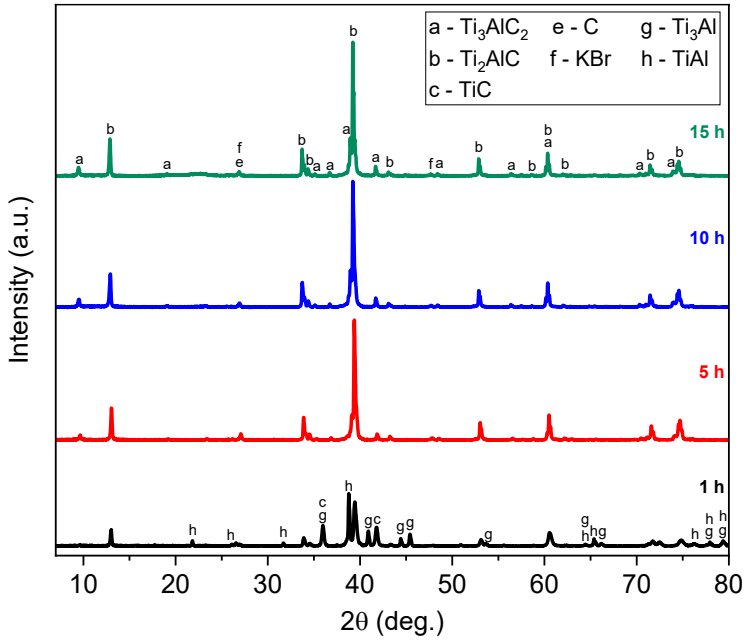

Figure 3. 3: XRD diffractograms obtained for different holding times at constant molar ratio Ti:Al:C = 2:1:1 and temperature T = 1000 °C.

Accordingly, short holding times were not suitable for completion of reactions. After 1 h, the amount of impurities was substantial. After 5 h, the composition was mainly biphasic and samples predominantly contained Ti_2AlC and Ti_3AlC_2. After 10 h, the amount of Ti_2AlC

decreased by 8%, as a result of gradual phase transformation, even though Ti_2AlC and Ti_3AlC_2 were still the only two detected phases. Thereby, an optimal holding time of 5 h was retained. Finally, the third parameter was optimized, where both Al and C contents were varied alternately (Figure 3. 4 and Table 2. 1), keeping the temperature and holding time constant according to former optimization. The stoichiometric sample served as reference. Sub-stoichiometric carbon contents as well as minor excesses of Al were investigated. Al hyper-stoichiometries were reported by various authors [61,71,227] as a way to promote reactions between TiC and intermetallics and to counterbalance losses of high vapor pressure A-element during the synthesis of Al MAX phases. A decrease of 20% in the carbon content as compared to the stoichiometric ratio suppressed the formation of Ti_3AlC_2. Reflections of Ti-aluminides, TiC as well as unreacted Ti were observed. Carbon deficiency limited the overall reaction, though unreacted graphite was still observed after magnifying XRD diffractograms in the specific 2θ range. High content of Ti_2AlC (90 wt. %, Table 3. 1) suggested fast completion of Equation 19. However, remaining Ti showed that Equation 14 was limited by the lack of graphite. Not enough TiC is formed to promote Equation 20. At a molar ratio of 2:1:0.9 the intermetallic phases reacted. In that case, more TiC is formed, which reacts with Ti_2AlC to promote formation of Ti_3AlC_2. The content of TiC was therefore strongly reduced and detected as traces, meanwhile presence of unreacted Ti was still evidenced. The maximum Ti_2AlC and MAX phase (Ti_2AlC + Ti_3AlC_2) yields were achieved (91 wt. % and 97 wt. % respectively). At a molar ratio of 2:1:0.95, contents of Ti_3AlC_2 and TiC increased to the expense of the Ti_2AlC MAX phase (Equation 20).

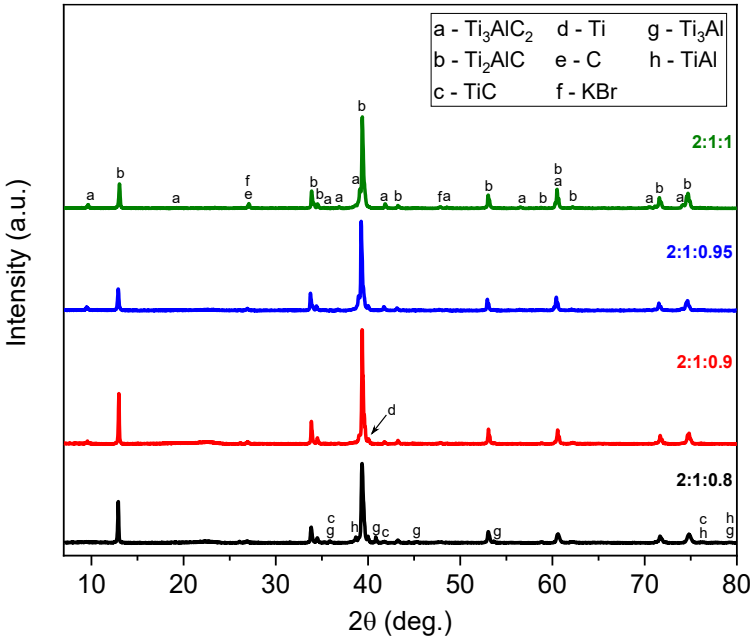

Figure 3. 4: XRD diffractograms obtained for different Ti:Al:C molar ratios of elemental reactants at constant holding time t = 5 h and temperature T = 1000 °C.

An increase in the Al content did not lead to higher Ti_2AlC phase purity (Table 3. 1). The excess of Al is confined in the salt bed during MS[3], hence losses of A-element are not expected, unlike during conventional synthesis routes. Al-rich intermetallic compounds, known as type-II aluminides [225], such as titanium trialuminide ($TiAl_3$) and Ti_2Al_5 were evidenced. Ti-rich

compounds (TiAl and Ti_3Al) were not detected. Their free energies of formation are higher than that of $TiAl_3$ for the considered temperature range [225]. The formation of $TiAl_3$ can be given by Equation 21. Ti_2Al_5 is known to require TiAl as intermediate product [225] and forms through a series of reactions. Its formation can be explained via Equations 16, 22 and 23.

$Ti_{(s)} + 3Al_{(l)} \rightarrow TiAl_{3(s)}$ (Equation 21)
$TiAl_{(s)} + Al_{(l)} \rightarrow TiAl_{2(s)}$ (Equation 22)
$TiAl_{3(s)} + TiAl_{2(s)} \rightarrow Ti_2Al_{5(s)}$ (Equation 23)

In this way, slight hyper-stoichiometries of Al were not required to compensate A-element losses. They were even detrimental, because of Ti-aluminide formation. For the same reason, high deficiencies in carbon content were not favorable to increase Ti_2AlC purity. The highest yield was obtained with a 10% carbon deficient stoichiometry. As a result, the Ti:Al:C = 2:1:0.9 stoichiometry was selected for further processing steps.
Traces of Al_2O_3 were detected by powder XRD and confirmed by SEM observations. The oxygen content in elemental raw powders was found to be non-negligible as shown in Table 3. 2. It was one of the reasons for the presence of alumina after MS^3. Potassium cations were also detected in minute amounts by ICP-OES, which may be due to the residual amount of KBr present in uncrushed agglomerates.
Secondary electron (SE) SEM images (Figure 3. 5) show features of as-synthesized Ti_2AlC. Figure 3. 5A shows one of these large hard agglomerates contained in the as-synthesized Ti_2AlC powder. They had an irregular/angular shape.

Table 3. 2: ICP-OES elemental analysis of raw powders and of the optimized MS^3-Ti_2AlC composition (B_{1-5} are five different batches).

Powders	Element content (wt. %)				
	O	K	Ti	Al	C
Ti	0.855 ± 0.010	-	Balance	-	-
Al	0.420 ± 0.040	-	-	Balance	-
C	0.242 ± 0.003	-	-	-	Balance
TAC-8-B_1	2.399 ± 0.003	0.308 ± 0.005	71.800 ± 0.800	21.800 ± 0.800	7.957 ± 0.012
TAC-8-B_2	1.910 ± 0.090	0.324 ± 0.004	69.700 ± 0.600	22.900 ± 0.300	7.926 ± 0.007
TAC-8-B_3	1.760 ± 0.060	0.509 ± 0.003	69.700 ± 0.500	22.700 ± 0.300	8.010 ± 0.050
TAC-8-B_4	1.820 ± 0.020	0.389 ± 0.004	50.750 ± 0.060	24.300 ± 0.300	7.918 ± 0.003
TAC-8-B_5	1.791 ± 0.005	0.437 ± 0.004	41.800 ± 0.300	24.300 ± 0.400	7.923 ± 0.016

They can be detrimental to further processing steps, such as hindering the densification process or decreasing some properties such as the mechanical response. After passing the synthesized powder through a 500-mesh sieve, the large agglomerates were removed (Figure 3. 5, B) and the following particle size values were obtained: D_{10}=7.5 µm, D_{50}=13.6 µm and D_{90}=22.9 µm. The morphology of single Ti_2AlC particles synthesized by MS^3 was rather globular, not acicular like Ti_3AlC_2 [66,122]. Galvin et al. [66] reported broad peaks in their XRD patterns and pointed out the presence of nanocrystals. In this work, submicron sized primary particles were also observed (Figure 3. 5, C). These primary particles formed larger clusters with smooth surfaces,

unlike Ti_3SiC_2 for which the sharp nanolaminated structure has been distinctly seen [81]. Higher magnifications were required to identify individual layers (Figure 3. 5, D).

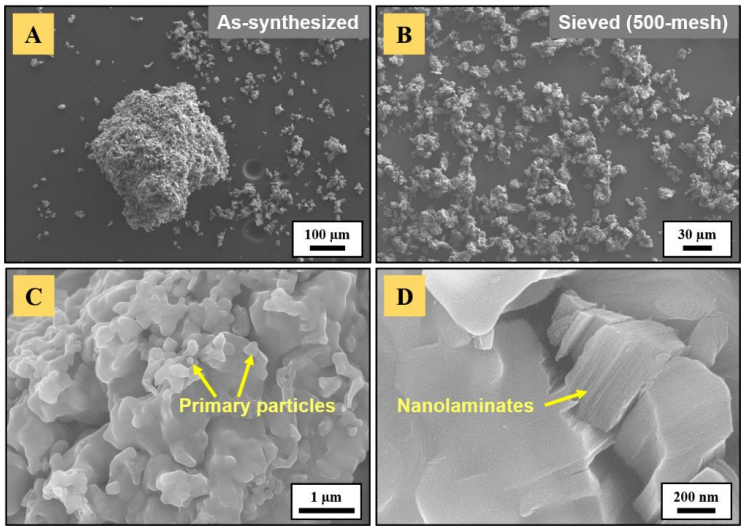

Figure 3. 5: Features of Ti_2AlC powder produced by MS[3]: (A) presence of uncrushed hard agglomerates, (B) removed after sieving, (C) their surface morphology and (D) nanolaminated structure.

The powder showed a bimodal PSD, with D_{10}, D_{50} and D_{90} values of 8.4 µm, 18.8 µm and 54.8 µm respectively (Figure 3. 6). A narrow monomodal PSD was achieved using a 500-mesh sieve, attaining D_{10}, D_{50} and D_{90} values of 7.5 µm, 13.6 µm and 22.9 µm, respectively.

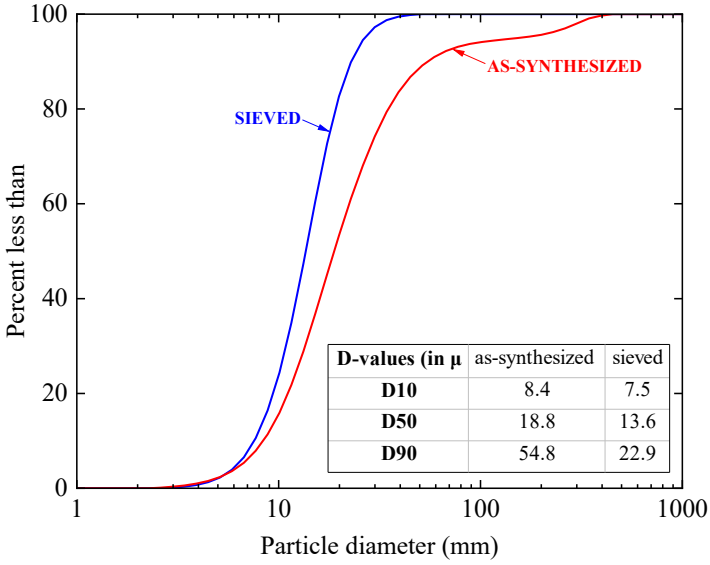

Figure 3. 6: Particle size distribution for as-synthesized and sieved Ti_2AlC.

EBSD analyses of cold-compacted as-synthesized Ti_2AlC powders (Figure 3. 7) gave an insight into primary particle size, particle shape and phases. The phase map (Figure 3. 7, B) corresponding to the yellow dashed area in Figure 3. 7A shows that Ti_2AlC particles are agglomerates of Ti_2AlC nanocrystals with a mean size of ~ 0.9 µm (Table 3. 3). In addition, isolated grains of Al_2O_3 and Ti_3AlC_2 in small proportions were detected. EBSD images demonstrated that Ti_2AlC particles were composed of a multitude of primary particles and highlighted the fine-grained microstructure of Ti_2AlC synthesized by MS^3. It is potentially due to multiple nucleation of product phases on particles of elemental reactants assisted by the molten salt during synthesis. Grain size was submicrometric for both Ti_2AlC and Ti_3AlC_2, and average grain aspect ratio was between 1 and 2, indicating a quasi-equiaxed grain morphology (Table 3. 3). Additionally, no dominant texturing was observed, and inverse pole figures (Figure 3. 7, C) highlighted random crystallographic orientations. This powder was used for subsequent processing steps, including sintering of substrates and ceramic injection molding.

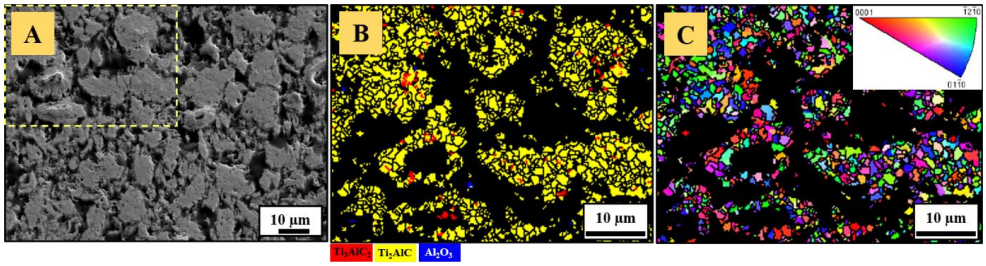

Figure 3. 7: EBSD analysis of compacted as-synthesized Ti_2AlC powder: (A) SE image, (B) phase map corresponding to the dashed area, (C) corresponding Ti_2AlC orientation map (Z_0).

Table 3. 3: Grain size and grain aspect ratio outcomes of EBSD analyses for as-synthesized Ti_2AlC powder.

Average grain size (µm)		**Average grain aspect ratio**	
Ti_2AlC	Ti_3AlC_2	Ti_2AlC	Ti_3AlC_2
0.93 ± 0.42	0.66 ± 0.12	1.75 ± 0.52	1.73 ± 0.63

Chapter IV: Injection molding of complex shapes

Large quantities of Ti_2AlC powders were produced by MS^3 with the optimized parameters leading to the highest purity (≥ 91 wt.%). These could now be used for the production of feedstocks and the subsequent injection molding (IM) of complex shapes.
A cutaway view of the IM process is given in Figure 4. 1. The conditioned feedstock (granulated, dried, properly stored) is poured into the feed hopper, where it enters the barrel containing the reciprocating screw. In order to avoid the build-up of bridges, the shape of the feedstock granules needs to be adapted to the inlet hole and to flow properly through it. The moving platen moves forward and closes the mold cavity. The screw then rotates and progressively moves the granulated material forward in the heated barrel, where it slowly melts. The mass accumulates at the tip of the screw and builds-up pressure while the screw moves backwards. The adjusted volume is dosed in front of the screw. This step is known as plasticizing. The diameter of the screw gradually increases, thus exerting more shear forces on the molten material, which is forced through a narrower space. This participates in homogenization and assists melting through friction. Once the required volume is reached, the mass exits the nozzle, gets in the runner channel(s) and penetrates the mold cavity, rapidly shaping the desired volume. As soon as the part is cooled down and solidified, the moveable platen moves backwards, and pins eject the molded component.

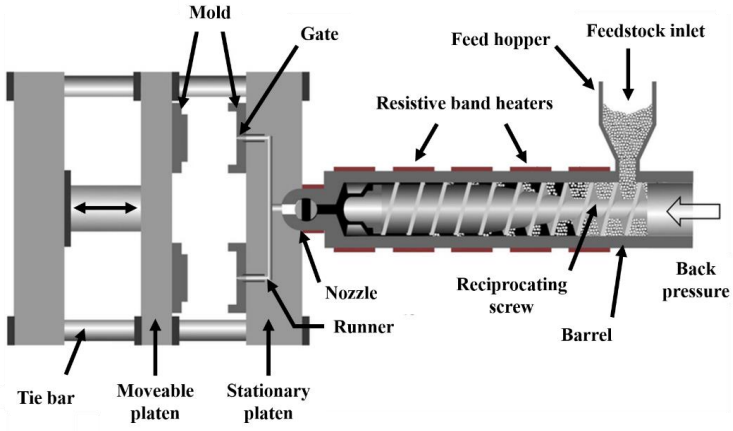

Figure 4. 1: Cutaway view of the injection molding process, adapted from [228].

IV-1 Powder injection molding

The estimation of suitability of MS^3-synthesized Ti_2AlC powders for PIM was done using the distribution slope parameter S_w [111], which gives an indication of the agglomerate size distribution. It was calculated according to Equation 24:

$$S_w = \frac{2.56}{log_{10}\left(\frac{D_{90}}{D_{10}}\right)} \quad \text{(Equation 24)}$$

It yielded a value of ~5.3, which corresponds to a narrow particle size distribution and allows easier injection molding in the case of ceramic powders. However, with decreasing agglomerate size and due to irregular/angular particle shape, the interparticle friction is more significant and

feedstock viscosity increases. Contrary to a previous study [101] for which feedstocks containing 62 vol.% of Ti_2AlC powder were successfully injection molded, preliminary experiments in this work employing solids loading of up to 65 vol.% turned out to be unsuitable for injection molding. In fact, the mixing in the duplex kneader showed that binder and powder were insufficiently homogenized, and this resulted in feedstocks having a "dry" aspect close to that of pure powder. Generally, a toothpaste-like consistency is expected, as a proof of proper covering of individual powder particles/agglomerates with binder and appropriate feedstock viscosity as depicted earlier (Figure 2. 2, B and Figure 4. 2).

Figure 4. 2: Consistency of a monolithic 50 vol.% Ti_2AlC feedstock upon mixing in a duplex kneader at 170 °C.

Accordingly, a binder content of 50 vol.% was necessary to allow a homogenous mixture and proper viscous flow. In addition, short desized Al_2O_3 fibers were used to produce composite feedstocks. According to the *3M™ Nextel™ Ceramic Fibers and Textiles: Technical Reference Guide*, single filament diameter was 11-14 µm for 610 and 720 fiber types. Thereby, their aspect ratio was found to vary from 80 to 270. They are composed of nanosized crystallites and were selected for their highest potential compatibility with Ti_2AlC.
PIM was first carried out in the BOY XS micro-injection molding machine, which was easier to handle and optimal for preliminary tests. The standard mold was a simple cylinder, not a complex shape. The interest lied in the production of more elaborate geometries, as most often required in industrial applications, but considering the limitation brought by the reduced size of the standard mold cavity (diameter of 37 mm, depth of 6 mm). Therefore, 3D models for molds of a 9-tooth sprocket and an hexagonal nut were first created by the IEK-1's workshop by computer-aided design (CAD). The former is depicted on Figure 4. 3.

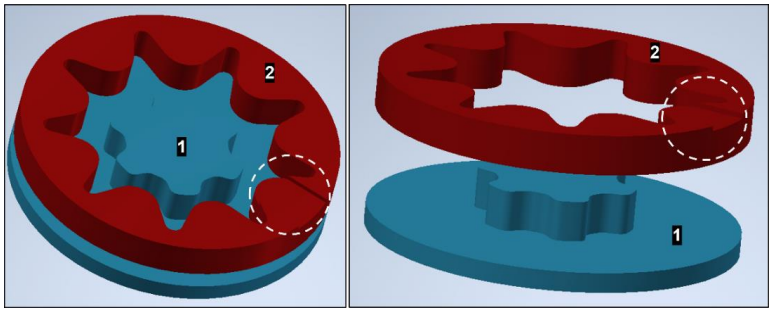

Figure 4. 3: CAD model of the 9-tooth sprocket insert showing the two-part mold. A similar model was created for the hexagon nut.

The white dashed circles indicate a thin rectangular-shaped recess, which was machined in the manufactured steel mold inserts to allow a continuity with the mold gate and injection channel. These connections are visible on Figure 4. 4C and D. The molten feedstock was injected in the in-house produced two-part inserts (Figure 4. 4, C and D) which could be adapted in the cylindrical standard mold cavity (Figure 4. 4, A and B).

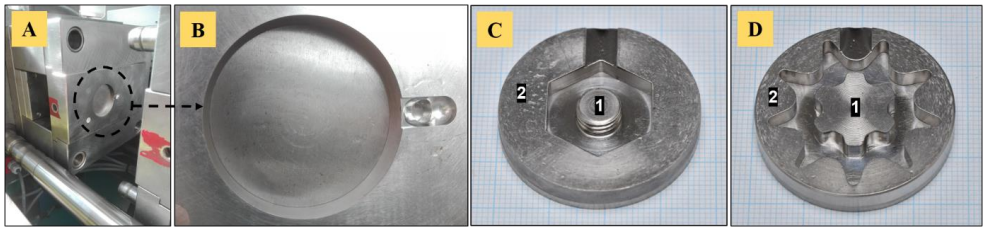

Figure 4. 4: PIM molds for the BOY XS injection molding machine: (A, B) standard mold cavity, (C) two-part inserts for hexagonal nuts and (D) for 9-tooth sprockets.

Figure 4. 5 depicts the corresponding powder injection molded components. At this stage, these are called “green” parts. Standard M8 hexagonal nuts (Figure 4. 5, A) and 9-tooth sprockets (Figure 4. 5, C) with a diameter of 31 mm were produced. The thickness of both components was 4 mm. The two-part (1 and 2 on Figure 4. 4, C and D) mold inserts allowed for high shape variability in component manufacturing. In fact, nuts could be produced with and without a threaded hole and its size was adjustable by changing the bottom element (1). Likewise, sprockets with internal geared geometry or with simple holes were manufactured, depending on the application tool requirements.

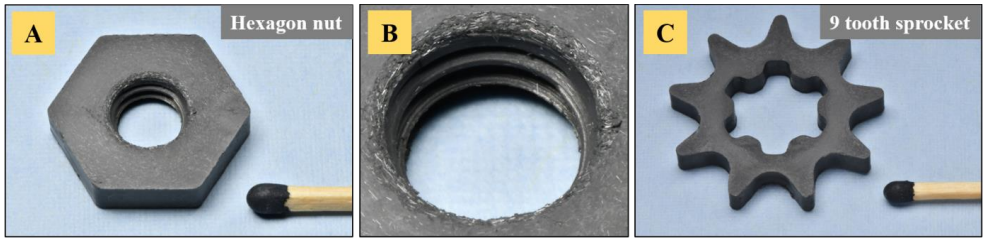

Figure 4. 5: Powder injection molded Ti_2AlC-based components: (A) M8 hexagon nut, (B) magnified threaded hole and (C) 9-tooth sprocket.

Near net shape nuts and sprockets – here fiber-reinforced – were produced with minor defects, for instance of the threaded hole (Figure 4. 5, B), but the finish quality was high. In general, single cavities and cracks at the end junction between the two mass flows in the mold cavity were sometimes observed for sprockets injected from monolithic feedstocks. Fiber-containing feedstocks allowed for easier molding and less defects. This might be on account of differences in flow properties. Rapid volumetric shrinkage due to thermal contraction upon cooling caused minimal flaking at edges during specimen removal. Injection molding was carried out in semi-automatic mode so as to place back the ejected inserts within the standard cavity after each run. However, parts could be injected at high pace, with cycles of less than 2 min.
Further, the suitable feedstock viscosity allowed the injection molding of retaining plates, even though use of the external temperature regulating unit was not possible. For that, the mold (Figure 4. 6) provided by Schunk Sintermetalltechnik GmbH was used, initially manufactured for Rolls Royce. To the contrary of the BOY XS mold for which the cavity was located on a single side (Figure 4. 4A), here, it was split on both blocks (Figure 4. 6). Despite some parts

exhibiting broken edges, the injection molding of monolithic and alumina fiber-reinforced near net shape retaining plates went smoothly, and a large number of pieces were defect-free (Figure 4. 7, A). Figure 4. 7B depicts an overview of moldable assemblies, to wit, retaining plates, gears (or sprockets, see above), nuts with different thread diameters – the threading being possible upon injection molding or after a machining step.

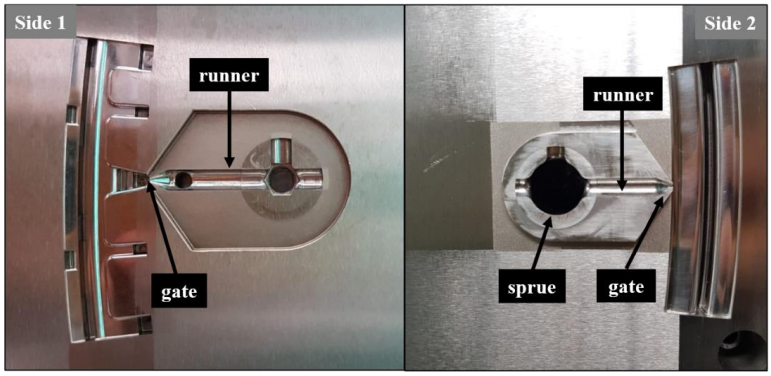

Figure 4. 6: Mold for the production of retaining plates, made available by Schunk Sintermetalltechnik GmbH and Rolls Royce.

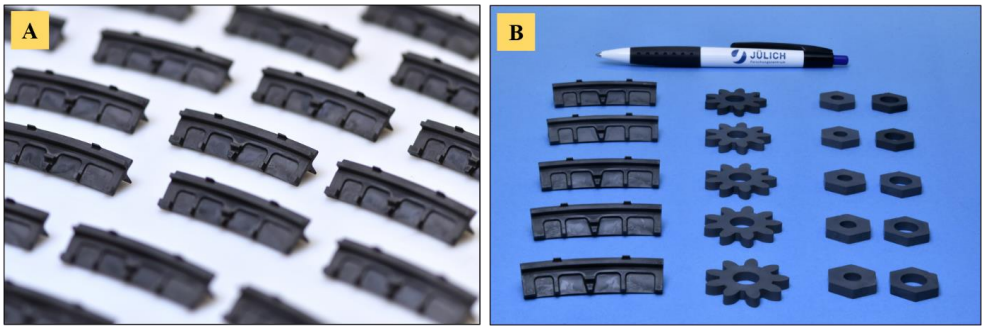

Figure 4. 7: Powder injection molding of Ti_2AlC-based components: (A) Rolls-Royce retaining plates, (B) overview of moldable parts (retaining plates, gears, nuts with different thread size).

The powder injection molding of complex geometries, amongst which, one advanced component (retaining plate) is employed in turbine engines, turned out to be successful. However, these parts cannot be used at that stage. They still contain the organic binder. If employed at high-temperature, the polymeric component would simply melt, and the unsintered part would collapse. Therefore, a two-step debinding procedure has to be undertaken to extract the binder. It has to be carefully controlled to avoid microcrack formation, soaking and uptake of undesired organics (during chemical debinding) and collapsing of the weak structural part before densification.

IV-2 Chemical and thermal debinding

Debinding is a mandatory step to extract the organics from injection-molded components before proceeding to the consolidation of Ti_2AlC.
Chemical debinding in n-hexane of PIM parts was a preliminary step essential to promote egress of waxy binder components (paraffin wax, stearic acid) without removing the polymer

backbone (polyethylene) [111] and creating porosity to facilitate residual binder burnout during thermal debinding. All PIM parts lost ~11–14% of their initial mass, on account of binder extraction and slight flaking.

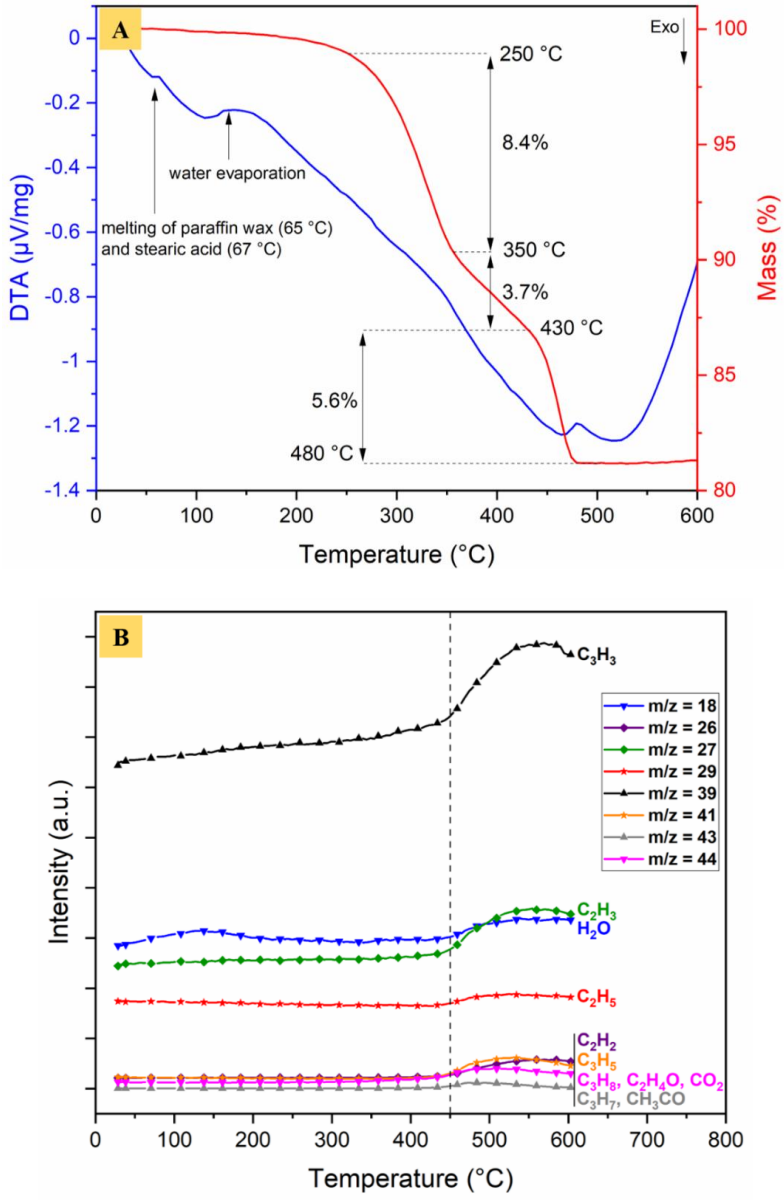

Figure 4. 8: Binder burnout analysed by (A) DTA/TG coupled to (B) mass spectrometry with corresponding QMID ion current curves. Masse to charge ratio is given by m/z.

Figure 4. 8 highlights features of thermal binder burnout. The DTA signal and the thermogravimetric curve (Figure 4. 8, A) demonstrated a slight mass loss (~1 wt.%) before 250 °C on account of the gradual evaporation of low-molecular-weight oligomers – most probably

from residual paraffin wax and stearic acid – and adsorbed water molecules. This was confirmed by the quasi-multiple ion detection (QMID) current curves (Figure 4. 8, B) showing a bump around 130 °C for the mass-to-charge ratio m/z=18 (H_2O) and a gradual increase of m/z=39. The onset of the first decomposition segment was around 250 °C (Figure 4. 8, A). Until 350 °C, this corresponded to the major mass loss (8.4 wt.%). An intermediate decomposition stage was observed with a lower mass loss rate before reaching the third segment above 430 °C, where mass spectrometry (Figure 4. 8, B) retrieved an increase in ion current of multiple hydrocarbon compounds. The debinding temperature was set to 500 °C, at which no further sample mass variation was observed. Above this temperature, the persistence of C_xH_y species (Figure 4. 8, B) in the gaseous phase would explain the retrieval of a spectrometric signal. The interest of using polyethylene as a binder constituent resides in the lowest residue weight fraction left after thermal burnout [111].

At this stage, the components are referred to as "brown" parts. These were extremely fragile as the polymeric bridges between loose-packed Ti_2AlC particles were removed. The fragility of thermally debound Ti_2AlC components was even higher than uniaxially-pressed green bodies so that their handling was impossible. That is why, in the same furnace cycle, the subsequent pressureless sintering was conducted in order to endow the components with sufficient strength. The next section describes the meticulous sintering procedure followed to achieve the highest possible density. In addition, a thorough analysis of fiber orientation and distribution is provided.

Chapter V: Densification of Ti_2AlC

V-1 Pressureless sintering

Conventional solid-state sintering is the traditional technique used to densify polycrystalline materials. It is often referred to as free sintering or pressureless sintering, as no external pressure is applied. Further, as no chemical reactions are involved in this specific case, the reduction of the system's free energy – i.e., its driving force – relies solely on the curvature of the particles surfaces. In solid-state sintering, different diffusion mechanisms (surface, lattice, grain boundary diffusion) take place and are often described in a two or three-particle model (Figure 5. 1) [229].
Usually, three sintering stages are identified, knowing, the initial, intermediate and final stages. In the initial stage, right after particles have been adjoining each other and an elastic deformation of their surfaces has been initiated, so called necks grow at the interparticle contact points through the different diffusion mechanisms described in Figure 5. 1. It generally corresponds to an increase in relative density up to ~65% of the theoretical. In the intermediate stage, the cross-section of pores, arranged in continuous networks, gradually decreases. When reaching a relative density of ~90%, these become unstable and isolated. In the final stage of sintering, the isolated porosity located at grain corners progressively vanishes.

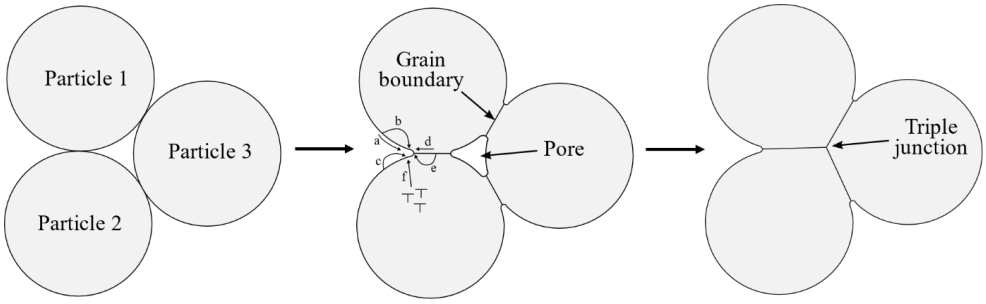

Figure 5. 1: Three-particle model showing the mechanisms of sintering: a) surface diffusion, b) lattice diffusion from the surface, c) vapor transport, d) grain boundary diffusion, e) lattice diffusion from the grain boundary and f) plastic flow (dislocation motion). Adapted from [229].

V-1.1 Pressureless sintering of cylindrical compacts

Pressureless sintering (PS) of Ti_2AlC in argon and vacuum was investigated with the final objective of producing fully dense components with high purity. Bulk green density of cold-compacted bodies was 54% of the theoretical. PS in vacuum was quickly discarded as a layer of decomposed Ti_2AlC formed on the surface due to the sublimation of high vapor pressure Al. This has been already reported in literature [230]. Therefore, PS in argon was further investigated, as the external gas pressure allowed to contain the aluminum in the Ti_2AlC samples. At 1300 °C (Figure 5. 2, A), samples (PS-1300) exhibited a relative density of ~70-75% with a continuous network of large and interconnected pores (~20 µm). At 1400 °C (Figure 5. 2, B), samples (PS-1400) achieved higher relative density (~88-90% of the theoretical), similar to values mentioned in literature [74,101]. The microstructure of these samples showed a homogeneous distribution of submicrometer-sized pores scattered between a few larger ones (~5-10 µm).

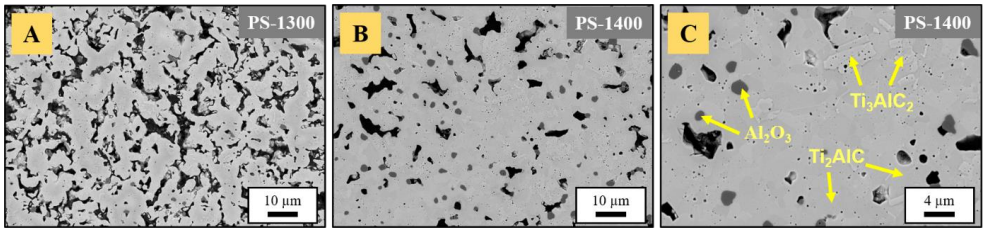

Figure 5. 2: Pressureless sintering of Ti_2AlC for 3 h in argon at 10 °C/min: (A) T = 1300 °C , (B) T = 1400 °C and (C) T = 1400 °C, higher magnification.

Higher magnification (Figure 5. 2, C) showed the presence of needle-shaped grains/clusters of grains of Ti_3AlC_2 in a dominant matrix of Ti_2AlC, which were confirmed by energy-dispersive X-ray spectroscopy (EDS) (Figure 5. 3, A and B). The submicrometer-sized pores were predominantly located within clusters of Ti_3AlC_2 grains. Dark-grey Al_2O_3 grains were observed with backscattered electrons (BSE) and detected by EDS too (Figure 5. 3, C). The sintering atmosphere certainly contained few ppm of oxygen, responsible for local oxidation of Al, though, it is believed that Al_2O_3 was essentially present before PS, as evidenced by the oxygen content in as-synthesized Ti_2AlC powders (Table 3. 2). The observed relief was due to disparate etching of Ti_2AlC and Ti_3AlC_2 MAX phases during the final polishing step. The Al content being higher in Ti_2AlC, it is more predisposed to etching by the alkaline silica suspension than Ti_3AlC_2. The differences in topography between Ti_2AlC and Ti_3AlC_2 were not caused by differences in hardness.

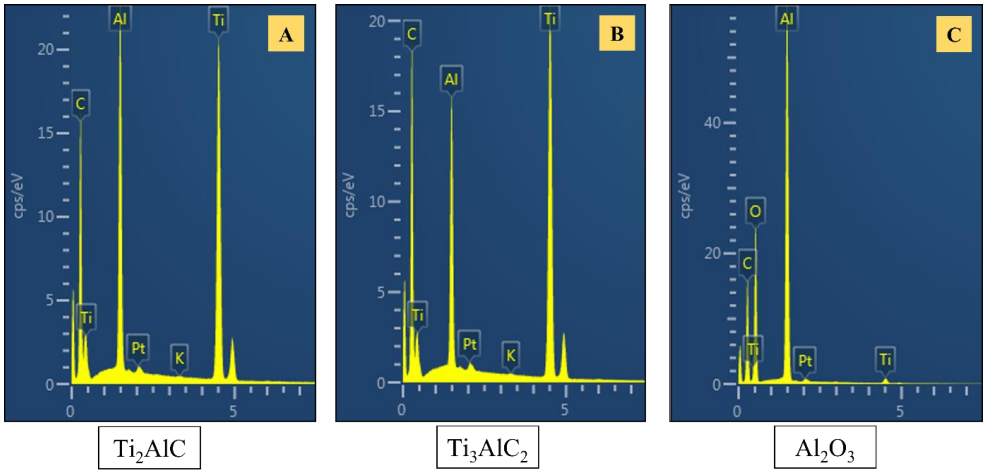

Figure 5. 3: EDS spectra of (A) Ti_2AlC, (B) Ti_3AlC_2 and (C) Al_2O_3 detected in PS samples.

Specimens sintered at both temperatures showed a substantial increase in the Ti_3AlC_2 phase content (Figure 5. 4, Table 5. 1). Rietveld refinement evidenced 81 wt. %, 17 wt. % and 2 wt. % of Ti_2AlC, Ti_3AlC_2 and Al_2O_3 respectively for PS-1300 samples. The PS-1400 samples contained 78 wt. %, 20 wt. % and 2 wt. % of Ti_2AlC, Ti_3AlC_2 and Al_2O_3, respectively. Unreacted graphite was gradually consumed (disappearance of the C (002) reflection at 2θ = 27°) and contributed to the formation of Ti_3AlC_2 via mechanisms described earlier (see *Chapter III: Synthesis of Ti_2AlC powders*). Additionally, a phenomenon of phase interconversion following the mechanism of Equation 20 is believed to occur, as described by Kisi et al [49].

Al planes are thought to slowly diffuse out of Ti_2AlC into TiC. Ti_6C octahedra come close to each other forcing Ti to diffuse out. The Ti_2AlC structure eventually collapses into Ti_3AlC_2. The March-Dollase parameter calculated for PS-1300 and PS-1400 samples was unequal to 1, which is actually an indication for texturing or preferred orientation. However, considering the large fraction of pores, it seems not counterintuitive to think that these might have strongly contributed to these outcomes, probably acting on the way X-rays were diffracted. Especially as the sample containing the largest fraction of porosity (PS-1300) showed a lower March-Dollase parameter, respectively a higher degree of preferred orientation.

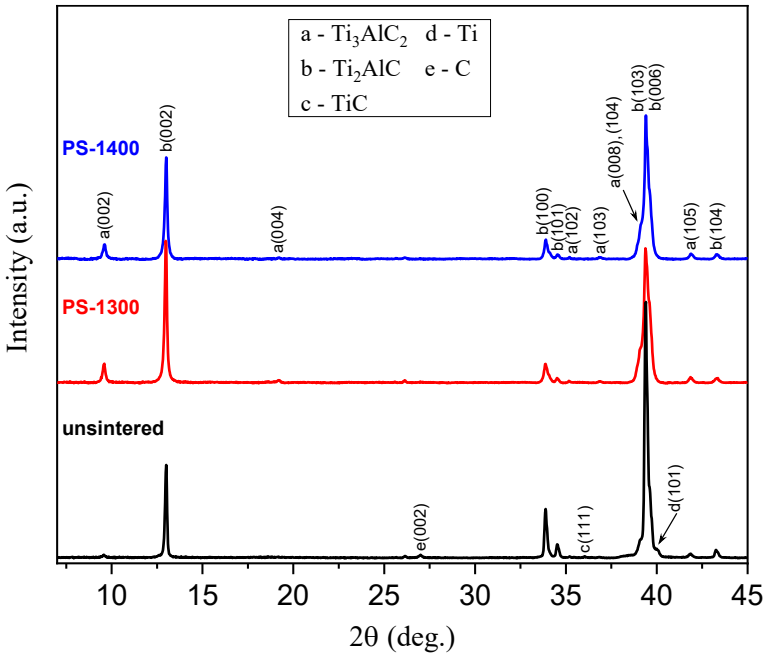

Figure 5. 4: XRD diffractograms of pressureless-sintered Ti_2AlC compared to raw powder (unsintered).

Table 5. 1: Corresponding Rietveld refinement and texture analysis outcomes. *Indicates the presence of traces, †measured for Ti_2AlC (002), §measured for Ti_3AlC_2 (002). Density is given as compared to the theoretical density (TD).

Sample	Detected phases (mass fraction)	Density (% of TD)	March-Dollase parameter (r)	Degree of preferred orientation (η)
Unsintered	Ti_2AlC (91%), Ti_3AlC_2 (6%), Ti (2%), TiC*,C*	54	$1^{\dagger}$ $1^{\S}$	$\rightarrow 0^{\dagger}$ $\rightarrow 0^{\S}$
PS-1300	Ti_2AlC (81%), Ti_3AlC_2 (17%), Al_2O_3 (2%)	70-75	$0.77^{\dagger}$ $0.86^{\S}$	$14.96^{\dagger}$ $8.68^{\S}$
PS-1400	Ti_2AlC (78%), Ti_3AlC_2 (20%), Al_2O_3 (2%)	88-90	$0.81^{\dagger}$ $0.92^{\S}$	$12.10^{\dagger}$ $4.81^{\S}$

As a result, full densification of Ti_2AlC without any alteration could not be attained by pressureless sintering. Consequently, an electric field/pressure assisted sintering technique was employed in order to rapidly reach near full densification with minimal purity degradation. The outcomes are described in the section *V-2. FAST/SPS*.

V-1.2 Pressureless sintering of complex shapes

Complex shapes produced by PIM of monolithic and composite Ti_2AlC were densified by PS at different temperatures, of which the outcomes are presented in Figure 5. 5 and Figure 5. 6. At 1250 °C, monolithic hexagon nuts as well as sprockets (Figure 5. 5, B and G) experienced up to 13% isotropic shrinkage. The components achieved a relative density of 70.1% (Figure 5. 6, A) and revealed a large fraction of porosity with high degree of interconnectivity.

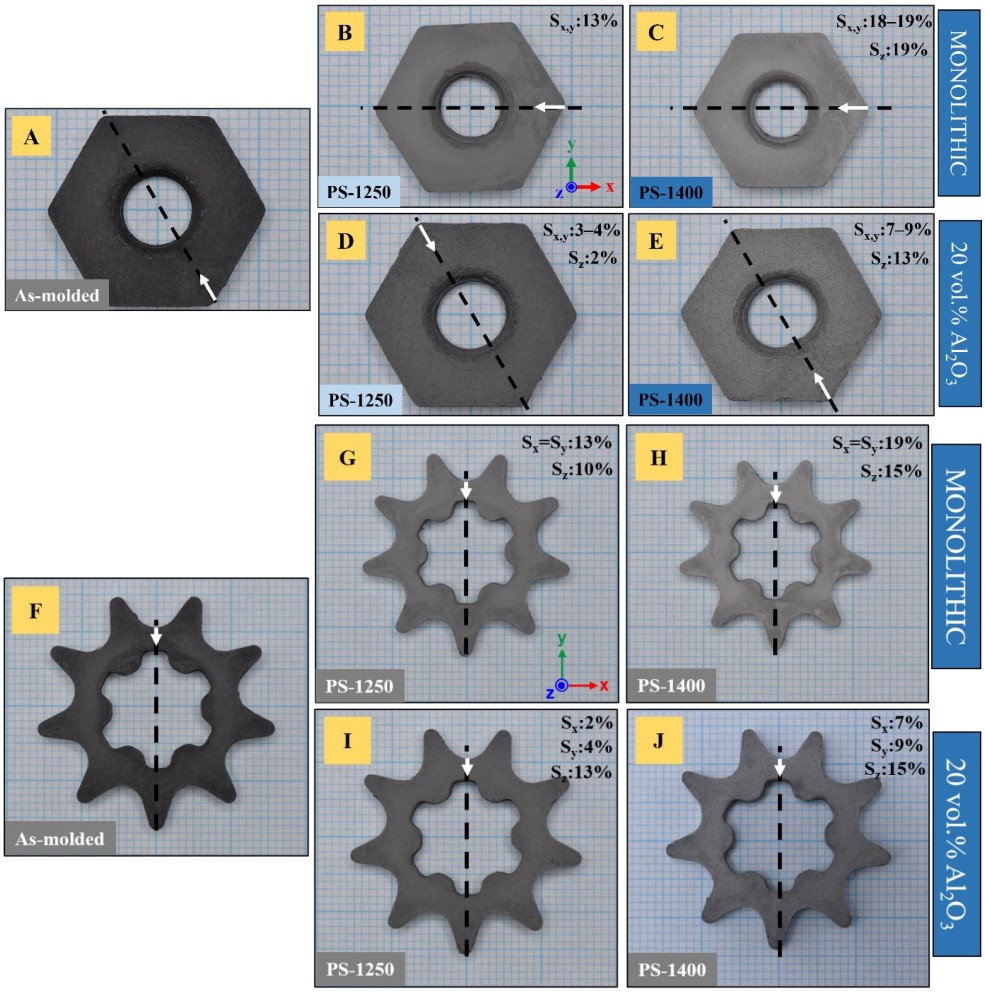

Figure 5. 5: Pressureless-sintered monolithic and N720 alumina fiber-reinforced (20 vol.%) Ti_2AlC nuts and sprockets. White arrows and dashed lines indicate the location of the gate and the axis parallel to the injection channel, respectively. Sintering shrinkage in each direction is given by the S values.

Recently, Tabares et al. [112] demonstrated that pressureless sintering in vacuum at 1300 °C for 4 h of injection-molded Ti_3SiC_2 led to porosity ranging from 47 to 53%. Up to 1300 °C under pressureless condition, it has been shown previously (Figure 5. 2, A) that the driving force for sintering of Ti_2AlC is low and its full densification is challenging. In contrast, aluminosilicate fiber-reinforced (20 vol.% N720) composites shrank anisotropically and markedly less – around 2-4% – than their monolithic homologs.
Both nuts (Figure 5. 5, D) and sprockets (Figure 5. 5, I) demonstrated minimal dimensional change compared to the as-molded components (Figure 5. 5, A and F). The thicknesses of sprockets decreased more significantly, by 13%. The microstructural characterization of composite parts highlighted a porosity areal fraction of 34.5% (± 2.8%) (Figure 5. 6, C).
It is known that the inherent sintering ability of the MAX phases is poor without sintering additives [74], and temperatures as high as 1400 °C are a requirement to reach a relative density of at least 90% in PS conditions. For Ti_2AlC, Hashimoto et al. [74] reached a relative density of 94.2% under pressureless conditions after 2 h at 1400 °C in argon without sintering additives; additions of Al_2O_3 increased the relative density to 96.0%. Lu et al. [231] proceeded to investigate the pressureless sintering of Ti_3AlC_2 and reported relative densities of 92.7% and 96.2% when performed at 1500 °C (10 min) and 1450 °C (150 min), respectively. Additionally, they mentioned the issue of phase decomposition into binary carbides, resulting from higher sintering temperatures or longer dwelling times.
Some components were further sintered at 1400 °C by PS. The monolithic samples significantly shrank in an isotropic manner, up to 19% (Figure 5. 5, C and H) and reached a relative density of 92.6% (Figure 5. 6, B). The microstructure highlights non-interconnected porosity and the transition towards a final stage of sintering. The relatively high sintering shrinkage at 1400 °C (almost 20%) is correlated with the relatively low feedstock solids loading (50 vol.%) [111]. However, Al_2O_3 fiber-reinforced Ti_2AlC composites did not achieve similar densities and shrank even less than monolithic samples that were sintered at lower temperatures.

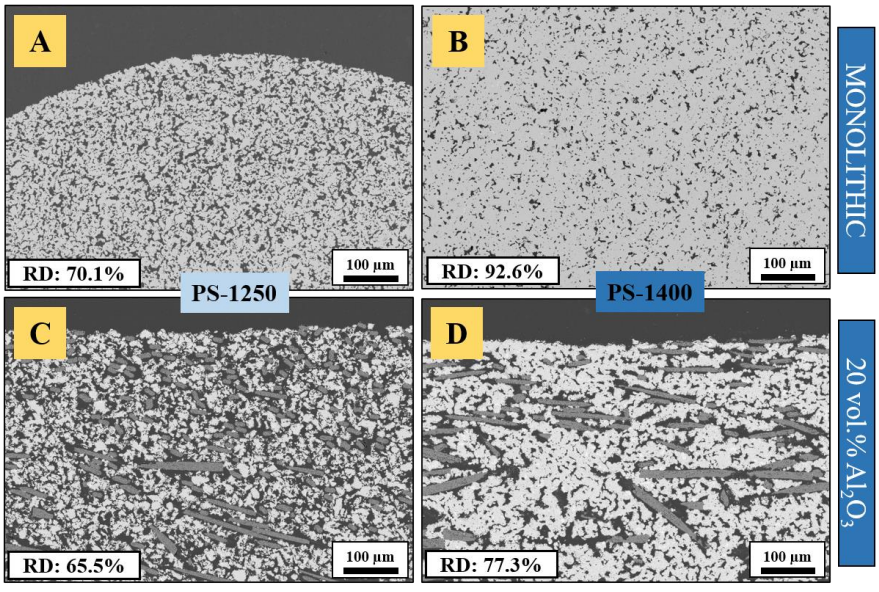

Figure 5. 6: Microstructure of pressureless-sintered monolithic and N720 alumina fiber-reinforced (20 vol.%) Ti_2AlC. RD designates the achieved relative density in % of the theoretical value.

The dimensional change in the nuts (Figure 5. 5, E) and sprockets (Figure 5. 5, J) was anisotropic. The areal fraction of pores yielded 22.7% (± 1.8%) after the second PS step at 1400 °C (Figure 5. 6, D) and were mainly located in the vicinity of fibers.
Additionally, a deflection along the z-axis was observed for all parts, more pronounced for sprockets, probably due to their less compact geometry and, thus, lower bending stiffness. In particular, fiber-reinforced components became strongly undulated when sintered at 1400 °C. Similar warpage was observed for composites containing a lower volume fraction of fibers (10 vol.%), while this effect was barely visible for monolithic samples. It might find its origin in the stresses arising during injection molding, due to a more complex solidification pattern in more tortuous shapes. In fact, uneven cooling is an essential cause of warpage [110]. The longer the path that the mass followed in the sprocket mold, the larger the stress gradients and the greater the dimensional distortion upon sintering. In addition, the low solids loading (Ti_2AlC powder, Al_2O_3 fibers) contributed to greater sintering shrinkage, and the presence of aligned fibers promoted the asymmetrical change in shape.
As compared to monolithic samples, the presence of a dispersed inert phase (short Al_2O_3 fibers) hindered the densification process. In fact, the difference in the shrinkage rate of a shrinking cladding (matrix) around dispersoids leads to the buildup of an effective hydrostatic stress [229,232,233]. The latter is directly correlated with the volume fraction of the dispersed phase, when the dimensions of the reinforcing elements are significantly larger than the matrix grain size [232]. This is expressed as follows:

$$\sigma_m = -\sigma_i \frac{f}{(1-f)} \qquad \text{(Equation 25)}$$

where f and σ_i are the volume fraction and the hydrostatic stress in the rigid second phase, respectively, and σ_m represents the backstress generated in the matrix. As the mean hydrostatic stress or backstress σ_m counteracts the sintering stress, the linear densification rate is reduced [229]. Sintering stops when the ratio of peak matrix hydrostatic stress normalized by the sintering stress approaches unity, which is the case for a volume fraction of spherical inclusions above 10% [233]. For fibers with a larger aspect ratio than spherical inclusions, shrinkage anisotropy is more pronounced [234]. In fact, due to differential shrinkage in fiber composite assemblies, the threaded hole of nuts (Figure 5. 5, D) and the internal geared geometry of sprockets (Figure 5. 5, I) became warped. The distortion was more pronounced at higher sintering temperatures (Figure 5. 5, E and J) at which, in the case of the nut component, the initially circular threaded hole became elliptical. The thread compression induced by anisotropic sintering shrinkage was more important along the axis parallel to the injection channel. The larger shrinkage along the sample thickness and the observed deflection are believed to result from fiber orientation, which is further discussed below. In brief, as most of the fibers were oriented in the (x,y) plane, their total surface area in contact with the matrix represented less opposition to shrinkage along the z-axis, as would be the case if their axes were parallel to the direction of concern.
In addition, higher processing temperatures involve the risk of phase transformation/inter-conversion from Ti_2AlC to the more stable Ti_3AlC_2, as already reported by another study [49], or thermal decomposition, when coming closer to the incongruent melting point of Ti_2AlC [64].
In summary, it is assumed that the inherent low sinterability of Ti_2AlC, the limitation in maximal sintering temperature, the absence of an additional driving force in the form of applied external pressure, the irregular agglomerate shape and the presence of rigid non-sintering fibers with high aspect ratio, did not allow for thorough densification. As such, the route of FAST/SPS in a bed of graphite powder was employed to achieve the near-complete densification of injection-molded monolithic and composite Ti_2AlC assemblies.

V-2 FAST/SPS

Field assisted sintering technology/spark plasma sintering (FAST/SPS) is a pressure-assisted sintering technique (Figure 5. 7) employing low voltages (below 10 V) and high pulsed direct currents (1-10 kA) [78].

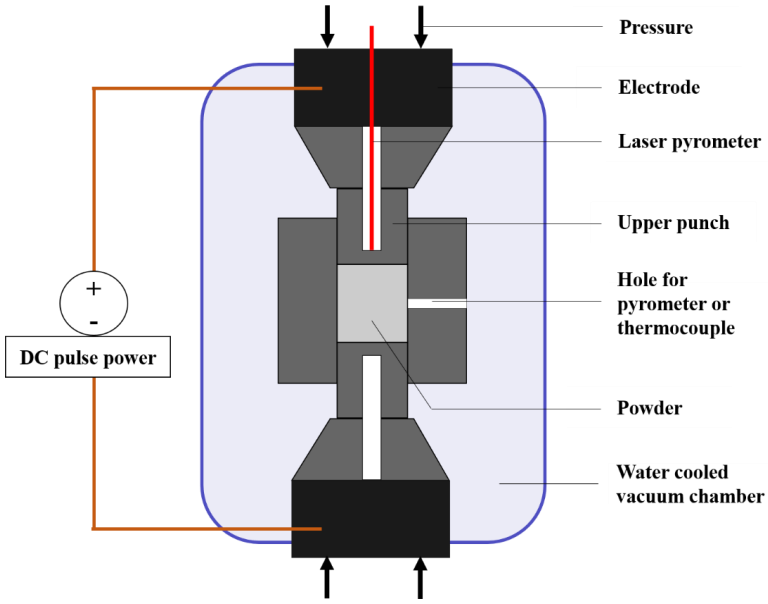

Figure 5. 7: Schematic of the FAST/SPS technology.

The electrically conductive tooling (traditionally graphite) allows Joule heating to take place. Thus, it is possible to employ heating rates as high as 1000 °C/min. Coupled to the fact that high cooling rates can also be reached (150-400 °C/min), the residence time of the sample at sintering temperature is drastically shortened as compared to conventional routes. Uniaxial mechanical loading (classically between 50 and 250 kN) assists densification. The chamber can either be filled with inert gases or a vacuum can be drawn. The temperature control ensues via laser pyrometry or thermocouples.

V-2.1 FAST/SPS of cylindrical compacts

V-2.1.1 Monolithic Ti_2AlC

Ti_2AlC powders were sintered by FAST/SPS at lower temperatures (1200 °C) than PS under a pressure of 50 MPa in vacuum. Aim was to achieve near full densification by concomitantly limiting phase transformation, drawbacks encountered for free sintering. A higher heating rate (100 °C/min) as compared to PS (5 °C/min) was used.
The onset of densification was around 800-850 °C, and the specimens (Figure 5. 8, A) definitely exhibited higher relative density (98.5% of the theoretical) after a 10 min dwell time at 1200 °C as compared to pressureless sintered samples, with pore sizes below 5 µm.
Topographical differences were also observed due to different chemical etching of Ti_2AlC and Ti_3AlC_2 phases during the final polishing step. On account of denser microstructures, clusters of Ti_3AlC_2 grains were more discernable on SEM images of SPS-1200 samples (Figure 5. 8, B)

as compared to previous micrographs of PS-1300 or PS-1400 (Figure 5. 2). They were ~10-20 µm in size.

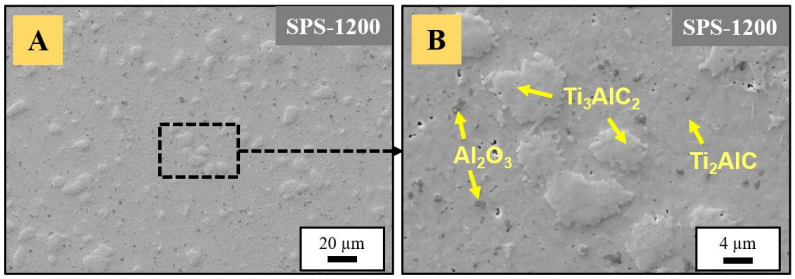

Figure 5. 8: Microstructure of Ti_2AlC powder "SPSed" at 100 °C/min to 1200 °C, 50 MPa for 10 min in vacuum.

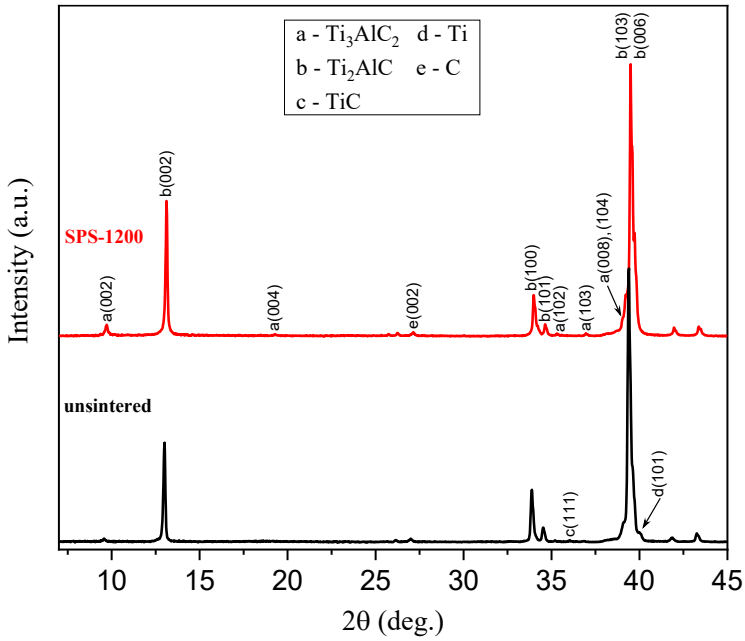

Figure 5. 9: XRD diffractogram of "SPSed" Ti_2AlC compared to the raw powder (unsintered).

Phase transformation (Figure 5. 9, Table 5. 2) was observed, but to a smaller degree as compared to PS samples. Shorter sintering times slightly reduced the extent to which Ti_3AlC_2 was formed (Equation 20). Quantitative phase analysis evidenced 84 wt. %, 14 wt. % and 2 wt. % of Ti_2AlC, Ti_3AlC_2 and Al_2O_3, respectively. Traces of unreacted Ti present in as-synthesized Ti_2AlC were entirely consumed (disappearance of the Ti (101) reflection at $2\theta = 40.1°$), contributing to the formation of Ti_2AlC and Ti_3AlC_2. The TiC (111) reflection at $2\theta = 35.9°$, hardly discernable for Ti_2AlC powder (unsintered sample), was not evidenced after SPS. It was consumed during sintering (Equation 20), proving that the remainder of unreacted Ti did not promote the formation of additional TiC. However, minute amounts of free carbon were still detectable. A non-negligible amount of Al_2O_3 was detected in SPS-1200, as for PS. The degree of preferred orientation was 7.37 for SPS-1200, indicating a slight texturing (Table 5. 2).

Table 5. 2: Rietveld refinement and texture analysis outcomes for "SPSed" samples. PS samples are indicated for comparison. *Indicates the presence of traces, †measured for Ti_2AlC (002), §measured for Ti_3AlC_2 (002). Density is given as compared to the theoretical density (TD).

Sample	Detected phases (mass fraction)	Density (% of TD)	March-Dollase parameter (r)	Degree of preferred orientation (η)
Unsintered	Ti_2AlC (91%), Ti_3AlC_2 (6%), Ti (2%), TiC*,C*	54	1† 1§	→ 0† → 0§
SPS-1200	Ti_2AlC (84%), Ti_3AlC_2 (14%), Al_2O_3 (2%), C*	98.5	0.88† 1§	7.37† → 0§
PS-1300	Ti_2AlC (81%), Ti_3AlC_2 (17%), Al_2O_3 (2%)	70-75	0.77† 0.86§	14.96† 8.68§
PS-1400	Ti_2AlC (78%), Ti_3AlC_2 (20%), Al_2O_3 (2%)	88-90	0.81† 0.92§	12.10† 4.81§

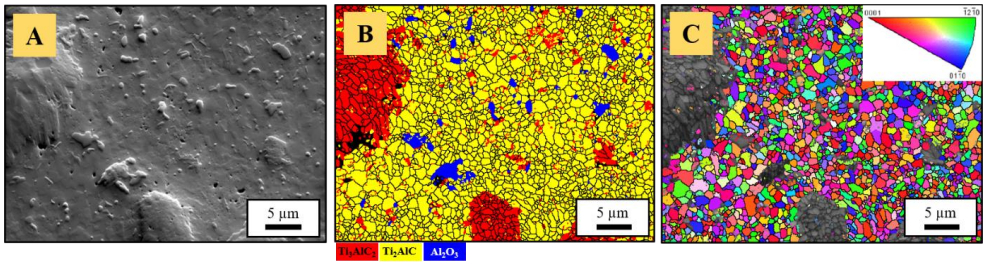

Figure 5. 10: EBSD analysis of "SPSed" Ti_2AlC: (A) SE image, (B) corresponding phase map (C) corresponding Ti_2AlC orientation map (Z_0).

EBSD analyses (Figure 5. 10) gave an insight into grain size, grain orientation, grain shape and phases of SPSed samples. The previously observed relief, also appearing on Figure 5. 10A, are either single grains of Al_2O_3 or clusters of Ti_3AlC_2, as displayed on the phase map (Figure 5. 10, B). Ti_2AlC produced by MS[3] and sintered by FAST/SPS showed a submicron fine-grained microstructure. Grain sizes of the three phases are below 1 µm (Table 5. 3), indicating that sintering by FAST/SPS under these conditions did not promote grain growth. Increasing holding times had no influence on grain growth and the microstructure remained the same after one hour of sintering. It seems to be the smallest grain size reported so far for Ti_2AlC. For instance, direct synthesis of Ti_2AlC by FAST/SPS of elemental reactants at 1100 °C and 30 MPa in vacuum, using a heating rate of 80 °C/min and a dwell time of one hour, yielded large elongated grains of 20 µm by 5 µm [71]. Another work [58] based on FAST/SPS of TiAl-carbon nanotube powder at 1200 °C and 160 MPa in vacuum produced coarse grains as well (>10 µm according to SEM images). In the present work, FAST/SPS did not produce strong texture in the samples and grains were randomly oriented (Figure 5. 10, C). The relatively low uniaxial pressure during sintering (50 MPa) and the isometric nature of grains, as well as the absence of grain growth, can explain the absence of texture. The average aspect ratio of Ti_2AlC grains was close to 1.6 (Table 5. 3), indicating a more symmetric nature than for Ti_3AlC_2 grains. Longer holding times had no influence on grain aspect ratio either. Al_2O_3 grains were in the same size range. The average aspect ratio was closer to that of Ti_2AlC. Al_2O_3 grains, when not spherical, had a more equiaxed morphology as compared to both Ti_2AlC and Ti_3AlC_2 grains.

Table 5. 3: Grain size and grain aspect ratio outcomes of EBSD analyses for three samples sintered by SPS for 10, 30 and 60 min, respectively.

Sample	Average grain size (µm)			Average grain aspect ratio		
	Ti_2AlC	Ti_3AlC_2	Al_2O_3	Ti_2AlC	Ti_3AlC_2	Al_2O_3
TAC-SPS-10	0.75 ± 0.34	0.62 ± 0.30	0.70 ± 0.37	1.62 ± 0.46	1.85 ± 0.65	1.58 ± 0.43
TAC-SPS-30	0.78 ± 0.36	0.60 ± 0.31	0.62 ± 0.28	1.64 ± 0.48	1.96 ± 0.69	1.50 ± 0.33
TAC-SPS-60	0.79 ± 0.36	0.64 ± 0.30	0.74 ± 0.36	1.62 ± 0.49	1.85 ± 0.65	1.47 ± 0.34

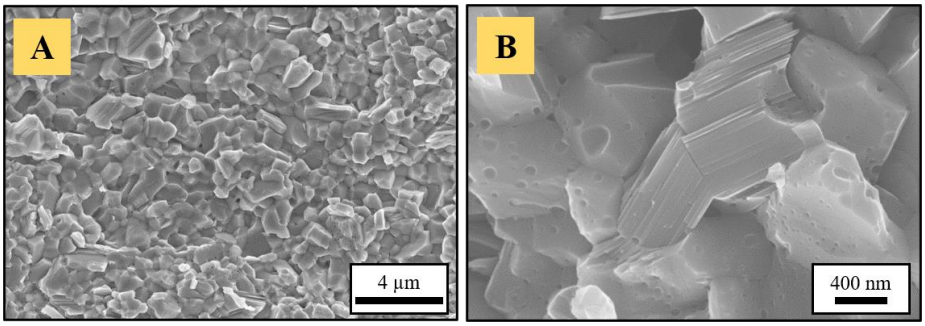

Figure 5. 11: Fractographic analysis of Ti_2AlC densified by SPS: (A) insight into the fine-grained microstructure and (B) required high magnification in order to evidence the layered structure.

Fractured surfaces (Figure 5. 11, A) confirmed the fine-grained microstructure evidenced with EBSD analysis. Higher magnifications (Figure 5. 11, B) were required to visualize single MAX phase layers and mesopores.
Thereby, FAST/SPS turned out to be a rapid sintering method to enable near full densification of Ti_2AlC powders with 10 min of dwell time at 1200 °C. At the same time, phase transformation/conversion was limited and original grain size was retained, which are important features for good oxidation resistance [143].

V-2.1.2 Fiber-reinforced Ti_2AlC

FAST/SPS is a rapid and effective way to densify monolithic MAX phases and more specifically, within the scope of this work, Ti_2AlC. However, when it comes to the sintering of composites, the dispersion of the reinforcement phase can be challenging depending on the nature of the material and the aspect ratio of the reinforcement constituents.
The length of fibers – and hence, their aspect ratio – is a critical parameter to consider, in order to avoid their entanglement. The preliminary solvent desizing experiments performed in water and acetone under magnetic stirring highlighted the propensity of Al_2O_3 fibers to immediately agglomerate in the suspension and form small wool-ball-like structures as depicted in Figure 5. 12A. The dispersion was better in ethanol, and therefore undertaken for fibers/powder suspensions as well. However, after solvent evaporation, the sedimented fibers formed an entangled "mat", generally found above the denser Ti_2AlC powder (Figure 5. 12, B). Scratching the sedimented deposit with a spatula resulted in pieces of agglomerated fibers being dispersed in the MAX phase powder. Initially, experiments were performed with 3.2 mm long N720 fibers, the shortest fiber length provided by the company 3M.

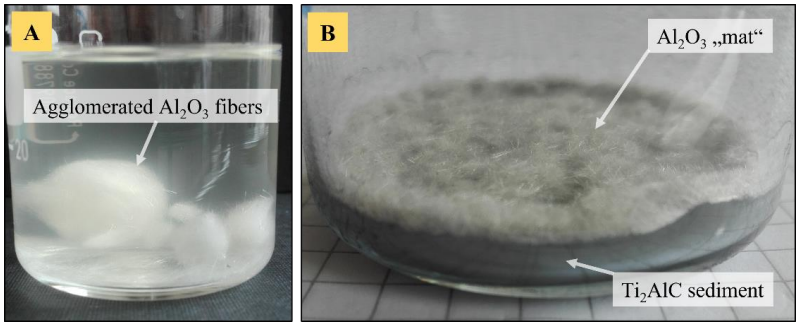

Figure 5. 12: Issues encountered when dispersing short Al_2O_3 fibers: (A) agglomerated fibers form wool-ball-like structures in water and (B) Al_2O_3 fiber “mat” forming atop Ti_2AlC after sedimentation and drying of an ethanol-based suspension.

These were mixed with Ti_2AlC powder and sintered by FAST/SPS to produce composite pellets. After grinding and polishing, darker structures were identified on the surface and turned out to be large agglomerates of fibers (Figure 5. 13, A).

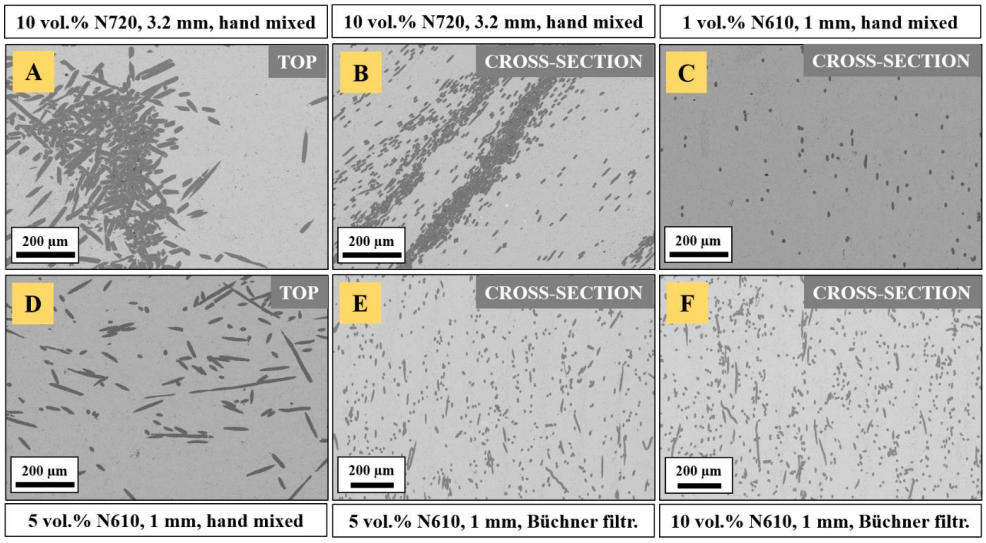

Figure 5. 13: Fiber dispersion in $Ti_2AlC/Al_2O_{3(f)}$ composites manufactured by FAST/SPS. The dispersion was done by (A), (B), (C), (D) a simple dry mixing of powder and fibers and (E), (F) a filtration of the suspension in a vacuum (Büchner) filtration setup, directly in the SPS die.

Cross-sections highlighted stripes of agglomerated fibers (Figure 5. 13, B), similarly to patterns reported by Go et al. [199] for Cr_2AlC/Al_2O_3 composites with 1 mm long fibers. The use of organic dispersants would have required an additional burnout step. In addition, wetting and dispersing additives from the company BYK-Chemie GmbH (Wesel, Germany) were used to deagglomerate Al_2O_3 fibers, but these were found ineffective by a simple dipping method. These organic species are rather used to keep the dispersion homogeneous, but are not suitable in the present case, involving a drying step to recover the powder/fiber mixture. Therefore, the reduction in fiber length was assumed to be a way to avoid agglomeration and chopping continuous N610 alumina fibers down to 1 mm helped to reduce their propensity to entangle and agglomerate. Adding 1 vol.% N610 fibers to Ti_2AlC showed a good dispersion (Figure 5.

13, C), as expected from this low volume fraction. At 5 vol.% (Figure 5. 13, D), the fibers started to agglomerate, and the effect worsened with increasing fiber content. Another method of filtration was used, which consisted in pouring a fiber/powder-ethanol suspension directly in the FAST/SPS die. However, homogeneous composites could not be achieved this way, as the less dense fibers were found atop the sedimented Ti_2AlC powder. Thus, Büchner filtration was employed to force the simultaneous sedimentation of particles and fibers through vacuum suction. The outcomes for 5 and 10 vol.% N610 fibers are depicted in Figure 5. 13E and Figure 5. 13F, respectively, and showed that a more homogeneous dispersion was possible via this technique. Obviously, for complex shapes, this method cannot be applied and near net shaping techniques such as injection molding are required.

V-2.2 Powder bed sintering of complex shapes

V-2.2.1 FAST/SPS procedure

In the case of complex shapes as well, pressureless sintering, even at an elevated temperature of 1400 °C, did not provide the required driving force to densifying the material. Instead, a pressure-assisted technique is typically required to achieve near-complete densification. Conventionally, hot isostatic pressing [235] is employed for metals and ceramics, but this is costly and often requires an encapsulation to avoid fluid penetration within pores. Therefore, powder bed sintering in graphite powder, using a FAST/SPS furnace [215–217,236,237] was found to be an alternative to achieving the near-full densification of complex shapes, as it granted the required driving force at a reduced sintering temperature (1200 °C) and dwell time (10-15 min). This procedure has not been reported in the literature for MAX phases. The pre-sintering PS step at 1250 °C was essential, as thermally debound parts exhibited high fragility and would have yielded under low loads. As compared to the PS-1250 sample, a lower shrinkage percentage of ~7-9% of the PBS parts was noticeable in the (*x,y*) plane (Figure 5. 14, C and D), relative to the initial dimensions (Figure 5. 14, A and B). However, the samples significantly shrank in *z* direction, which is parallel to the applied pressure. The thickness of the sprockets, sintered by PBS, was halved, while the nuts shrank up to 43%. For the latter, this was accompanied by a significant reduction in the thread pitch, while the thread diameter increased asymmetrically. In addition, subsequent sample conditioning (sandblasting and grinding), to remove the residual graphite foil and graphite particles, contributed to the decrease in thickness. The bed of coarse graphite powder may not have allowed for an optimal load transfer that was transversal to the pressing direction, so that the densification mainly occurred uniaxially. In fact, it might come from the small ratio of tool to sample size used in this work. Hocquet et al. [217] mentioned the advantage of using larger dies and its correlation with an improved repartition of the load around the sample. By convention, the transverse diameter of the powder bed should be at least twice that of the maximum transverse dimension of the body [215].

The relative densities of monolithic nuts and sprockets were found to be 97.0-97.5% and 98.1-98.6%, respectively (Figure 5. 15, A). The higher density of the latter can be ascribed to greater compaction during the injection molding process, on account of a supposedly larger volume being “forced” into the mold cavity. The higher green densities of sprockets may have facilitated densification during sintering. The remaining 2-3% porosity was visible at higher magnification (inset of Figure 5. 15, A) and the largest pores were less than 15 µm in size. Additionally, alumina grains were found to be homogeneously distributed across the samples. Image analysis showed that these accounted for 2-3% of the considered surface areas.

As for monolithic parts that were sintered by PBS, composite assemblies were almost fully densified following the same procedure (Figure 5. 15, B), albeit presenting lower relative

densities than their monolithic counterparts. These were 96.1-96.5% and 96.9-97.2% of the theoretical for nuts and sprockets, respectively.

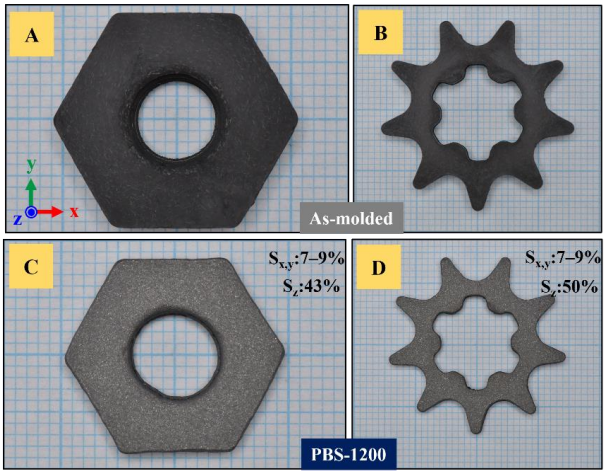

Figure 5. 14: Powder bed sintered monolithic and N720 alumina fiber-reinforced (20 vol.%) Ti_2AlC nuts and sprockets: (A) and (B) are as-molded, (C) and (D) are PBS parts. Sintering shrinkage in each direction is given by the S values.

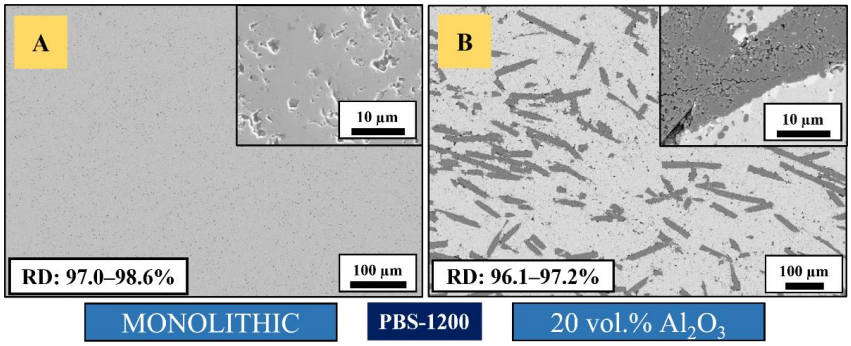

Figure 5. 15: Microstructure of powder bed sintered monolithic and N720 alumina fiber-reinforced (20 vol.%) Ti_2AlC. RD designates the achieved relative density.

From SEM and optical micrographs, it was evident that the fiber aspect ratio decreased upon feedstock granulation, as compared to the raw fibers. The maximal length was found to be less than 500 µm. Considering the diameter as unchanged (11-14 µm) and the cross-section as circular, this accounts for a maximal aspect ratio of 35-45. However, the broad fiber length distribution (as a result of fiber breakage) accounted for a broad aspect ratio variation, to the point that 100 µm fibers had an aspect ratio of 7-9. It is a well-known fact that the fractional packing density decreases with an increasing length-to-diameter (L/D) fiber ratio. For instance, a 48% random dense packing can be achieved with L/D = 10, while only a 9% fractional density is achieved with L/D = 60 [110]. Similarly, this decreases the more irregular the particle (or agglomerate) shape, as is the case here (Figure 3. 5B). In addition, the presence of porosity within fibers (inset of Figure 5. 15, B) was observed. It occurred as soon as after the first PS step at 1250 °C and strictly concerned composites reinforced with N720 fibers, which contain

15 wt.% SiO_2. Patches of a Si-rich phase were detected in the vicinity of fibers and were visible on backscattered electron images. It is likely that the mullite phase was decomposed at 1250 °C in a reducing atmosphere, as reported for lower temperatures [238], and led to the formation of submicrometric pores within N720 fibers. Tian et al. [238] further showed that the equilibrium total vapor pressure of mullite in argon increased by nearly four orders of magnitude from 1000 to 1250 °C and by almost six orders of magnitude when also in presence of carbon. In the present work, aside from the reducing effect of the argon atmosphere, the surrounding Ti_2AlC matrix probably contributed to the decomposition of the $3Al_2O_3 \cdot 2SiO_2$ phase at 1250 °C. A few cavities located nearby fibers were identified and might have been generated during sintering, as the decomposition of mullite resulted in the formation of gaseous species [238]. No such phenomenon was observed for composites reinforced by N610 alumina fibers, of which the fiber diameter remained unaltered even after PBS.

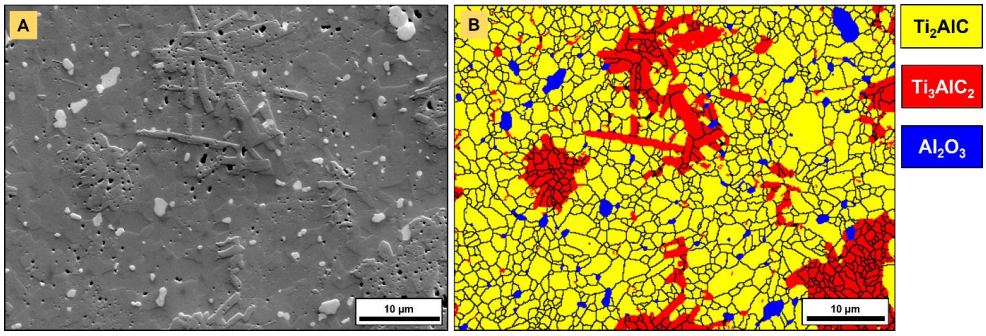

Figure 5. 16: Electron backscattered diffraction (EBSD) analysis of an injection molded monolithic Ti_2AlC nut specimen after sintering procedure 1 (PS1250 + PBS1200): (A) SE image shows height offset and porosity in Ti_3AlC_2 grains and (B) corresponding EBSD phase map with areal fractions of 77.5% Ti_2AlC, 18.8% Ti_3AlC_2 and 3.2% Al_2O_3.

An insight into grain size distribution, average grain size and grain aspect ratio of a monolithic PBS-1200 sample is given in Figure 5. 16 and Table 5. 4. The height offset of Ti_3AlC_2 grains, organized in clusters, as well as the presence of submicrometric pores concentrated in these specific areas, were observed (Figure 5. 16, A). The presence of cavities, essentially located in and nearby Ti_3AlC_2 grains, might either arise from a minor loss of Al and the interconversion of Ti_2AlC to Ti_3AlC_2 [49], or from the etching of potential minor impurities (titanium aluminides) during metallographic preparation. As mentioned previously, a major advantage of FAST/SPS is the inhibition of grain growth (Figure 5. 10) and the preservation of a fine-grained microstructure, as well as a limited alteration of phase composition.

Table 5. 4: Grain size and grain aspect ratio outcomes of EBSD analyses for monolithic PBS-1200. The previous values for unsintered powder and TAC-SPS-10 are indicated for comparison.

Samples	**Average grain size (µm)**			**Average grain aspect ratio**		
	Ti_2AlC	Ti_3AlC_2	Al_2O_3	Ti_2AlC	Ti_3AlC_2	Al_2O_3
PBS-1200	1.28 ± 0.64	0.98 ± 0.55	0.77 ± 0.43	1.69 ± 0.49	1.96 ± 0.79	1.51 ± 0.38
TAC-SPS-10	0.75 ± 0.34	0.62 ± 0.30	0.70 ± 0.37	1.62 ± 0.46	1.85 ± 0.65	1.58 ± 0.43
unsintered	0.93 ± 0.42	0.66 ± 0.12	N/A	1.75 ± 0.52	1.73 ± 0.63	N/A

The alumina grains found at Ti_2AlC grain boundaries mostly arise during the synthesis and sintering procedures [44] on account of a low oxygen content in raw materials or non-negligible oxygen partial pressure in furnace chambers. The average grain size (Table 5. 4) yielded 1.28 µm (± 0.64 µm), 0.98 µm (± 0.55 µm) and 0.77 µm (± 0.43 µm) for Ti_2AlC, Ti_3AlC_2 and Al_2O_3, respectively.
These values correspond to microstructures observed after a first 5 h PS step at 1250 °C and a second 10 min PBS step at 1200 °C. The EBSD phase map (Figure 5. 16, B) highlighted the broad particle size distributions for all three detected phases. In addition, the morphology of Ti_3AlC_2 grains was more elongated than Ti_2AlC and Al_2O_3 grains. This was also found in the average aspect ratio, yielding 1.69 (± 0.49), 1.96 (± 0.79) and 1.51 (± 0.38) for Ti_2AlC, Ti_3AlC_2 and Al_2O_3, respectively. The aspect ratio of equiaxed Ti_2AlC grains remained constant after the PBS procedure (1.69 ± 0.49) as compared to the as-synthesized powders (1.75 ± 0.52). The 13% increase in average aspect ratio of Ti_3AlC_2 grains indicated their plate-like growth. For Al_2O_3, no changes were observed.
In addition, the process of powder bed sintering was employed to attempt densifying retaining plates (Figure 5. 17), which had a more elaborate geometry and presented thin segments. Even though the relative density of these parts could be significantly increased, the thinner sections yielded, resulting in fragmented parts.

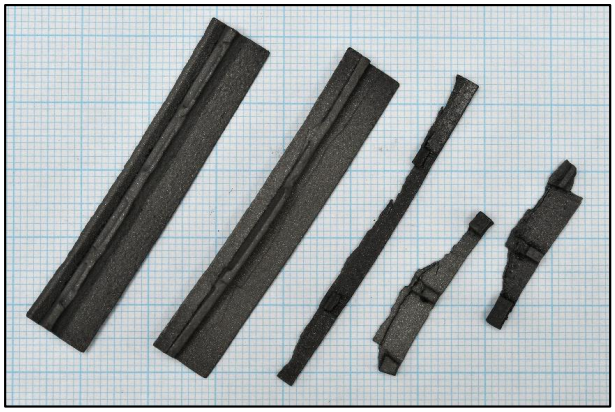

Figure 5. 17: Powder bed sintering outcomes for two Rolls Royce retaining plates, sintered in the FCT-HPD25 FAST/SPS furnace. Thin sections are sensitive to loading rates and easily yield, resulting in fragmented products.

It has to be emphasized that the process has been introduced recently in the institute and solely applied to MAX phases so far. It is obviously subject to optimization but shows promising potential as an alternative to existing expensive densification methods of complex shapes, such as HIP. Future trials would have to focus on the particle size of the refractory pressure-transmitting bed as well as its nature, even though carbonaceous particles – more specifically graphite – were reported as optimal load and heat transfer media [216]. Finer particles could be required to fit the shape of the body to be densified more closely and avoid empty spaces. These might have been responsible for the premature rupture, as the force applied on one side of the component did not encounter a homogeneous counterforce exerted by the coarse graphite particles on the opposite side. However, very fine graphite (APS 7-11 µm, 99%, Alfa Aesar) was found to readily sinter, react and entirely consume parts intended for PBS within short times (10 min at 1200 °C). A bimodal distribution of graphite particles would be interesting to investigate. Additionally, the stepwise increase in pressure and temperature would be a sensible approach to study and document.

Even though the process of FAST/SPS in a graphite powder bed did not enable a homogenous shape retention, high relative densities could be reached (> 98%). For the first time, complex shapes of Ti_2AlC MAX phase could achieve near full densification. Dimensional changes after PBS of Al_2O_3 fiber-reinforced composites – independent of fiber type and volume fraction – were similar to those observed for monolithic counterparts. Unlike the differential shrinkage observed in pressureless conditions, the confinement of samples in a carbon powder bed limited their warpage. The process, though being highly promising, is subject to optimization, especially when thin geometries are used.

V-2.2.2 Fiber orientation and distribution in composites

Fiber orientation and the distribution in fiber-reinforced Ti_2AlC composites sintered by PBS were characterized qualitatively and quantitatively (Figure 5. 18-Figure 5. 22). These showed that, even at the highest fiber-load fraction (20 vol.%), homogeneous composites were obtained. A prevalent challenge in existing studies [63,188,199] has been the dispersion of fibers and whiskers. In this work, no agglomerates were observed, unlike those reported for $Cr_2AlC/Al_2O_{3(f)}$ [199], even at lower fiber-volume fraction or $Ti_2AlC/Al_2O_{3(f)}$ [63] processed via conventional dry mixing routes. The higher shear forces involved during PIM in the viscous molten material allowed for an optimal distribution of fibers in the mold cavity. It is necessary to have the reinforcement phase occupying the entire volume to avoid weak spots in the matrix. However, due to mass flow constriction, the fibers were oriented differently in each section of the injected composite assemblies. The orientation of fibers indicated the streamlines in every considered area. The constriction of the molten feedstock in the thin runner channel, upstream of the mold gate, resulted in a fiber alignment that was parallel to the runner walls. Once the molten mass penetrated the cavity (Figure 5. 18, A, yellow arrows), it essentially flowed straight towards the inner solid core of the first mold insert (1 in Figure 4. 4, C). This is why a thin strip of material, with the fibers aligned parallel to the mold's entering channel, was observed (area (i) in Figure 5. 18, A, Figure 5. 18, B). At the mold's entering (Figure 5. 19, A), the color hue indicated a 90° orientation of the fibers and two side flows with a dominant +45° and -45° (+135°) orientation. The corresponding fiber orientation distribution (FOD) (Figure 5. 20, A) confirmed the ±90° dominant direction, in which fibers were aligned, in addition to a high percentage of fibers in +45° direction. Once the mass reached the central solid cylinder of the mold insert 1, two sideways streams (Figure 5. 18, B and Figure 5. 19, A, B and C) were observed in the vicinity of the oriented strip. As a result of the compression between the downwards entering mass flow and the opposite upwards stream, the FOD were quasi-monomodal (Figure 5. 20, B and C). This indicated that most of the fibers were oriented perpendicular to the entering flow.

In segments parallel to the injection channel (Figure 5. 19, E) and in all four of the other sides of the hexagonal nut (Figure 5. 19, D), the dominant orientations were ±90° and ±45°, respectively (Figure 5. 20, D and E), indicating the good alignment of fibers with the flow. At corners (area (ii) in Figure 5. 18, A, Figure 5. 18, C), fibers were essentially oriented in the *z*-direction, where their quasi-circular cross-section was visible. In the central ring (area (iii) in Figure 5. 18, A, Figure 5. 18, D), the orientation pattern was more random, while in nearby mold walls (area (iv) in Figure 5. 18, A, Figure 5. 18, E and Figure 5. 19, E), the fibers were aligned in the (*x,y*) plane along the edges.

In each section of the nut mold cavity, an analogy to the model of viscous flow between two parallel plates can be established [239,240], with a quasi-parabolic mass flow velocity profile. Due to higher shear stress in the near-wall regions, the flow velocity is lower. In the centerline, the flow velocity reaches a maximum. In addition, velocity gradients are higher at mold walls, and are lower in the center [241]. This explains the random orientation of the fibers in the center and their parallel alignment near the wall, as stronger velocity gradients significantly act on the

rotational motion of fibers. In turn, the hydrodynamic drag force created on fibers aligned alongside walls increased.

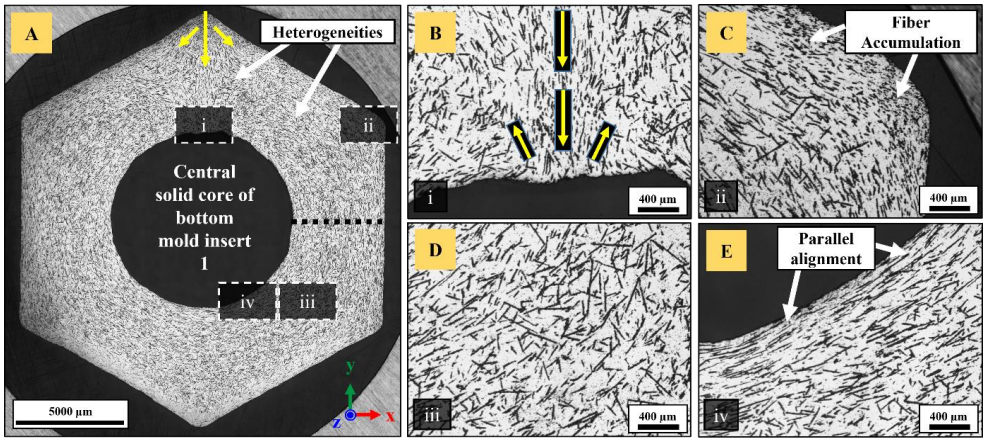

Figure 5. 18: Optical micrographs showing fiber dispersion and orientation in the (x,y) plane in a PBS-1200 nut reinforced with 20 vol.% N720 Al_2O_3 fibers: (A) reconstructed image from ~140 overlapped tiles using the AxioVision MosaiX function, and fiber orientation in the area opposite the mold gate (B), at corners (C), in bulk (D) and along thread (E). The dotted black line in (A) is an indication for Figure 5. 21 and Figure 5. 22.

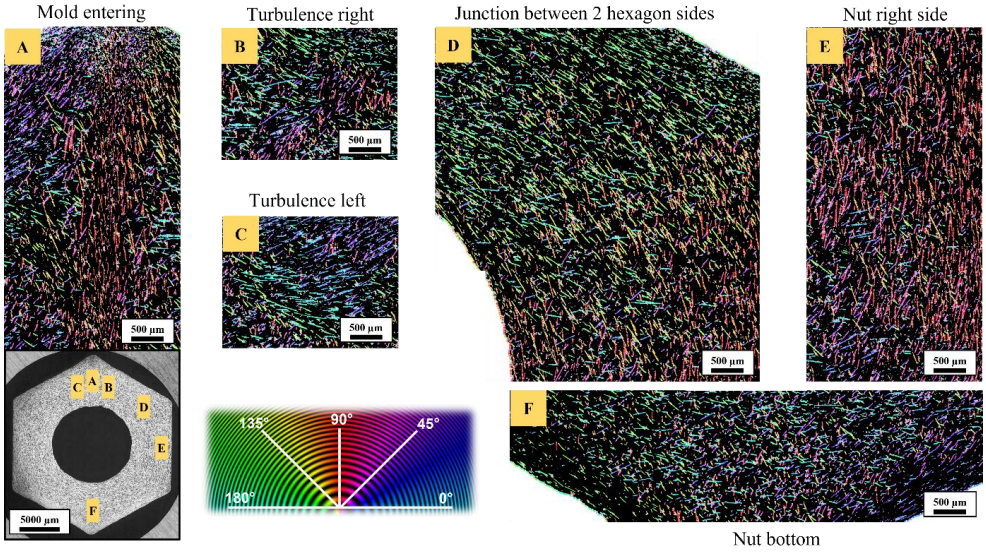

Figure 5. 19: Fiber orientation pattern in a 20 vol.% fiber-reinforced Ti_2AlC hexagon nut.

Further, Marchioli et al. [241] reported fiber deposition and accumulation in near-wall regions. In the present work, such outcomes were noticed at corners of the nut-shaped mold (Figure 5. 18, C). A higher density of fibers was observed in these areas, probably retained by larger frictional forces. Their preferential orientation towards the *z*-axis was deduced from optical micrographs, as their cross-section could mostly be identified. The first fibers reaching the walls may have been pinned at one end and, due to the pressure exerted by the flowing material filling

the cavity, may have been subjected to torque, inducing their rotation and dominant orientation along the orthogonal (*x,z*) plane. The viscous material in the near-wall regions (in direct contact with the colder mold) is known to cool faster due to heat dissipation, and builds up a thin solidified layer – known as "fountain flow" – leaving the mass in a "frozen" state [110].

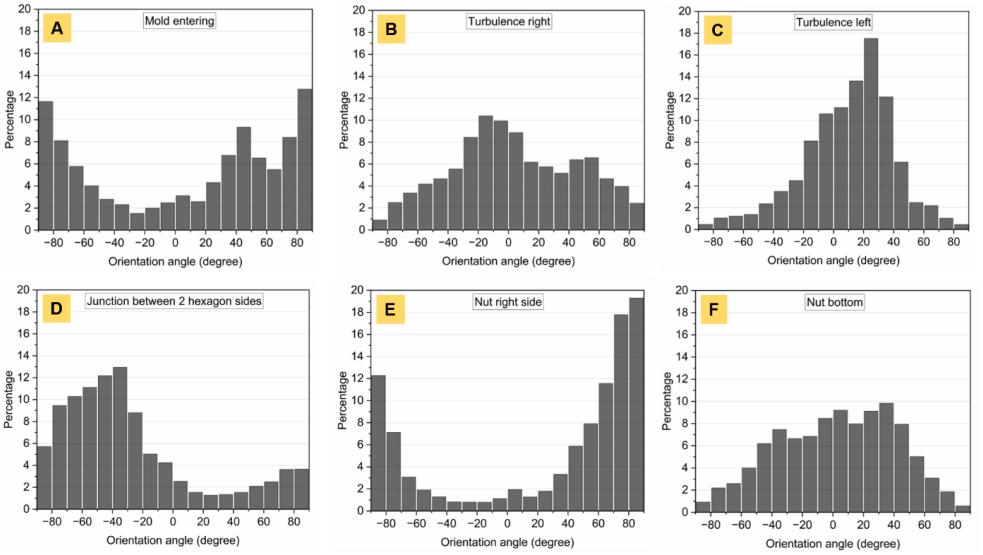

Figure 5. 20: Fiber orientation distribution (FOD) in a 20 vol.% fiber-reinforced Ti_2AlC hexagon nut for corresponding areas in Figure 5. 19.

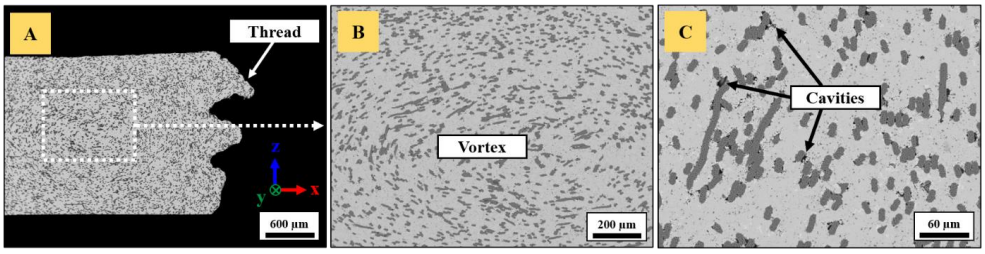

Figure 5. 21: Cross-sectional SEM analysis showing fiber distribution and orientation in the orthogonal (x,z) plane (see dotted black line in Figure 5. 18, A) in a PBS-1200 nut reinforced with 20 vol.% N720 Al_2O_3 fibers: (A) Overview image with thread deformation, (B) vortex in the core and (C) flattened fiber cross-section and cavities.

Heterogeneities in the bottom area of the nut (Figure 5. 19, F) were observed, which resulted from mass flows in both last ±45° sections meeting and causing rotation of fibers. There was no dominant orientation as fibers were equally aligned in different directions and the FOD indicated a broad distribution over a large angle range (Figure 5. 20, F).

Figure 5. 21 shows cross-section SEM micrographs of composite nut parts reinforced with N720 alumina fibers. These were taken at the nut's mid-plane as indicated by the dotted black line in Figure 5. 18, A. Fibers were homogeneously dispersed in the entire mold volume as now shown in the orthogonal (*x,z*) plane (Figure 5. 21, A). The deformation of the thread arising during the PBS step is highlighted too. A magnification in the central area (Figure 5. 21, B) indicated the presence of a vortex-like pattern, probably due to turbulent flow in the core of the nut mold. A few cavities located nearby alumina fibers were identified (Figure 5. 21, C), but

solely in the case of N720 fiber-reinforced composites. These might have been generated during the decomposition of mullite and the formation/accumulation of gaseous species [238] according to Equations 26-28.

$3Al_2O_3{\cdot}2SiO_{2(s)} \rightarrow 3Al_2O_{3(s)} + 2SiO_{(g)} + O_{2(g)}$, (mullite decomposition) (Equation 26)
$2C_{(s)} + O_{2(g)} \rightarrow 2CO_{(g)}$, (oxygen consumption) (Equation 27)
$2C_{(s)} + SiO_{(g)} \rightarrow SiC_{(s)} + CO_{(g)}$, (SiO consumption) (Equation 28)

The slight mismatch in coefficient of thermal expansion (CTE) between Ti_2AlC matrix (8.2 x 10^{-6} K^{-1} for 25 °C≤T≤1300 °C [44]) and N720 fibers (6.0 x 10^{-6} K^{-1} for 100 °C≤T≤1100 °C according to the 3M™ Nextel™ technical reference guide) might have contributed to the formation of cavities as well, but to a lesser extent. In fact, tensile stresses may arise at the interface upon contraction of the matrix, after sintering, during cooling. The better match in CTE between Ti_2AlC and N610 fibers (8.0 x 10^{-6} K^{-1} for 100 °C≤T≤1100 °C according to the *3M™ Nextel™ Ceramic Fibers and Textiles: Technical Reference Guide*) explains why cavities were not generated under the same sintering conditions (Figure 5. 22, A). In addition, N610 fibers exhibited negligible – if none – changes in diameter contrary to their mullite-containing counterparts, for which the prolate flattened cross-section made a software-based analysis of their orientation uneasy.
The analysis of circularity is given in Figure 5. 22 and was performed on N610 and N720-containing composites. The cross-sections were taken at the nut's mid-plane, as indicated by the dotted black line in Figure 5. 18A and highlighted a homogeneous fiber distribution in the entire mold volume. Circularity is calculated as follows:

$$C = 4\pi \frac{A}{P^2} \quad \text{(Equation 29)}$$

with A as the area and P as the perimeter of the fiber's cross-section. The closer to 1, the more circular the analyzed element. N610 Al_2O_3 fibers (Figure 5. 22, A) presented almost no variation in fiber diameter after sintering, as the average circularity determined from 260 fiber cross-sections yielded 0.797 ± 0.091. It also confirmed that fiber axes were orthogonal to the sectional plan, i.e., that fibers were mostly oriented parallel to the flow. The same analysis performed in the composite's core (Figure 5. 22, B) highlighted minima in circularity down to ~0.2, indicating fibers with more elongated shape, as visible on the SEM image. The average circularity decreased to 0.758 ± 0.133. The core might have been subjected to turbulent flow, leading to the formation of vortices. These vortex-like patterns were observed for all fiber-composite types and at various fiber volume fractions. Essentially, they may have acted on the rotational motion of fibers, the latter axes of which were found to be parallel to the cutaway plane. The analysis of circularity for N720 fiber-reinforced composites (Figure 5. 22, C) was challenging due to the higher fiber content. The presence of small clusters and porosity made arduous the discrimination of single fibers and the elimination of artefacts upon image binarization. Nevertheless, the decrease in circularity (0.411 ± 0.118) in areas around the core region was not due to an alignment of fibers perpendicular to the flow. Instead, it indicated the change of shape occurring during creep of mullite-deprived N720 fibers during sintering in argon and their more prolate/flattened cross-section. In general, as circularity is inversely proportional to the square of the analyzed perimeter, the calculated values were slightly underestimated, as image artefacts (alumina grains, cavities in contact with fibers) were partly included in the analysis.
However, these outcomes provided clues for the prediction of shrinkage anisotropy. The consideration of the overall FOD, which was averaged over each individual section of the nut composite assemblies, indicated that the mean dominant direction was favorable to a greater

shrinkage along the injection axis. In fact, only the two sides parallel to the injection axis (±90° on Figure 5. 19) and the strip at the mold entering genuinely appeared as a hindrance to sintering, while all four of the other segments (±45°) were less counteracting densification. An analogous reasoning could be established for the sprocket assemblies.

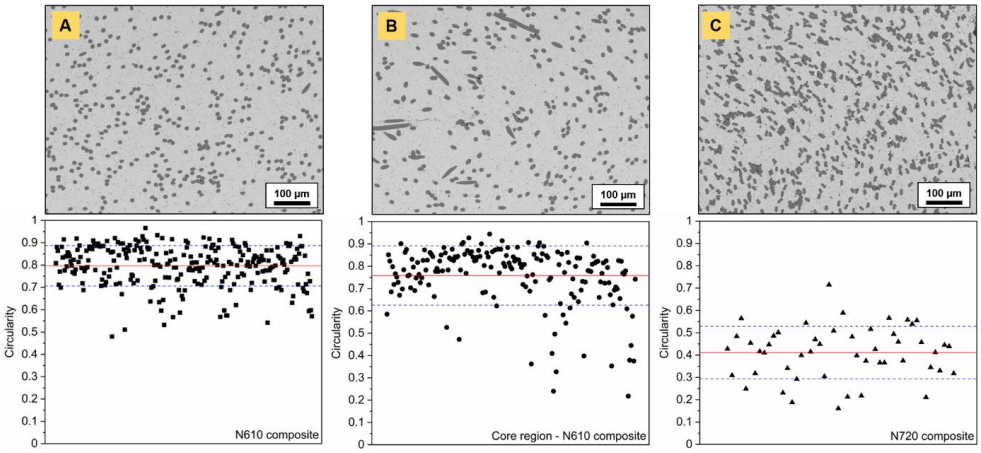

Figure 5. 22: Circularity of fiber cross-sections determined for: A) 10 vol.% N610 fiber-reinforced, B) 10 vol.% N610 fiber-reinforced (core region) and C) 20 vol.% N720 fiber-reinforced Ti_2AlC composites.

To summarize, the feasibility of fabricating monolithic and fiber-reinforced Ti_2AlC components with complex geometries and their subsequent sintering was exposed previously. Powder injection molding was found to be highly effective to evenly distribute the alumina fibers in the MAX phase matrix. While pressureless sintering did not provide the sufficient driving force to densify these parts, FAST/SPS in a bed of graphite powder resulted in near-complete consolidation, even for the samples containing a high volume fraction of fibers.
Afterwards, these components had to be characterized in terms of oxidation resistance and mechanical properties. This will be described further in the present thesis.
The next section deals with the oxidation performance of Ti_2AlC and presents various interesting outcomes depending on previous processing conditions.

Chapter VI: Oxidation response

The oxidation resistance of Ti_2AlC is known from several studies to be excellent up to temperatures around 1300 °C. This is due to the fact that the grown alumina scale is dense and continuous, so it forms a protection against further oxidation. Despite the competition in the formation of Al_2O_3 and TiO_2, the preferential oxidation of aluminum is usually observed. In some specific conditions though, the development of oxide scales does not follow this classical scheme and can result in non-passivating oxidation. The present section brings an insight into various correlations between the oxide scale growth and prior processing steps.

VI-1 Isothermal oxidation

VI-1.1 Surface roughness-dependent oxide morphology

All oxidation studies performed so far in the literature have mentioned about perfectly smooth/polished surfaces prior to oxidation. A single NASA report [157] briefly touched upon the influence of surface roughness on the growth of oxide scales on Ti_2AlC. In industrial applications, roughening of surfaces are often required to apply coatings. Additionally, surface micro or macro-damaging can also lead to localized variations in surface height profiles.
In this work, preliminary isothermal oxidation experiments were carried out in static air at 1200 °C, at a rate of 10 °C/min, to compare the scale morphology obtained for MS^3-synthesized Ti_2AlC and that produced by other routes. 1200 °C was selected based on the range of potential operating temperature of Ti_2AlC [134,137,157,165]. The dwell times were first varied between 24 and 50 h at the beginning, while these were extended later to more than 1000 h for long-term studies. The effect of surface quality was studied, by means of three degrees of finishing, to wit, polished (OPS), ground (P80) and sandblasted (SB) samples. Aim was to establish – if at all existing – a correlation between the surface roughness prior to oxidation and the build-up of oxides.
The different surface roughness values are listed in Table 6. 1. TAC refers here to Ti_2AlC. It is obvious that surfaces of TAC-SB samples were the roughest (highest R_a value) due to the harsh abrading conditions. Other parameters such as the mean and maximum roughness depth (R_z and R_{max} respectively) provided additional information.

Table 6. 1: Surface roughness of polished, ground and sandblasted Ti_2AlC before oxidation. Values for polished and ground samples are indicated with a cut-off wavelength λ_c = 250 µm and for sandblasted samples with a cut-off wavelength λ_c =800 µm. R_a = arithmetical mean roughness, R_q = root mean squared roughness, R_z = mean roughness depth, R_{max} = maximum roughness depth.

Samples	R_a (µm)	R_q (µm)	R_z (µm)	R_{max} (µm)
Polished (OPS)	0.09 ± 0.01	0.12 ± 0.01	0.77 ± 0.08	0.96 ± 0.15
Ground (P80)	1.18 ± 0.14	1.46 ± 0.18	6.23 ± 0.74	8.33 ± 1.96
Sandblasted (F36)	3.26 ± 0.40	4.05 ± 0.50	19.42 ± 4.37	24.77 ± 19.34

Table 6. 1 shows that SB samples exhibited deep troughs (up to R_{max} = 24.77 µm ± 19.34 µm and R_z = 19.42 µm ± 4.37 µm in average). These are due to strong impacts of F36 Al_2O_3 particles, projected at 4 bar on the surface of Ti_2AlC. TAC-P80 had different R-values, almost

three times lower than TAC-SB. Depressions of less than R_{max} = 1 µm were achieved by polishing Ti_2AlC, the R_a value being close to 100 nm.
When Ti_2AlC is oxidized at 1200 °C, the coexisting and stable oxides are α-Al_2O_3 and rutile-TiO_2. The first cross-section and EDS analysis of a polished sample confirmed this, as depicted on Figure 6. 1. From the substrate/oxide to the oxide/air interfaces, it revealed a continuous Al_2O_3 scale of constant thickness (the dark phase on the backscattered electron (BSE) scanning electron microscopy (SEM) image and Figure 6. 1B), followed by discontinuous clusters of TiO_2 grains (Figure 6. 1A). In the MAX phase base material, the Al-richer Ti_2AlC (Figure 6. 1C), as well as Ti_3AlC_2 (Figure 6. 1D) and small Al_2O_3 grains were detected.

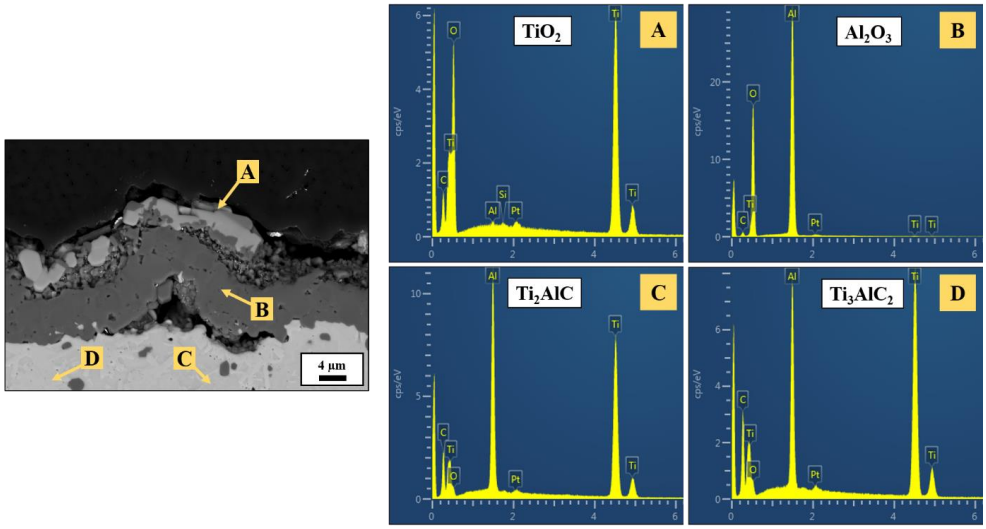

Figure 6. 1: EDS analysis of oxide scales present on Ti_2AlC, here on a TAC-OPS cross-section.

Detailed cross-sectional analyses (Figure 6. 2) further revealed the thickness of the Al_2O_3 scale and the size of the TiO_2 islands. For the three samples, the Al_2O_3 scale was ~8 µm thick, highlighting similar Al-oxidation rates. These results are consistent with reported oxidation outcomes of fine-grained Ti_2AlC [143]. Improved short-term oxidation resistance is indeed expected in such cases due to the fast build-up of the Al_2O_3 scale. In fact, fine-grained microstructures provide multiple pathways through grain boundaries for Al out diffusion, leading to the rapid formation of a thin protective Al_2O_3 layer. Thin TiO_2 islands/nodules were found atop the Al_2O_3 scale of TAC-OPS (Figure 6. 2, A and D) samples. The smooth surface of polished samples (see Table 6. 1) allowed for a smooth Al_2O_3 scale growth (Figure 6. 2, A and D), with few localized spots where delamination occurred. This Al_2O_3 scale appearance is what is most observed in literature, for mirror polished samples [134,137,165]. A more porous and irregular thin Al_2O_3/TiO_2 layer was observed above the dense protective Al_2O_3 scale. The former layer might be the one observed in Figure 6. 3A, there appearing as small protuberances. Secondary electron (SE) images, taken from the top, showed different oxide morphologies for the three samples after oxidation (Figure 6. 3). The oxide morphology on TAC-OPS samples (Figure 6. 3, A) was globular with interconnected fine-grained blisters. They were ~10-20 µm in size. In between, larger faceted grains were evidenced.
The Ti_2AlC/Al_2O_3 interface of TAC-P80 showed a more pronounced formation of pores and cracks (Figure 6. 2, B and E). On cross-sections, the TiO_2 nodules were of similar size as those observed on TAC-OPS (Figure 6. 2, B and E). On top views, TAC-P80 (Figure 6. 3, B)

exhibited unidirectional grooves, in which preferred growth of the large faceted TiO_2 grains was observed. Their size slightly exceeded 10 µm in length for the larger ones.

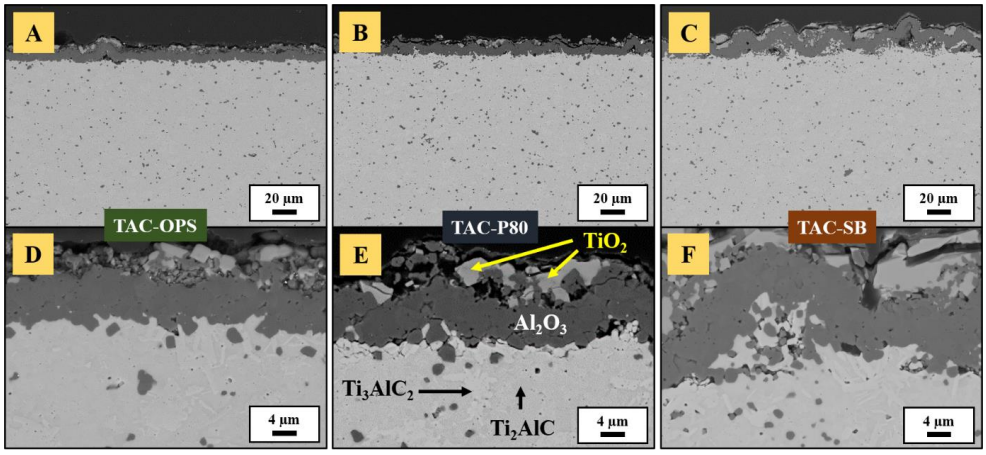

Figure 6. 2: Cross-sectional BSE images of oxidized Ti_2AlC samples with different surface finish: (A and D) polished to 50 nm colloidal silica, (B and E) ground with P80 abrasive SiC paper, (C and F) sandblasted with F36 alumina particles. Oxidation conditions were 1200 °C, 50 h in static air.

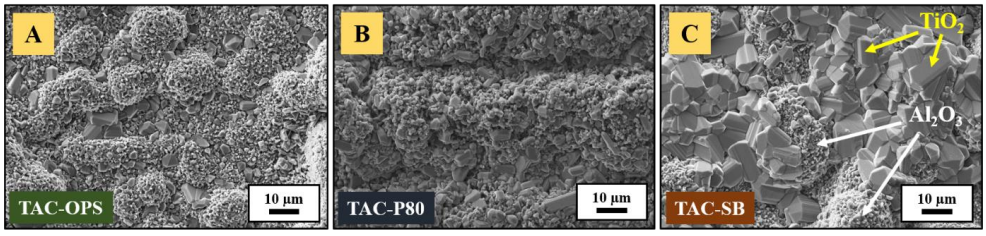

Figure 6. 3: SE images of oxidized Ti_2AlC samples with different surface finish: (A) polished to 50 nm colloidal silica, (B) ground with P80 abrasive SiC paper, (C) sandblasted with F36 alumina particles. Oxidation conditions were 1200 °C, 50 h in static air.

TAC-SB showed a strong undulated profile already before oxidation due to surface preparation (Figure 6. 4A and Table 6. 1). The impact of hard F36 Al_2O_3 particles created a cratered surface profile. SEM analyses of the SB surface before oxidation showed that the Al_2O_3 content was non-negligible. In fact, top views (Figure 6. 4B) and cross-sections (Figure 6. 4C) in BSE mode evidenced embedding of hard Al_2O_3 particles in the surface of Ti_2AlC after surface preparation. Subsurface cracks also appeared after this procedure (Figure 6. 4D).

After oxidation, strong rippling/rumpling/ratcheting of the oxide scale was observed on cross-sections (Figure 6. 2, C and F) of TAC-SB. This phenomenon is defined and described further. Above the Al_2O_3 scale, the sections between ripples were filled with large rutile grains as. On top views, SB specimen (Figure 6. 3, C) exhibited similar blister-like structures as for polished samples. They were additionally covered with a substantial fraction of large crystals (~10-20 µm) organized in islands.

BSE images (Figure 6. 5) from the top view visually confirmed the distribution of α-Al_2O_3 and rutile TiO_2. Rutile's typical elongated prismatic crystal habit with striation along the *c*-axis [242] was noticed on TAC-SB (Figure 6. 3, C) because grains were large enough. TAC-OPS showed small rutile grains (~3-5 µm), scattered across the fine-grained blistered surface of

Al_2O_3, and TiO_2 islands of less than 20 µm (Figure 6. 5, A). The higher content in MAX phases as compared to TAC-P80 and TAC-SB is on account of less TiO_2 in the analyzed volume. TAC-P80 (Figure 6. 5, B) exhibited a significant increase in TiO_2 content and larger light grey patches were observed on BSE images. The TiO_2 grain size ranged from submicron to ~15 µm in length, while fine grains of Al_2O_3 composed the remainder of the oxide layer.

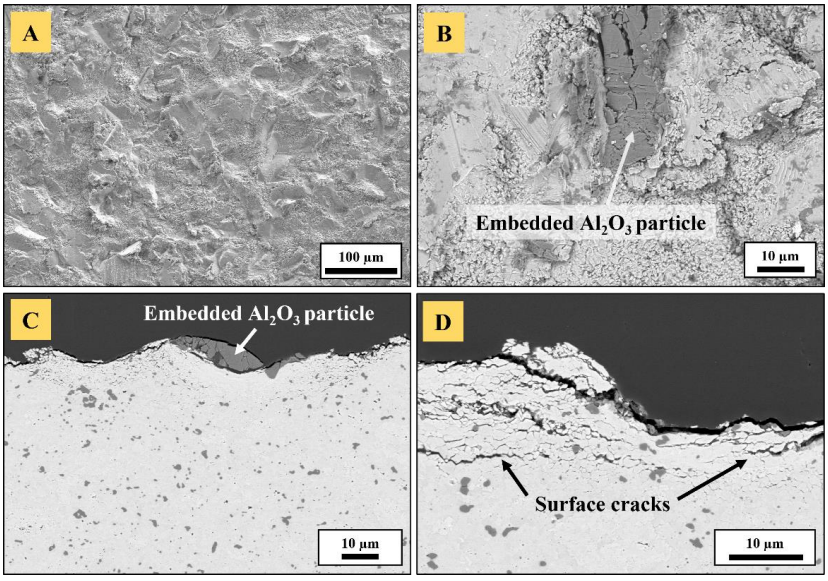

Figure 6. 4: Ti_2AlC after F36 Al_2O_3 sandblasting: (A) SE image showing the cratered surface profile, (B) and (C) BSE images highlighting the surface-embedded Al_2O_3 particles and (D) BSE image evidencing cracks in the surface.

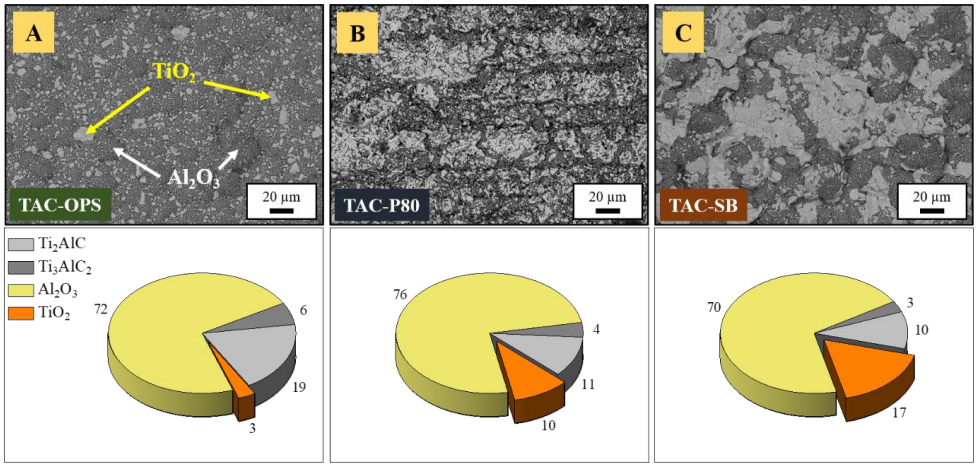

Figure 6. 5: BSE images of oxidized Ti_2AlC samples with different surface finish: (A) polished to 50 nm colloidal silica, (B) ground with P80 abrasive SiC paper, (C) sandblasted with F36 alumina particles. Oxidation conditions were 1200 °C, 50 h in static air. Corresponding pie charts show results from Rietveld refinement (in wt. %).

These results are in agreement with reported features [123,125,127,133,134,137,165]. TAC-SB showed a strong increase in TiO_2 content (Figure 6. 5, C). In fact, large colonies of TiO_2 crystals, reaching several hundreds of micrometers in size, were observed with BSE images, almost covering the whole surface of the sample.
A model was proposed [134] in which rutile TiO_2 grains preferentially grow over depressions initially existing in the base material. The higher roughness is supposed to be the reason of excessive TiO_2 expansion and ensuing grain coarsening.

VI-1.2 Oxide scale rumpling

Rumpling is a phenomenon of undulations that develop in the thermally grown oxide layer. In alumina-forming materials, it is caused by in-plane lateral growth of this oxide and the resulting induced compressive strain [243].
Rumpling was observed for MAX phases already, in the case of thermal cycling of SB Cr_2AlC substrates coated with an yttria stabilized zirconia thermal barrier coating [169]. A recent study by Go et al. [199] also mentioned about this phenomenon for bare Cr_2AlC substrates exposed to burner rig conditions. Despite uncertainties as for the cause(s) of rumpling, it was alluded to fast thermal shock conditions, leading to substantial strain during oxide scale growth and thickening. However, in the present case, Ti_2AlC was isothermally oxidized within shorter times (50 h) as compared to thermal cycling experiments (several hundreds, even thousands of hours) and not under cyclic conditions. In fact, rumpling usually appears under harsher conditions, e.g., when the material is tested in a burner rig facility, where heating and cooling rates can easily reach 1600-1900 °C/min [170]. A common feature though, is the surface roughening procedure employed before oxidation, which in both cases led to initial undulations on the surface of the MAX phase base material and, in all likelihood, to the build-up of internal stresses in the near surface area. The amplitude of these undulations prior to oxidation has a determining role in promoting ratcheting and its critical value, above which rumpling is triggered, tends to decrease with the substrate yield strength [244]. The higher the amplitude, the higher the stresses which initiate rumpling. Additionally, the build-up of in-plane stresses in the Al_2O_3 scale due to lateral growth strain were found by He et al. [244] to arise in the first oxidation cycle and did not substantially change with further cycling. In the present work, this would contribute to explain why ratcheting was observed in the case of isothermal oxidation (one-cycle) of Ti_2AlC. In addition, undulation in the oxide scale potentially gave rise to a normal stress component at the Al_2O_3/Ti_2AlC interface, consequently deforming the first layers of the Ti_2AlC base material [243], which is known to plastically deform at 1200 °C [67]. In fact, the equivalent stresses induced in the substrate by the in-plane stresses in the oxide scale were determined to be the largest right underneath recessions in the Al_2O_3 scale [244]. Upon cooling, when the compressive stresses exceed the yield strength of the substrate, the latter plastically deforms allowing the oxide scale to move downwards.
The Al_2O_3 scale is believed to accommodate increasing in-plane compressive stresses by stretching [243], a phenomenon of release of elastic energy. Thus, the increase in the overall length of the Al_2O_3 scale caused localized buckling and folds, which irremediably led to decohesion between Al_2O_3 and Ti_2AlC as a result of substantial tensile stresses (Figure 6. 2, C and F). Unlike platinum-modified nickel aluminide (PtNiAl) bond coats, for which thermal expansion misfit between thermally grown oxide (TGO) and alloy is well known [243,245], the mismatch in CTE between Ti_2AlC (8.2×10^{-6}/K between 25 °C and 1300 °C) [44], Al_2O_3 (8.0×10^{-6}/K and 9.0×10^{-6}/K in the 25 °C-1000 °C and 25 °C-1500 °C ranges respectively) [45] and TiO_2 (8-9 $\times 10^{-6}$/K in the 25 °C-1000 °C range) [45] is reduced, hence a decrease of the misfit stresses in the Al_2O_3 scale. In addition, for rumpling in EB-PVD TBC systems, typically, the mismatch between substrate and bond coat also plays a significant role. As no bond coat is used here, the given explanations can only be partly applicable. Even though several studies

performed on PtNiAl bond coats exist [243,245], straightforward conclusions about the origin of rumpling and a generalization to other materials (e.g. MAX phases) are still missing.
In the present work, we propose a simplified model to introduce the phenomenon of rumpling observed in the case of isothermal oxidation of Ti_2AlC and to highlight a potential correlation with surface roughness prior to oxidation. Growth stresses emerging in the TGO will induce radial stresses at a wavy interface between Ti_2AlC and TGO. TGO growth stresses are assumed to be 1000 MPa in the present model, according to values found in literature, while stress relaxation in the TGO is overlooked. The presented model aims to estimate deformation and rumpling of the TGO as a consequence of these stresses. Therefore, the creep deformation of the Ti_2AlC first upper layers as a function of the initial substrate's surface roughness prior to oxidation is calculated. The stress approximation model is based on the stresses in a homogeneous hollow sphere, made of an elastic perfectly plastic material, subjected to an internal pressure *P*. The internal and external radii are denoted *a* and *b* respectively (Figure 6. 6, A). In the system of spherical coordinates (r, θ, φ), the solution in terms of stress (Figure 6. 6, B) for a pure elastic response are as follows:

$$\sigma_r = \frac{E}{1-2\nu} \cdot C_1 - \frac{2E}{1+\nu} \cdot C_2 \cdot r^{-3} = -\frac{a^3}{b^3-a^3} \cdot \left(\frac{b^3}{r^3} - 1\right) \cdot p \qquad \text{(Equation 30)}$$

$$\sigma_\theta = \sigma_\varphi = \frac{E}{1-2\nu} \cdot C_1 + \frac{E}{1+\nu} \cdot C_2 \cdot r^{-3} = \frac{a^3}{b^3-a^3} \cdot \left(\frac{b^3}{2r^3} + 1\right) \cdot p \qquad \text{(Equation 31)}$$

$$\sigma_\varphi(a) = \frac{a^3}{b^3-a^3} \cdot \left(\frac{b^3}{2a^3} + 1\right) \cdot p = \frac{b^3}{2(b^3-a^3)} \cdot p + \frac{a^3}{b^3-a^3} \cdot p = \frac{\frac{b^3}{2}+a^3}{(b^3-a^3)} \cdot p \qquad \text{(Equation 32)}$$

$$\sigma_\varphi(b) = \frac{a^3}{b^3-a^3} \cdot \left(\frac{1}{2} + 1\right) \cdot p = \frac{3}{2}\frac{a^3}{(b^3-a^3)} \cdot p \qquad \text{(Equation 33)}$$

$$\text{At } r = a,\ \sigma_r = p = \frac{(b^3-a^3)}{\frac{b^3}{2}+a^3}\sigma_\varphi \qquad \text{(Equation 34)}$$

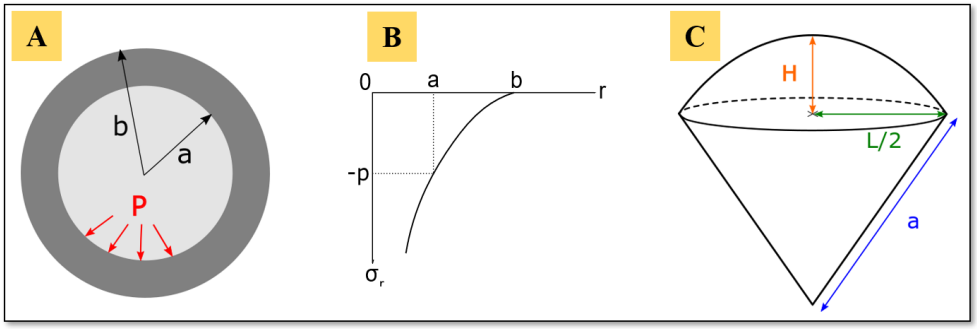

Figure 6. 6: Stress approximation model based on stresses in a hollow sphere: (A) homogeneous hollow sphere subjected to internal pressure P, (B) solution in terms of radial stress versus radius of the sphere, (C) section of the sphere considered for the present model.

A section of the base material (Ti_2AlC) is considered by taking part of the sphere (Figure 6. 6, C), so that one ends up with a cone of slant length *a* attached to a spherical cap of height *H* and base radius *L/2*. In the 2D plane, following relations are verified:

$$a^2 = \frac{L^2}{4} + (a - H)^2 \quad \text{(Equation 35)}$$

$$\rightarrow 0 = \frac{L^2}{4} - 2aH + H^2 \; ; \; a = \frac{H}{2} + \frac{L^2}{8H} \quad \text{(Equation 36)}$$

From Equation 35,

$$\rightarrow a - H = \pm\sqrt{a^2 - \frac{L^2}{4}} \quad \text{(Equation 37)}$$

$$\rightarrow H = a \pm \sqrt{a^2 - \frac{L^2}{4}} \quad \text{(Equation 38)}$$

In this case, only the minus sign gives a meaningful condition. The surface roughness of the material can be approximated by a series of these 3D geometric shapes, the amplitude of surface peaks being directly linked to *H*. The volume of interest is the volume *V* of the spherical dome, which is expressed as follows:

$$V = \frac{\pi}{3}H^2(3a - H) = \pi a H^2 - \frac{\pi}{3}H^3 \quad \text{(Equation 39)}$$

The time derivative of the volume *V* is equivalent to the time derivative of deformation ε, which is the creep rate. The creep rate is expressed as follows:

$$\frac{\dot{V}}{V} = \dot{\varepsilon} = \dot{\varepsilon_0}\sigma^n \exp\left(-\frac{U}{RT}\right) \quad \text{(Equation 40)}$$

The creep data was retrieved from Barsoum et al. [191], i.e., an activation energy *U* of 362 kJ/mol, a stress exponent *n* of 2.5, a minimum creep rate of 1.86 x 10^{-7} s^{-1} (at 20 MPa, 1000 °C). The constant $\dot{\varepsilon_0}$ was calculated using this data and Equation 40, yielding a value of 1.07 x 10^{-10} s^{-1}. MPa^{-n}. The TGO thickness is given by:

$$d(t_n) = b(t_n) - a(t_n) = k_{ox} \cdot \sqrt{t_n} \quad \text{(Equation 41)}$$

where t_n is the time at increment *n* and k_{ox} is the oxidation constant.
During isothermal oxidation at 1200 °C, rumpling corresponds to an increase of dome height *H*, respectively, a decrease of cone slant length *a*. The determination of the time derivative of *a* is the next step. According to Equation 38, using the minus sign:

$$\frac{dH}{dt} = \frac{da}{dt} - \frac{2a\frac{da}{dt}}{2\sqrt{a^2 - \frac{L^2}{4}}} = \left(1 - \frac{a}{\sqrt{a^2 - \frac{L^2}{4}}}\right)\frac{da}{dt} = B(a)\frac{da}{dt} \quad \text{(Equation 42)}$$

$$\frac{dV}{dt} = 2H\frac{\pi}{3}\frac{dH}{dt}(3a - H) + \frac{\pi}{3}H^2\left(3\frac{da}{dt} - \frac{dH}{dt}\right) \quad \text{(Equation 43)}$$

$$\frac{dV}{dt} = \left\{\frac{2\pi}{3}(3aH - H^2)B(a) + \pi H^2 - \frac{\pi}{3}H^2B(a)\right\}\frac{da}{dt} \quad \text{(Equation 44)}$$

Using Equations 34, 40 and 41:

$$\frac{da}{dt} = \dot{\varepsilon}_0 \exp\left(-\frac{U}{RT}\right) \cdot \sigma^n \left(\frac{(a+d(t))^3 - a^3}{a^3 + \frac{(a+d(t))^3}{2}}\right)^n \cdot \left\{\frac{2\pi}{3}(3aH - H^2)B(a) + \pi H^2 - \frac{\pi}{3}H^2 B(a)\right\}^{-1} \cdot V \quad \text{(Equation 45)}$$

$$\frac{da}{dt} = \dot{\varepsilon}_0 \exp\left(-\frac{U}{RT}\right) \cdot \sigma^n \left(\frac{(a+d(t))^3 - a^3}{a^3 + \frac{(a+d(t))^3}{2}}\right)^n \cdot \{(2\pi aH - \pi H^2)B(a) + \pi H^2\}^{-1} \cdot V \quad \text{(Equation 46)}$$

The evolution of a with time increments is calculated by a linear approximation:

$$a(t_{n+1}) = a(t_n) + \frac{da(t_n)}{dt} \cdot (t_{n+1} - t_n) \quad \text{(Equation 47)}$$

The evolution of H is then calculated using Equation 38 and with the values of $\frac{da}{dt}$ using Equation 46.

As rumpling appeared to be triggered by increasing surface roughness, the case of sandblasted samples is considered using the model above. H is retrieved from roughness measurements (see Table 6. 1) and L can be estimated by considering SEM cross-sections of Ti_2AlC right after surface preparation and before oxidation: $H = 3.26$ µm and $L = 100$ µm. According to Equation 36, a is then 13 µm. The TGO thickness is approximately 8 µm after 50 h at 1200 °C (Figure 6. 2, F).

The extent to which rumpling occurs is then given by the following relation:

$$X = \frac{H(t_{50}) - H(t_0)}{H(t_0)} \cdot 100\% \quad \text{(Equation 48)}$$

with t_0 and t_{50} being the start and the end of the isothermal (T = 1200 °C) plateau, respectively. By plotting the degree of rumpling versus Ti_2AlC surface roughness prior to oxidation (Figure 6. 7, A), a steep increase is observed. Smooth surfaces ($R_a < 1$ µm) experience indeed almost no rumpling (max. 0.49%) – the buildup of oxides being smooth Figure 6. 7B – while rumpling can exceed 600% for surfaces presenting an initial roughness higher than 6.45 µm – i.e., with initial waviness Figure 6. 7C.

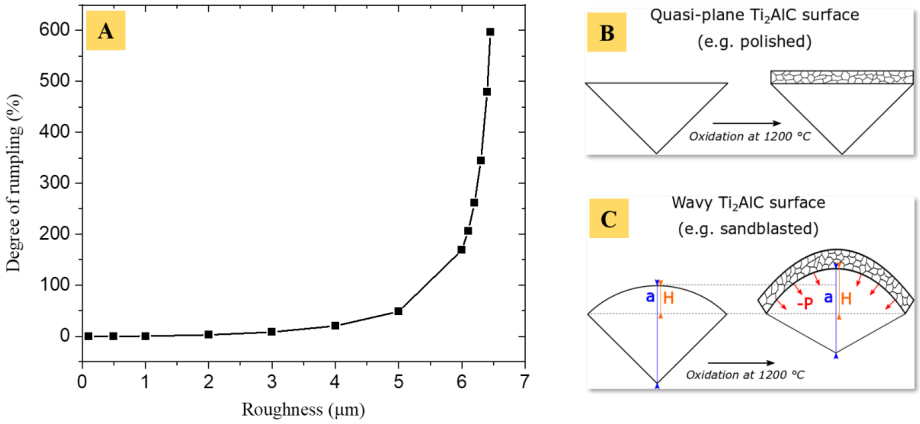

Figure 6. 7: TGO Rumpling during isothermal oxidation of Ti_2AlC: (A) Evolution of TGO rumpling with increasing Ti_2AlC surface roughness prior to oxidation, (B) quasi-plane surfaces (typically polished or gently ground) do not experience rumpling while (C) rough surfaces (typically sandblasted) show significant rumpling.

As sandblasted surfaces exhibit higher R values than polished and ground surfaces (Table 6. 1), rumpling is essentially observed in these conditions (Table 6. 2). The limit to which the system accommodates the deformation is dictated by the interfacial adhesion between TGO and Ti_2AlC and localized decohesion occurs at spots where stress concentration reaches a maximum.
This model shows that rough surfaces (typically achieved with sandblasting) present higher propensity to rumpling. As mentioned earlier, the phenomenon of rumpling is believed to be caused synergistically by different mechanisms and needs further investigation for Ti_2AlC and in general, for MAX phases used in oxidizing environments. The present model thus paves the way for more exhaustive considerations in order to potentially prevent rumpling in systems subjected to similar conditions.

Table 6. 2: Surface roughness-rumpling correlation.

Surface finish	Average mean roughness (R_a, µm)	Maximal roughness depth (R_{max}, µm)	Modeled degree of rumpling (%) for R_a	Modeled degree of rumpling (%) for R_{max}
Polishing	0.1	1	0.1	0.7
Coarse grinding	1.2	> 8	1	> 600
Sandblasting	3.3	> 20	12	> 600

Studies on Ti_3AlC_2 mentioned about the preferential formation of TiO_2 in porous areas [246,247] because of the nature of Al_2O_3 crystal growth. In fact, it was found that low packing of Al_2O_3 crystals in larger cavities facilitate the outward grain boundary diffusion of Ti ions leading to the formation of TiO_2 atop Al_2O_3. Here, similar features may account for the excessive formation of TiO_2 on TAC-SB. More TiO_2 was found above the Al_2O_3 layer as it appears that more from the Ti_2AlC base material was oxidized. At the base material/oxide scale interface, no Ti-rich layer was observed, contrary to what has been reported in literature [143].

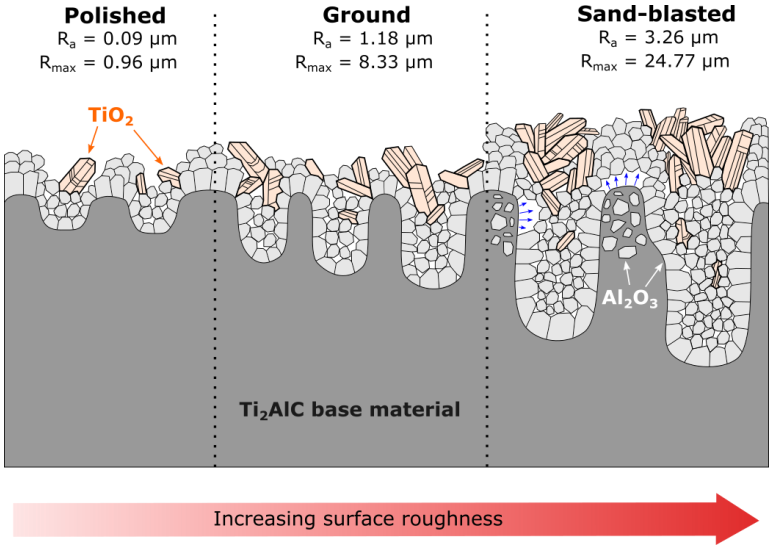

Figure 6. 8: Schematic of surface roughness/oxidation response relationship for Ti_2AlC. Blue arrows indicate decohesion of the Al_2O_3 scale.

Instead, the presence of Ti_3AlC_2 clusters was noticed, the same way these clusters were present in the bulk. However, they were always present in the vicinity of TiO_2 colonies.
The oxidation outcomes in the present work can complement the model proposed by Yang et al. [134], which only considered localized cavities in case of a mirror polished surface. Their theory can be corroborated by taking into account several recesses in the base material and, herewith, a schematic is proposed (Figure 6. 8). With cavities less than 2 µm in size, they found that the thickness of rutile was almost zero. No large TiO_2 colonies were indeed observed in the present work for polished surfaces with a roughness below 1 µm. Some rutile grains were disseminated over the Al_2O_3 scale, without forming a consistent layer. Valleys are filled with Al_2O_3 first since Al atom self-diffusion along (0001) basal planes in Ti_2AlC requires low activation energy [114]. Al is not entirely depleted in the surface's vicinity. Al_2O_3 within cavities are found to be present in small equiaxed grains on account of curved surfaces and subsequent multiple nucleation on existing grains [134]. When larger depressions are present, additional Al diffuses out, gradually leading to exhaustion of the A-element content in near-surface areas. For cavity sizes ranging from 2 to 6 µm, Yang et al. [134] observed ~3-5 µm thick rutile crystals. In the present work, an increase in rutile content was also observed for ground surfaces with similar roughness (see R_z in Table 6. 1), with preferential growth within recesses (grooves in the non-oxidized state).
The depletion in Al is even more pronounced with increasing surface roughness because its diffusion from peaks towards valleys is multidirectional. The same occurred with Ti, hence more TiO_2 was found filling valleys above Al_2O_3 in TAC-SB. Diffusion pathways for Ti across the equiaxed microstructure are numerous and eased due to loose packing of Al_2O_3 crystals. For cavities larger than 6 µm, the thickness of TiO_2 almost doubled [134]. Additionally, the growth rate of TiO_2 is much higher than that of Al_2O_3 [134]. Therefore, a great number of large rutile grains were observed in SB samples in the present work. Some of them formed up to ~10 µm thick layers within valleys of ripples above the Al_2O_3 scale.
A trend was observed in which increasing roughness leads to the formation of larger amounts of TiO_2 above the protective Al_2O_3 scale. The thickness of the latter is invariant with increasing roughness, though, due to large undulations on the substrate's surface before oxidation, the total length of Al_2O_3 after oxidation of sandblasted samples was the largest, hence more Al was depleted in that case. Above a critical amplitude of undulations present before oxidation, the oxide scale started to rumple, followed by localized failure of the Ti_2AlC/Al_2O_3 interface.

VI-2 Breakaway oxidation

The good oxidation resistance of MAX phases up to temperatures around 1200 °C can be compromised for long exposure due to the disruption of the protective alumina layer. This section unveils a mechanism of breakaway oxidation of the Ti_2AlC MAX phase, identifying the main trigger and the solutions to avoid it. It is caused by excessive rumpling of the oxide scale on surfaces with arithmetical mean roughness (R_a) > 3 µm and constitutes a key factor in subsequent consumption of Ti_2AlC. While the previous section described the initial stages of rumpling, the following part describes more accurate mechanisms and is organized in three steps: the evolution of rumpling, the scale blistering and the breakaway oxidation.

VI-2.1 Evolution of rumpling

The previous section showed the determinant role of the surface topography prior to isothermal oxidation and the post-oxidation oxide morphology. The two major observations were: i) the amount and size of TiO_2 crystals above the thermally grown alumina scale increase with the Ti_2AlC surface roughness, and ii) the alumina scale is subject to rumpling as its growth

creates large radial stresses at the interface between Ti_2AlC and thermally grown oxides (TGO), and becomes significantly folded for intensively sandblasted Ti_2AlC surfaces, i.e., when the surface has an initial wavy profile. Flat Ti_2AlC surfaces (Figure 6. 9, A) presented few infrequent spots of decohesion of the thermally grown alumina layer, but the adhesion was notable and the overall build-up of the scale followed the smooth surface topography of Ti_2AlC. Rough surface finishing led to substantial buckling of the alumina scale, revealing cavities 5 to 6 times the size of the scale thickness as shown on Figure 6. 9B. As discussed previously, the theoretical degree of rumpling could be estimated versus surface roughness. It has been found that the percent increase of roughness after oxidation at 1200 °C, related to its initial value prior to oxidation, yielded an impressive 600% for initial roughness values above 6.5 µm (Table 6. 2). These were reached for abrasive grit blasted surfaces, of which the arithmetic mean roughness (R_a) and maximal roughness depth (R_{max}) were ~3.3 µm and > 20 µm, respectively. However, in surface metrology, solely considering R_a is biased and amounts to ignoring extrema (deeper valleys and higher peaks). In fact, even though Al_2O_3 scale rumpling was significant for sandblasted samples, it could also be noticed – to a lesser extent – for coarsely ground surfaces (Figure 6. 2, B and E). Consequently, additional R-values are provided, showing that the modeled degree of rumpling is strongly dependent on which value is considered.
Excessive rumpling of the thermally grown oxide scale is believed to engender blisters on areas where the stress concentration is high, as a continuity of the scale buckling mechanism.

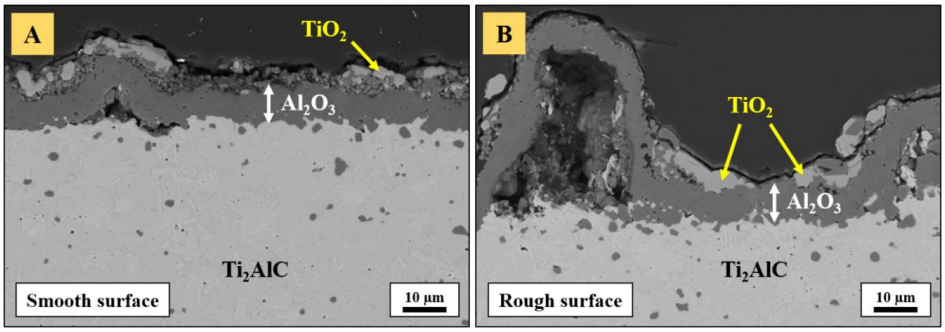

Figure 6. 9: Thermally grown oxides on Ti_2AlC after 50 h at 1200 °C in static air: (A) normal growth for smooth and (B) rumpling for rough surfaces.

VI-2.2 Oxide scale blistering

Ti_2AlC samples with rough surfaces exhibited localized blistering of the protective oxide scale at 1200 °C in static air, occurring within short times. After only 24 h of oxidation, several blisters were visible to the naked eye (Figure 6. 10, A). The largest blisters were mostly formed on sharp edges, although some were also identified on the top flat surface. SEM showed that blisters can reach a considerable size (~0.7 mm) on ground surfaces (FEPA P800 grade SiC paper) after only one day of isothermal oxidation at 1200 °C (Figure 6. 10, B). The largest blisters exhibited high contact angles and presented a circular morphology. The top surface of the oxidized Ti_2AlC was scattered with a multitude of smaller blisters (0.05-0.1 mm) as well. A clear contrast in the grey scale between blisters and their surrounding area was observed. The surface of blisters is composed of alumina (Figure 6. 10, C) containing individual and homogeneously dispersed islands of rutile (TiO_2) crystals, of which the largest reached 10-20 µm, while the area around blisters was evenly covered with a layer of rutile TiO_2 (Figure 6. 10, D). The surface analysis of blisters and their surrounding area helped to estimate the starting point of the phenomenon, which seemed to take place in the first stages of the oxidation

timeline. In fact, the presence of a discontinuous layer of rutile TiO_2 on the blisters' surface suggests that the oxide scale separated from Ti_2AlC soon enough to prevent the further diffusion of Ti from the bulk material. The unblistered surrounding area presented the classical patches of TiO_2 islands generally observed atop the Al_2O_3 scale. Surprisingly, rumpling was barely observed on coarsely ground Ti_2AlC surfaces (with FEPA P80 SiC paper), for which an average mean roughness (R_a) of approximately 1.2 µm was measured (Table 6. 1 and Table 6. 2).
In the present work, a gentler grinding was used (FEPA P800 SiC paper), necessarily leading to lower average surface roughness (comprised between 0.1 and 1.2 µm) yet blistering could be observed. As mentioned above, maximal roughness depth and other R-values must be considered. Large bulges/throughs can act as "rumpling-initiating" spots, progressing towards the blistering stage.

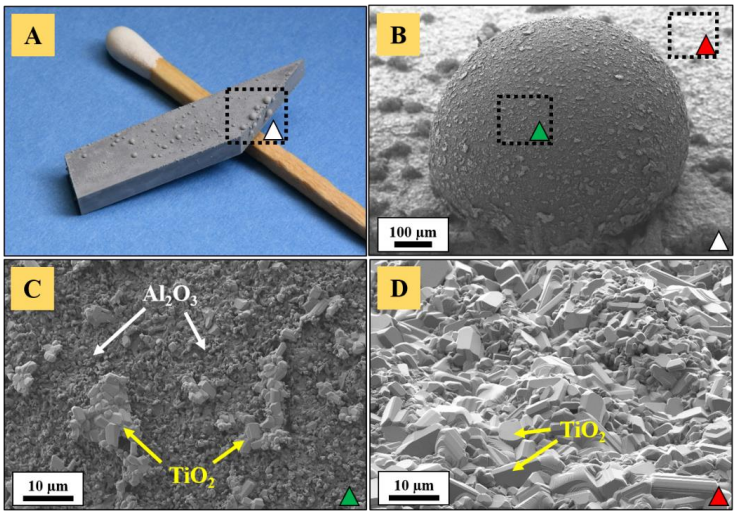

Figure 6. 10: Blistering on the surface of Ti_2AlC samples oxidized for 24 h at 1200 °C in static air: (A) sample's surface ground with P800 SiC paper prior to oxidation, (B) SEM image of a large blister from (A), (C) clusters of TiO_2 crystals on the blisters' surface and (D) TiO_2 layer covering the surrounding area.

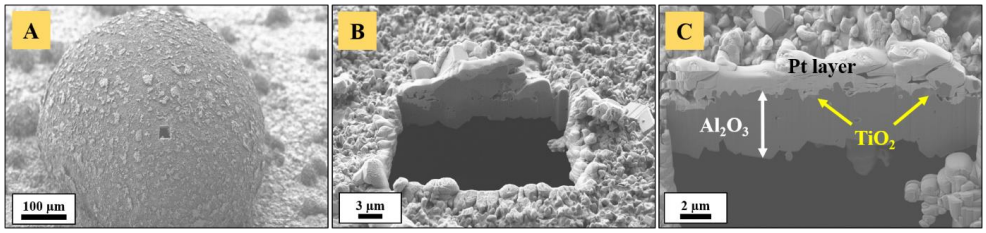

Figure 6. 11: Blister cross-sectional SEM analysis: (A) FIB cut within a large blister from sample on Figure 6. 10A, (B) and (C) higher magnification showing thickness and phases.

In order to predict a potential origin of the blistering phenomenon, the second concern of the study was to determine if blisters were solid or hollow. Figure 6. 11A shows a FIB cut in a large blister, revealing that blisters are, in fact, hollow (this statement relies on FIB cuts in several blisters). The analysis of its cross-section (Figure 6. 11, B and C) highlighted its thickness and composition. EDS confirmed the presence of Al_2O_3 as main oxide and TiO_2. The alumina scale thickness was measured at three different points and yielded 3.2 µm, 3.4 µm and 4.8 µm. The fact that blisters are mainly composed of Al_2O_3 and have a thickness 100 times less than their

diameter foreshadows the fragility of such structures, which were observed to collapse with ease under low load during specimen handling or in case of cyclic temperature variation. The presence of TiO_2, despite its CTE (8-9 x 10^{-6}/K in the 25 °C-1000 °C range) [45] close to that of Ti_2AlC and Al_2O_3, certainly contributes to additional stress generation in the oxide scale as its growth rate was found to be several orders of magnitude superior to that of α-Al_2O_3 [134]. In addition, it precludes the hypothesis of liquid phase formation at high temperature during oxidation as, first, no liquid phase formers are present in the initial Ti_2AlC powder (Table 5. 2) and second, the blisters would necessarily be solid.
Blistering occurred also for Ti_2AlC samples with R_a > 3 µm, and the phenomenon seemed to be more pronounced on sandblasted surfaces (Figure 6. 12). Figure 6. 12A shows a 2.7 mm large blister after 50 h of oxidation at 1200 °C. Its size is about 4 times the size of the largest blisters found on ground surfaces (P800) observed after 24 h at 1200 °C. A fractured blister (Figure 6. 12, B) confirmed the previous statement about hollowness, exposing the surface of the underlying Ti_2AlC.

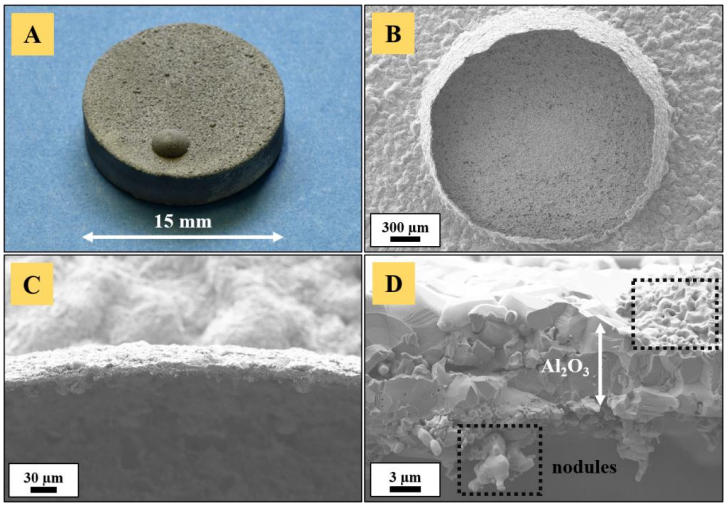

Figure 6. 12: Ruptured blister that formed on a sandblasted Ti_2AlC surface after 50 h at 1200 °C: (A) intact axisymmetrically grown circular blister, (B) evidence of craters on the Ti_2AlC surface inside the blister, (C) and (D) higher magnification on the blister‘s wall.

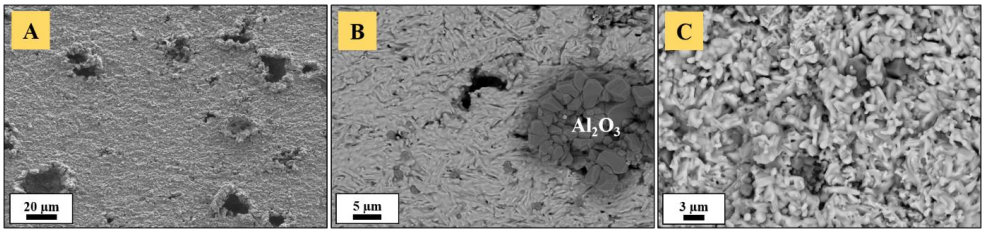

Figure 6. 13: Ti_2AlC surface inside the blister on sample in Figure 6. 12B: (A) SE image showing multiple excavations, (B) BSE image evidencing Al_2O_3 clusters and (C) BSE image presenting the thermo-oxidatively “etched” microstructure.

Multiple cavities were observed, and their nature and potential origin is discussed further in the present section. The wall thickness of the large blister was evidenced at higher magnifications (Figure 6. 12, C and D) and yielded 6-8 µm, which is consistent with previous reported values

(Figure 6. 2). Al_2O_3 was found to be fine-grained, single grains being discernable on the fracture surface on Figure 6. 12D. Nodules of even finer microstructure were observed on both sides of the blister's wall. Higher magnifications of the Ti_2AlC surface inside the blister (Figure 6. 13, A) revealed numerous small craters. BSE images (Figure 6. 13, B and C) highlighted the presence of large Al_2O_3 nodules and Al_2O_3 grains (dark phase) scattered across the Ti_2AlC matrix. The surface of Ti_2AlC presented an irregular microstructure and porosity was observed due to thermo-oxidative "etching" (mainly resulting from depletion of Al). The craters are believed to result from surface-embedded Al_2O_3 particles used in the sandblasting process, sintering to the TGO via oxide/oxide bonding at high temperature and being extracted from the Ti_2AlC surface during the oxide scale spallation caused by severe rumpling. It seems to be even more probable as no such cavities were observed on ground surfaces.

In general, blistering may result from an accumulation of gaseous species at the substrate/oxide scale interface, if the TGO acts as a gas-tight barrier and if the pressure exerted by the gas exceeds the Ti_2AlC/oxide adhesion strength. In fact, such a phenomenon was reported by Subanovic et al. [248] for NiCoCrAlY-coatings exposed at 1100 °C in an atmosphere containing both H_2O and H_2 species. Macroscopic blisters were generated due to plastic deformation arising from the evolution of H_2-gas in coatings. In the present work, the oxidation of Ti_2AlC being restricted to its surface, the formation of carbon oxide species is likely to occur in negligible amounts, so that it may not suffice to induce blisters in the alumina scale. Further, upon FIB cutting, relaxation of stresses assumably induced by inner gas pressure would have resulted in elastic strain recovery and a modification of the blister morphology. None of these were observed. Additionally, it was often reported that carbon diffuses through the oxide scale and oxidizes into CO_2 at the oxide/atmosphere interface [118]. However, the fact that these gaseous species may, to a minimal degree, assist rumpling in the initial stage is not counterintuitive, especially as more of them are produced for higher surface roughness, meaning for a larger surface area.

Blistering is therefore found to be the second stage of the oxide scale deformation. The quantitative evolution of buckle-driven film delamination was investigated by Hutchinson et al. [249]. The established mathematical models for thin elastic films under equi-biaxial compressive stresses demonstrated that blisters emanate from the initially debonded film buckling away from the substrate. Such delaminated areas, of which the number and intensity increased with the substrate surface roughness (Figure 6. 2 and Figure 6. 9), were evidenced in the present work. Buckling of the TGO layer resulted from an accommodation of compression induced in the scale by oxide growth stresses. The formation of an incipient blister generated a driving force on the circular interface crack tip [249], promoting crack advance when the adhesion strength between the TGO and Ti_2AlC was exceeded. The continuous nucleation and growth of new alumina grains at grain boundaries in the non-detached scale of the surrounding area contributed to the steady generation of significant in-plane stresses [250]. These participated in the lateral lengthening of the TGO. The bending stiffness of the Al_2O_3 scale is in direct correlation with its thickness [243], more exactly with its moment of inertia. Its deflection is therefore easier when thinner, as is the case in the first 24 h of isothermal oxidation. As such, the resulting deformation of the Al_2O_3 layer and the gradual formation of a blister might be due to stress relaxation, so as to ideally drive the system towards a stress-free state. It is known that in-plane compressive stresses decrease when the amplitude of the buckled alumina scale increases, as the total length of the layer is larger than in the equivalent planar state [243]. The shear strength of the Ti_2AlC/Al_2O_3 interface must be weak enough at 1200 °C to allow plastic flow towards the blister. More precisely, it was emphasized that the relative proportion of failure mode 2 (through shear) to failure mode 1 (in tension) increases upon crack propagation and that the description of buckling-induced film debonding necessitates buckling and fracture to be non-linearly coupled [249]. The diameter of the blister could increase upon further evolution of in-plane stresses and stress-relaxation, as the Al_2O_3 scale was lifted and

caused progressive delamination of the bonded interface at the circular crack tip. The quasi-perfect circularity of the blisters – maintained even at long oxidation times (see further in this section) – suggests their axisymmetric growth and the high stability of the crack front [249]. The significant deflection of the Al_2O_3 scale together with the relatively small surface area of the debonded patch (Figure 6. 10, B and Figure 6. 12, B) resulted in highly spherical blister morphologies. Hutchinson et al. [249] alluded to a decrease of the crack driving force above a certain value of stress exceeding the critical stress for buckling. This might have led to such peculiar blister morphologies in the present work. The Al_2O_3 scale may be allowed to deform through superplastic flow, as already reported for alumina with average grain size of 1.6 µm [251]. In the present work, the Al_2O_3 scale grain size could be roughly estimated with contrast-modified SEM images and yielded similar values. An insight into the scale microstructure is also provided via Figure 6. 9B, visible within the large cavity. This microstructure was found on fine-grained Ti_2AlC as a result of a larger amount of nucleation sites (grain boundaries) per unit area. However, the deformation at 1200 °C of the thin detached strip of TGO is limited in time. Alumina is known to have a high anisotropic grain boundary energy, which is believed to decrease the grain boundary cohesive strength [252]. In addition, grain growth may induce cavitation and a decrease of ductility. Moisture-induced spallation [253] is also known to fragilize the Al_2O_3 scale. It is indeed probable that Al_2O_3 might react with moisture, leading to the formation of hydroxyl groups [254]. These phenomena are possible factors assisting the mechanism of blister disruption. However, the main cause was ascertained later in this work. In brief, massive rutile TiO_2 grains grew within the unharmed Al_2O_3 blister and subsequently collided with the alumina scale, causing its rupture. The subsequent collapse of the blister(s) is believed to be the starting point of breakaway oxidation.

VI-2.3 Breakaway oxidation phenomenon

Breakaway oxidation of Ti_2AlC at 1200 °C in static air was found to instantly occur at collapsed blisters and promoted intense surface nodulation of large ocher clusters of Ti-rich oxides. It was observed for samples with rough surface finish, as rumpling and blistering of the protective oxide scale are more likely to occur for large R_a values (typically larger than 3 µm, Table 6. 2). To understand and confirm this effect, TGA analyses at 1200 °C for up to 100 h were performed for polished and sandblasted samples. Mass gain curves (Figure 6. 14, A) depict normal oxidation kinetics for both polished and sandblasted samples during the first 50 h of isothermal oxidation, supplementing data for fine-grained Ti_2AlC from a previous study [143].

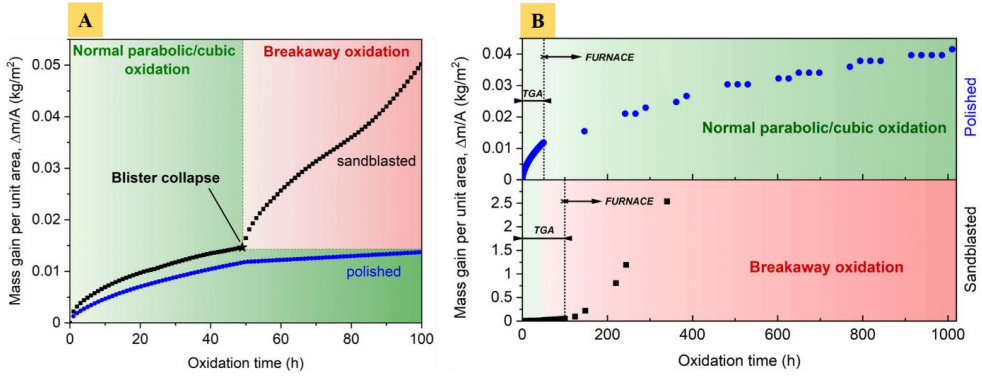

Figure 6. 14: Mass gain curves for polished and sandblasted Ti_2AlC samples oxidized at 1200 °C, retrieved from (A) TGA experiments and (B) long-term furnace cycling experiments.

The mass gain per unit area (Δm/A) was lower for the polished sample, as less TiO_2 formed – as compared to the sandblasted sample. However, it must be noted that the curve of the sandblasted sample is slightly overestimated as its geometrical surface area was considered, not its real value taking into account the surface microtopography. The polished sample did not exhibit blisters or surface-specific structures foretelling potential breakaway oxidation and a parabolic ($R^2 = 0.997$) fitting $(\Delta m/A)^2$ of the time-dependent mass gain was found to be more representative of the oxidation kinetics than a cubic ($R^2 = 0.961$) fitting $(\Delta m/A)^3$ before t = 30 h. After t = 30 h, both parabolic ($R^2 = 0.999$) and cubic ($R^2 = 0.998$) fitting showed high goodness-of-fit. Conversely, the sandblasted sample showed a large blister on one of its flat surfaces. However, at this stage, the blister was not damaged and the protective characteristic of the alumina scale was probably retained. Fitting the mass gain curve showed that parabolic oxidation kinetics can be expected before t = 20 h and, as in the case of the polished sample, both parabolic ($R^2 = 0.997$) and cubic ($R^2 = 0.999$) fitting can be considered after t = 20 h.
The second TGA run for the sandblasted sample showed that, after intentional blister collapse, breakaway oxidation could be triggered. It translated into a sudden increase of the mass gain per unit area and manifested through a wavy Δm/A = f (oxidation time) curve following a quasi-linear trend, diverging from the parabolic/cubic kinetics observed before t = 50 h. The mass gain could not be fitted to a parabolic or cubic behavior and showed strong non-linearity. The data for the polished sample for 50 h < t < 100 h shown on Figure 6. 14A was not obtained from TGA but through interpolation with the data point at t = 146 h (furnace experiment), explaining the kink at t = 50 h. Figure 6. 14B depicts the mass gain curves retrieved from long-term high-temperature furnace cycling experiments. The polished sample was cycled for more than 1000 h without showing abrupt changes in the mass gain curve. The data points follow the trend of parabolic more than of cubic oxidation kinetics. This is in agreement with values reported in previous studies [41,126]. A mass gain of ≈ 4 mg/cm^2 was also obtained by Tallman et al. [41] after 1000 h at 1200 °C, as in the present work. As they mentioned, the diffusion of oxygen through the alumina scale grain boundaries is the rate-limiting step in the oxidation of Ti_2AlC. With increasing Al_2O_3 scale thickness and grain growth, the diffusion length increases and diffusion paths become less, hence a reduction in the oxidation rate at longer times. Concerning the sandblasted sample, breakaway oxidation started as soon as the blister collapsed (Figure 6. 14, A) and manifested through a tremendous increase in mass gain over time (Figure 6. 14, B). $(\Delta m/A)_{sandblasted}$ was even greater at t = 100 h than $(\Delta m/A)_{polished}$ at t = 1000 h. Within the following 240 h (t_{total} = 340 h), the mass gain reached 250 mg/cm^2, an impressive 63 times more than the mass gain yielded by the polished sample at t = 1000 h.
Visually, the outcomes of long-term furnace cycling experiments are depicted on Figure 6. 15. Cycling the polished sample for longer times showed that its smooth surfaces were unaffected after ~250 h (Figure 6. 15, A). Convex structures appeared on the edge of the cylindrical sample's curved surface but no sign of large blister formation or initiating breakaway oxidation was evidenced. Alumina blisters and rutile nodules are pointed at by white and yellow arrows, respectively. More rigorously, these exclusively appeared on the ring created during the metallographic preparation of the specimen, resulting from the attempt to smoothen the lateral surface of the pellet. As mentioned earlier, even minimal changes in the surface such as slightly protruding edges can act as stress concentrators and promote rumpling/blistering. After 362 h (Figure 6. 15, B), the first rutile nodules (yellow arrow) were visible as well as a white coloring (white arrows) of some of the blisters. The white coloring may be an indication of an increase in the Al_2O_3 scale thickness, reflecting the light differently as for thinner blister walls. Slight changes could be noticed after 1010 h (Figure 6. 15, C), such as blister growth (white arrow), although, overall, the sample retained its initial appearance. Figure 6. 15D shows that, even though oxide scale blisters formed at specific spots, the polished sample survived 1274 h at 1200 °C without harmful breakaway oxidation.

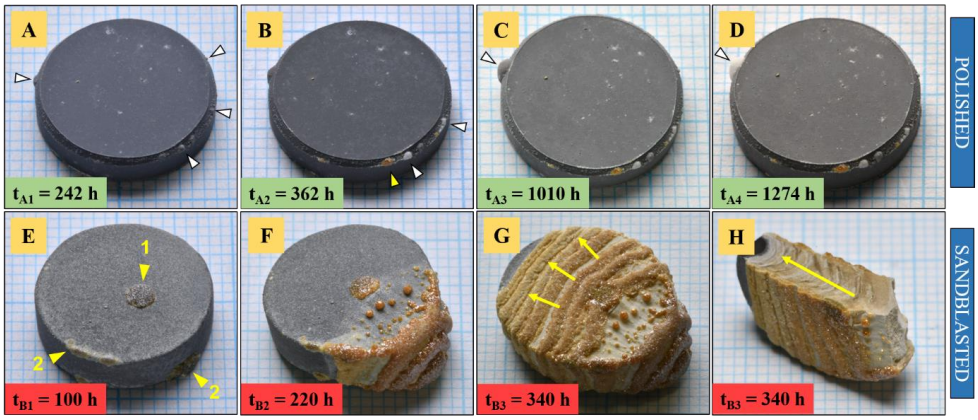

Figure 6. 15: Post-TGA re-oxidation at 1200 °C: (A) polished sample after 242 h (50 h TGA + 192 h in furnace) showing a starting of blistering, (B) same sample after a total of 362 h, (C) 1010 h, and (D) 1274 h, (E) sandblasted sample after 100 h (two TGA runs) with oxide nodules at ruptured blister (1) and at edges (2), (F) same sample after a total of 220 h and (G and H) 340 h showing gradual specimen consumption.

Impressively, thin brittle Al_2O_3 blisters can remain unscathed for long oxidation times. Figure 6. 15E depicts the sandblasted sample after two TGA runs, totalizing 100 h of oxidation at 1200 °C. Large ocher nodules on the sample's sharp edges and at the spot where the blister was initially located were observed confirming that breakaway oxidation took place at these specific locations. Once it is initiated, these spots act as short circuit channels through which oxygen easily diffuses and reaches the Ti_2AlC bulk material. In fact, rutile-TiO_2 is known to be present in a non-stoichiometric, oxygen-deficient form at high temperatures [255]. Oxygen vacancies promote oxygen diffusion, while Ti interstitials facilitate the diffusion of Ti and other cations such as Al^{3+}. The presence of Al^{3+} impurities in the rutile lattice emanates from the diffusion of these species from the surrounding Al_2O_3 phase – these outcomes being highlighted further in this section – and oxygen vacancies are present to compensate the charge arising from these impurities. The non-stoichiometric rutile may act like an Al-getter. Further down, indeed, it is shown that an Al-depleted area is always present underneath these nodules. That would explain why a continuous Al_2O_3 layer is unable to form. A proof that breakaway oxidation kinetics are a rapid, runaway phenomenon is given by Figure 6. 15F, only 120 h after the second TGA run. It highlights a clear wavelike propagation of rutile-rich oxides from one of the side nodules, having consumed a good third of the Ti_2AlC sample. Near-complete consumption of the bulk material is achieved after 340 h (Figure 6. 15, G and H). Yellow arrows indicate the direction of bulk/oxide interface shift. The tremendous mass gain of 2.5 kg/m^2 (Figure 6. 14, B) is due to the massive uptake of oxygen and the full conversion of Ti_2AlC into TiO_2 and Al_2O_3 as evidenced by the sample's cross-section.

Figure 6. 16 highlights the features from the polished sample after oxidation for 1274 h (Figure 6. 15, D). The largest white-colored blister (1) reached a diameter of 1.75 mm (Figure 6. 16, A). In addition, the clear demarcation (white dotted line) of the ring (2) is visible. As a reminder, it resulted from an attempt to curve the lateral pellet surface during metallographic preparation. Interestingly, preferential growth of smaller blisters occurred on that surface (3) as well as at the corner of the pellet (4), where the Al_2O_3 scale formed a thin bulge. Latter might be caused by upward displacement of material leading to pile-up [250]. The large blister (1) was generated at the protruding junction between ring and lateral surface. These outcomes evidenced that those areas are subject to significantly higher radial stresses – when the substrate moves downwards – than on flat polished surfaces. A fractured blister (Figure 6. 16, B) revealed the presence of large rutile grains covering the area. It proved that Al_2O_3 blisters are not as impervious to

oxygen and as protective as scales found on flat substrates. The increase in oxygen partial pressure accompanying the formation of a blister promotes the formation of TiO_2, as Al from the base material was consumed earlier to form the Al_2O_3 scale. This, precisely, was the concern of the present study. As briefly mentioned in section B, the growth rate of TiO_2 is several orders of magnitude higher than that of Al_2O_3 [134]. This leads to the formation of large (> 30 µm) grains of rutile underneath the Al_2O_3 blisters (Figure 6. 16, B and C), filling up the free volume. TiO_2 occupying the available void and fitting closely the shape of blisters resulted in perfectly spherical nodules, as can be seen on Figure 6. 15F.

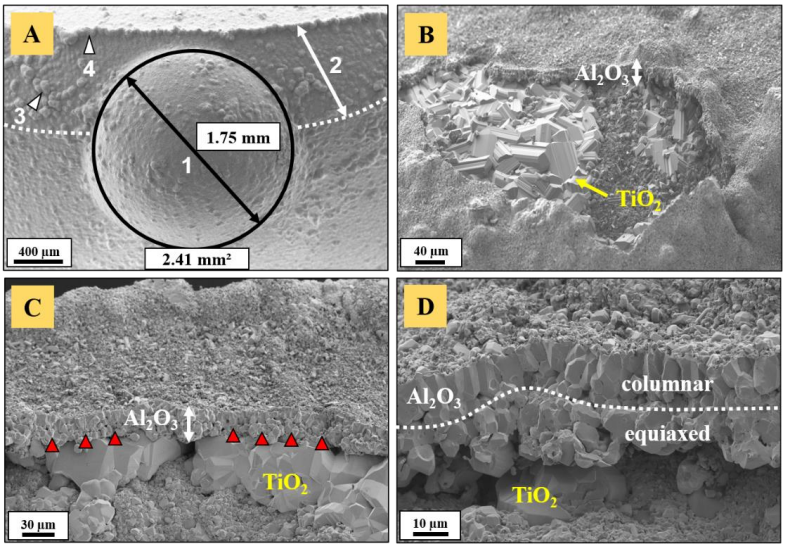

Figure 6. 16: Oxide microstructure and morphology of the polished sample after 1274 h at 1200 °C. A) micrograph of the large white blister in Figure 6. 15D (white arrow), B) presence of large TiO_2 grains growing underneath, C) pressure exerted by rutile grains on the Al_2O_3 scale and D) Al_2O_3 scale morphology. All micrographs are taken at different spots.

Single grains were almost three times the thickness of the entire Al_2O_3 layer. As soon as these grains collide and exert pressure on the thin and brittle Al_2O_3 scale (red spots), the fragile blister wall is breached and collapses. This constitutes the onset of breakaway oxidation, with massive penetration of oxygen. The alumina scale was ~23 µm (Figure 6. 16, D) thick and was composed of two distinct layers, of which the arrangement differed from scale cross-sections on plane surfaces [134]: the inner was composed of equiaxed grains, the outer layer of columnar grains, both approximately accounting for similar thicknesses. At mid-height, the blister walls were thinner (14 µm, evidenced by FIB cuts and fractured surfaces, not shown here). By following the reasoning of lateral TGO lengthening mentioned in section *VI-2.2 Oxide scale blistering*, there might be a gradient of Al_2O_3 scale thickness from blister's dome to base.

The re-oxidation at 1200 °C for 5 min of blistered samples after intentional blister disruption showed an extremely rapid build-up of large, intertwined rutile TiO_2 crystals entirely covering the exposed area (Figure 6. 17, A and B). The vestige of a burst blister can be observed on Figure 6. 17A, as the BSE SEM mode revealed the darker Al_2O_3 phase highlighting its contour. The large TiO_2 grains (Figure 6. 17, B) present after 5 min of re-oxidation indicated rapid grain coarsening. These outcomes corroborate two facts: Firstly, breakaway oxidation of blistered Ti_2AlC samples after blister disruption is fast and characterized by the formation of a continuous and thick layer of large TiO_2 crystals. Secondly, as a consequence of an exhaustion of Al-reservoir (required to initially form the Al_2O_3 blister), the Ti_2AlC base material is found

unable to form back a continuous protective Al_2O_3 layer. Breakaway oxidation translated into the inability of the material to self-heal in a proper way due to a decrease of the near-surface concentration of Al below a certain critical level [156] and selective oxidation of Ti.
Breakaway oxidation was found to steadily occur for machined surfaces as well, such as cut with a diamond-studded wire saw (Figure 6. 18).

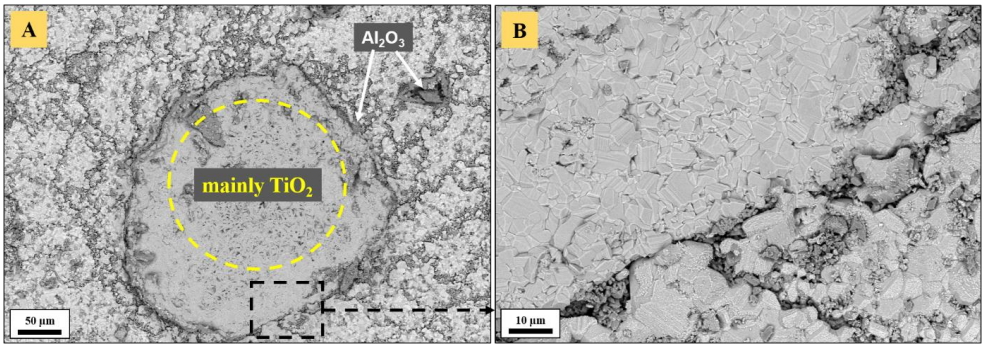

Figure 6. 17: Post-blistering re-oxidation of the P800-ground specimen at 1200 °C for 5 min: (A) oxidized area of re-oxidized blistered sample after intentional blister disruption and (B) magnified area.

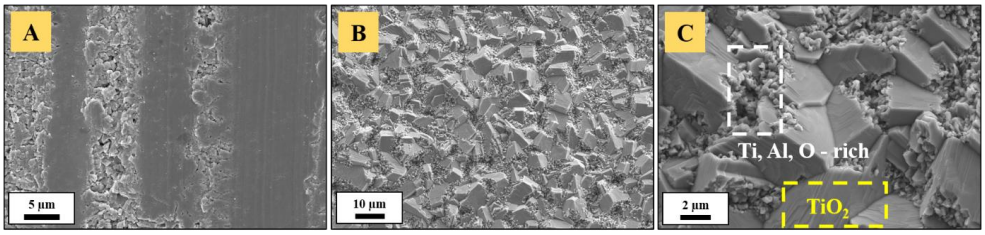

Figure 6. 18: Breakaway oxidation at machined surfaces: (A) micro-damaged Ti_2AlC surface cut with a diamond-studded wire saw, (B) and (C) oxide morphology after oxidation at 1200 °C for 15 min.

The sharp diamond particles caused superficial micro-damaging in form of trenches, when the upward wire movement tore apart the surface of the softer Ti_2AlC MAX phase (Figure 6. 18, A).
As a result, a larger surface area was exposed, in a similar way as for the thermo-oxidatively Al-depleted surface mentioned earlier (Figure 6. 13, C). Consequently, when oxidized at 1200 °C, a peculiar oxide morphology comparable to the one depicted on Figure 6. 17B was observed. Within a short time (15 min), large faceted TiO_2 crystals formed – reaching a size of up to 10 µm – surrounded by sub-micrometer fine grains (Figure 6. 18, B and C). EDS analysis showed that these were essentially composed of Al, Ti and O, likely an alumina-titania solid solution [121,122]. At higher magnification, the foliated structure of TiO_2 is visible. There is clear evidence that a dense protective Al_2O_3 scale could not be formed. The presence of cavities due to surface tearing somehow promotes the formation of a less compact stacking of Al_2O_3 and TiO_2 grains [134]. The subsequent overgrowth of TiO_2 is outpacing the slower growing Al_2O_3.
While normal oxidation of Ti_2AlC is distinguished by the build-up of dense and quasi-impervious Al_2O_3 (Figure 6. 19, B) decorated with small TiO_2 clusters, a complex layering of mixed oxides (Al_2O_3 and TiO_2) and pores was observed for areas undergoing breakaway oxidation, as revealed on Figure 6. 19C. This was already reported by Barsoum et al. [122] and it was the reason why Ti_2AlC was, at the beginning (2001), not considered as efficient high

temperature material. The swollen/deformed area nearby the large TiO_2 nodule on Figure 6. 19A turned out to be composed of a thin (max. 10 µm) delaminated strip of Al_2O_3 (Figure 6. 19, C). At the interface between oxide scale (areas "2" and "3") and underlying MAX phase (area "0"), a TiC-rich layer (area "1") was observed (Figure 6. 19, C and D). Its thickness ranged from a couple tenth to several hundredth of micrometers on different samples. It composed the first line of the internal oxidation front and elongated pores are evidence of the remains of aluminum out-diffusion. On top, a thin layer (~5-20 µm depending on the oxidation dwell time) of Al_2O_3-rich rutile TiO_2 was visualized in area "2", the presence of alumina being correlated to the outward diffusion of Al from area "1" and the dissolution of Al^{3+} ions in TiO_2 [122]. It was reported that, at 1200 °C, both oxides coexist as a solid solution of Al_2O_3 in rutile TiO_2 [256] and that below 1240 °C, corundum is the stable solute phase, hence no aluminum titanate (Al_2TiO_5) was evidenced here.

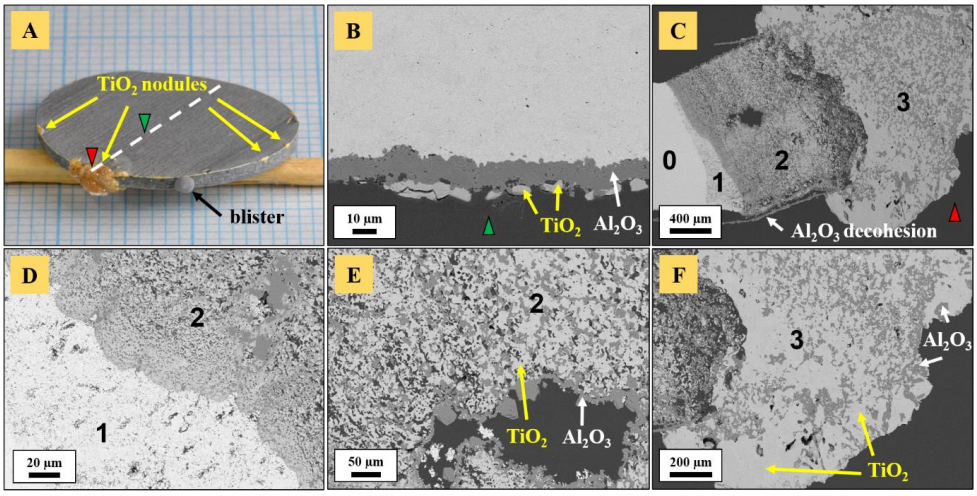

Figure 6. 19: Breakaway oxidation of Ti_2AlC after 72 h at 1200 °C in air: (A) thin pellet presenting ocher oxide nodules and blister, (B) normal TGO build-up at the corresponding green mark, (C) BSE image showing the extent of breakaway oxidation at the red mark with distinct zones, (D) first TiC-rich diffusion layer, (E) second diffusion layer (light phase: TiO_2, dark phase: Al_2O_3) and (F) last diffusion layer mainly composed of TiO_2.

In the middle section of area "2", a large number of pores was evidenced (Figure 6. 19, E), in addition to a significant volume fraction of more homogeneously dispersed Al_2O_3 grains in the dominant TiO_2 matrix. The pores might be caused by outgassing CO_2 during oxidation of carbon, volumetric distortion, or coalescence of Kirkendall voids [121,122] resulting from the diffusion of metallic ions (Al^{3+}, Ti^{4+}) and the clustering of vacancies. Above, in the vicinity of area "3", a higher fraction of Al_2O_3 and a larger pore network was detected, spreading over ~200-300 µm (visible on Figure 6. 19, C and F). It delimits the initial bulk/oxide interface, where a continuous Al_2O_3 scale used to form before the sample experienced breakaway oxidation. It was followed by a more than 1000 µm thick region of TiO_2 (Figure 6. 19, F), identified with a lower volume fraction of Al_2O_3 than in area "2". The porous nature of the mixed oxide layer and the absence of dense Al_2O_3 allowed oxygen to reach and gradually consume the underlying base material. Breakaway oxidation around corners, edges and tips can be described in such way, that more surfaces are exposed and Al-depletion is accelerated by a multidirectional diffusion process. Additionally, surface micro-damaging may also expose/orient more sensitive MAX phase planes (cleavage planes), not having the same ability as prismatic surfaces (direction normal to fast-diffusion basal planes) to form protective Al_2O_3

scales [136,144]. It can also be triggered after the collapse of blisters appearing in the TGO at the early stages in the oxidation timeline, as the exposed surface consists of thermally "etched" Ti_2AlC, hence providing high surface area and channels for a rapid growth of TiO_2. A similar reason was found for surfaces cut by a diamond studded wire-saw. Once the phenomenon of breakaway oxidation is engaged, the lifespan of the compound is drastically shortened, since the protective conditions are not fulfilled anymore.

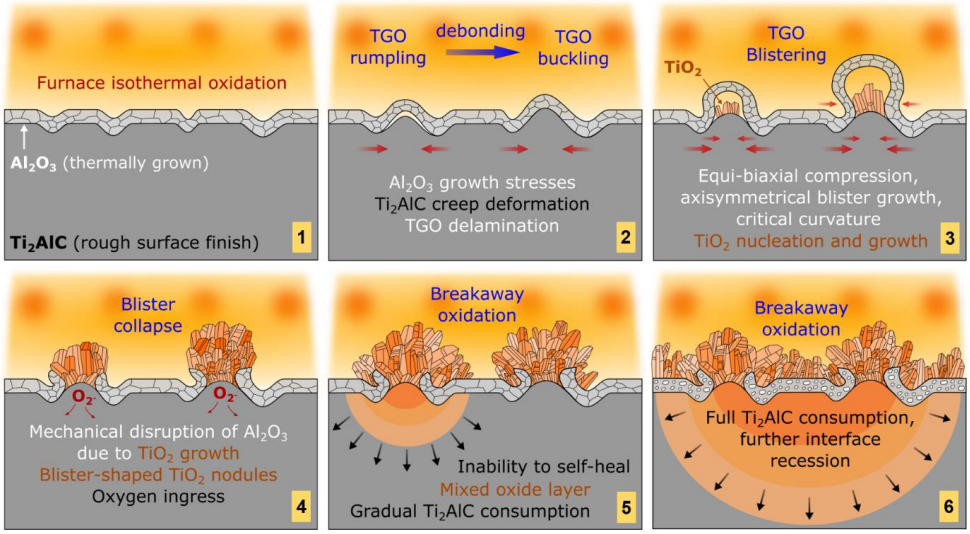

Figure 6. 20: Schematic representation of oxide scale rumpling/buckling, blistering and subsequent breakaway oxidation.

A summarizing schematic is proposed (Figure 6. 20) to explain the evolution of abnormal oxidation caused by blistering described in the present section. For the sake of clarity, the formation of patches of rutile atop the Al_2O_3 scale on rough surfaces (Figure 6. 3C) was not represented (1), to distinguish the rutile TiO_2 exclusively formed in breakaway oxidation conditions. On rough surfaces (typically with arithmetic mean roughness $R_a > 3$ µm, but average (R_z) and maximum roughness depth (R_{max}) also need to be considered) the growth of the Al_2O_3 protective scale follows the initial Ti_2AlC surface undulations. The distribution of stresses on a wavy surface topography is heterogeneous and Al_2O_3 growth stresses provoke significant radial stresses to rise at the bulk/oxide interface (2). The more compliant Ti_2AlC upper layers are dragged by the deforming Al_2O_3 scale, the whole forming large ripples. This phenomenon is known as rumpling. The increase in the amplitude of undulations leads to bulk/oxide interfacial delamination when the work of adhesion of the interface between Ti_2AlC and Al_2O_3 is exceeded [257]. A new degree of freedom is added for the Al_2O_3 scale to deform transversally to the bulk surface. The evolution of equi-biaxial compressive stresses require the TGO to buckle away from the substrate [249]. The nucleation and growth of new Al_2O_3 grains at internal grain boundaries causes lateral straining and an evolution towards blisters (3). The change in oxygen partial pressure in the void created between Ti_2AlC and oxide must be the reason of initiating growth of TiO_2 grains. These – when located at the curved base of blisters – could potentially expedite the lifting of the Al_2O_3 layer at the circular interface crack tip. In-plane stresses generated by growth of existing and newly nucleated Al_2O_3 grains are accommodated. Again, the contribution of outer TiO_2 is neglected, even though its growth rate is higher than Al_2O_3 and certainly affects the overall stress field in the TGO. The evolution of the equi-biaxial

compressive state in the Al_2O_3 scale manifests into the growth of large axisymmetrical blisters due to superplastic flow of Al_2O_3. Large TiO_2 grains form and gradually fill the blister volume. These structures can grow and persist for more than 1200 h until disrupted by mechanical or thermo-mechanical stresses (4). In a long-term scenario, the growth of single TiO_2 grains several times the total thickness of the entire alumina scale cause pressure to be exerted on it, and hence, its breaching. However, on account of their fragility, Al_2O_3 blisters can also yield due to external interventions, such as sample handling. The exposed Ti_2AlC surfaces being depleted with Al below the critical concentration, the selective oxidation of Ti leads to rapid (5 min) growth of large (5-10 µm) TiO_2 crystals. Blister disruption can be considered as the onset of breakaway oxidation, as the MAX phase is unable to heal and form a second protective Al_2O_3 scale (5). Instead, large rutile-TiO_2 nodules gradually cover the affected area. Collapsed blisters are short-circuit paths for oxygen inward diffusion. Inward-developing oxidation of Ti, Al and C creates a complex layering of mixed oxides and pores. The structural material is progressively consumed as the inward oxidation front progresses. The formation of solid solutions of Al_2O_3 in TiO_2 is accompanied by the generation of vacancies, which, in turn, coalesce to Kirkendall voids. These develop towards interconnected pores which facilitate oxygen transport to the new Ti_2AlC/oxide interface and explain the fast kinetics of breakaway oxidation. With further recession of the bulk/oxide interface, it is only a matter of time until the entire specimen is converted to oxide (6).

VI-2.4 Corrosion-induced blistering

Similar to corrosion of metals and alloys facilitated in presence of salt (e.g., NaCl), experiments were conducted in this work to determine if traces of KBr – found as residues of the MS^3 route – can alter the good oxidation resistance of Ti_2AlC. Depending on the washing procedure after MS^3, the residual content of KBr varies. Classically, the mass fraction of potassium detected by ICP-OES is between 0.3 and 0.5 wt.% (Table 3. 2). The outcomes of the isothermal oxidation of polished Ti_2AlC containing 1 and 5 wt.% KBr are shown in Figure 6. 21C, D and E. The surfaces were mirror-polished (Figure 6. 21, A) in order to essentially link the results to the influence of KBr additions and not to the effect of surface roughness, as is well-known from the previous sections.

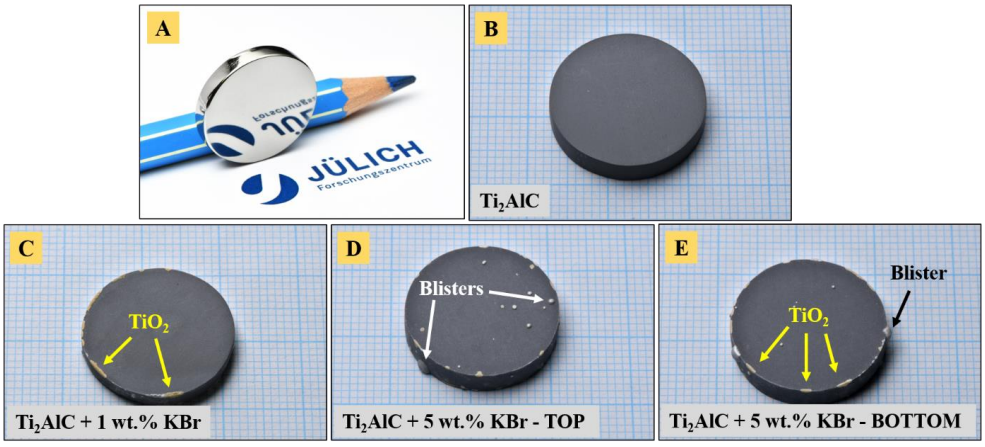

Figure 6. 21: Isothermal oxidation at 1200 °C for 24 h of polished Ti_2AlC with and without KBr additions: (A) mirror-polished pristine sample, and oxidized (B) pristine sample, (C) with 1 wt.% KBr, (D) and (E) with 5 wt.% KBr.

The sample without KBr addition (Figure 6. 21, B) was pristine after 24 h at 1200 °C in air. The addition of 1 wt.% KBr triggered the apparition of TiO_2 nodules at the edges between upper plane and lateral surfaces (Figure 6. 21, C). Increasing the content to 5 wt.% KBr caused large blisters to appear on the lateral surface (also at edges) and small ones on the plane upper surface (Figure 6. 21, D). In addition, TiO_2 nodules were also observed growing on sharp edges (Figure 6. 21, E). These results highlight the fact that residual KBr salt can be detrimental to the good oxidation performance of Ti_2AlC. The effect seems to be intensified with increasing concentrations. The concentration of KBr during densification of the Ti_2AlC/KBr powder mixture in a FAST/SPS furnace must have remained stable because of short residence times (10 min dwell at 1200 °C, and max 5 min above the melting point of KBr). Later, during oxidation, the evaporation of KBr above its melting point (735 °C), and the confinement of gaseous species accumulating in the dense pellets may have resulted in blistering of the oxide scale, when the gas pressure caused alumina to creep at the oxidation temperature. Surprisingly, the blistering phenomenon described in the previous section was observed for bare Ti_2AlC, i.e., for a residual mass fraction of KBr in the 0.3-0.5 wt.% range, whereas no such blisters were observed here for a similar sample (Figure 6. 21, B). That is because, as mentioned before, in the present case, the surface roughness was low enough to prevent blistering, while in the previous section, blisters appeared on ground and sandblasted surfaces. Therefore, there cannot be a single cause to the phenomenon of blistering, which is rather believed to originate from a synergy of different aspects. As to avoid the entrapment of residues of KBr in agglomerated Ti_2AlC powder after MS^3 and further decrease its content in the as-synthesized product, an additional low-energy milling step could be reasonable to consider.

VI-3 Oxidation of YSZ-coated Ti_2AlC

The potential of Ti_2AlC for high-temperature applications is known, albeit the competition between TiO_2 and Al_2O_3 and the ease with which breakaway oxidation is triggered can limit its scope and implementation. In this work, the combination of Ti_2AlC substrates with YSZ topcoats and thermal cycling thereof (Figure 2. 10, Figure 2. 13 and Figure 2. 14) demonstrated the good compatibility of these two materials and showed promising outcomes alongside existing burner rig tests performed both at Forschungszentrum Jülich GmbH (Germany) [169,170] and at the NASA Glenn Research Laboratory (USA) [168,171]. It also highlighted and confirmed that the oxidation of Ti_2AlC is strongly dependent on numerous external factors.
This section presents the outcomes of post-APS coating adhesion, thermal shock experiments of YSZ-coated Ti_2AlC-based systems using cycling conditions, as well as the issues encountered in each case.

VI-3.1 YSZ coating adhesion

Applying a YSZ coating on Ti_2AlC substrates requires the surface to be roughened beforehand. Preliminary trials showed that grinding did not provide the sufficient “grip” and coatings were found to spall off during the APS procedure. As such, sandblasting was employed, initially at a pressure of 4 bar. The surface topography profile of four substrates used for furnace thermal cycling is shown in Figure 6. 22: Sample *A* (Figure 6. 22, A), destined to thermal cycling at 1100 °C, sample B_2 (Figure 6. 22, B) for thermal cycling at 1200 °C, sample C_1 (Figure 6. 22, C) for thermal cycling at 1300 °C, and sample *D* (Figure 6. 22, D) containing aluminosilicate fibers and planned for thermal cycling at 1200 °C. The 3D contour maps of monolithic Ti_2AlC substrates (Figure 6. 22, A, B and C) presented large variations of height,

oscillating between +16 µm and -20 µm. A slightly flatter profile was observed for the sample containing fibers (Figure 6. 22, D), more resistant to abrasion.
An overview of the YSZ coating microstructure and adhesion was given by SEM cross-sectional analyses (Figure 6. 23). The YSZ coatings had an average thickness of ~300 µm (Figure 6. 23, A) and were composed of inter-splat cracks (Figure 6. 23, B) and porosity, which are typical features of APS coatings [169].

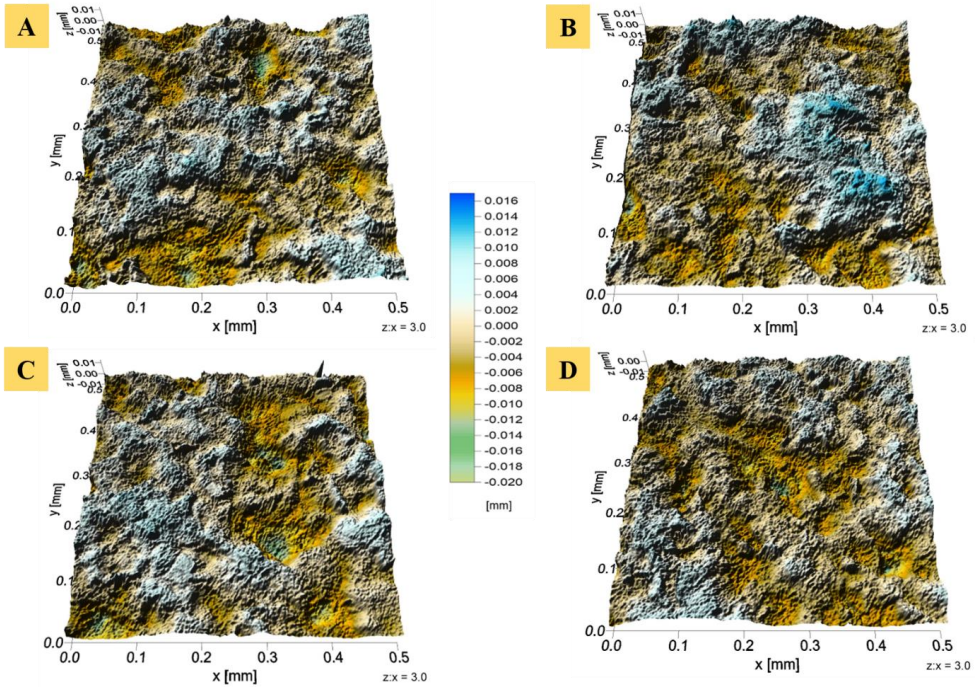

Figure 6. 22: 3D topography profiles of Ti_2AlC-based substrates sandblasted at 4 bar: (A) monolithic, sample *A*, (B) monolithic, sample B_2, (C) monolithic, sample C_1 and (D) fiber-reinforced, sample *D*.

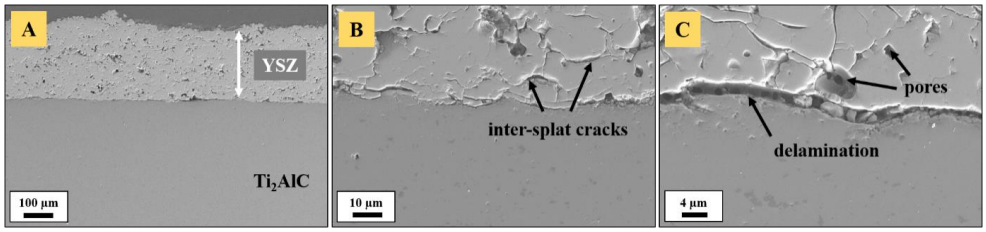

Figure 6. 23: 300 µm thick YSZ coating on Ti_2AlC substrate after the APS coating procedure: (A) Overview SE image, (B) and (C) higher magnification showing cracks, delamination and pores.

Molten particles deform upon impact, solidify and form a first layer before the next particles are deposited on top. The entrapped gas, the formation of cracks and partially molten particles in the plasma were responsible for the formation of pores. The high number of cracks was due to poor inter-splat cohesion. However, the presence of these cracks allowed a certain strain tolerance during thermal cycling [168,169].

In general, the coatings were homogeneous and showed good adhesion on the roughened (sandblasted) Ti_2AlC substrates, though some infrequent spots presented a delaminated interface (Figure 6. 23, C). As cracks were observed in the upper region of the substrate by Gonzalez et al. [169] for Cr_2AlC due to harsh sandblasting conditions, the pressure was adjusted here for Ti_2AlC and reduced later to around 2-2.5 bar.

VI-3.2 Thermal cycling of YSZ-coated Ti_2AlC

Figure 6. 24 shows the first sample (sample *A*) thermally cycled at 1100 °C in an automatic vertical high-temperature furnace. Initially, the issue of sample cutting and rutile TiO_2 overgrowth was unknown. That is why, only one half of the pellet was oxidized (Figure 6. 24, A), while the second half was used to characterize the YSZ/Ti_2AlC interface quality after the APS coating procedure (Figure 6. 23). After ~135 h of repeated oxidation at 1100 °C, a slight orangish coloration was visible on the cut surface – located nearby a machining defect – indicating growth of rutile TiO_2 in sufficient amount to have it visible to the naked eye. The YSZ coating was well-adhering, without any sign of spallation.

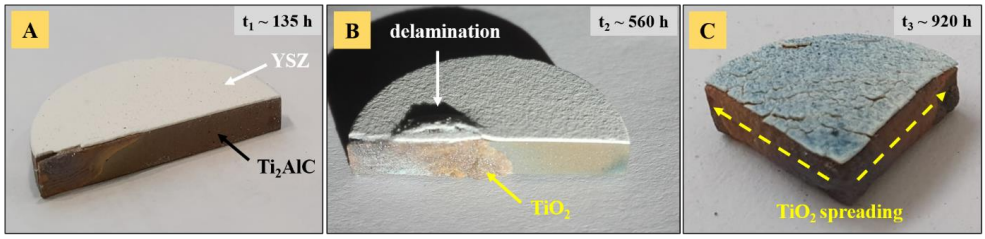

Figure 6. 24: Sample *A*: thermally cycled YSZ-coated Ti_2AlC half pellet at 1100 °C showing TiO_2 overgrowth essentially due to sample conditioning. Pictures (A), (B) and (C) were taken after 60, 250 and 410 cycles.

After ~560 h (Figure 6. 24, B), the first delaminated spot was observed above a growing TiO_2 nodule. Cross-sectional analysis (Figure 6. 25, A) revealed the continuous Al_2O_3 scale growing between Ti_2AlC and YSZ, reaching a thickness of ~8-10 µm after ~500 h at 1100°C. Higher magnification (Figure 6. 25, B and C) showed that the TGO was slightly rumpled and cavities/delamination at certain locations were observed. However, the overall adhesion turned out to be excellent between substrate and TGO as well as between TGO and YSZ. Multiple Al_2O_3 grains were dispersed in the Ti_2AlC substrate, resulting from a partial oxidation during MS^3, FAST/SPS and the present thermal cycling experiment. On account of their inert nature and higher hardness, these can be seen as particulate reinforcements which contribute, to a certain extent, to mechanically strengthen the Ti_2AlC matrix. Therefore, they are not detrimental to the good oxidation or thermal shock resistance of the MAX phase.

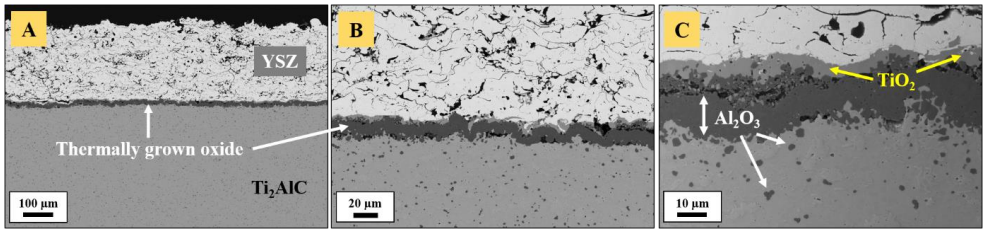

Figure 6. 25: Sample *A*: cross-section BSE images after 223 cycles (~500 h) at 1100 °C showing features of the thermally grown oxides: (A) overview image, (B) and (C) higher magnification on the TGO.

Figure 6. 25C highlights the presence of a thin and discontinuous layer of rutile TiO_2 above the Al_2O_3 scale. Cavities were present at the Ti_2AlC/Al_2O_3 and Al_2O_3/TiO_2 interfaces. These were partially filled/healed with alumina due to internal oxidation.
Additional steps were required to characterize these areas, resulting in a fourth of the pellet left for the thermal cycling experiment. It was interrupted after ~920 h (Figure 6. 24, C), for several reasons: the YSZ coating began to crackle, rutile TiO_2 propagated along the whole cut surfaces and contamination (bluish deposit) from other samples – used for the same purpose – was observed.
In parallel, "manual" thermal cycling experiments were conducted on entire samples at 1200 °C and 1300 °C. An investigation of the temperature drop upon removal of the samples from the high-temperature furnace was performed with a high-temperature pyrometer and an infrared thermometer (refer to Figure 2. 10) and is depicted in Figure 6. 26A. It highlights the rapid cooling

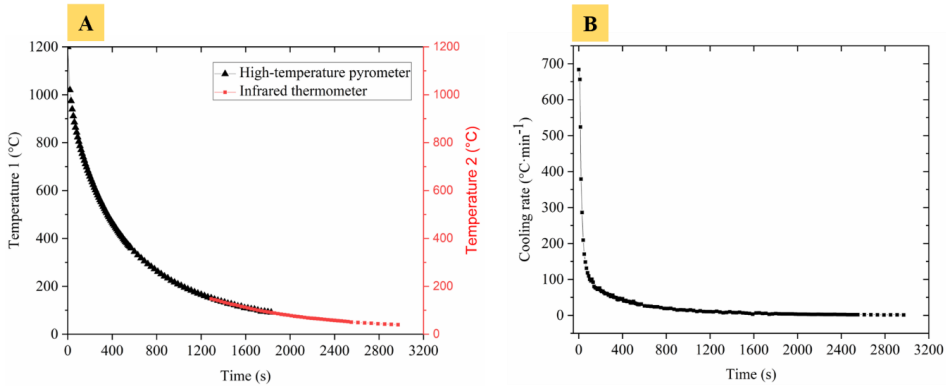

Figure 6. 26: Temperature drop measurement during thermal cycling: (A) temperature drop profile measured with two devices, (B) cooling rate drop profile.

of the sample and the significant thermal shock conditions to which it is exposed. The first order derivative of the temperature variation over time – i.e., the cooling rate – is given by Figure 6. 26B. It demonstrated that the cooling rate drastically decreased from ~700 °C·min^{-1} to 150 °C·min^{-1} in the first minute after the sample was taken out of the furnace, before experiencing a less sharp decrease around 2 min, when the temperature reached ~770 °C. After 3 min, the cooling rate was below 100 °C·min^{-1} and eventually reached a plateau.
The first sample (sample B_1) cycled at 1200 °C (Figure 6. 27) showed excellent YSZ adhesion, as expected from the low mismatch in coefficient of thermal expansion between YSZ, Ti_2AlC and thermally grown alumina and titania. However, on the lateral surface of the pellet, a blister appeared after 168 h (Figure 6. 27, B). The lateral surface was ground, which may be the trigger of blister formation, as already extensively described in the previous sections. The blister was perfectly spherical and grew axisymmetrically, which shows that the evolution of the circular crack tip was smooth and homogeneous. After 336 h (Figure 6. 27, C), different features could be observed: first, the blister's color changed from grey to white, which may be an indication of an increase in thickness of the Al_2O_3 scale; second, the fractured blister highlighted its inner volume filled with a spherical TiO_2 nodule; third, the area in the immediate vicinity of the blister was bulged and decorated with patches of rutile-TiO_2. With the description provided in the section *VI-2 Breakaway oxidation*, it is obvious that breakaway oxidation started from this specific time. Figure 6. 27D depicts the sample after 504 h, when half of the pellet was consumed. It clearly shows that the blister constituted the spot where breakaway oxidation started and led to catastrophic runaway oxidation with propagation of periodic band-like TiO_2

oxide morphologies. Consequently, the overgrowth of titania provoked the progressive delamination of the YSZ coating.
Cross-sections of the sample after 504 h at 1200 °C are shown in Figure 6. 28. Continuous thermally grown alumina found between the YSZ topcoat and the Ti_2AlC base (Figure 6. 28, A and B) reached a thickness of approximately 23 µm. The TGO was slightly rumpled, but significantly less than compared to the outcomes presented in previous sections.

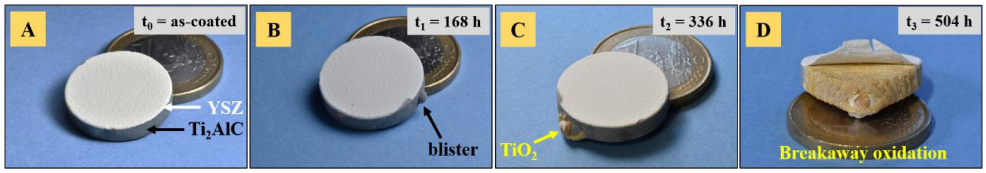

Figure 6. 27: Sample *B1*: thermally cycled YSZ-coated Ti_2AlC at 1200 °C: (A) as-coated sample, (B) blister formation after 168 h of cycling, (C) breakaway oxidation starting after ~336 h and (D) catastrophic propagation after 504 h.

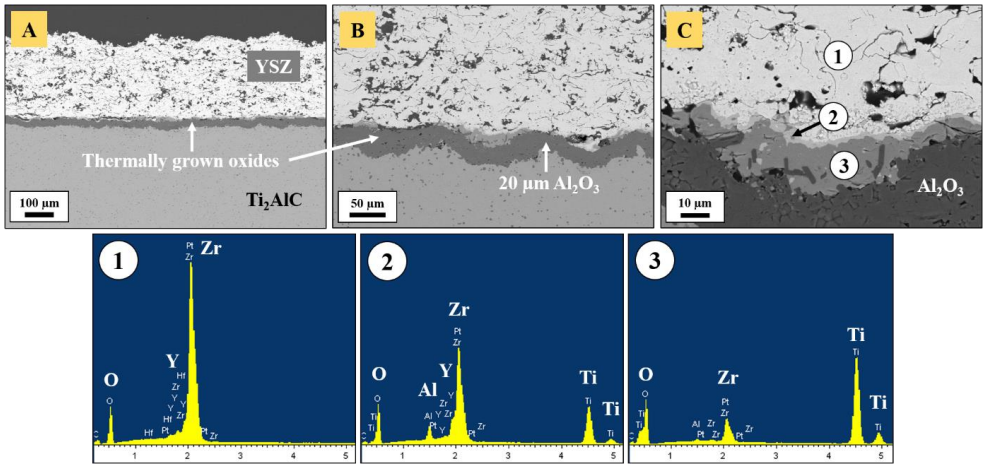

Figure 6. 28: Sample *B1*: cross-section BSE images after 504 h at 1200 °C on the "safe" side of the pellet shown in Figure 6. 27D showing features of the thermally grown oxides: (A) overview image, (B) and (C) higher magnification on the TGO. Corresponding EDS spectra are shown.

Contrary to non-coated Ti_2AlC, the presence of YSZ is believed to contribute to slow down the process of rumpling as it exerts compressive forces on Al_2O_3. Higher magnification (Figure 6. 28, C) showed the presence of diffusion layers above the Al_2O_3 scale, arising from interdiffusion of elements in the considered oxides (Y_2O_3, ZrO_2, TiO_2, Al_2O_3). Such diffusion layers were already reported by Smialek et al. [168] as reacted YSZ-TiO_2-Al_2O_3 and mostly observed for APS-coated YSZ/Ti_2AlC systems. As shown by the corresponding point EDS spectra, these layers are enriched with Y, Zr, Ti, Al and O. The side consumed by breakaway oxidation showed the same features as those highlighted in Figure 6. 19C.
Figure 6. 29 shows mass gain curves corresponding to sample *B1*, which can be related to visual outcomes provided in Figure 6. 27. Figure 6. 29A highlights the usual power fitted oxidation kinetics observed for Ti_2AlC at 1200 °C. The goodness-of-fit is demonstrated through the low reduced χ^2 value of 0.004. On Figure 6. 29B, the onset of breakaway oxidation is visible as the mass gain curve is subject to a steep increase around a thermal cycling time of 300 h. As depicted on Figure 6. 27C, this corresponded to the rapid formation of rutile-TiO_2 nodules and

the starting point of internal consumption of the Ti_2AlC base material. The second part of the curve, between ~350 h and 500 h could be fitted with a linear behavior, even though the goodness-of-fit was more mediocre than for the previous power law fitting (Figure 6. 29, A). Contrary to sample *B1*, sample *B2* (Figure 6. 30) did not experience the same fate. Instead, the adhesion of YSZ was found unaltered up to 1517 h of thermal cycling at 1200 °C (Figure 6. 30, F). No blister formed on the lateral surface (Figure 6. 30, A), though a TiO_2 nodule was found to grow on the bottom flat uncoated surface of the Ti_2AlC pellet, at the spot where a small cavity existed in the porous alumina plate used as sample holder for the cycling experiment (Figure 6. 30, B).

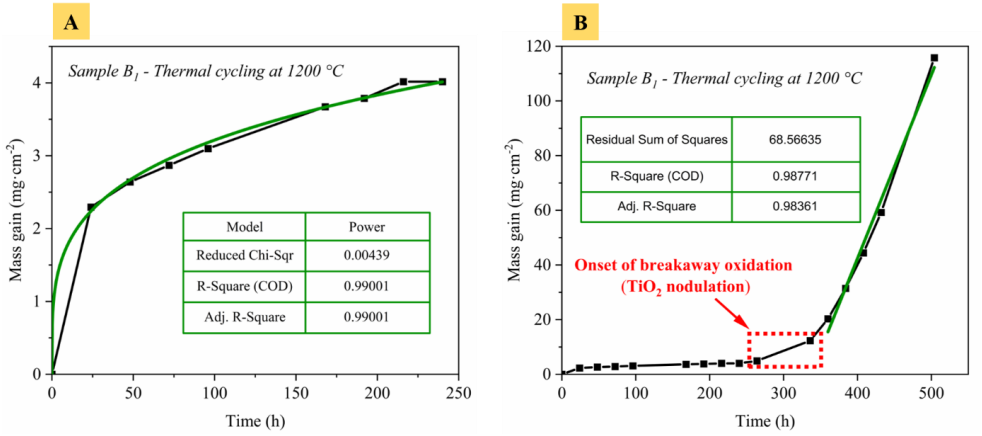

Figure 6. 29: Sample *B1*: mass gain curves retrieved (A) before 250 h showing power law fitting oxidation kinetics and (B) start of breakaway oxidation around 300 h.

During the whole thermal cycling experiment, the nodule remained stable and did not grow (Figure 6. 30, D, E and G). Due to sintering of TiO_2 with the porous Al_2O_3 plate (oxide/oxide bonding), a small fragment of the latter remained attached to the nodule (Figure 6. 30, E). At a later stage of the thermal cycling experiment, other nodules appeared on sharp edges (Figure 6. 30, G). Again, halving the pellet for characterization purposes was found to be detrimental, as it triggered overgrowth of TiO_2 and gradual spallation of the YSZ coating (Figure 6. 30, H).

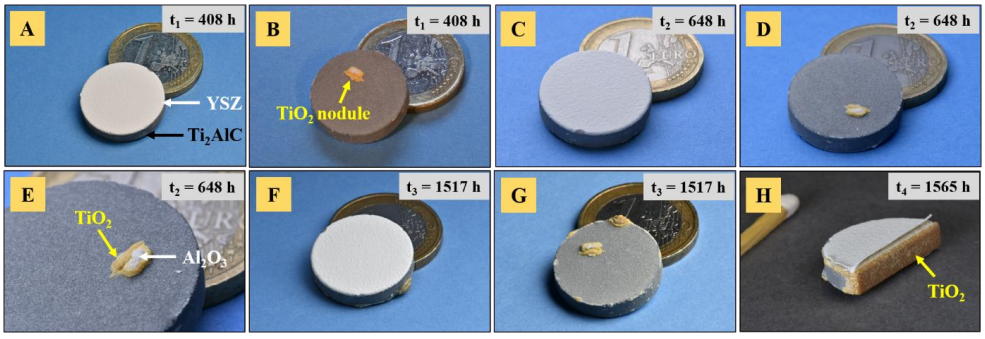

Figure 6. 30: Sample *B2*: thermally cycled YSZ-coated Ti_2AlC at 1200 °C showing long-term performance and experiment interruption due to TiO_2 nodulation: (A) sample after 408 h (top), (B) bottom, (C) after 648 h (top), (D) and (E) bottom, (F) after 1517 h (top), (G) bottom and (H) half-pellet after 1565 h of cycling.

Cross-sections of the sample after 1517 h at 1200 °C are shown in Figure 6. 31. The continuous thermally grown alumina (Figure 6. 31, A and B) reached a thickness of approximately 33-36 µm, a similar order of magnitude as APS and PS-PVD-coated samples thermally cycled for 500 h at 1300 °C [168]. These thickness values are 6-7 times larger than those reported for conventional bond coats on superalloys at failure. The same reacted Y, Zr, Ti, Al-oxides as mentioned earlier were found atop the Al_2O_3 scale (Figure 6. 31, C). These spread over a thickness of 10-13 µm in the YSZ-TBC coating.

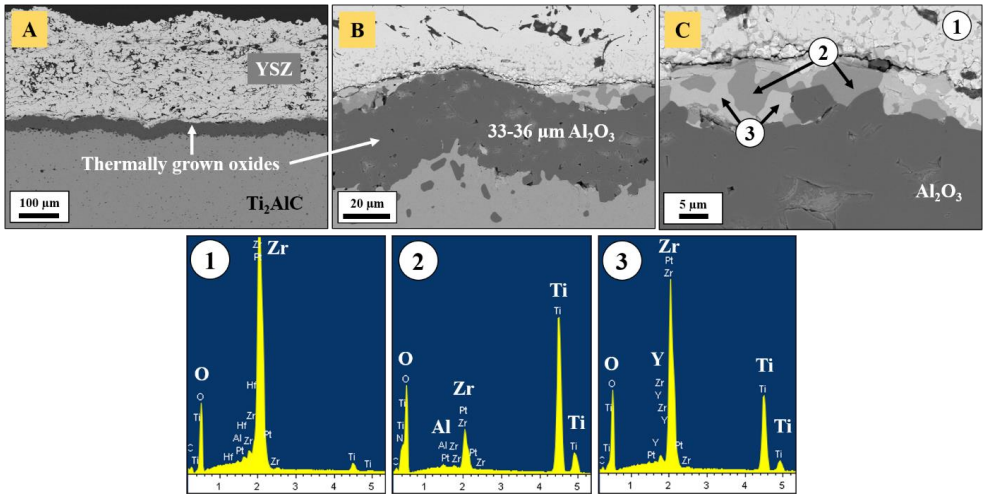

Figure 6. 31: Sample B_2: cross-section BSE images after 1517 h at 1200 °C of sample shown in Figure 6. 30F: (A) overview image, (B) and (C) higher magnification on the TGO. Corresponding EDS spectra are shown.

The analysis of the sample's mass gain is given in Figure 6. 32. Even though the experiment was interrupted due to the formation of TiO_2 nodules (Figure 6. 30, G) foretelling the onset of breakaway oxidation kinetics (Figure 6. 32), this demonstrated the long-term performance of such systems. The considered thermal cycling duration of 1500 h at 1200 °C constitutes the longest time reported so far, as previous experiments usually stopped after 500 h [168].

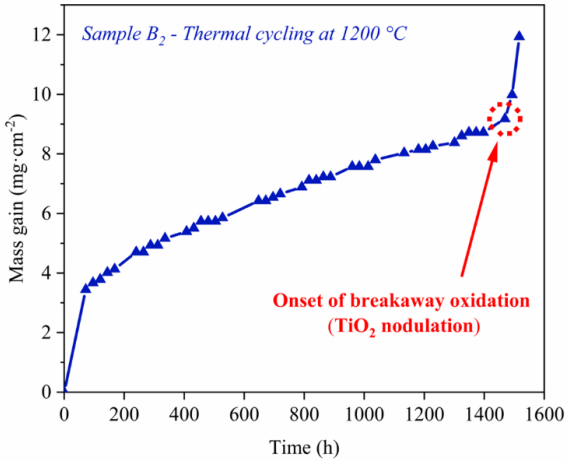

Figure 6. 32: Sample B_2: mass gain curve showing the long-term performance of a YSZ/Ti_2AlC system.

However, the study of Smialek et al. [168] also reported excellent outcomes after 500 h at 1300 °C. In this work, thermal cycling of samples C_1 (Figure 6. 33 and Figure 6. 34, A) and C_2 (Figure 6. 34, B) at 1300 °C indicated the limit temperature of such systems. The YSZ coating prematurely spall off the Ti_2AlC substrate. After the fourth cycle (96 h, Figure 6. 33, B), it was almost entirely detached, before being separated from the base material during the next cycle (Figure 6. 33, C). A second sample (sample C_2 not shown here, as similar to C_1) cycled under the same conditions presented premature coating spallation after 48 h.

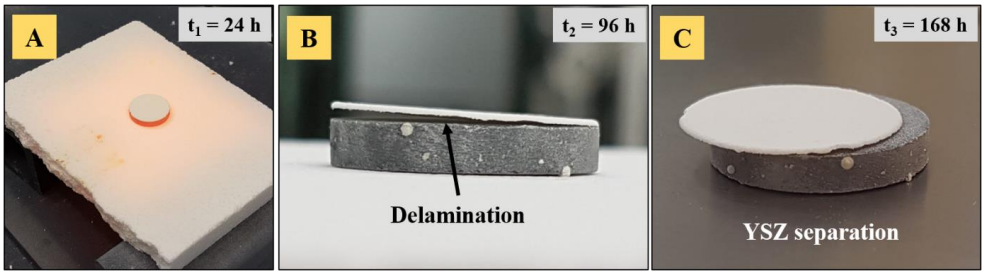

Figure 6. 33: Sample C_1: thermally cycled YSZ-coated Ti_2AlC at 1300 °C showing premature delamination and separation of the YSZ topcoat: (A) sample outside the furnace after 24 h of cycling, (B) delamination after 96 h and (C) complete spallation after 168 h.

Cross sections (Figure 6. 34) highlighted the classical features described previously. A 26 µm thick thermally grown Al_2O_3 scale was observed (Figure 6. 34, A and B). In addition, EDS point analysis of oxides above the Al_2O_3 layer showed that, alongside YSZ (3) and the Y, Zr, Ti, Al-oxide phase (2), a Ti-Al-O rich phase (1) also coexisted (Figure 6. 34, C). It might be aluminum titanate (Al_2TiO_5) arising from the reaction of α-Al_2O_3 with TiO_2 and generally found at temperatures above 1300 °C [258]. A cracked interface between the continuous Al_2O_3 scale and Al_2TiO_5 was noticed along the whole length of the sample and spread in the upper area of the Al_2O_3 scale.
Mass gain curves (Figure 6. 35) highlighted obvious larger values than for samples B_1 and B_2 cycled at lower temperature on account of more thermally grown Al_2O_3.

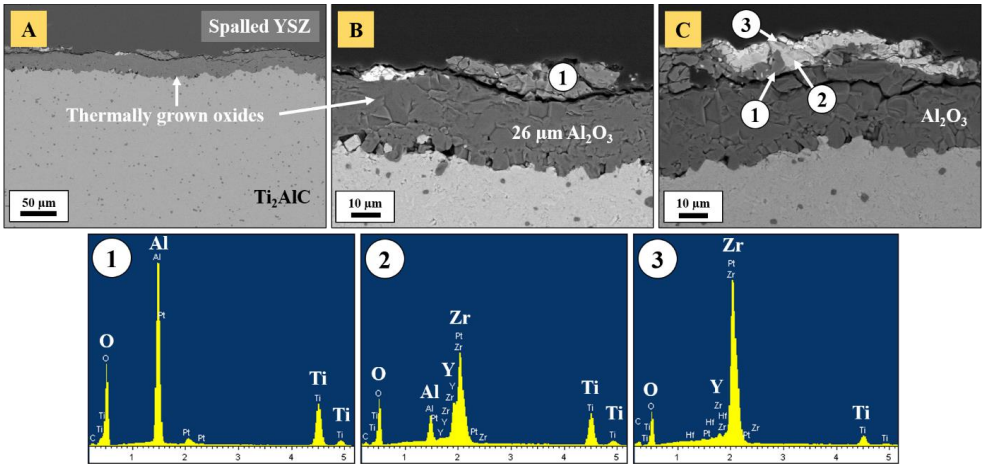

Figure 6. 34: Sample C_1: cross-section BSE images after 168 h at 1300 °C of sample shown in Figure 6. 33C: (A) overview image, (B) and (C) higher magnification on the TGO. Corresponding EDS spectra are shown.

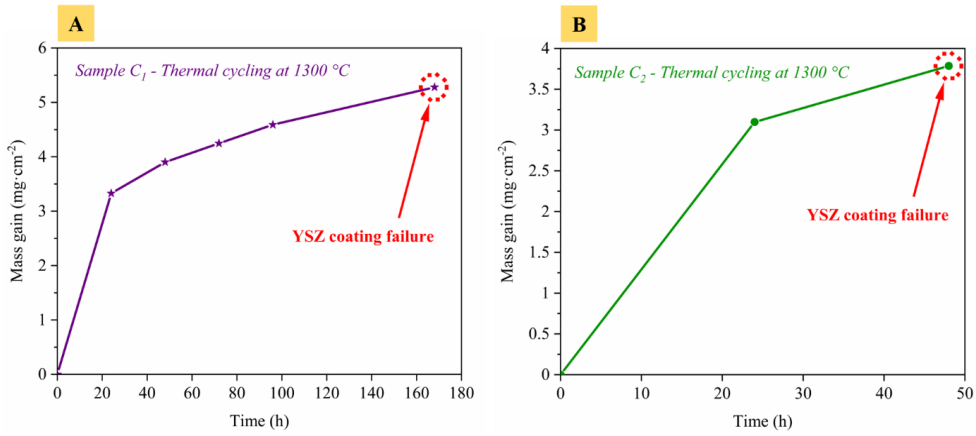

Figure 6. 35: Mass gain curves retrieved (A) for sample C_1 and (B) for sample C_2, both showing premature failure of the YSZ coating.

Apart from harsher conditions which obviously contributed to the premature coating spallation, the use of YSZ in the current temperature range is known to be critical due to phase transformation. Especially the one leading to the formation of low-temperature monoclinic ZrO_2 from the intermediate-temperature tetragonal phase is accompanied with a strong variation of volume (~3-5%) [259,260]. It can sometimes occur when the high-temperature cubic ZrO_2 phase experiences diffusionless transformation into an unstable tetragonal phase, which, in turn, separates upon high-temperature exposures.

In addition, it is known that the higher temperatures promote sintering and creep of plasma-sprayed coatings [261] and that APS-based systems experience splat-sliding as main deformation mechanism.

Nevertheless, high cycling temperatures (1300 °C) and more extreme conditions (high-velocity burner rig) were recently used by Smialek et al. [171] and demonstrated the excellent performance of PS-PVD YSZ-coated Ti_2AlC, which survived more than 500 h. The coating procedure plays an essential role, and APS-coated systems are known to be less efficacious than PS-PVD coatings [168], for which the typical columnar "cauliflower" microstructure presents a better adhesion to the substrate, and allows more strain tolerance due to the high density of fine dispersed pores. That would also partly explain the premature detachment of the APS-coated YSZ in the present case. The reaction of thermally grown oxides and the presumed formation of Al_2TiO_5 might as well contribute to the early YSZ coating failure, as the interface between Al_2O_3 and Al_2TiO_5 was fissured probably due to thermal stress generation. In fact, Al_2TiO_5 is known to have a strong thermal expansion anisotropy, with a CTE along *a*, *b* and *c* axes of -3 x 10^{-6} °C^{-1}, 11.8 x 10^{-6} °C^{-1} and 21.8 x 10^{-6} °C^{-1} in the 20-1020 °C range, respectively [258]. The spalling off of the APS coating as a single flake is a typical failure fashion of such types of systems [168].

VI-3.3 Oxidation of YSZ-coated Ti_2AlC composites

A brief thermal cycling experiment at 1200 °C was undertaken with a fiber-reinforced Ti_2AlC sample (Figure 6. 36), coated with YSZ by APS. The substrate contained 3.2 mm N720 aluminosilicate fibers, dispersed by dry mixing Ti_2AlC powder with the fibers. This procedure, upon sintering in the FAST/SPS, was found not to be effective to produce homogeneous composites. Nevertheless, these outcomes of thermal cycling presented a certain interest and were included here.

The poor dispersion of alumina fibers and their tendency to form agglomerates turned out to drastically decrease the performance of such systems. Right above the fiber agglomerates (Figure 6. 36, A), large nodules of mixed oxides were observed, typical of the striated pattern of oxide layers presented in the section *VI-2 Breakaway oxidation*. These were composed of a continuous alumina layer in the immediate vicinity of the substrate (Figure 6. 36, A and E), followed by a complex arrangement of Al_2O_3, TiO_2 and pores. A third layer of TiO_2 was located above, containing large cavities. The rapid overgrowth of such massive nodules led to decohesion of the YSZ coating. Latter was observed at the edges of the nodules (Figure 6. 36, A and B), where the deflection of the rigid topcoat ceramic was maximal. The adhesion between YSZ and TiO_2 was good and interdiffusion was observed (Figure 6. 36, A) as described in the previous section.

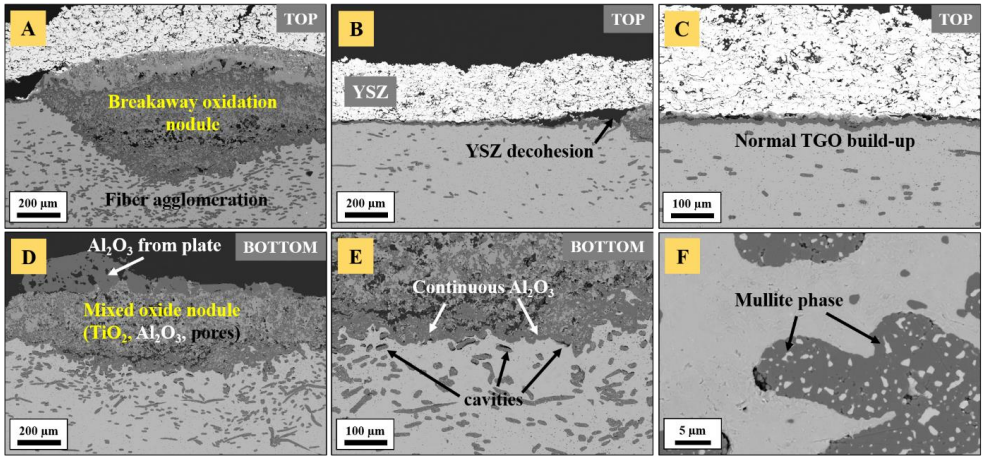

Figure 6. 36: Sample *D*: oxidation at 1200 °C for 24 h of N720 fiber-reinforced Ti_2AlC composite coated with YSZ by APS: (A) mixed oxide nodule above fiber agglomerate below YSZ, (B) nearby decohesion of YSZ, (C) continuous alumina above well-dispersed fibers, (D) mixed oxide nodule on the bottom, (E) and (F) higher magnification evidencing cavities next to fibers.

Interestingly, areas without fiber agglomerates (Figure 6. 36, B and C) presented a normal build-up of the TGO (continuous alumina layer decorated with discontinuous clusters of titania). Nodules were observed both on top (beneath the YSZ coating, Figure 6. 36, A) and bottom (Figure 6. 36, D and E, in contact with the porous alumina plate visible in Figure 6. 33, A) of the sample. In latter case, after detaching the sample from the plate, a fragment of porous alumina was found sintered to the nodule (as seen previously in Figure 6. 30, E). Higher magnification evidenced the presence of cavities nearby aluminosilicate fibers (Figure 6. 36, E), more precisely, right below the continuous thermally grown Al_2O_3 scale. Figure 6. 36F shows that the composition of fibers was unaltered after FAST/SPS – as the mullite phase was detected – to the contrary of PIM composites processed in argon, described previously in sections *V-1.2 Pressureless sintering of complex shapes* and *V-2.2 Powder bed sintering of complex shapes*. These outcomes demonstrated that fiber dispersion plays an essential role in the oxidation of fiber-reinforced Ti_2AlC. Agglomerated fibers hinder densification, even when assisted by pressure and electric-field, resulting in the formation of cavities which might facilitate oxygen ingress once breakaway oxidation is triggered. However, it is still not clear why a continuous alumina scale formed at the bottom of the nodule and through which precise mechanisms the oxidation of Ti_2AlC at these specific spots was catastrophic. As explained in the section *VI-2 Breakaway oxidation*, a porous network within the Ti_2AlC substrate can be detrimental to the oxidation performance, as more oxidation-sensitive crystallographic planes

(other than those present on the flat surface) are exposed. In this way, the selective oxidation of Al is hampered. Instead, all elements (Ti, Al, C) are oxidized in an uncontrolled manner.

VI-3.4 Burner rig testing

The issues related to the machining of burner rig substrates (see Figure 2. 11) and the availability of the facility restrained the number of tested samples to a single one and made it challenging to conduct a systematic thermal cycling study. Figure 6. 37 depicts the monolithic Ti_2AlC sample after 503 cycles at a surface temperature of ~1400 °C in a Mach 0.03 burner rig (velocity of the exhaust gas stream ~ 8 m/s). Large fissures propagating in the YSZ topcoat were observed. An orangish/ocher-colored tinge was seen below the coating. Overall, in spite of crack evolution, the YSZ coating remained on the Ti_2AlC substrate and did not significantly spall off, apart from two delaminated spots.

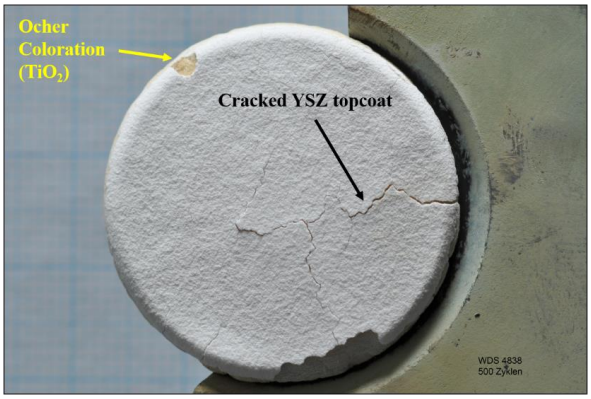

Figure 6. 37: Burner rig thermally cycled APS-YSZ/Ti_2AlC sample after 503 cycles (~60 h) at 1400 °C.

The recorded temperatures are displayed in Table 6. 3 and Figure 6. 38. The surface temperature (front side) was maintained close to a mean value of 1402 °C, the minimum of 939 °C being recorded at the beginning of the experiment and the maximum of 1494 °C resulting from the system's inertia and the time to stabilize. Considering the percentiles T_{10}, T_{50} and T_{90}, the surface temperature can be considered as fairly constant. The substrate temperature (measured on the back side), to the contrary, was subjected to significant variations. While initially set at 1100 °C, it gradually decreased for two main reasons.

Table 6. 3: Temperatures recorded during burner rig cycling (minimum, maximum, mean values, as well as percentiles T_{10}, T_{50} and T_{90} are indicated).

Statistics	Surface temperature (°C)	Substrate temperature (°C)
minimum	939	730
mean	1402	977
maximum	1494	1110
T_{10}	1384	912
T_{50}	1400	981
T_{90}	1426	1068

The first arouse due to the formation of a thick oxide scale (visible on cross-sections below) and, hence, the change in the thermal conductivity of the considered thickness (not being taken into account in the measurement software). In addition, the emissivity of the substrate changed, which led to a bias in the measurement of the substrate temperature with the pyrometer. The second resulted from the first cracks, presumably appearing after ~350 cycles, with a sudden drop in temperature. This may be caused by the strongly insulating air gaps at cracks, while the software still considered the initial values of thickness and thermal conductivity.

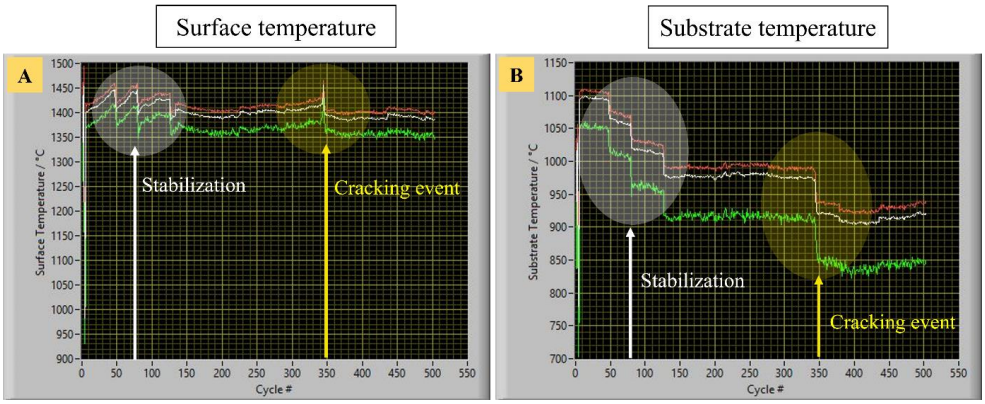

Figure 6. 38: Recorded surface and substrate temperatures versus cycle number.

Figure 6. 39 presents the sample cross-section. An ~520 µm thick mixed oxide scale composed of Al_2O_3 (dark-grey phase), TiO_2 (light-grey phase) and pores grew between the Ti_2AlC substrate and the YSZ coating, typical of the breakaway oxidation micro-banding morphology described in the section *VI-2 Breakaway oxidation*. Interdiffusion of YSZ in the upper area of the mixed oxide layer (white dots) and TiO_2 in the bottom area of YSZ was observed.

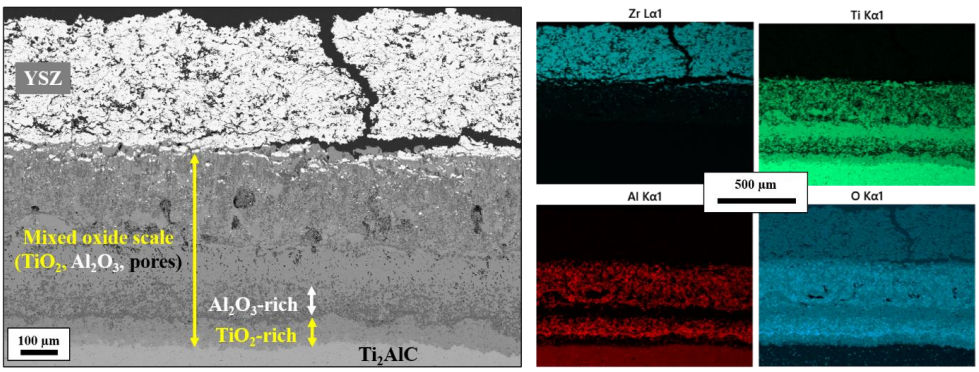

Figure 6. 39: Thermal cycling experiment under burner rig condition of APS YSZ-coated Ti_2AlC with cross-sectional view and corresponding EDS elemental maps.

Additionally, two large cracks were observed, one transversal in the YSZ coating and the other along the YSZ/oxide interface. The EDS mapping highlights the micro-banding morphology in more details, with alternating stripes of Al_2O_3-rich and TiO_2-rich bands, as well as highly porous layers. Even though the outcomes of the present experiment highlighted coating fissuring after ~42 hot hours, the APS-YSZ/Ti_2AlC system still exhibited a better performance

than a new generation PS-PVD-Gadolinium Zirconate/YSZ double-layered thermal barrier coating applied on Inconel-738 substrates with a NiCoCrAlY bond coat [262].
Further, the study published by Smialek et al. [171] showed that YSZ/Ti_2AlC systems can be highly durable and survive more than 500 cycles at a surface temperature of 1300 °C. Again, the advantage of PS-PVD coatings over APS was mentioned.

VI-4 Oxidation of PIM components

Powder injection molded components, densified by the two routes described in sections *V-1.2 Pressureless sintering of complex shapes* and *V-2.2 Powder bed sintering of complex shapes*, were oxidized at three different temperatures to investigate the effect of relative density on the oxidation response of complex shapes. All these components were gently sandblasted before oxidation, so as to obtain a homogeneous surface finish and the same roughness entirely on the sample. These are preliminary results and obviously, there is room for optimization. However, the present thesis can serve as base for future work.
Figure 6. 40 shows the outcomes at an oxidation temperature of 1000 °C. The monolithic nut densified by PS at 1400 °C, i.e., with a relative density around 92.6%, was slightly tinged with a beige-colored oxide, most probably a thin layer of a mixed oxide (Figure 6. 40, A). The monolithic sample which was further densified by PBS at 1200 °C (Figure 6. 40, D), i.e., with a relative density around 97.0-97.5%, did not exhibit any sign of breakaway oxidation. Only corners/edges showed a slight orangish coloration, spots where larger rutile TiO_2 patches must have formed.

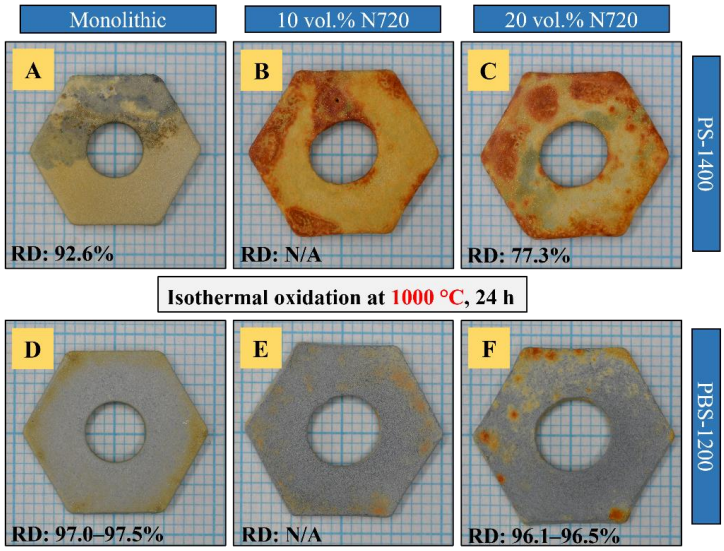

Figure 6. 40: PIM hexagonal nuts densified via 2 different techniques and isothermally oxidized in static air at 1000 °C for 24 h. As a reminder, PS-1400 stands for pressureless sintering, PBS for powder bed sintering. RD designates the relative density after sintering.

The incorporation of 10 vol.% (Figure 6. 40, B) and 20 vol.% (Figure 6. 40, C) N720 aluminosilicate fibers presented a detrimental effect to the composite's oxidation response when densified by PS-1400. In fact, the sample was covered with the typical breakaway oxidation color, which has been extensively described in the previous sections. The strong orange coloration indicated that thick mixed oxide scales must have formed. It is believed that

the poor densification (~77.3% of the TD) resulting from fibers hindering sintering was the main reason of abnormal oxidation, as less oxidation-resistant planes were exposed in micro-cavities. A significant difference was observed for the PBS samples containing the same volume fraction of fibers (Figure 6. 40, E and F). The RD of such samples reached ~96.1-96.5% of the TD. The oxidation outcome of the 10 vol.% N720 hexagon nut (Figure 6. 40, E) was similar to the equivalent monolithic sample (Figure 6. 40, D), while the specimen with the largest volume fraction of fibers (Figure 6. 40, F) presented isolated spots of TiO_2 nodulation, most of the time located nearby corners and edges.

Figure 6. 41 depicts the outcomes at an oxidation temperature of 1100 °C. Apart from more pronounced effects arising from the higher oxidation temperature, the oxidation pattern was more or less similar to that observed for samples oxidized at 1000 °C. PIM parts densified by PS at 1400 °C, i.e., with the lowest RD, were covered with breakaway mixed oxides in their entirety, whether without (Figure 6. 41, A) or with fibrous reinforcement (Figure 6. 41, B and C). The PBS monolithic Ti_2AlC nut (Figure 6. 41, D) presented a thicker rutile covering than its counterpart oxidized at 1000 °C recognisable from the orange coloration found on the whole sample.

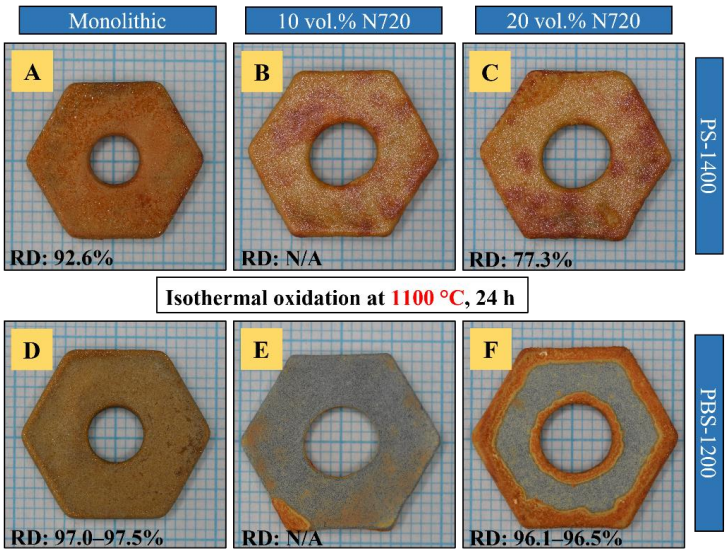

Figure 6. 41: PIM hexagonal nuts densified via 2 different techniques and isothermally oxidized in static air at 1100 °C for 24 h.

Surprisingly, the sample containing 10 vol.% N720 fibers (Figure 6. 41, E) presented a better oxidation response. With 20 vol.% fibers (Figure 6. 41, F), the central area of the specimen had a good oxidation resistance (with the grey color of the substrate filtering through the transparent Al_2O_3 scale). However, sharp edges, such as at the thread and each side of the hexagon nut, were decorated with large overgrown TiO_2-rich oxides.

At a higher oxidation temperature of 1200 °C (Figure 6. 42), the same trend was observed, again with more pronounced formation of oxides due to accelerated diffusional phenomena and thicker scales. Monolithic samples densified by PS-1400 (Figure 6. 42, A and D) experienced breakaway oxidation for reasons mentioned above. The higher density of PBS parts (Figure 6. 42, B and E) resulted in a better response to oxidation, with most of the surface area covered with a thin transparent alumina scale. As described before, rutile overgrowth took place at specific spots, e.g., at the thread edge or nearby nut sides and at tips of sprocket teeth.

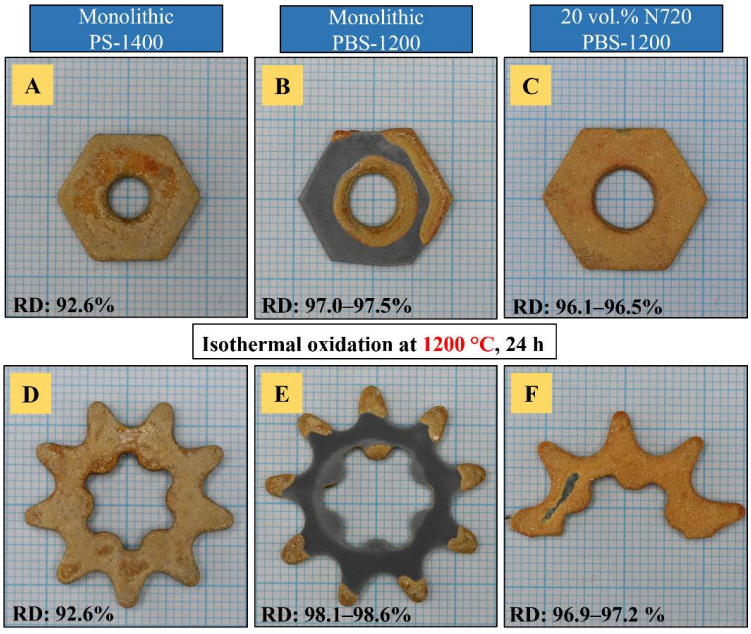

Figure 6. 42: PIM components densified via 2 different techniques and isothermally oxidized in static air at 1200 °C for 24 h.

These areas are either subject to different stress states – a sharp side being non-planar and experiencing a different type of oxide growth than a plane surface – or depleted faster with Al in reason of their thin geometry (tips). Breakaway oxidation was also noticed for 20 vol.% N720 composites densified by PBS (Figure 6. 42, C and F). Whereas it was limited to some specific locations at lower temperatures (1000 °C, 1100 °C), the overgrowth of TiO_2 affected the entire component at 1200 °C.

These outcomes demonstrated that full or near-full densification is required to allow the excellent oxidation resistance of Ti_2AlC to be exploited. As the inherent sinterability of MAX phases without sintering additives or external pressure is low, field and pressure-assisted techniques are required to fulfil these conditions.

In summary, a normal build-up of continuous and dense Al_2O_3 with small clusters of TiO_2 was observed for smooth surfaces. To the contrary, rough surfaces – e.g., abraded through sandblasting – experienced rumpling, buckling and, eventually, blistering of the alumina scale. This, in turn, could facilitate the transition to a breakaway oxidation regime. When these blisters collapsed, breakaway kinetics were immediately engaged. The resulting mixed oxide scales were pervious to oxygen. This is why short-circuit channels and pores accelerated the recession of the Ti_2AlC/oxide interface and promoted a rapid consumption of the specimen. In a similar fashion, porous samples were subject to breakaway oxidation. However, not only the oxidation performance is strongly affected by the density, but also the mechanical properties.

Chapter VII: Mechanical properties

The present thesis targets three major work packages: 1) the optimization and scaling-up of the synthesis of Ti_2AlC, 2) the manufacturing of monolithic and composite Ti_2AlC components by powder injection molding and 3) the evaluation of the oxidation performance of Ti_2AlC-based assemblies. As such, mechanical characterization was only undertaken as peripheral investigation. Therefore, the outcomes displayed here serve as preliminary data and can give rise to future experimental considerations.

VII-1 Fractographic analyses

VII-1.1 Monolithic Ti_2AlC

The fine-grained microstructure of FAST/SPS sintered MS^3-Ti_2AlC was presented in section *V-2. FAST/SPS*. It has been shown that dwell time has little influence on grain growth. As such, the fractographic analysis performed on these samples (Figure 7. 1) highlighted typical fracture surfaces of fine-grained material (Figure 7. 1, A) and a dominant intergranular fracture mode (Figure 7. 1, B). Higher magnification on these surfaces showed, that each single grain was well-defined as cracks essentially propagated on grain boundaries, leading to grain boundary decohesion. The intergranular fracture mode is generally caused by the formation of dislocation pileups. A few grains evidenced a transgranular fracture mode, as a result of stress accumulation on cleavage planes and cracks propagating along them [263]. The layered structure of the MAX phase was therefore visible. The absence of texturing evidenced in section *V-2. FAST/SPS* indicated that a strong random orientation of crystallographic planes was found in sintered MS^3-Ti_2AlC. Therefore, it resulted in a strong misalignment of slip systems, partly explaining why transgranular fracture was less observed. The prevalent intergranular fracture mode over the transgranular one is essentially due to the fine-grained microstructure. In fact, coarse-grained microstructures generally highlight more fractured grains [73], potentially resulting from a higher probability of slip systems alignment. While fine-grained microstructures possess advantages such as higher hardness or better oxidation response, coarse-grained microstructures allow for numerous local transitions from intergranular to transgranular fracture and a reduction of crack propagation rates [263].

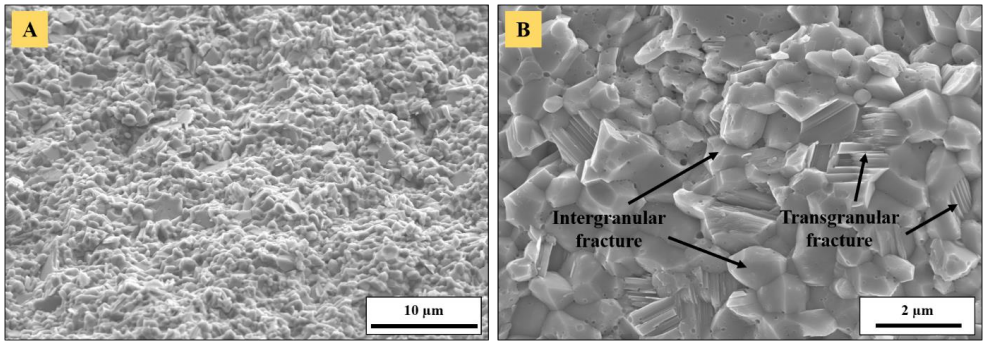

Figure 7. 1: Fracture surface of Ti_2AlC sintered by FAST/SPS at 1200 °C, 50 MPa for (A) 30 min (overview at low magnification) and (B) 60 min (higher magnification to evidence dominant fracture modes).

VII-1.2 Fiber-reinforced Ti_2AlC composites

VII-1.2.1 FAST/SPS sintered composites

Fracture surfaces of Ti_2AlC reinforced with N720 aluminosilicate fibers, sintered by FAST/SPS via the classical dry mixing route are depicted in Figure 7. 2. Fibers and matrix were at the same level, no offset was observed (Figure 7. 2, A). The absence of topographical differences was confirmed by SE images (Figure 7. 2, C), but here, BSE mode images were used to better discern fibers (Figure 7. 2, A and B). Fracture surfaces highlighted neat cuts and absence of fiber debonding and pullout (Figure 7. 2, B). That is caused by strong fiber/matrix interfaces. In addition, a slight coarsening of edge grains in fibers were observed, at the interface between fiber and Ti_2AlC matrix (Figure 7. 2, C). This interfacial grain growth phenomenon has already been reported for aluminosilicate [197] and sapphire fibers [196].

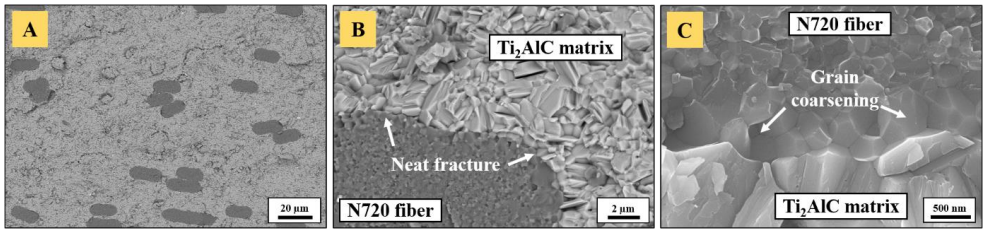

Figure 7. 2: Fracture surface of Ti_2AlC + 10 vol.% N720 aluminosilicate fibers sintered by FAST/SPS at 1200 °C, 50 MPa: (A) low magnification BSE image, (B) neat equal cut through fiber and matrix and (C) grain coarsening at the interface.

VII-1.2.2 Powder injection molded components

Outcomes of the fractographic analysis of an injection-molded $Ti_2AlC/N720\text{-}Al_2O_{3(f)}$ composite are depicted in Figure 7. 3. Graphite residues were trapped in the thread (Figure 7. 3, A) after PBS and could not be removed by sandblasting. Although this work demonstrated the feasibility of injection molding of hexagon nuts with threaded holes, a post-sintering machining step would be required to adjust the thread pitch.

As nuts were mainly uniaxially pressed during PBS, the thread pitch and angle changed and diverged from the initial M8 DIN standard dimension. Figure 7. 3B highlights the presence of submicrometric cavities that are generated by the decomposition of the mullite phase. Even though the integrity of fibers was not altered, and the alumina grain size remained submicrometric, the presence of pores within the reinforcement phase surely led to a decrease of its strength [238]. Therefore, the fibers could easily deform even in pressureless conditions due to expected higher creep rates. Limited fiber pull-out – the length of which was approximately 15-20 µm for the considered area – was observed (Figure 7. 3, C and D) as for $Cr_2AlC/Al_2O_{3(f)}$ [199], and may have contributed, to a minimal extent, to the overall strain energy-absorbing behavior of the composite. The absence of matrix/fiber interfacial coating usually results in a fairly strong interface, and the fracture surfaces of Al_2O_3 fiber-reinforced Ti_2AlC generally demonstrated neat cuts throughout the matrix and fibers, as shown before. Here, the near-fiber porosity may have facilitated interfacial crack propagation and fiber sliding, as it directly affects the work for debonding and the work to pullout. Fiber flattening (Figure 7. 3, D) may have resulted from the decrease in strength induced by the decrease in the amount of mullite and the generation of porosity. As mentioned earlier, this was observed after the first PS step at 1250 °C, at which temperature N720 fibers must have plastically deformed. Typically, they exhibited an elliptical cross-section with a major axis of 20 µm and a minor axis

of 8 µm, deviating from the initial circular cross-section with Ø 12-14 µm. Even though prolate fiber cross-sections were also observed for composites produced by the dry mixing method and conventional FAST/SPS of the powder/fiber mixture (Figure 7. 2), it is not clear – as no fiber pullout was observed – if it resulted from fiber flattening or if the cutaway plane was not perfectly orthogonal to the fiber axis.

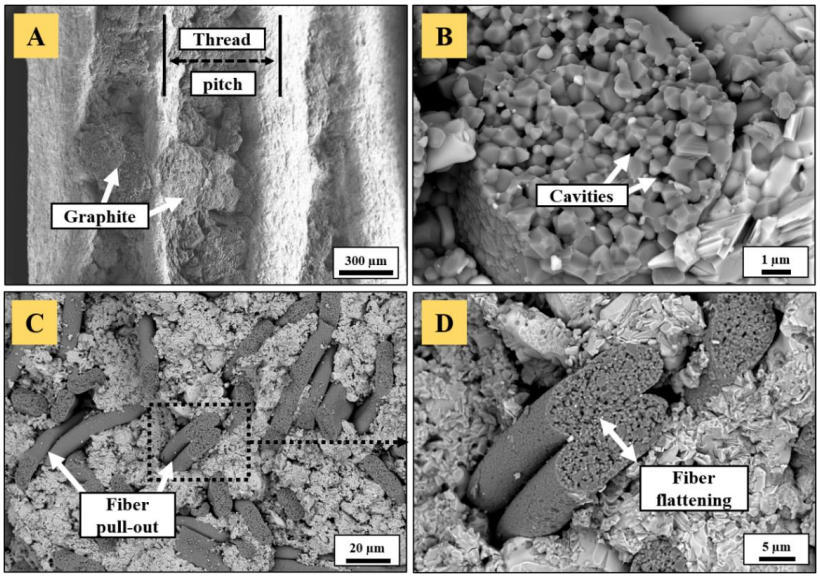

Figure 7. 3: Fracture surface of a Ti_2AlC nut reinforced with 20 vol.% N720 fibers: (A) thread containing graphite residues after PBS, (B) submicrometric pores arising from mullite decomposition, (C) partial fiber pull-out observed at (D) higher magnification with fiber flattening.

VII-2 Vickers hardness and apparent fracture toughness

Vickers indentation (Figure 7. 4) was carried out at different loads to evaluate the response of monolithic and fiber-reinforced Ti_2AlC composites. At loads of up to a 10 kilogram-force (~98 N), no radial cracks were visible for monolithic samples (Figure 7. 4, A). Instead, the chipping of the deformed material was observed, and started to appear at loads of 5 kgf (~49 N), probably as a result of subsurface crack propagation around the indent and subsequent collective grain pullout. This flaking was more pronounced with increasing applied load, as also reported by Amini et al. [264] for Ti_2SC, due to it having a larger pseudo-plastic zone. These outcomes are in agreement with one of the hallmarks of MAX phases – their damage tolerance [18,264,265] as a result of basal slip activation. At higher loads (30 kgf), monolithic Ti_2AlC accommodated the stresses in the form of massive material pileup (Figure 7. 4, B). This mechanism is well known for MAX phases and takes place as the material absorbs the strain energy through the formation of kink-bands, delamination, and buckling [86,265]. Radial cracks propagating from the four corner points of the indents were observed for applied loads of 20 kgf (~196 N) and 30 kgf (~294 N) (Figure 7. 4, C). They belong to the Palmqvist type of crack as their crack-to-indent ratio size $\left(\frac{l}{a}\right)$ was below 2.5 [219,266]. These have not usually been observed for coarse-grained monolithic MAX phases, such as Ti_3SiC_2 [265], Ti_2SC [264] or Cr_2AlC [198]. However, fine-grained Ti_2SC presented radial cracks that started to appear from loads of 50 N, indicating its greater brittleness compared to its coarse-grained Ti_2SC counterparts [264] and Ti_2AlC with the equivalent grain size (Figure 5. 16 and Table 5.

4). From the apparent crack length, a rough estimation of the apparent toughness K_{IC} could be made using the following formula [219]:

$$\frac{K_{IC}\Phi}{Ha^{\frac{1}{2}}}\left(\frac{H}{E\Phi}\right)^{\frac{2}{5}} = 0.048\left(\frac{l}{a}\right)^{-\frac{1}{2}} \qquad \text{(Equation 48)}$$

with Φ as a constraint factor (~3), H as the hardness, E (=277 GPa [220]) representing the Young's modulus, a as the half-diagonal of the indent and l representing the Palmqvist crack length. The apparent fracture toughness yielded 10.04 ± 0.47 MPa·m$^{1/2}$ for pure Ti_2AlC. This value is within the range of K_{IC}, reported for various MAX phases [18], though is higher than that measured by a single-edge notched beam test for coarse-grained Ti_2AlC (6.5 MPa·m$^{1/2}$) [73] and fine-grained $Ti_2AlC_{0.7}$ (6.5 MPa·m$^{1/2}$) [223]. It has to be emphasized that the toughness determined here accounts for Ti_2AlC with ancillary phases of Ti_3AlC_2 and Al_2O_3 (Figure 5. 16) and solely provides an estimation of the critical stress intensity factor. As the formula contained approximations, such as Φ and the E-modulus, retrieved from other studies, measured crack length diverging from the real crack length and the consideration of a Palmqvist crack regime, the accuracy of the calculated value is less reliable than conventional fracture toughness measurement methods.

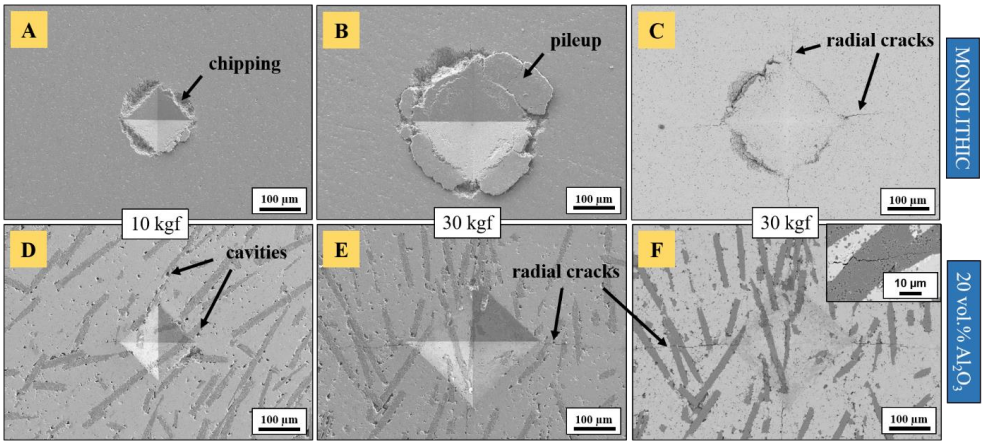

Figure 7. 4: Vickers indentations on powder bed sintered monolithic and aluminosilicate fiber-reinforced (20 vol.%) Ti_2AlC composites. (A), (B), (D) and (E) are SE images, (C) and (F) are BSE images.

While monolithic samples clearly exhibited energy-absorbing mechanisms, such as material chipping (Figure 7. 4, A) and pileup (Figure 7. 4, B), these were inhibited in the presence of fibers (Figure 7. 4, D-F). While chipping was sometimes observed for indentations present in the bare Ti_2AlC matrix, material delamination, pileup and flaking off were not observed when the indenter tip hit fibers. Instead, the indentations were perfectly pyramidal. The near-fiber cavities that were mentioned earlier were evidenced on secondary electron images (Figure 7. 4, D and E). Radial cracks emanating from indentation corners were observed at lower loads (5 kgf, ~49 N) than for their monolithic counterparts, here visible on Figure 7. 4E and F at 30 kgf (~294 N). The presence of cracks at lower loads justified the increase in brittleness of Ti_2AlC composites as compared to their monolithic homolog, due to the incorporation of a large volume fraction of the brittle reinforcement phase. Likewise, these radial cracks were reported for $Cr_2AlC/SiC_{(f)}$ systems [198] at loads of 5 and 20 kgf. The apparent toughness was estimated the same as for monolithic samples and yielded 7.90 ± 0.66 MPa·m$^{1/2}$. The decrease in

toughness can be explained by two joint facts: the addition of stiff ceramic fibers curbing the energy-absorbing abilities of Ti_2AlC and the strong bonding between the fibers and matrix, not allowing cracks to be deflected at the interface. In fact, in general, through-fiber crack propagation was observed (inset in Figure 7. 4, F) with limited deflection. Even though the addition of alumina fibers without coating or tailoring of the interface/interphase did not promote an increase in toughness, it is expected that the overall strength, for example, in compression, can be improved [212], and that creep rates could potentially be reduced.
The evolution of Vickers hardness versus applied indentation load is given in Table 7. 1. In general, little influence of fiber addition on the hardness was observed, as the values remained within the range of the standard deviation. These fall into the 2-8 GPa range, known for polycrystalline MAX phases [18]. They were mostly between 5.5 GPa and 6.7 GPa and were higher than those reported for coarse-grained Ti_2AlC [18,44,67,73]. A closer hardness value (5.8 GPa) was reported for fine-grained (~6 µm) non-stoichiometric $Ti_2AlC_{0.7}$ [223]. At low loads, the surface area of indents was small, and the average diagonal length yielded 54 µm and 123 µm for 1 kgf and 5 kgf, respectively. Therefore, hardness values in the case of composite samples with low to intermediate fiber volume fraction cannot be as accurate as for monolithic Ti_2AlC. These are rather an average representation of hardness, with selective consideration for either the bare Ti_2AlC matrix or of single alumina fibers. From 10 kgf, the surface area of indents was large enough to provide a realistic estimation of composite hardness (average diagonal length was 172 µm) and the maximum average diagonal length of indents produced at 30 kgf yielded 289 µm. A slight increase in hardness was measured at the lowest fiber volume fraction (5 vol. %), while it decreased for the highest content (20 vol. %). The latter can be explained by the lowest densities which reached for composites with significant addition of fibers. Furthermore, with a finer grain size distribution, the decrease in Vickers hardness with the applied load is less marked [18], as compared to coarse-grained microstructures. This is why, in most cases, hardness curves tended towards an asymptote, as demonstrated for Ti_2SC [264].

Table 7. 1: Vickers hardness of powder bed sintered monolithic and Al_2O_3 fiber-reinforced Ti_2AlC composites. Vickers hardness is given for loads of 1, 5, 10, 20 and 30 kgf. Blank values for HV1, 5 and 20 are account of non-pyramidal indentations.

Samples	**Hardness (GPa)**					**Apparent K_{1C} ($MPa \cdot m^{1/2}$)**
	HV1	**HV5**	**HV10**	**HV20**	**HV30**	
Monolithic	6.14 (±0.31)	5.82 (±0.35)	6.16 (±0.45)	5.92 (±0.49)	5.87 (±0.54)	10.04 (±0.47)
5 vol.% N720	N/A	N/A	6.67 (±0.59)	6.17 (±0.15)	6.13 (±0.32)	N/A
10 vol.% N610	6.21 (±0.77)	6.17 (±0.34)	5.95 (±0.43)	N/A	5.79 (±0.32)	N/A
20 vol.% N720	5.51 (±0.39)	5.89 (±0.38)	5.52 (±0.34)	5.62 (±0.35)	5.39 (±0.16)	7.90 (±0.66)

VII-3 High-temperature compressive strength

Initially, in the framework of the PhD, a research stay was planned in Japan, in order to conduct high-temperature mechanical characterization. However, due to the outbreak of COVID-19 and the restrictions arising during the pandemic, this plan was discarded. Instead, the samples were sent to Saitama University, Department of Mechanical Engineering in Japan. Room temperature (RT) and high-temperature (HT) (at 1000 °C and 1100 °C) static compressive strength of monolithic and N610-reinforced Ti_2AlC was investigated. The results are listed in Table 7. 2. Due to the limited number of samples, only 2 specimens per condition

were tested. The outcomes presented here are not part of the main objectives of the thesis but rather provide an order of magnitude for the compressive strength of Ti_2AlC-based systems.
At RT, the compressive strength of monolithic Ti_2AlC was 523 MPa, which is surprisingly twice less than the value reported at a strain rate of 10^{-4} s^{-1} for fine-grained (~5-6 μm) pure Ti_2AlC (3-5 vol% $TiAl_x$, without ancillary phases of Ti_3AlC_2 or TiC) [181]. Intermetallics can contribute to the ductile deformation and therefore increase the compressive strength, as mentioned by Bei et al. [267] for $Ti_3Al_{0.8}Sn_{0.2}C_2$. The higher content of Ti_3AlC_2 in this work (Table 5. 2) may have influenced the measurements. Ancillary phases can indeed drastically modify the compressive performance of Ti_2AlC. Such variations were observed by Bei et al. [267] as the bare Ti_3AlC_2 sample exhibited significantly lower strength (545 MPa) than the solid solution $Ti_3Al_{0.8}Sn_{0.2}C_2$ (839 MPa). In fact, the measured compressive strength would rather correspond to the values of Ti_3AlC_2 for quasi-static loadings, which were reported to be 560 MPa [227] or 545 MPa [267]. There is little chance that the observed low value is on account of a length-to-diameter ratio (8:4) of the samples, that is higher than that used by Parrikar et al. [181] (8:5), since Bai et al. [177] measured a RT compressive strength of almost 1200 MPa with a ratio of 12.5:5 and close to 1000 MPa with a ratio of 8:5. At a loading rate of 10^{-4} s^{-1} and a length-to-diameter ratio of 8.5:6, the RT compressive strength of coarse-grained Ti_2AlC (~570 MPa) was found closer to the value measured in the present work [268]. With increasing temperature, above the BPTT, the compressive strength naturally decreased as expected and yielded 369 MPa and 158 MPa at 1000 °C and 1100 °C, respectively. Again, these values are lower than those generally reported in literature, even for coarse-grained microstructures [181]. For fine-grained Ti_2AlC, Parrikar et al. [181] indeed reported values around 550 MPa (1000 °C) and 300 MPa (1100 °C). For coarse-grained Ti_2AlC, though, Meng et al. [268] reported a lower value at 1000 °C (slightly above 300 MPa) but higher at 1100 °C (~250 MPa). The BPTT measured here was 741 °C under a load of 100 MPa, which is in the 700-950 °C range reported for Ti_2AlC under compression [176,177]. The addition of N610 alumina fibers significantly increased the RT compressive strength of Ti_2AlC by a factor 2.5. However, above the BPTT, the HT compressive strength decreased more rapidly than for monolithic samples. The measured BPTT for composites also falls within the classically observed range.

Table 7. 2: Compressive strength at room temperature, 1000 °C and 1100 °C for monolithic and composite Ti_2AlC. *Difficult measurement due to failure at low stress. †Too soft to evaluate.

Samples	Compressive strength (MPa)			BPTT (under 100 MPa)
	RT	1000 °C	1100 °C	
Monolithic	523	369	158	741
5 vol.% N610	1349	50-200*	69	672*
10 vol.% N610	1286	335	10-40†	775

To summarize, the characterization of mechanical properties constitutes a preliminary investigation, which was undertaken alongside the main objectives of the present thesis. The above-average Vickers hardness of Ti_2AlC samples can be on account of its finer microstructure and the Hall-Petch strengthening phenomenon. While monolithic samples tend to dissipate the fracture energy with micro-mechanisms typical of the MAX phases, the addition of rigid alumina fibers impeded this ability. The latter allowed no increase neither in hardness nor in fracture toughness, but they improved the room-temperature compressive strength of Ti_2AlC. Fiber coatings and tailoring the matrix/fiber interface could potentially contribute to improve the composite's toughness, but these were out of the scope of this PhD.

Chapter VIII: Conclusion and outlook

The present thesis demonstrates the successful development of Ti_2AlC/fiber composites destined to be used in harsh oxidizing environments. Several different aspects were investigated. The focus was essentially set on the oxidation response of Ti_2AlC-based systems, in addition to providing a thorough description of the synthesis of raw materials, the injection molding of near net shape components, the densification thereof and preliminary mechanical characterization. A detailed point-by-point summary and an outlook are given as follows:

- Synthesis of Ti_2AlC powders

The Ti_2AlC MAX phase powders were synthesized by means of the newly developed molten salt shielded synthesis (MS^3) route. At a temperature of 1000 °C, a dwelling time of 5 h and with a Ti:Al:C = 2:1:0.9 molar ratio, Ti_2AlC powders with an optimal purity of 91 wt. % were produced. These optimized parameters were used for the scaling up procedure, which allowed for the synthesis of up to 1 kg batches and the rapid formation of a stock of Ti_2AlC powders for injection molding feedstocks.

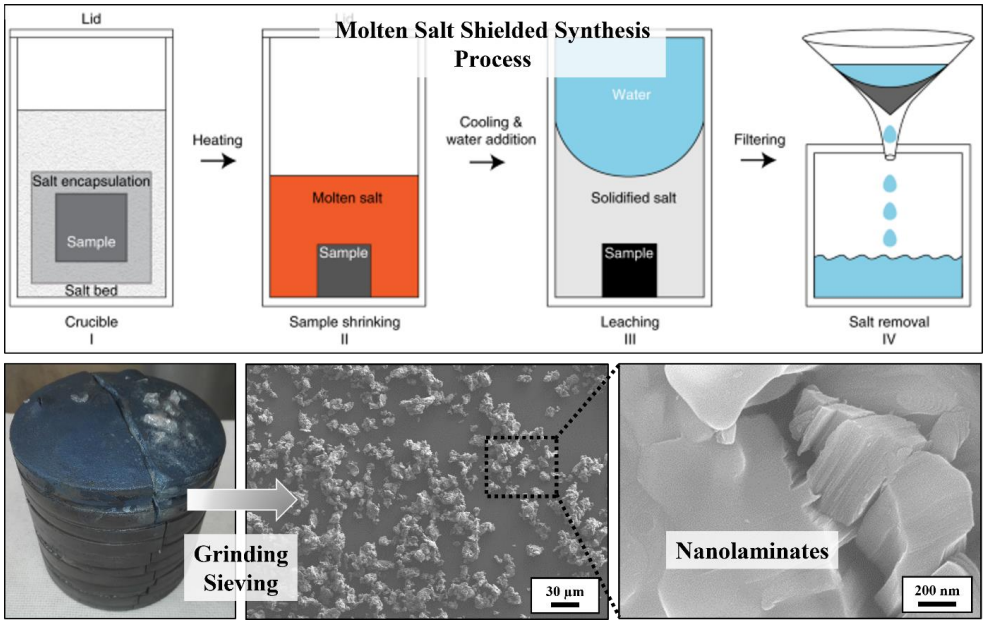

- Injection molding of complex shapes

Powder injection molding enabled the rapid manufacturing of complex near net shapes made of monolithic and alumina fiber-reinforced Ti_2AlC. As such, hexagonal nuts, sprockets and components for turbine engines with limited defects were produced, by using a solids loading of 50 vol.%. The distribution of fibers was excellent, even in composites containing a significant volume fraction of reinforcement (20 vol. %). These were essentially aligned in the direction of flow. Specific areas, such as at the mold entering, at corners and in the specimen's core, were also subject to heterogeneities. Afterwards, the optimal two-step debinding procedure consisted in a solvent extraction in n-hexane at 60 °C for 2 days, followed by thermal burnout at 500 °C for 2 h in argon.

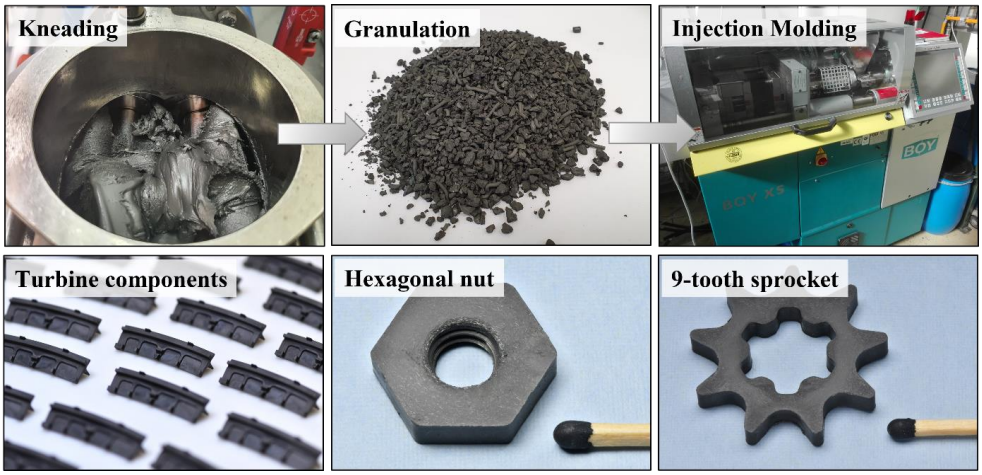

- Densification of Ti_2AlC

Pressureless sintering of cylindrical test samples at 1300 °C in argon resulted in incomplete densification, with a relative density of ~70-75%. Increasing the sintering temperature to 1400 °C helped to achieve a relative density of ~88-90%, but it promoted the phase conversion of Ti_2AlC to Ti_3AlC_2 and a reduction in Ti_2AlC purity. Therefore, FAST/SPS was required to almost fully densify Ti_2AlC, achieving a relative density of 98.5% at 1200 °C and 50 MPa. Dense Ti_2AlC samples exhibited a fine-grained microstructure, with an average grain size below 1 µm, and experienced limited phase alteration.
In the case of powder injection molded complex shapes, after binder removal, the pre-sintering step at 1250 °C without external pressure resulted in highly porous samples with relative densities of 70.1 and 65.5% for monolithic and fiber-reinforced Ti_2AlC, respectively.

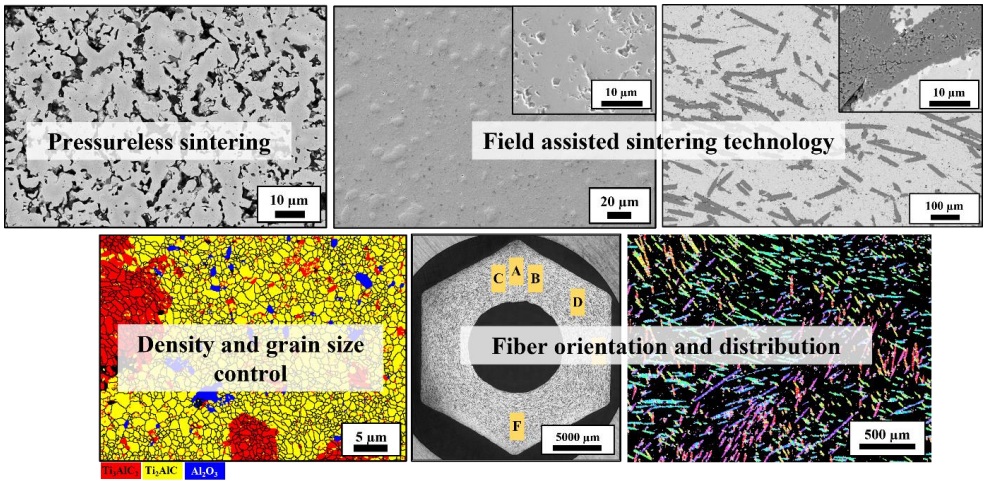

Pressureless sintering at 1400 °C notably increased the relative density of monolithic parts to 92.6%, but fiber composites experienced little changes, especially when high fiber content was used. The relative density reached 77.3%. While monolithic components experienced between 13 and 19% isotropic shrinkage in the 1250-1400 °C range, anisotropic sintering shrinkage of

composite parts led to significant warpage at higher temperature. FAST/SPS in a bed of graphite powder provided a sufficient driving force to densify monolithic parts up to 98.6% and fiber composites up to 97.2% of the theoretical, while preserving the phase composition and fine-grained microstructure. The overall fiber orientation distribution resulted in a more pronounced shrinkage along the axis parallel to the injection channel leading to asymmetrical dimensions. In addition, the reducing atmosphere during the sintering procedure caused a decomposition of the mullite phase contained in Nextel™ 720 alumina fibers and resulted in the formation of micro-cavities within alumina. In turn, the strength of fibers was reduced, and their cross-section became elliptical due to compression.

- Oxidation response

The fine-grained microstructure was an advantage during oxidation experiments. Multiple pathways for Al out-diffusion allowed for fast buildup of protective Al_2O_3 scales atop Ti_2AlC specimen. Interestingly, surface roughness strongly influenced the morphology of the oxide scale, a phenomenon which has practically not been explored so far. While smooth surfaces were mainly composed of dense and continuous α-Al_2O_3, decorated with small rutile-TiO_2 clusters, rough surfaces showed more disproportionate formation of TiO_2 crystals. It is believed that protrusions are areas where rapid depletion of aluminum occurs, followed by outward diffusion of titanium through Al_2O_3 grain boundaries. Larger TiO_2 islands covered Al_2O_3 scales on sandblasted samples. In addition, a phenomenon of scale rumpling – i.e., strong undulation of the oxide scale – was noticed for the latter samples, oxidized at 1200 °C for short times (24 h at most), most probably due to a synergy between various mechanisms. It may have found its origin in a lateral straining of the alumina scale caused by growth stresses. In turn, the significant equi-biaxial compressive stress state, coupled to premature delamination of the Al_2O_3 scale, induced its buckling. This rapidly evolved towards a phenomenon of blistering of the protective alumina scale.

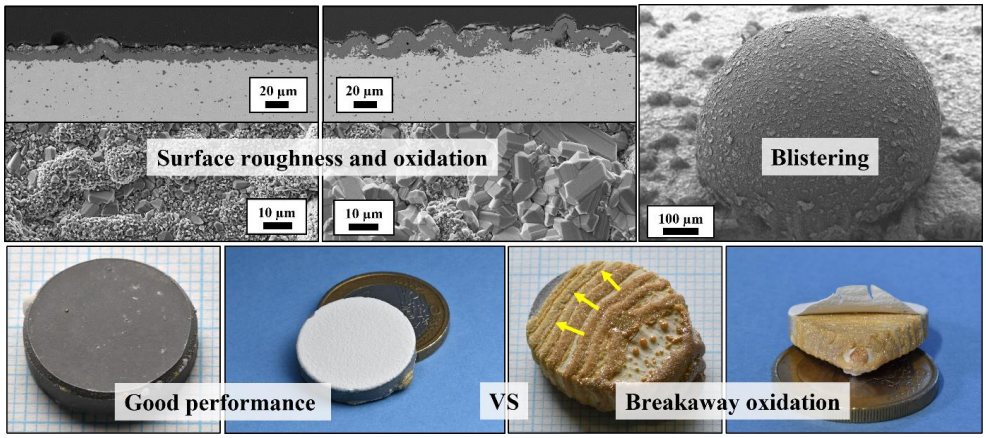

The most remarkable result remained the ability of alumina to plastically deform at high temperature, resulting in millimeter-sized macro-blisters, undamaged for oxidation times longer than 1200 h. These showed high diameter to thickness ratio within, at most, 24 h. Low force was required for their mechanical disruption and breakage could ensue during sample handling. However, in a long-term scenario, the growth of TiO_2 within the free blister volume and its collision with the Al_2O_3 scale was responsible for the collapse. The subsequent rupture of these convex structures is believed to initiate breakaway oxidation, which manifested through the

formation of a highly porous and striated arrangement of mixed oxide layers. Large ocher-colored nodules were scattered across the sample and were preferentially located at sharp edges or area where the alumina layer was disrupted. As a consequence, the protective characteristic was lost as no continuous dense alumina layer could form, and the base material was catastrophically consumed by inward growth of oxides.
Despite breakaway oxidation issues, the long-term cyclic performance of YSZ-coated Ti_2AlC was demonstrated, with samples surviving up to 1517 h at 1200 °C without any sign of coating spallation. Burner rig testing, at an extreme surface temperature of 1400 °C, also showed the ability of YSZ/Ti_2AlC systems to withstand high surface temperatures better than conventional superalloys coated with new generation double-layered thermal barrier coatings.

- Preliminary mechanical testing

A preliminary study of mechanical properties was also conducted, the outcomes of which point out interesting aspects to be investigated in the future.
Fractographic analysis evidenced the dominant intergranular fracture mode due to the fine-grained microstructure of MS^3-based Ti_2AlC.
Fractured surfaces of composites did not show significant fiber pullout as the strong bonding between matrix and fibers facilitated through-fiber crack propagation instead of interfacial deflection. Indentation showed that the addition of fibers did not contribute to increase the material's hardness, while monolithic samples demonstrated energy-absorbing mechanisms such as material pileup, chipping or absence of cracks up to intermediate loads. The addition of fibers helped to improve the room-temperature compressive strength by a factor 2.5, though the high-temperature compression performance was found to be lower for fiber-reinforced Ti_2AlC composites.
Even though the incorporation of alumina fibers did not increase either hardness or toughness, it is expected that the creep resistance can be improved.

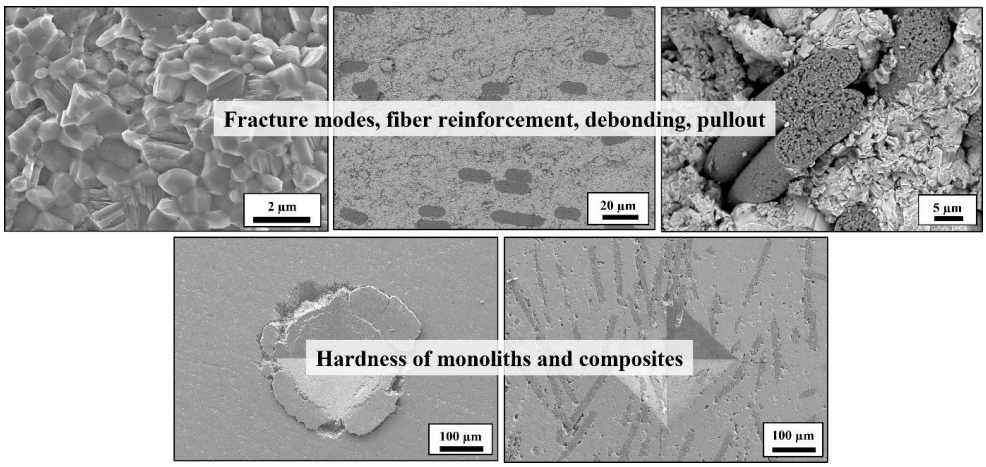

The outcomes presented in this thesis complement data about synthesis and oxidation of Ti_2AlC gathered in the last decades and are worth being considered in the case of high-temperature applications in oxidative media. Overgrowth of rutile is detrimental to the system's integrity and future works focusing on how to constrain its formation would be highly beneficial. Furthermore, the build-up of mixed oxide layers with a micro-banding morphology observed in breakaway conditions suggests a specific diffusional pattern of alternate depletion of

aluminum and titanium. Future fundamental studies performed at the atomic scale, such as by means of transmission electron microscopy, tracers or *in situ* electron probe microanalysis, would be required to bringing a deeper understanding of this phenomenon.

The design of fiber-reinforced MAX phase composites with the tailoring of suitable coatings for alumina fibers would be an interesting track to pursue. Future optimization studies would have to focus on the control of the sintering procedure, as it appeared to be the key step in avoiding mullite-containing fibers to decompose. Additionally, mold design considerations, such as the determination of cavity expansion coefficients [111], could help maintaining homogeneous dimensions.

Last but not least, the procedure of powder bed sintering applied to MAX phases requires optimization studies. The influence of the tool dimensions and the nature of the refractory pressure-transmitting particulate bed would provide a better apprehension of the consolidation mechanisms.

List of Figures

List of Tables

References

1. UNEP CLIMATE ACTION. UNFCCC COP 21 Paris France - 2015 Paris Climate Conference. 2017. Available from: https://www.cop21paris.org/about/cop21/

2. United Nations Climate Change. What is the Kyoto Protocol?. United Nations Climate Change. 2019. p. 1–6. Available from: https://unfccc.int/kyoto_protocol

3. Reed RC. The Superalloys: Fundamentals and Applications. Cambridge: Cambridge University Press; 2006.

4. Pollock TM, Tin S. Nickel-Based Superalloys for Advanced Turbine Engines: Chemistry, Microstructure and Properties. J Propuls Power. 2006;22(2):361–74.

5. Lagow BW. Materials Selection in Gas Turbine Engine Design and the Role of Low Thermal Expansion Materials. JOM. 2016;68(11):2770–5.

6. Ohnabe H, Masaki S, Onozuka M, Miyahara K, Sasa T. Potential application of ceramic matrix composites to aero-engine components. Compos Part A Appl Sci Manuf. 1999;30(4):489–96.

7. Christin F. CMC Materials for Space and Aeronautical Applications. In: Ceramic Matrix Composites. Weinheim, Germany: Wiley-VCH Verlag GmbH & Co. KGaA; 2008. p. 327–51.

8. Naslain RR. Ceramic matrix composites. Philos Trans R Soc London Ser A Phys Eng Sci. 1995;351(1697):485–96.

9. Steibel J. Ceramic matrix composites taking flight at GE Aviation. Vol. 98, American Ceramic Society Bulletin. 2019. p. 30–3.

10. Naslain RR. SiC-Matrix Composites: Nonbrittle Ceramics for Thermo-Structural Application. Int J Appl Ceram Technol. 2005;2(2):75–84.

11. Opila EJ, Smialek JL, Robinson RC, Fox DS, Jacobson NS. SiC Recession Caused by SiO_2 Scale Volatility under Combustion Conditions: II, Thermodynamics and Gaseous-Diffusion Model. J Am Ceram Soc. 1999;82(7):1826–34.

12. Lee KN, Fox DS, Bansal NP. Rare earth silicate environmental barrier coatings for SiC/SiC composites and Si_3N_4 ceramics. J Eur Ceram Soc. 2005;25(10):1705–15.

13. Fahrenholtz WG, Hilmas GE. Ultra-high temperature ceramics: Materials for extreme environments. Scr Mater. 2017;129:94–9.

14. Justin J-F, Julian-Jankowiak A, Guérineau V, Mathivet V, Debarre A. Ultra-high temperature ceramics developments for hypersonic applications. CEAS Aeronaut J. 2020;11(3):651–64.

15. Zoli L, Vinci A, Galizia P, Melandri C, Sciti D. On the thermal shock resistance and mechanical properties of novel unidirectional UHTCMCs for extreme environments. Sci Rep. 2018;8(1):9148.

16. Wuchina E, Opila E, Opeka M, Fahrenholtz B, Talmy I. UHTCs: Ultra-High Temperature Ceramic Materials for Extreme Environment Applications. Electrochem Soc Interface. 2007;16(4):30–6.

17. Fahrenholtz WG, Hilmas GE, Talmy IG, Zaykoski JA. Refractory Diborides of Zirconium and Hafnium. J Am Ceram Soc. 2007;90(5):1347–64.

18. Barsoum MW. MAX phases: Properties of machinable ternary carbides and nitrides. 2013. 1–421 p.

19. Barsoum MW. The $M_{N+1}AX_N$ phases: A new class of solids. Prog Solid State Chem. 2000;28(1–4):201–81.

20. Jeitschko W, Nowotny H, Benesovsky F. Kohlenstoffhaltige ternäre Verbindungen (H-Phase). Monatshefte für Chemie. 1963;94(4):672–6.

21. Jeitschko W, Nowotny H, Benesovsky F. Carbides of formula T_2MC. J Less Common Met. 1964;7(2):133–8.

22. Jeitschko W, Nowotny H. Die Kristallstruktur von Ti_3SiC_2—ein neuer Komplexcarbid-Typ. Monatshefte für Chemie - Chem Mon. 1967;98(2):329–37.

23. Sokol M, Natu V, Kota S, Barsoum MW. On the Chemical Diversity of the MAX Phases. Trends Chem. 2019;1(2):210–23.

24. Barsoum MW, El-Raghy T. Synthesis and characterization of a remarkable ceramic: Ti_3SiC_2. J Am Ceram Soc. 1996;79(7):1953–6.

25. Son W, Duong T, Talapatra A, Prehn E, Tan Z, Radovic M, et al. Minimal effect of stacking number on intrinsic cleavage and shear behavior of $Ti_{n+1}AlC_n$ and $Ta_{n+1}AlC_n$ MAX phases. J Appl Phys. 2018;123(22):225102.

26. Palmquist J-P, Li S, Persson POÅ, Emmerlich J, Wilhelmsson O, Högberg H, et al. $M_{n+1}AX_n$ phases in the Ti−Si−C system studied by thin-film synthesis and *ab initio* calculations. Phys Rev B. 2004;70(16):165401.

27. Liu Z, Wu E, Wang J, Qian Y, Xiang H, Li X, et al. Crystal structure and formation mechanism of $(Cr_{2/3}Ti_{1/3})_3AlC_2$ MAX phase. Acta Mater. 2014;73:186–93.

28. Tao Q, Dahlqvist M, Lu J, Kota S, Meshkian R, Halim J, et al. Two-dimensional $Mo_{1.33}C$ MXene with divacancy ordering prepared from parent 3D laminate with in-plane chemical ordering. Nat Commun. 2017;8(1):14949.

29. Hamm CM, Bocarsly JD, Seward G, Kramm UI, Birkel CS. Non-conventional synthesis and magnetic properties of MAX phases $(Cr/Mn)_2AlC$ and $(Cr/Fe)_2AlC$. J Mater Chem C. 2017;5(23):5700–8.

30. Fashandi H, Dahlqvist M, Lu J, Palisaitis J, Simak SI, Abrikosov IA, et al. Synthesis of Ti_3AuC_2, $Ti_3Au_2C_2$ and Ti_3IrC_2 by noble metal substitution reaction in Ti_3SiC_2 for high-temperature-stable Ohmic contacts to SiC. Nat Mater. 2017;16(8):814–8.

31. Horlait D, Middleburgh SC, Chroneos A, Lee WE. Synthesis and DFT investigation of new bismuth-containing MAX phases. Sci Rep. 2016;6(1):18829.

32. Ding H, Li Y, Lu J, Luo K, Chen K, Li M, et al. Synthesis of MAX phases Nb_2CuC and $Ti_2(Al_{0.1}Cu_{0.9})N$ by A-site replacement reaction in molten salts. Mater Res Lett. 2019;7(12):510–6.

33. Li M, Lu J, Luo K, Li Y, Chang K, Chen K, et al. Element Replacement Approach by Reaction with Lewis Acidic Molten Salts to Synthesize Nanolaminated MAX Phases and MXenes. J Am Chem Soc. 2019;141(11):4730–7.

34. Gonzalez-Julian J. Processing of MAX phases: From synthesis to applications. J Am Ceram Soc. 2021;104(2):659–90.

35. Ho CY, Powell RW, Liley PE. Thermal Conductivity of the Elements. J Phys Chem Ref Data. 1972;1(2):279–421.

36. Wood C, Emin D, Gray PE. Thermal conductivity behavior of boron carbides. Phys Rev B. 1985;31(10):6811–4.

37. Radosevich LG, Williams WS. Thermal Conductivity of Transition Metal Carbides. J Am Ceram Soc. 1970;53(1):30–3.

38. Slack GA. Thermal Conductivity of Pure and Impure Silicon, Silicon Carbide, and Diamond. J Appl Phys. 1964;35(12):3460–6.

39. Nakano H, Watari K, Kinemuchi Y, Ishizaki K, Urabe K. Microstructural characterization of high-thermal-conductivity SiC ceramics. J Eur Ceram Soc. 2004;24(14):3685–90.

40. Volz E, Roosen A, Hartung W, Winnacker A. Electrical and thermal conductivity of liquid phase sintered SiC. J Eur Ceram Soc. 2001;21(10–11):2089–93.

41. Tallman DJ, Anasori B, Barsoum MW. A critical review of the oxidation of Ti_2AlC, Ti_3AlC_2 and Cr_2AlC in air. Mater Res Lett. 2013;1(3):115–25.

42. Wang X., Zhou Y. Oxidation behavior of Ti_3AlC_2 at 1000–1400 °C in air. Corros Sci. 2003;45(5):891–907.

43. Qian XK, He XD, Li YB, Sun Y, Li H, Xu DL. Cyclic oxidation of Ti_3AlC_2 at 1000–1300°C in air. Corros Sci. 2011;53(1):290–5.

44. Barsoum MW, El-Raghy T, Ali M. Processing and characterization of Ti_2AlC, Ti_2AlN, and $Ti_2AlC_{0.5}N_{0.5}$. Metall Mater Trans A. 2000;31(7):1857–65.

45. Morrell R. Handbook of properties of technical & engineering ceramics Pt.1, an introduction for the engineer and designer. H.M. Stationery Office; 1985. 348 p.

46. Ti_2AlC reinforced bronze-based brake pad material used for high-speed railway and preparation method thereof. China; CN103273058A, 2013.

47. Cr_2AlC reinforced bronze-based brake pad material used for high-speed railway and preparation method thereof. China; CN103273057A, 2013.

48. Ti_3SiC_2 reinforced-bronze-based brake pad material for high speed railway and preparation method thereof. China; CN103273059A, 2013.

49. Kisi EH, Wu E, Zobec JS, Forrester JS, Riley DP. Inter-conversion of $M_{n+1}AX_n$ phases in the Ti-Al-C system. J Am Ceram Soc. 2007;90(6):1912–6.

50. Łopaciński M, Puszynski J, Lis J. Synthesis of Ternary Titanium Aluminum Carbides Using Self-Propagating High-Temperature Synthesis Technique. J Am Ceram Soc. 2001;84(12):3051–3.

51. Ivchenko VI, Kosolapova TY. Conditions of preparation of ternary Ti-Al-C alloy powders. Sov Powder Metall Met Ceram. 1975;14(6):431–3.

52. Ivchenko VI, Lesnaya MI, Nemchenko VF, Kosolapova TY. Some physical properties of ternary compounds in the system Ti-Al-C. Sov Powder Metall Met Ceram. 1976;15(5):367–9.

53. Ohls K, Bogdain B. History of inductively coupled plasma atomic emission spectral analysis: from the beginning up to its coupling with mass spectrometry. J Anal At Spectrom. 2016;31(1):22–31.

54. Rietveld HM. A profile refinement method for nuclear and magnetic structures. J Appl Crystallogr. 1969;2(2):65–71.

55. Pietzka MA, Schuster JC. Summary of constitutional data on the Aluminum-Carbon-Titanium system. J Phase Equilibria. 1994;15(4):392–400.

56. Benitez R, Kan WH, Gao H, O'Neal M, Proust G, Radovic M. Room temperature stress-strain hysteresis in Ti_2AlC revisited. Acta Mater. 2016;105:294–305.

57. Zhou AG, Barsoum MW. Kinking nonlinear elastic deformation of Ti_3AlC_2, Ti_2AlC, $Ti_3Al(C_{0.5},N_{0.5})_2$ and $Ti_2Al(C_{0.5},N_{0.5})$. J Alloys Compd. 2010;498(1):62–70.

58. Kulkarni SR, Wu AVDK-H. Synthesis of Ti_2AlC by spark plasma sintering of TiAl–carbon nanotube powder mixture. J Alloys Compd. 2010;490(1–2):155–9.

59. Sleptsov S V., Bondar AA, Witusiewicz VT, Hecht U, Hallstedt B, Petyukh VM, et al. Cocrystallization of MAX-Phases in the Ti–Al–C System. Powder Metall Met Ceram. 2015;54(7–8):471–81.

60. Yeh CL, Shen YG. Effects of TiC and Al_4C_3 addition on combustion synthesis of Ti_2AlC. J Alloys Compd. 2009;470(1–2):424–8.

61. Hendaoui A, Vrel D, Amara A, Langlois P, Andasmas M, Guerioune M. Synthesis of high-purity polycrystalline MAX phases in Ti–Al–C system through mechanically activated self-propagating high-temperature synthesis. J Eur Ceram Soc. 2010;30(4):1049–57.

62. Rutkowski P, Huebner J, Kata D, Chlubny L, Lis J, Witulska K. Thermal properties and laser processing of hot-pressed materials from Ti–Al–C system. J Therm Anal Calorim. 2019;137(6):1891–902.

63. Spencer CB, Córdoba JM, Obando N, Sakulich A, Radovic M, Odén M, et al. Phase evaluation in Al_2O_3 fiber-reinforced Ti_2AlC during sintering in the 1300°C-1500°C temperature range. Zhou Y, editor. J Am Ceram Soc. 2011;94(10):3327–34.

64. Pang WK, Low IM, O'Connor BH, Peterson VK, Studer AJ, Palmquist JP. In situ diffraction study of thermal decomposition in Maxthal Ti_2AlC. J Alloys Compd. 2011;509(1):172–6.

65. Zhang Z, Lim SH, Lai DMY, Tan SY, Koh XQ, Chai J, et al. Probing the oxidation behavior of Ti_2AlC MAX phase powders between 200 and 1000 °C. J Eur Ceram Soc. 2017;37(1):43–51.

66. Galvin T, Hyatt NC, Rainforth WM, Reaney IM, Shepherd D. Molten salt synthesis of MAX phases in the Ti-Al-C system. J Eur Ceram Soc. 2018;38(14):4585–9.

67. Barsoum MW, Brodkin D, El-Raghy T. Layered machinable ceramics for high temperature applications. Scr Mater. 1997;36(5):535–41.

68. Merzhanov AG, Borovinskaya IP. Historical retrospective of SHS: An autoreview. Int J Self-Propagating High-Temperature Synth. 2008;17(4):242–65.

69. Khoptiar Y, Gotman I. Ti_2AlC ternary carbide synthesized by thermal explosion. Mater Lett. 2002;57(1):72–6.

70. Liang B, Wang M, Li X, Sun S, Zou Q, Mu Y, et al. Synthesis of Ti_2AlC by laser-induced self-propagating high-temperature sintering. J Alloys Compd. 2010;501(1):L1–3.

71. Zhou WB, Mei BC, Zhu JQ, Hong XL. Rapid synthesis of Ti_2AlC by spark plasma sintering technique. Mater Lett. 2005;59(1):131–4.

72. Vershinnikov VI, Kovalev DY. Synthesis of the Ti_2AlC MAX Phase with a Reduction Step via Combustion of a TiO2 + Mg + Al + C Mixture. Inorg Mater. 2018;54(9):949–52.

73. Wang X, Zhou Y. Solid-Liquid Reaction Synthesis and Simultaneous Densification of Polycrystalline Ti_2AlC. Zeitschrift für Met. 2002;93(1):66–71.

74. Hashimoto S, Takeuchi M, Inoue K, Honda S, Awaji H, Fukuda K, et al. Pressureless sintering and mechanical properties of titanium aluminum carbide. Mater Lett. 2008;62(10–11):1480–3.

75. Hendaoui A, Vrel D, Amara A, Benaldjia A, Langlois P. Ti-Al-C MAX phases by aluminothermic reduction process. Int J Self-Propagating High-Temperature Synth. 2008;17(2):125–8.

76. Gauthier-Brunet V, Cabioc'h T, Chartier P, Jaouen M, Dubois S. Reaction synthesis of layered ternary Ti_2AlC ceramic. J Eur Ceram Soc. 2009;29(1):187–94.

77. Hong X, Mei B, Zhu J, Zhou W. Fabrication of Ti_2AlC by hot pressing of Ti, TiC, Al and active carbon powder mixtures. J Mater Sci. 2004;39(5):1589–92.

78. Guillon O, Gonzalez-Julian J, Dargatz B, Kessel T, Schierning G, Räthel J, et al. Field-assisted sintering technology/spark plasma sintering: Mechanisms, materials, and technology developments. Vol. 16, Advanced Engineering Materials. 2014. p. 830–49.

79. Li L, Zhou A, Xu L, Li Z, Wang L. Synthesis of high pure Ti_3AlC_2 and Ti_2AlC powders from TiH_2 powders as Ti source by tube furnace. J Wuhan Univ Technol Sci Ed. 2013;28(5):882–7.

80. Dash A, Vaßen R, Guillon O, Gonzalez-Julian J. Molten salt shielded synthesis of oxidation prone materials in air. Nat Mater. 2019;18(5):465–70.

81. Dash A, Sohn YJ, Vaßen R, Guillon O, Gonzalez-Julian J. Synthesis of Ti_3SiC_2 MAX phase powder by a molten salt shielded synthesis (MS^3) method in air. J Eur Ceram Soc. 2019;39(13):3651–9.

82. Asthana R, Kumar A, Dahotre NB. Powder Metallurgy and Ceramic Forming. In: Materials Processing and Manufacturing Science. Elsevier; 2006. p. 167–245.

83. Wilhelmsson O, Palmquist J-P, Nyberg T, Jansson U. Deposition of Ti_2AlC and Ti_3AlC_2 epitaxial films by magnetron sputtering. Appl Phys Lett. 2004;85(6):1066–8.

84. Wilhelmsson O, Palmquist J-P, Lewin E, Emmerlich J, Eklund P, Persson POÅ, et al. Deposition and characterization of ternary thin films within the Ti–Al–C system by DC magnetron sputtering. J Cryst Growth. 2006;291(1):290–300.

85. Rosén J, Ryves L, Persson POÅ, Bilek MMM. Deposition of epitaxial Ti_2AlC thin films by pulsed cathodic arc. J Appl Phys. 2007;101(5):056101.

86. Zhou A, Barsoum M, Basu S, Kalidindi S, El-Raghy T. Incipient and regular kink bands in fully dense and 10 vol.% porous Ti_2AlC. Acta Mater. 2006;54(6):1631–9.

87. Hu L, Benitez R, Basu S, Karaman I, Radovic M. Processing and characterization of porous Ti_2AlC with controlled porosity and pore size. Acta Mater. 2012;60(18):6266–77.

88. Gonzalez-Julian J, Bram M. Processing and Characterization of Porous Ti_2AlC Using Space Holder Technique. Key Eng Mater. 2016;704:197–203.

89. Velasco B, Gordo E, Hu L, Radovic M, Tsipas SA. Influence of porosity on elastic properties of Ti_2AlC and Ti_3SiC_2 MAX phase foams. J Alloys Compd. 2018;764:24–35.

90. Sun Z, Liang Y, Li M, Zhou Y. Preparation of Reticulated MAX-Phase Support with Morphology-Controllable Nanostructured Ceria Coating for Gas Exhaust Catalyst Devices. J Am Ceram Soc. 2010;93(9):2591–7.

91. Potoczek M, Guzi de Moraes E, Colombo P. Ti_2AlC foams produced by gel-casting. J Eur Ceram Soc. 2015;35(9):2445–52.

92. Frodelius J, Sonestedt M, Björklund S, Palmquist J-P, Stiller K, Högberg H, et al. Ti_2AlC coatings deposited by High Velocity Oxy-Fuel spraying. Surf Coatings Technol. 2008;202(24):5976–81.

93. Zhang Z, Lim SH, Chai J, Lai DMY, Lim PC, Cheong AKH, et al. Kerosene-fuelled high velocity oxy-fuel (HVOF) spray of Ti_2AlC MAX phase powders. J Alloys Compd. 2018;735:377–85.

94. Trache R, Puschmann R, Leyens C, Berger LM, Matthey B, Herrmann M. Thermally sprayed Ti_3SiC_2 and Ti_2AlC MAX-phase coatings. In: Proceedings of the International Thermal Spray Conference. 2013. p. 74–8.

95. Zhang Z, Lim SH, Chai J, Lai DMY, Cheong AKH, Cheong KL, et al. Plasma spray of Ti_2AlC MAX phase powders: Effects of process parameters on coatings' properties. Surf Coatings Technol. 2017;325:429–36.

96. Gutzmann H, Gärtner F, Höche D, Blawert C, Klassen T. Cold Spraying of Ti_2AlC MAX-Phase Coatings. J Therm Spray Technol. 2013;22(2–3):406–12.

97. Markocsan N, Manitsas D, Jiang J, Björklund S. MAX-phase coatings produced by thermal spraying. J Superhard Mater. 2017;39(5):355–64.

98. Belmonte M, Koller M, Moyano JJ, Seiner H, Miranzo P, Osendi MI, et al. Multifunctional 3D-Printed Cellular MAX-Phase Architectures. Adv Mater Technol. 2019;4(9):1900375.

99. Nan B, Yin X, Zhang L, Cheng L. Three-Dimensional Printing of Ti_3SiC_2-Based Ceramics. J Am Ceram Soc. 2011;94(4):969–72.

100. Ma Y, Yin X, Fan X, Wang L, Greil P, Travitzky N. Near-Net-Shape Fabrication of Ti_3SiC_2-based Ceramics by Three-Dimensional Printing. Int J Appl Ceram Technol. 2015;12(1):71–80.

101. Gonzalez-Julian J, Classen L, Bram M, Vaßen R, Guillon O. Near net shaping of monolithic and composite MAX phases by injection molding. Travitzky N, editor. J Am Ceram Soc. 2016;99(10):3210–3.

102. Stumpf M, Fan X, Biggemann J, Greil P, Fey T. Topological interlocking and damage mechanisms in periodic Ti_2AlC-Al building block composites. J Eur Ceram Soc. 2019;39(6):2003–9.

103. Hull C. Apparatus for production of three dimensional objects by Stereolithography. United States; US4575330, 1986.

104. Wong K V., Hernandez A. A Review of Additive Manufacturing. ISRN Mech Eng. 2012;2012:1–10.

105. Ngo TD, Kashani A, Imbalzano G, Nguyen KTQ, Hui D. Additive manufacturing (3D printing): A review of materials, methods, applications and challenges. Compos Part B Eng. 2018;143:172–96.

106. Elsayed H, Chmielarz A, Potoczek M, Fey T, Colombo P. Direct ink writing of three dimensional Ti_2AlC porous structures. Addit Manuf. 2019;28:365–72.

107. Depka T, Flores Renteria A, Laux B, Ott M, Piegert S. Verfahren zur Herstellung eines Bauteils aus MAX-Phasen. WO 2016/156082 AI, 2016.

108. Hyatt IS, Hyatt JW. Improvement in Process and Apparatus for Manufacturing Pyroxyline. USA; US133229A, 1872.

109. Friedrich Johannaber. Injection Molding Machines: A User's Guide. Munich: Carl Hanser Publishers; 2008.

110. German RM. Powder Injection Molding. Metal Powder Industries Federation. 1990. 521 p.

111. German RM, Bose A. Injection Molding of Metals and Ceramics. Metal Powder Industries Federation; 1997. 413 p.

112. Tabares E, Cifuentes SC, Jiménez-Morales A, Tsipas SA. Injection moulding of porous MAX phase Ti_3SiC_2 without using space-holder. Powder Technol. 2021;380:96–105.

113. Liao T, Wang J, Zhou Y. Ab initio modeling of the formation and migration of monovacancies in Ti_2AlC. Scr Mater. 2008;59(8):854–7.

114. Wang J, Zhou Y, Liao T, Zhang J, Lin Z. A first-principles investigation of the phase stability of Ti_2AlC with Al vacancies. Scr Mater. 2008;58(3):227–30.

115. Lin Z, Zhuo M, Zhou Y, Li M, Wang J. Microstructures and Adhesion of the Oxide Scale Formed on Titanium Aluminum Carbide Substrates. J Am Ceram Soc. 2006;89(9):2964-66.

116. Dahlqvist M, Alling B, Abrikosov IA, Rosén J. Phase stability of Ti_2AlC upon oxygen incorporation: A first-principles investigation. Phys Rev B. 2010;81(2):024111.

117. Wagner C. Beitrag zur Theorie des Anlaufvorgangs. Zeitschrift für Phys Chemie. 1933;21B(1):25–41.

118. Sauceda D, Singh P, Falkowski AR, Chen Y, Doung T, Vazquez G, et al. High-throughput reaction engineering to assess the oxidation stability of MAX phases. npj Comput Mater. 2021;7(1):6.

119. Prescott R, Graham MJ. The formation of aluminum oxide scales on high-temperature alloys. Oxid Met. 1992;38(3–4):233–54.

120. Umakoshi Y, Yamaguchi M, Sakagami T, Yamane T. Oxidation resistance of intermetallic compounds Al_3Ti and TiAl. J Mater Sci. 1989;24(5):1599–603.

121. Barsoum MW. Oxidation of $Ti_{n+1}AlX_n$ (n=1-3 and X=C, N): I. Model. J Electrochem Soc. 2001;148(8):C544.

122. Barsoum MW, Tzenov N, Procopio A, El-Raghy T, Ali M. Oxidation of $Ti_{n+1}AlX_n$ (n=1-3 and X=C, N): II. Experimental results. J Electrochem Soc. 2001;148(8):C551.

123. Wang XH, Zhou YC. High-temperature oxidation behavior of Ti_2AlC in air. Oxid Met [Internet]. 2003;59(3–4):303–20.

124. Sundberg M, Malmqvist G, Magnusson A, El-Raghy T. Alumina forming high temperature silicides and carbides. Ceram Int. 2004;30(7):1899–904.

125. Byeon JW, Liu J, Hopkins M, Fischer W, Garimella N, Park KB, et al. Microstructure and Residual Stress of Alumina Scale Formed on Ti_2AlC at High Temperature in Air. Oxid Met. 2007;68(1–2):97–111.

126. Basu S, Obando N, Gowdy A, Karaman I, Radovic M. Long-term oxidation of Ti_2AlC in air and water vapor at 1000–1300°C temperature range. J Electrochem Soc. 2011;159(2):C90–6.

127. Sonestedt M, Frodelius J, Sundberg M, Hultman L, Stiller K. Oxidation of Ti_2AlC bulk and spray deposited coatings. Corros Sci. 2010;52(12):3955–61.

128. Wang QM, Garkas W, Renteria AF, Leyens C, Lee HW, Kim KH. Oxidation behaviour of Ti–Al–C films composed mainly of a Ti_2AlC phase. Corros Sci. 2011;53(9):2948–55.

129. Frodelius J, Lu J, Jensen J, Paul D, Hultman L, Eklund P. Phase stability and initial low-temperature oxidation mechanism of Ti_2AlC thin films. J Eur Ceram Soc. 2013;33(2):375–82.

130. Song GM, Li SB, Zhao CX, Sloof WG, van der Zwaag S, Pei YT, et al. Ultra-high temperature ablation behavior of Ti_2AlC ceramics under an oxyacetylene flame. J Eur Ceram Soc. 2011;31(5):855–62.

131. Xu J, Gao Z, Qian Y, Li M. Ultra-High-Temperature Oxidation and Thermal Stability of Ti_2AlC in Air at 1600–1800 °C. Oxid Met. 2016;86(3–4):327–38.

132. Rao JC, Pei YT, Yang HJ, Song GM, Li SB, De Hosson JTM. TEM study of the initial oxide scales of Ti_2AlC. Acta Mater. 2011;59(13):5216–23.

133. Cui B, Jayaseelan DD, Lee WE. Microstructural evolution during high-temperature oxidation of Ti_2AlC

ceramics. Acta Mater. 2011;59(10):4116–25.

134. Yang HJ, Pei YT, Rao JC, De Hosson JTM, Li SB, Song GM. High temperature healing of Ti_2AlC: on the origin of inhomogeneous oxide scale. Scr Mater. 2011;65(2):135–8.

135. Li S, Song G, Kwakernaak K, van der Zwaag S, Sloof WG. Multiple crack healing of a Ti_2AlC ceramic. J Eur Ceram Soc. 2012;32(8):1813–20.

136. Yang HJ, Pei YT, Rao JC, De Hosson JTM. Self-healing performance of Ti_2AlC ceramic. J Mater Chem. 2012;22(17):8304.

137. Song GM, Schnabel V, Kwakernaak C, van der Zwaag S, Schneider JM, Sloof WG. High temperature oxidation behaviour of Ti_2AlC ceramic at 1200°C. Mater High Temp. 2012;29(3):205–9.

138. Zhu H, Qian X, Wu H, Lei J, Song Y, He X, et al. Cyclic Oxidation of Ternary Layered Ti_2AlC at 600-1000°C in Air. Int J Appl Ceram Technol. 2015;12(2):403–10.

139. Smialek JL. Environmental resistance of a Ti_2AlC-type MAX phase in a high pressure burner rig. J Eur Ceram Soc. 2017;37(1):23–34.

140. Kong F, Feng K, Bai Y, Li N, Qi X, Zheng Y, et al. Oxidation behavior of high-purity nonstoichiometric Ti_2AlC powders in flowing air. J Mater Res. 2017;32(14):2747–54.

141. Guo L, Yan Z, Wang X, He Q. Ti_2AlC MAX phase for resistance against CMAS attack to thermal barrier coatings. Ceram Int. 2019;45(6):7627–34.

142. Yan Z, Guo L, Zhang Z, Wang X, Ye F. Versatility of potential protective layer material Ti_2AlC on resisting CMAS corrosion to thermal barrier coatings. Corros Sci. 2020;167:108532.

143. Yu W, Vallet M, Levraut B, Gauthier-Brunet V, Dubois S. Oxidation mechanisms in bulk Ti_2AlC: Influence of the grain size. J Eur Ceram Soc. 2020;40(5):1820–8.

144. Li X, Xie X, Gonzalez-Julian J, Malzbender J, Yang R. Mechanical and oxidation behavior of textured Ti_2AlC and Ti_3AlC_2 MAX phase materials. J Eur Ceram Soc. 2020;40(15):5258–71.

145. Evans HE, Donaldson AT, Gilmour TC. Mechanisms of breakaway oxidation and application to a chromia-forming steel. Oxid Met. 1999;52(5):379–402.

146. Jianian S, Longjiang Z, Tiefan L. High-temperature oxidation of Fe-Cr alloys in wet oxygen. Oxid Met. 1997;48(3–4):347–56.

147. Quadakkers WJ, Bongartz K. The prediction of breakaway oxidation for alumina forming ODS alloys using oxidation diagrams. Mater Corros. 1994;45(4):232–41.

148. Gurrappa I, Weinbruch S, Naumenko D, Quadakkers WJ. Factors governing breakaway oxidation of FeCrAl-based alloys. Mater Corros. 2000;51(4):224–35.

149. Feng Z, Ke P, Huang Q, Wang A. The scaling behavior and mechanism of Ti_2AlC MAX phase coatings in air and pure water vapor. Surf Coatings Technol. 2015;272:380–6.

150. Li W, Wang Z, Shuai J, Xu B, Wang A, Ke P. A high oxidation resistance Ti_2AlC coating on Zirlo substrates for loss-of-coolant accident conditions. Ceram Int. 2019;45(11):13912–22.

151. Wang XH, Zhou YC. Intermediate-temperature oxidation behavior of Ti_2AlC in air. J Mater Res. 2002;17(11):2974–81.

152. Wang XH, Zhou YC. Oxidation behavior of Ti_3AlC_2 powders in flowing air. J Mater Chem. 2002;12(9):2781–5.

153. Hanaor DAH, Sorrell CC. Review of the anatase to rutile phase transformation. J Mater Sci. 2011;46(4):855–74.

154. Lin ZJ, Li MS, Wang JY, Zhou YC. Influence of water vapor on the oxidation behavior of Ti_3AlC_2 and Ti_2AlC. Scr Mater. 2008;58(1):29–32.

155. Tang C, Steinbrück M, Große M, Bergfeldt T, Seifert HJ. Oxidation behavior of Ti_2AlC in the temperature range of 1400 °C–1600 °C in steam. J Nucl Mater. 2017;490:130–42.

156. Li X, Zheng L, Qian Y, Xu J, Li M. Breakaway oxidation of Ti_3AlC_2 during long-term exposure in air at 1100 °C. Corros Sci. 2016;104:112–22.

157. Smialek JL. Unusual oxidative limitations for Al-MAX phases. NASA/TM—2017-219444. 2017.

158. Li X, Zheng L, Qian Y, Xu J, Li M. Thickness-dependent oxidation behaviors of Ti_3AlC_2 foils at 1100 °C in air. Corros Sci. 2021;185:109431.

159. Donchev A, Schütze M, Ström E, Galetz M. Oxidation behaviour of the MAX-phases Ti_2AlC and $(Ti,Nb)_2AlC$ at elevated temperatures with and without fluorine treatment. J Eur Ceram Soc. 2019;39(15):4595–601.

160. Wang Z, Sun J, Xu B, Liu Y, Ke P, Wang A. Reducing the self-healing temperature of Ti_2AlC MAX phase coating by substituting Al with Sn. J Eur Ceram Soc. 2020;40(1):197–201.

161. Li C, Qian Y, Ma C, Wang S, Li M. Suppressing the anomalous rapid oxidation of Ti_3AlC_2 by incorporating TiB_2. J Mater Sci Technol. 2019;35(3):432–9.

162. Li M, Li C, Li J, Zhou Y. Oxidation Behavior of a Ti_3AlC_2/TiB_2 Composite at 1000°−1400°C in Air. J Am Ceram Soc. 2010;93(2):554–60.

163. Wang XH, Zhou YC. Improvement of intermediate-temperature oxidation resistance of Ti_3AlC_2 by pre-oxidation at high temperatures. Mater Res Innov. 2003;7(4):205–11.

164. Lin Z, Zhou Y, Li M, Wang J. Hot corrosion and protection of Ti_2AlC against Na_2SO_4 salt in air. J Eur Ceram Soc. 2006;26(16):3871–9.

165. Smialek JL. Oxidation of Al_2O_3 scale-forming MAX phases in turbine environments. Metall Mater Trans A. 2018;49(3):782–92.

166. Padture NP. Thermal Barrier Coatings for Gas-Turbine Engine Applications. Science. 2002;296(5566):280–4.

167. Smialek J, Miller R. Revisiting the Birth of 7YSZ Thermal Barrier Coatings: Stephan Stecura †. Coatings. 2018;8(7):255.

168. Smialek JL, Harder BJ, Garg A. Oxidative durability of TBCs on Ti_2AlC MAX phase substrates. Surf Coatings Technol. 2016;285:77–86.

169. Gonzalez-Julian J, Go T, Mack DE, Vaßen R. Thermal cycling testing of TBCs on Cr_2AlC MAX phase substrates. Surf Coatings Technol. 2018;340:17–24.

170. Gonzalez-Julian J, Mauer G, Sebold D, Mack DE, Vassen R. Cr_2AlC MAX phase as bond coat for thermal barrier coatings: Processing, testing under thermal gradient loading, and future challenges. J Am Ceram Soc. 2020;103(4):2362–75.

171. Smialek JL, Cuy MD, Harder BJ, Garg A, Rogers RB. Durability of YSZ coated Ti_2AlC in 1300°C high velocity burner rig tests. J Am Ceram Soc. 2020;103(12):7014–30.

172. Chen D, Shirato K, Barsoum MW, El-Raghy T, Ritchie RO. Cyclic Fatigue-Crack Growth and Fracture Properties in Ti_3SiC_2 Ceramics at Elevated Temperatures. J Am Ceram Soc. 2001;84(12):2914–20.

173. Orowan E. A type of plastic deformation new in metals. Nature. 1942;149(3788):643–4.

174. Frank FC, Stroh AN. On the Theory of Kinking. Proc Phys Soc Sect B. 1952;65(10):811–21.

175. Barsoum MW, Zhen T, Zhou A, Basu S, Kalidindi SR. Microscale modeling of kinking nonlinear elastic solids. Phys Rev B. 2005;71(13):134101.

176. Bai Y, He X, Zhu C, Chen G. Microstructures, Electrical, Thermal, and Mechanical Properties of Bulk Ti_2AlC Synthesized by Self-Propagating High-Temperature Combustion Synthesis with Pseudo Hot Isostatic Pressing. Zangvil A, editor. J Am Ceram Soc. 2012;95(1):358–64.

177. Bai Y, He X, Wang R, Sun Y, Zhu C, Wang S, et al. High temperature physical and mechanical properties of large-scale Ti_2AlC bulk synthesized by self-propagating high temperature combustion synthesis with pseudo hot isostatic pressing. J Eur Ceram Soc. 2013;33(13–14):2435–45.

178. Hu C, Sakka Y, Grasso S, Nishimura T, Guo S, Tanaka H. Shell-like nanolayered Nb_4AlC_3 ceramic with

high strength and toughness. Scr Mater. 2011;64(8):765–8.

179. Benitez R, Gao H, O'Neal M, Lovelace P, Proust G, Radovic M. Effects of microstructure on the mechanical properties of Ti_2AlC in compression. Acta Mater. 2018;143:130–40.

180. Poon B, Ponson L, Zhao J, Ravichandran G. Damage accumulation and hysteretic behavior of MAX phase materials. J Mech Phys Solids. 2011;59(10):2238–57.

181. Naik Parrikar P, Benitez R, Gao H, Radovic M, Shukla A. The Effect of Grain Size on Deformation and Failure of Ti_2AlC MAX Phase under Thermo-Mechanical Loading. Exp Mech. 2017;57(5):675–85.

182. Zhan Z, Radovic M, Srivastava A. On the non-classical crystallographic slip in $Ti_{n+1}AlC_n$ MAX phases. Scr Mater. 2021;194:113698.

183. Zhou YC, Wang XH. Deformation of polycrystalline Ti_2AlC under compression. Mater Res Innov. 2001;5(2):87–93.

184. Benitez R, Kan WH, Gao H, O'Neal M, Proust G, Srivastava A, et al. Mechanical properties and microstructure evolution of Ti_2AlC under compression in 25–1100 °C temperature range. Acta Mater. 2020;189:154–65.

185. Naik Parrikar P, Benitez R, Gao H, Radovic M, Shukla A. Mechanical response of fine grained Ti_2AlC under extreme thermo-mechanical loading conditions. Mater Sci Eng A. 2016;658:176–84.

186. Radovic M, Barsoum M., El-Raghy T, Wiederhorn S. Tensile creep of fine grained (3–5 μm) Ti_3SiC_2 in the 1000–1200°C temperature range. Acta Mater. 2001;49(19):4103–12.

187. Radovic M, Barsoum MW, El-Raghy T, Wiederhorn SM. Tensile creep of coarse-grained Ti_3SiC_2 in the 1000–1200°C temperature range. J Alloys Compd. 2003;361(1–2):299–312.

188. Dash A, Malzbender J, Dash K, Rasinski M, Vaßen R, Guillon O, et al. Compressive creep of SiC whisker/Ti_3SiC_2 composites at high temperature in air. J Am Ceram Soc. 2020;103(10):5952–65.

189. Dash A, Malzbender J, Vaßen R, Guillon O, Gonzalez-Julian J. Short SiC fiber/Ti_3SiC_2 MAX phase composites: Fabrication and creep evaluation. J Am Ceram Soc. 2020;103(12):7072–81.

190. Bao YW, Zhou YC. Bending Creep and Stress Relaxation of Ti_3AlC_2 at High Temperature. Key Eng Mater. 2007;280–283:1373–8.

191. Tallman DJ, Naguib M, Anasori B, Barsoum MW. Tensile creep of Ti_2AlC in air in the temperature range 1000–1150°C. Scr Mater. 2012;66(10):805–8.

192. Drouelle E, Joulain A, Cormier J, Gauthier-Brunet V, Villechaise P, Dubois S, et al. Deformation mechanisms during high temperature tensile creep of Ti_3AlC_2 MAX phase. J Alloys Compd. 2017;693:622–30.

193. Bai Y, Kong F, He X, Li N, Qi X, Zheng Y, et al. Thermal shock behavior of Ti_2AlC from 200°C to 1400°C. J Am Ceram Soc. 2017;100(9):4190–8.

194. Krenkel W. Ceramic Matrix Composites: Fiber Reinforced Ceramics and their Applications. Wiley; 2008. 1–418 p.

195. Chollon G. Oxidation Behavior of Ceramic Fibers from the Si-C-N-O System and Sub-Systems. Key Eng Mater. 1998;164–165:395–8.

196. Morgan PED, Marshall DB. Functional interfaces for oxide/oxide composites. Mater Sci Eng A. 1993;162(1–2):15–25.

197. Hay RS, Boakye EE. Monazite Coatings on Fibers: I, Effect of Temperature and Alumina Doping on Coated-Fiber Tensile Strength. J Am Ceram Soc. 2001;84(12):2783–92.

198. Gonzalez-Julian J, Llorente J, Bram M, Belmonte M, Guillon O. Novel Cr_2AlC MAX-phase/SiC fiber composites: Synthesis, processing and tribological response. J Eur Ceram Soc. 2017;37(2):467–75.

199. Go T, Vaßen R, Guillon O, Gonzalez-Julian J. Processing and oxidation response of Cr_2AlC MAX-phase composites containing ceramic fibers. Open Ceram. 2021;6:100090.

200. Zhou WB, Mei BC, Zhu JQ. Rapid reactive synthesis of Ti_2AlC-TiB_2 composites by spark plasma

sintering. J Ceram Process Res. 2009;10(1):102–4.

201. Li C, Li M, Zhou Y, Zhang J, He L. In Situ Synthesis and Properties of Ti_3AlC_2/TiB_2 Composites. J Am Ceram Soc. 2007;90(11):3615–20.

202. Li Z, Zhou A, Li L, Wang L, Hu M, Li S, et al. Synthesis and characterization of novel Ti_3SiC_2–cBN composites. Diam Relat Mater. 2014;43:29–33.

203. Tian W, Sun Z, Hashimoto H, Du Y. Synthesis, microstructure and mechanical properties of Ti_3SiC_2–TiC composites pulse discharge sintered from Ti/Si/TiC powder mixture. Mater Sci Eng A. 2009;526(1–2):16–21.

204. Ho-Duc LH, El-Raghy T, Barsoum MW. Synthesis and characterization of 0.3 V_f TiC–Ti_3SiC_2 and 0.3 V_f SiC–Ti_3SiC_2 composites. J Alloys Compd. 2003;350(1–2):303–12.

205. Yang J, Pan LM, Gu W, Gu XB, Song K, Qiu T, et al. Oxidation behavior and kinetics of in situ (TiB_2+TiC)/Ti_3SiC_2 composites in air. Ceram Int. 2012;38(1):159–68.

206. Zhu J, Jiang H, Wang F, Yang C, Xiao D. Synthesis, microstructure and mechanical properties of Cr_2AlC/Al_2O_3 in situ composites by reactive hot pressing. J Eur Ceram Soc. 2014;34(16):4137–44.

207. Lagos MA, Pellegrini C, Agote I, Azurmendi N, Barcena J, Parco M, et al. Ti_3SiC_2-Cf composites by spark plasma sintering: Processing, microstructure and thermo-mechanical properties. J Eur Ceram Soc. 2019;39(9):2824–30.

208. Spencer CB, Córdoba JM, Obando NH, Radovic M, Odén M, Hultman L, et al. The Reactivity of Ti_2AlC and Ti_3SiC_2 with SiC Fibers and Powders up to Temperatures of 1550°C. J Am Ceram Soc. 2011;94(6):1737–43.

209. Wang K, Li M, Liang Y, Wang J, He L, Du S, et al. Interface modification of carbon fibers with TiC/Ti_2AlC coating and its effect on the tensile strength. Ceram Int. 2019;45(4):4661–6.

210. Guo S, Hu C, Gao H, Tanaka Y, Kagawa Y. SiC(SCS-6) fiber-reinforced Ti_3AlC_2 matrix composites: Interfacial characterization and mechanical behavior. J Eur Ceram Soc. 2015;35(5):1375–84.

211. Guo S. Improvement of mechanical properties of SiC(SCS-6) fibre-reinforced Ti_3AlC_2 matrix composites with Ti barrier layer. J Eur Ceram Soc. 2016;36(6):1349–58.

212. Naik Parrikar P, Gao H, Radovic M, Shukla A. Static and Dynamic Thermo-Mechanical Behavior of Ti_2AlC MAX Phase and Fiber Reinforced Ti_2AlC Composites. In: Conference Proceedings of the Society for Experimental Mechanics Series. Springer New York LLC; 2015. p. 9–14.

213. Gonzalez-Julian J, Kraleva I, Belmonte M, Jung F, Gries T, Bermejo R. Multifunctional performance of Ti_2AlC MAX phase/2D braided alumina fiber laminates. J Am Ceram Soc. 2021;jace.18043.

214. Barbosa APC, Bram M, Stöver D, Buchkremer HP. Realization of a Titanium Spinal Implant with a Gradient in Porosity by 2-Component-Metal Injection Moulding. Adv Eng Mater. 2013;15(6):510–21.

215. Lange FF, Terwilliger GR. Method of compacting shaped powdered objects. US4041123, 1972.

216. Lichti WP, Hofstatter AF. Method of object consolidation employing graphite particulate. US4640711, 1985.

217. Hocquet S, Dupont V, Cambier F, Ludewig F, Vandewalle N. Densification of complex shape ceramics parts by SPS. J Eur Ceram Soc. 2020;40(7):2586–96.

218. Gonzalez-Julian J, Go T, Mack DE, Vaßen R. Environmental resistance of Cr_2AlC MAX phase under thermal gradient loading using a burner rig. J Am Ceram Soc. 2018;101(5):1841–6.

219. Niihara K. A fracture mechanics analysis of indentation-induced Palmqvist crack in ceramics. J Mater Sci Lett. 1983;2(5):221–3.

220. Hettinger JD, Lofland SE, Finkel P, Meehan T, Palma J, Harrell K, et al. Electrical transport, thermal transport, and elastic properties of M_2AlC (M = Ti , Cr, Nb, and V). Phys Rev B. 2005;72(11):115120.

221. Zolotoyabko E. Determination of the degree of preferred orientation within the March–Dollase approach. J Appl Crystallogr. 2009;42(3):513–8.

222. Wang C-A, Zhou A, Qi L, Huang Y. Quantitative phase analysis in the Ti–Al–C ternary system by X-ray diffraction. Powder Diffr. 2005;20(3):218–23.

223. Bai Y, He X, Li Y, Zhu C, Zhang S. Rapid synthesis of bulk Ti_2AlC by self-propagating high temperature combustion synthesis with a pseudo–hot isostatic pressing process. J Mater Res. 2009;24(8):2528–35.

224. Fan Q, Chai H, Jin Z. Microstructural evolution in the combustion synthesis of titanium carbide. J Mater Sci. 1996;31(10):2573–7.

225. Sujata M, Bhargava S, Sangal S. On the formation of $TiAl_3$ during reaction between solid Ti and liquid Al. J Mater Sci Lett. 1997;16(14):1175–8.

226. Liu X, Zhang S. Low-temperature preparation of titanium carbide coatings on graphite flakes from molten salts. J Am Ceram Soc. 2008;91(2):667–70.

227. Tzenov N V., Barsoum MW. Synthesis and characterization of Ti_3AlC_2. J Am Ceram Soc. 2004;83(4):825–32.

228. Lim L-T, Auras R, Rubino M. Processing technologies for poly(lactic acid). Prog Polym Sci. 2008;33(8):820–52.

229. Rahaman MN. Sintering of ceramics. Boca Raton, USA: CRC Press, Taylor & Francis Group; 2007. 1–389 p.

230. Low I-M. An Overview of Parameters Controlling the Decomposition and Degradation of Ti-Based $M_{n+1}AX_n$ Phases. Materials (Basel). 2019;12(3):473.

231. Lu X, Zhou Y. Pressureless Sintering and Properties of Ti_3AlC_2. Int J Appl Ceram Technol. 2010;7(6):744–51.

232. Weiser MW, De Jonghe LC. Inclusion Size and Sintering of Composite Powders. J Am Ceram Soc. 1988;71(3):C-125-C–127.

233. Hsueh C-H. Sintering behaviour of powder compacts with multiheterogeneities. J Mater Sci. 1986;21(6):2067–72.

234. Stedman SJ, Evans JRG, Brook RJ, Hoffmann MJ. Anisotropic sintering shrinkage in injection-moulded composite ceramics. J Eur Ceram Soc. 1993;11(6):523–32.

235. Helle AS, Easterling KE, Ashby MF. Hot-isostatic pressing diagrams: New developments. Acta Metall. 1985;33(12):2163–74.

236. Goldberger WM, Merkle BD. Electroconsolidation offers fast, low-cost densification. Met Powder Rep. 2001;56(2):30–3.

237. Goldberger WM. Method for electroconsolidation of a preformed particulate workpiece. US5348694, 1993.

238. Tian J, Shobu K. Fracture strength of melt-infiltrated SiC-mullite composite. J Mater Sci. 2004;39(11):3751–5.

239. Tadmor Z. Molecular orientation in injection molding. J Appl Polym Sci. 1974;18(6):1753–72.

240. Gogos CG, Huang C-F, Schmidt LR. The process of cavity filling including the fountain flow in injection molding. Polym Eng Sci. 1986;26(20):1457–66.

241. Marchioli C, Fantoni M, Soldati A. Orientation, distribution, and deposition of elongated, inertial fibers in turbulent channel flow. Phys Fluids. 2010;22(3):033301.

242. Li W-J, Shi E-W, Yin Z-W. Growth habit of rutile and α-Al_2O_3 crystals. J Cryst Growth. 2000;208(1–4):546–54.

243. Balint D, Hutchinson J. An analytical model of rumpling in thermal barrier coatings. J Mech Phys Solids. 2005;53(4):949–73.

244. He MY, Evans AG, Hutchinson JW. The ratcheting of compressed thermally grown thin films on ductile substrates. Acta Mater. 2000;48(10):2593–601.

245. Tolpygo VK, Clarke DR. On the rumpling mechanism in nickel-aluminide coatings. Acta Mater. 2004;52(17):5115–27.

246. Drouelle E, Gauthier-Brunet V, Cormier J, Villechaise P, Sallot P, Naimi F, et al. Microstructure-oxidation resistance relationship in Ti_3AlC_2 MAX phase. J Alloys Compd. 2020;826:154062.

247. Song GM, Pei YT, Sloof WG, Li SB, De Hosson JTM, van der Zwaag S. Oxidation-induced crack healing in Ti_3AlC_2 ceramics. Scr Mater. 2008;58(1):13–6.

248. Subanovic M, Naumenko D, Kamruddin M, Meier G, Singheiser L, Quadakkers WJ. Blistering of MCrAlY-coatings in H_2/H_2O-atmospheres. Corros Sci. 2009;51(3):446–50.

249. Hutchinson JW, Thouless MD, Liniger EG. Growth and configurational stability of circular, buckling-driven film delaminations. Acta Metall Mater. 1992;40(2):295–308.

250. Karlsson AM. A fundamental model of cyclic instabilities in thermal barrier systems. J Mech Phys Solids. 2002;50(8):1565–89.

251. Venkatachari KR, Raj R. Superplastic Flow in Fine-Grained Alumina. J Am Ceram Soc. 1986;69(2):135–8.

252. Chen I-W, Xue LA. Development of Superplastic Structural Ceramics. J Am Ceram Soc. 1990;73(9):2585–609.

253. Smialek JL. Moisture-induced delayed spallation and interfacial hydrogen embrittlement of alumina scales. JOM. 2006;58(1):29–35.

254. Hass KC, Schneider WF, Curioni A, Andreoni W. The Chemistry of Water on Alumina Surfaces: Reaction Dynamics from First Principles. Science. 1998;282(5387):265–8.

255. Van Orman JA, Crispin KL. Diffusion in Oxides. Rev Mineral Geochemistry. 2010;72(1):757–825.

256. Slepetys RA, Vaughan PA. Solid solution of aluminum oxide in rutile titanium dioxide. J Phys Chem. 1969;73(7):2157–62.

257. Kwakernaak C, Sloof WG. Work of adhesion of interfaces between M_2AlC (M = Ti, V, Cr) MAX phases and α-Al_2O_3. Ceram Int. 2018;44(18):23172–9.

258. Bayer G. Thermal expansion characteristics and stability of pseudobrookite-type compounds, Me_3O_5. J Less Common Met. 1971;24(2):129–38.

259. Moon J, Choi H, Kim H, Lee C. The effects of heat treatment on the phase transformation behavior of plasma-sprayed stabilized ZrO_2 coatings. Surf Coatings Technol. 2002;155(1):1–10.

260. Patil RN, Subbarao EC. Monoclinic–tetragonal phase transition in zirconia: mechanism, pretransformation and coexistence. Acta Crystallogr Sect A. 1970;26(5):535–42.

261. Zhu D, Miller RA. Sintering and creep behavior of plasma-sprayed zirconia- and hafnia-based thermal barrier coatings. Surf Coatings Technol. 1998;108–109(1–3):114–20.

262. Mahade S, Curry N, Björklund S, Markocsan N, Joshi S. Durability of Gadolinium Zirconate/YSZ Double-Layered Thermal Barrier Coatings under Different Thermal Cyclic Test Conditions. Materials (Basel). 2019;12(14):2238.

263. Bond DM, Zikry MA. Differentiating between intergranular and transgranular fracture in polycrystalline aggregates. J Mater Sci. 2018;53(8):5786–98.

264. Amini S, Barsoum MW, El-Raghy T. Synthesis and Mechanical Properties of Fully Dense Ti_2SC. J Am Ceram Soc. 2007;90(12).

265. El-Raghy T, Zavaliangos A, Barsoum MW, Kalidindi SR. Damage Mechanisms around Hardness Indentations in Ti_3SiC_2. J Am Ceram Soc. 2005;80(2):513–6.

266. Liang KM, Orange G, Fantozzi G. Evaluation by indentation of fracture toughness of ceramic materials. J Mater Sci. 1990;25(1):207–14.

267. Bei G-P, Laplanche G, Gauthier-Brunet V, Bonneville J, Dubois S. Compressive Behavior of Ti_3AlC_2 and $Ti_3Al_{0.8}Sn_{0.2}C_2$ MAX Phases at Room Temperature. Zhou Y, editor. J Am Ceram Soc. 2013;96(2):567–

76.

268. Meng FL, Zhou YC, Wang JY. Strengthening of Ti_2AlC by substituting Ti with V. Scr Mater. 2005;53(12):1369–72.

Band / Volume 590
NiFe Layered Double Hydroxide Catalysts for Oxygen Evolution Reaction in Alkaline Water Electrolysis
W. Jiang (2022), 165 pp
ISBN: 978-3-95806-658-8

Band / Volume 591
Optimizing Cross-linked Infrastructure for Future Energy Systems
L. Welder (2022), xxiii, 360 pp
ISBN: 978-3-95806-659-5

Band / Volume 592
Evaluation von Reaktorkonzepten für die CO_2-basierte Methanolsynthese aus Wasserstoff und Kohlendioxid mithilfe von CFD-Simulationen
S. Weiske (2022), x, 369 pp
ISBN: 978-3-95806-661-8

Band / Volume 593
Spectral Induced Polarization of Biochar in Soil
Z. Gao (2022), XXVI, 155 pp
ISBN: 978-3-95806-662-5

Band / Volume 594
Eignung von nickelhaltigen Katalysatorsystemen in sauren Medien zur Nutzung im Betrieb von Brennstoffzellen
A. Karaca (2022), iv, 249 pp
ISBN: 978-3-95806-663-2

Band / Volume 595
Seasonal Comparison of the Chemical Composition and Source Apportionment of Aerosols during the Year-Long JULIAC Campaign
L. Liu (2022), VIII, 189 pp
ISBN: 978-3-95806-668-7

Band / Volume 596
Nanoscale Understanding and Control of Metal Exsolution in Perovskite Oxides
M. L. Weber (2022), ix, 160 pp
ISBN: 978-3-95806-669-4

Band / Volume 597
Nanostructures of Transition Metal Sulfides for Anion Exchange Membrane Water Electrolysis
L. Xia (2022), 161 pp
ISBN: 978-3-95806-670-0

Band / Volume 598
Recycling- und Defossilisierungsmaßnahmen der Energieintensiven Industrie Deutschlands im Kontext von CO_2-Reduktionsstrategien
F. Kullmann (2022), XII, 237 pp
ISBN: 978-3-95806-672-4

Band / Volume 599
IEK-14 Report 2022
Research contributions for the energy transition and structural change in the Rhineland
B. Emonts (Ed.) (2022), 83 pp
ISBN: 978-3-95806-676-2

Band / Volume 600
Development of Glass-based Sealants for the Joining of Oxygen Transport Membranes
X. Li (2022), IV, 159 pp
ISBN: 978-3-95806-677-9

Band / Volume 601
High-resolution imaging of transport processes with GPR full-waveform inversion
P. Haruzi (2022), iv, 173 pp
ISBN: 978-3-95806-678-6

Band / Volume 602
Synthesis of optimized cathode materials for all-solid-state lithium batteries
C. Roitzheim (2022), xv, 221 pp
ISBN: 978-3-95806-679-3

Band / Volume 603
Development of components based on Ti_2AlC/fiber composites for aggressive environmental conditions
S. Badie (2023), x, 161 pp
ISBN: 978-3-95806-680-9

Weitere ***Schriften des Verlags im Forschungszentrum Jülich*** unter
http://wwwzb1.fz-juelich.de/verlagextern1/index.asp

Energie & Umwelt / Energy & Environment
Band / Volume 603
ISBN 978-3-95806-680-9

Mitglied der Helmholtz-Gemeinschaft

JÜLICH
Forschungszentrum